Polymer-Free Carbon Nanotube Based Solar Cells

Zur Erlangung des akademischen Grades Doktor der Naturwissenschaften (Dr. rer. nat.)
genehmigte Dissertation von Moritz Pfohl aus Konstanz

Darmstadt 2018

TECHNISCHE
UNIVERSITÄT
DARMSTADT

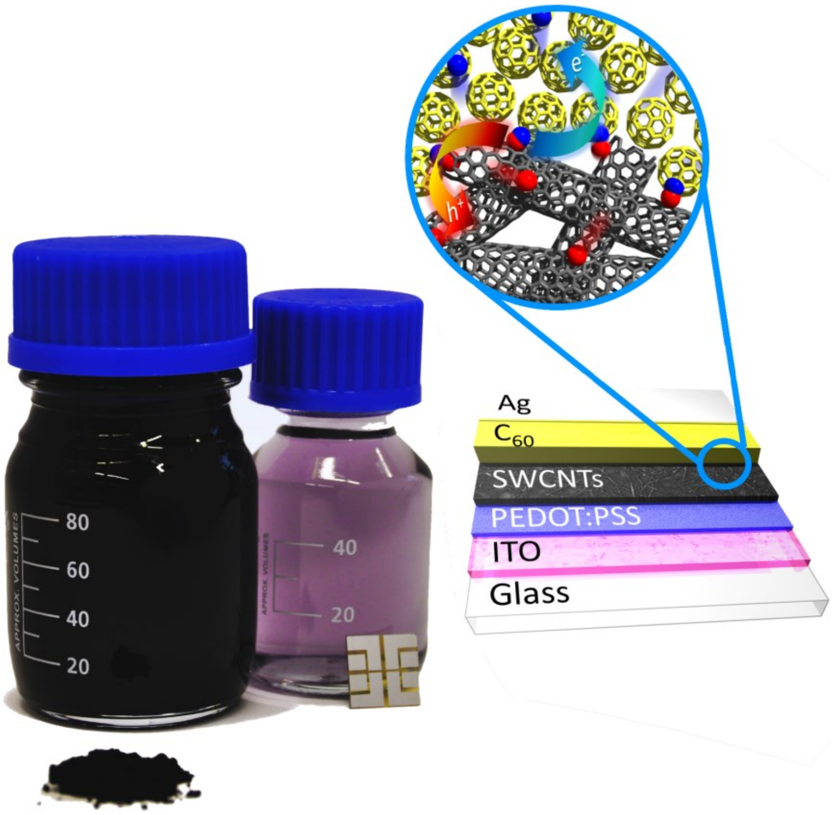

Nothing is too wonderful to be true if it be consistent with the laws of nature.

M. Faraday

Polymer-Free Carbon Nanotube Based Solar Cells
Polymerfreie Kohlenstoffnanoröhren Basierte Solarzellen

Dem Fachbereich Material- und Geowissenschaften der TU Darmstadt vorgelegte und genehmigte Dissertation zur Erlangung des akademischen Grade eines

Doktors der Naturwissenschaften (Dr. rer. nat.)

von MSc ETH Masch.-Ing. Moritz Pfohl aus Konstanz

Berichter: Prof. Dr. Ralph Krupke
Mitberichter: Prof. Dr. Wolfram Jägermann
Prüfer 1: Prof. Dr. Wolfgang Ensinger
Prüfer 2: Prof. Dr. Wolfgang Elsäßer

Tag der Einreichung: 24. März 2017
Tag der mündlichen Prüfung: 19. Oktober 2017

Darmstadt 2018, D17

– This page intentionally left blank –

Erklärung zur Dissertation

Hiermit versichere ich, die vorliegende Dissertation ohne Hilfe Dritter nur mit den angegebenen Quellen und Hilfsmitteln angefertigt zu haben. Alle Stellen, die aus Quellen entnommen wurden, sind als solche kenntlich gemacht. Diese Arbeit hat in gleicher oder ähnlicher Form noch keiner Prüfungsbehörde vorgelegen.

Darmstadt, den 09.01.2018

(Moritz Pfohl)

– This page intentionally left blank –

Scientific Pathway

06/2013 – 12/2016
Darmstadt, DE

TU Darmstadt – Institute for Material Science: Ph.D. in science

- Project: „Production and investigation of carbon nanotube based solar cells“
- 10 publications in total, 3 as first author
- Presented in front of ~60 attendants at the AMN 7 in Nelson, NZ
- Won a poster award (3 of 220 posters were awarded) at the NT 16 in Vienna, AUT

07/2010 – 03/2013
Zürich, CH

ETH Zürich - Laboratory of Thermodynamics in Emerging Technologies: Master

- Majoring in: Energy and fluid dynamics

02/2012 – 12/2012
Pasadena, USA

Caltech – Lab of Prof. Haile and Prof. Giapis: Master thesis

- Project: „ Performance Enhancement of Solid Acid Fuel Cells via Carbon Nanotubes”
- Published in Phys. Chem. Chem. Phys. 2013
- Patent filed in 2013

09/2007 – 06/2010
Zürich, CH

ETH Zürich – Department Mechanical and Methods Engineering: Bachelor

- Bachelor thesis: „ CFD Simulations of Heat Transfer in Microchannels“
- Majoring in: Energy, Flows and Processes

09/1998 – 06/2007
Bad Säckingen, DE

Scheffelgymnasium: Abitur

– This page intentionally left blank –

Zusammenfassung

Seit ihrer Entdeckung im Jahre 1991 und 1994 durch Iijima, haben einzel- und mehrwandige Kohlenstoffnanoröhren (engl.: SWCNTs und MWCNTs) auf Grund ihrer einzigartigen mechanischen (höhere Zugfestigkeit als Stahl), optischen (mehrere exzitonische Übergänge) und elektrischen (intrinsische Mobilität von 10^5 cm^2 V^{-1} s^{-1}) Eigenschaften großes Interesse in der Forschungsgemeinschaft geweckt. Diese herausragenden Eigenschaften können nur dann gezielt genutzt werden, wenn das schwarze Nanoröhrenpulver, welches während der Produktion anfällt, weiter aufbereitet wird, um die in etwa 2/3 halbleitenden und 1/3 metallischen Nanoröhren von verbliebenen katalytischen Partikeln, Kohlenstoffrückständen oder defekten Nanoröhren zu trennen. Nach einer ersten Aufbereitung ist es unerlässlich die Nanoröhren aufgrund ihrer elektrischen Eigenschaften weiter zu trennen, um sie beispielsweise in einem Transistor als Kanal- oder Elektrodenmaterial einsetzen zu können. Für optoelektronische Anwendungen, z.B. im Bereich der Photonenemitter oder Solarzellen, hingegen kann es von Vorteil sein halbleitende SWCNTs anhand ihrer einzigartigen Absorptionseigenschaften (abhängig von der Chiralität der SWCNT) zu trennen, so dass alle Kohlenstoffnanoröhren den gleichen optischen Übergang haben (sowohl im infraroten, als auch im visuellen und ultravioletten Bereich). Erst durch die Errungenschaft Nanoröhren mit gewünschter optischer Bandlücke gezielt zu sortieren und anreichern zu können, haben sich mehrere Möglichkeiten eröffnet den Absorptionsbereich klassischer Solarzellen zu erweitern oder gar gezielt zu gestalten; beispielsweise kann durch sorgfältige Wahl bestimmter Chiralitäten das Sonnenspektrum im visuellen oder infraroten Bereich optimal ausgenutzt werden.

Um die Vision von gezielter Lichtabsorption in die Tat umzusetzen, sind große Mengen aufbereiteter und nach elektrischer Eigenschaft und Chiralität getrennter SWCNTs nötig. In dieser Dissertation werden mit Hilfe von automatisierter Gel-Permeations-Chromatographie polymerfreie Kohlenstoffnanoröhren einer Chiralität im Milligramm Bereich sortiert, wobei die Diffusionslänge der Exzitonen nicht durch ein umgebendes Polymer beschränkt wird. Durch geschickte Wahl von Temperatur, Tensidkonzentration und Eluent können unterschiedlich gefärbte Lösungen erhalten werden, deren Nanoröhren entweder nach elektrischer Eigenschaft, Chiralität oder beidem getrennt wurden. Um interne Kurzschlüsse zu vermeiden dürfen Nanoröhren die in Solarzellen Verwendung finden nur einen Bruchteil und bestenfalls gar keine metallischen SWCNTs enthalten. Es ist deshalb unerlässlich die erhaltenen Nanoröhrenlösungen schnell und verlässlich auf ihren metallischen Gehalt und die Chiralitäten der gelösten SWCNTs hin zu untersuchen.

Eine Möglichkeit diese Untersuchung vorzunehmen ist die optische Absorptionsspektroskopie. Im Laufe dieser Dissertation wurde ein auf MATLAB® basierendes Programm entwickelt, mit dem mehrere Herausforderungen der optische Absorptionsspektroskopie gelöst werden können; u.a. das Abziehen verschiedener Hintergründe, die Wahl unterschiedlicher Linienprofile, die Berechnung der Spektrenentfaltung des zweiten, ersten oder beider Absorptionsbereiche oder das Berücksichtigen zusätzlicher metallischer SWCNTs, das die Berechnung der metallischen oder halbleitenden Reinheit der Nanoröhrenlösung erlaubt. Durch Erhalt des spektralen Gewichts jeder einzelnen Chirlität in Lösung können auch breite und überlappende Absorptionsspektren von SWCNT Filmen zuverlässig in Anteile einzelner Nanoröhren aufgeteilt werden.

Nach erfolgreicher Anreicherung und Charakterisierung einzelner Chiralitäten, werden großflächige Filme aus (6,5)er SWCNTs mit einheitlicher Morphologie mit Hilfe von „evaporationsgetriebener Selbstfertigung“ hergestellt. Die dadurch erhaltenen Nanoröhrenfilme werden mittels eines im Rahmen dieser Dissertation entwickeltem Übertragungsprozess, der die Zersetzung von hygroskopischen Schichten verhindert, in einer organischen Solarzelle integriert. In Kombination mit dem Fulleren C_{60} bilden die Nanoröhren eine zweilagige organische Solarzelle mit rein kohlenstoffhaltigem Donator- und Akzeptor-Paar. Transfer-Matrix-Berechnungen (engl.: TMC) werden eingesetzt, um die Lichtintensität an der Kontaktfläche von SWCNTs und C_{60} zu maximieren und um dadurch gezielt die Stromerzeugung durch den ersten (im Infraroten), den zweiten (im Visuellen) oder beide Absorptionsbereiche der Kohlenstoffnanoröhren zu erhöhen. Die Zuverlässigkeit dieses Ansatzes wird mit Hilfe einer umfangreichen Parameterstudie überprüft, wobei Spitzenwerte der internen Quanteneffizienz (IQE) von 86 % im Bereich des ersten Absorptionsbereichs der Nanoröhren erzielt werden.

Erst durch das Entwickeln einer zuverlässigen Solarzellenarchitektur, mit der sich hohe IQE Werte für SWCNTs mit kleinem Durchmesser erzielen lassen, kann die Machbarkeit von transparenten Solarzellen mit Nanoröhren großen Durchmessers (kleine Bandlücke) in Verbindung mit C_{60} getestet werden. Hierfür werden organische Solarzellen sowohl mit SWCNTs einzelner Chiralität und großem Durchmesser als auch mit Mixturen unterschiedlichster Durchmesser gebaut. Durch sorgsame Spektrenentfaltung von Absorptionsmessungen einzelner Nanoröhrenfilme und der dazugehörigen externen Quanteneffizienzmessungen, wird der größte SWCNT Durchmesser ermittelt für den kein Strom mehr erzeugt werden kann und dessen IQE folgerichtig 0 % ist. Die zugrunde liegenden Zusammenhänge für einen nach oben hin beschränkten Durchmesser werden diskutiert und mögliche Strategien aufgezeigt, um den Bereich nutzbarer Kohlenstoffnanoröhren über die Grenze der (8,6)er SWCNT (Durchmesser 0.95 nm) hinaus zu erweitern.

Abstract

Since their discovery in 1991 and 1994 by Iijima, multi walled (MWCNTs) and single walled carbon nanotubes (SWCNTs) have gained a lot of interest in the research community due to their unique mechanical (higher tensile strength than stainless steel), optical (multiple excitonic transitions) and electrical (intrinsic mobility of 10^5 cm^2 V^{-1} s^{-1}) properties. Being produced as black powder that contains roughly 1/3 metallic and 2/3 semiconducting nanotubes along with residual catalytic particles, carbon residues or defected nanotubes, it is important to further purify the raw nanotube powder to obtain pristine nanotubes only that can be used to exploit these remarkable properties. In order to incorporate SWCNTs as semiconducting channel material or as electrodes in transistors, it is of great importance to separate SWCNTs based on their electronic properties. Whereas, for optoelectronic applications, like photon emitters or solar cells it is necessary to sort semiconducting SWCNTs into chirality pure fractions with unique absorption features, i.e. the sorted nanotubes absorb at precise wavelengths (in the infrared, visible and UV). It is this ability to select SWCNTs with desired optical gaps that make SWCNTs an interesting material that also offers potential avenues to tailor or extend the light absorption within established solar cells. Through careful combination of the appropriate chiralities, a close match to the solar spectrum either in the visible or the infrared is possible.

To realize this vision of tailored light absorption, large amounts of purified, electronic type sorted and chirality enriched SWCNTs are needed. In this thesis, an automated aqueous based gel permeation chromatography (GPC) is used to sort milligrams of polymer-free single chirality enriched nanotube material, where the exciton diffusion length is not limited by a wrapping polymer. Depending on the temperature, surfactant concentration and eluent differently coloured solutions are obtained that can be electronic type pure, chirality pure or a mixture of chiralities and/or electronic types. In order to prevent internal shorts, SWCNTs employed in solar cells need to obtain as little metallic nanotubes as possible. It is therefore crucial to easily and reliably characterize the sorted nanotube solutions with respect to the contained chiralities and semiconducting or metallic purity.

One way of realizing such a characterization is optical absorption spectroscopy. A MATLAB® based program was developed throughout this thesis that is capable of addressing several issues involved in optical absorption spectroscopy of solutions: different approaches for background subtraction, the choice of different line profiles, the individual fit of the first or second transition (in the infrared and visible, respectively) or both at the same time and the inclusion of metallic nanotubes that allows for the evaluation of the metallic/semiconducting purity. Based on the spectral weight of each nanotube species identified in solution, absorbance spectra of carbon

nanotube films can be fitted, where overlapping peaks are decongested into individual nanotube contributions.

Following the sorting and characterization of single chirality SWCNTs, large-area films of (6,5) SWCNTs with uniform morphology are prepared using evaporation-driven self-assembly. The obtained SWCNT films are incorporated in an organic solar via a transfer process developed throughout this thesis that prevents the decomposition of hygroscopic layers in the solar cell. In conjunction with C_{60} a bi-layer organic solar cell with an all carbon donor and acceptor pair is formed. Transfer matrix calculations (TMCs) are employed to optimize the layer thicknesses of the solar cell in order to match the light intensity at the nanotubes first optical transition (in the infrared), their second transition (in the visible) or a combination thereof. The validity of this approach is verified by a detailed parameter study resulting in cutting edge internal quantum efficiency (IQE) of 86% through the nanotubes first transition.

Having established a reliable solar cell architecture resulting in large IQE values for small diameter SWCNTs (large bandgap), the feasibility of preparing transparent organic solar cells from large diameter SWCNTs (small bandgap) in combination with C_{60} is tested by preparing organic solar cells from single chirality large diameter SWCNTs as well as mixtures of nanotubes with varying diameters. By carefully decongesting film absorption spectra and associated external quantum efficiency measurements, the nanotube diameter resulting in 0 % IQE is determined. Underlying mechanisms of this limit are discussed and possible strategies to circumvent this cut-off are presented in order to extend the absorption range beyond the (8,6) SWCNT with a diameter of 0.95 nm.

Thesis Outline

This cumulative thesis consists of an introduction which provides the reader with a basic understanding of carbon nanotubes, their structural and electronic properties and why they can be utilized as the light absorbing material in solar cells. The introduction closes with an overview of organic solar cells, their basic working principle and light management in the solar cell to increase light harvesting in the active layer.

Following the introduction, the first paper “Fitting Single Walled Carbon Nanotube Optical Spectra” is reproduced which describes the analysis of carbon nanotube optical absorption spectroscopy; both from a fundamental and a practical point of view. It therefore presents not only a summary of previous work but also provides our current understanding of the underlying photophysics. The paper is structured in such a way that the reader is stepped through the decision process of fitting optical absorption data, including background subtraction, choice of different line shapes, the full width at half maximum (FWHM), the need of exciton phonon sidebands, different strategies to guess the initial peak heights and finally the selection of different (n,m) species to be fitted. Based on these fundamental properties, the paper goes on to highlight the additional benefits that come along with the provided fitting procedure; namely the fit of the entire spectrum, where the second excitonic transition region is constrained by the first one, inclusion of metallic nanotubes, indications of doping and the decongestion of broad and overlapping film absorption spectra based on the spectral weight of a solution fit. The paper closes, highlighting the usefulness of the provided fitting algorithms and the quantitative but yet reliable fitting routine, which was demonstrated by mixing (6,5) and (7,5) enriched starting solutions in known ratios and subsequently decongesting their absorption spectra into individual (n,m) concentrations. The presented fitting routine is then used in the following two papers to calculate the chiral purity of the carbon nanotube suspensions and in correlating film absorption measurements to external and internal quantum efficiency measurements.

In the second paper “Performance Enhancement of Polymer-Free Carbon Nanotube Solar Cells via Transfer Matrix Modeling” a detailed study of polymer-free single walled carbon nanotubes as the light active element in organic solar cells is presented. Previous work was focused on investigating and optimizing polymer wrapped carbon nanotubes, which have a limited exciton diffusion length. A proof-of-principle experiment conducted by Jain et al. indicated no such limit but raised the concern of mixing different (n,m) species without shielding them from one another with a polymer could cause a short; a concern, which will be addressed in the third paper presented in this thesis. The second paper summarizes the experimental principles and fundamental preparation techniques developed throughout this thesis. They include the description of an optimized sorting procedure to enrich (6,5) carbon nanotubes up to a purity of 93 % along with the ability to reproducibly prepare large area carbon nanotube films with comparable morphologies and a transfer mechanism to incorporate these films in solar cells. Furthermore, different characterization techniques such as scanning electron microscopy, photoluminescence measurements, atomic force microscopy, photo-electron yield spectroscopy in air, current voltage measurements and external and internal quantum measurements are presented. A detailed parameter study is conducted to evaluate the optimal layer thicknesses and solar cell design. This experimental study is complemented by a transfer matrix calculation, which can be used to calculate the distribution of the light intensity as a function of wavelength and position within the solar cell stack. One of the outcomes of this paper is that surfactant wrapped carbon nanotubes still have a minor but considerable quantity of metallic nanotubes that prevents the use of thick and dense polymer-free films, which ultimately limits the performance of polymer-free nanotubes in solar cells although they have comparable internal quantum efficiencies to polymer wrapped ones. Finally, the transfer matrix calculations are proven to be an important tool to tailor the light absorption and consequently the current production by the carbon nanotubes first, second or both optical transitions.

In the third and final paper of this thesis “Probing the Diameter Limit of Single Walled Carbon Nanotubes in SWCNT:C_{60} Solar Cells”, the diameter and absorption limits of polymer-free carbon nanotube solar cells are investigated. Having a reversed proportionality between diameter and bandgap, large diameter nanotubes absorb further in the infrared than small diameter ones. In previous work the diameter limit was speculated to be around 1.2 nm for polymer wrapped or bulk heterojunction solar cells but no experiment or study clearly indicated which (n,m) species would be the largest one to generate current in a solar cell. To resolve this question for polymer-free carbon nanotubes, mixtures of nanotubes with increasing average diameter are prepared and incorporated into solar cells. With the aids of transfer matrix calculations a sufficient electric field at the optical absorption of the nanotubes is guaranteed to prevent the mistake of assuming a missing signal in external quantum efficiency is due to the diameter cut-off instead of lacking light intensity. The fitting algorithm developed in paper one is used to decongest film absorption spectra in their individual nanotube contributions, which are then used to fit the external quantum efficiency measurements. In combination with internal reflectance measurements, the absorption of each nanotube film in the solar cell is calculated and together with the external quantum efficiency measurements the internal quantum efficiency and largest, current producing nanotube is derived. Finally, strategies to extend this limit further in the infrared are discussed. One important finding of this paper is that the initial concern of Jain et al., namely that mixing of different polymer-free (n,m) species results in a short in the solar cell, is disproved. However, a decreasing internal quantum efficiency for mixed chiralities compared to single chirality ones is observed and a detailed explanation for this observation is provided.

Additional information to all papers, a derivation of the transfer matrix formalism and a detailed description of the gel sorting approach is provided in the supporting information.

The thesis concludes with a summary of the most important findings and an outlook on future work that could deepen our understanding of carbon nanotube based solar cells and lead to potentially higher performing solar cells.

– This page intentionally left blank –

Acknowledgement

I would like to thank Prof. Dr. Ralph Krupke and Prof. Dr. Wolfram Jägermann for being the referee and co-referee, respectively, of this thesis. Furthermore I would like to express my gratitude towards Prof. Dr. Ralph Krupke for providing helpful insights, critical questions, experimental assistance and for many fruitful discussions.

I am also very grateful to Dr. Benjamin S. Flavel for being my supervisor. Without his ongoing advice, support, experimental expertise and patience during many rounds of draft revisions, this thesis would not have been possible.

I would like to thank the other members of the research group at the Institute of Nanotechnology (INT) for creating an open and helping working atmosphere and especially Dr. Daniel D. Tune who was a very pleasant office mate and a helping hand in idea crafting and draft corrections.

Additionally, several results presented in this thesis would not have been possible without the close collaboration with many research institutes.

Foremost I would like to express my gratitude to Dr. Alexander Colsmann, Konstantin Glaser and many of their group members at the Light Technology Institute (LTI) in Karlsruhe who helped to realize this work by providing equipment, expert knowledge on organic solar cells and their private time in assisting the production and testing of my devices.

I am also thankful to Arko Graf and Prof. Dr. Jana Zaumseil from the Institute for Physical Chemistry at the University Heidelberg who assisted with photoluminescence excitation maps and absorption spectra of polymer wrapped (6,5) nanotubes that were necessary for the development of my MATLAB® code.

I would also like to thank Prof. Yuan Chen and Dr. Li Wei from the School of Chemical and Biomolecular Engineering at the University of Sydney for providing large diameter (9,8) nanotubes needed for the verification of the diameter cut-off.

Finally, I would like to thank my family for their advice, support and motivation throughout my Ph.D. and of course my wife Miriam, for her ongoing patience, endorsement and love that gave me the energy to complete this work successfully.

– This page intentionally left blank –

Contents

List of Publications

The following contains a list of the original publications arising from the Author's Ph.D. studies, where publications (1), (2) and (5) are reproduced in Chapters 2 – 4. The corresponding supporting information is provided in the Appendices 7.3 – 7.5.

(1) A. Alam, S. Dehm, F. Hennrich, Y. Zakharko, A. Graf, **M. Pfohl**, I. M. Hossain, M. M. Kappes, J. Zaumseil, R. Krupke, B. S. Flavel, *Photocurrent Spectroscopy of Dye-Sensitized Carbon Nanotubes,* Nanoscale 2017, 9, 11205.

(2) **M. Pfohl**, D.D. Tune, A. Graf, J. Zaumseil, R. Krupke, B. S. Flavel, *Fitting Single Walled Carbon Nanotube Optical Spectra,* ACS Omega 2017, 2, 1163.

(3) **M. Pfohl**, K. Glaser, A. Graf, A. Mertens, D. D. Tune, T. Puerckhauer, A. Alam, L. Wei, Y. Chen, J. Zaumseil, A. Colsmann, R. Krupke, B. S. Flavel, *Probing the Diameter Limit of Single Walled Carbon Nanotubes in SWCNT:Fullerene Solar Cells*, Advanced Energy Materials 2016, 1600890.

(4) A. Graf, Y. Zakharko, S. P. Schießl, C. Backes, **M. Pfohl**, B. S. Flavel, J. Zaumseil, *Large Scale, Selective Dispersion of Long Single-Walled Carbon Nanotubes With High Photoluminescence Quantum Yield by Shear Force Mixing*, Carbon 2016, 105, 593

(5) D. D. Tune, B. W. Stolz, **M. Pfohl**, B. S. Flavel, *Dry Shear Aligning: a Simple and Versatile Method to Smooth and Align the Surfaces of Carbon Nanotube Thin Films*, Nanoscale 2016, 8, 3232

(6) **M. Pfohl**, K. Glaser, J. Ludwig, D. D. Tune, S. Dehm, C. Kayser, A. Colsmann, R. Krupke, B. S. Flavel, *Performance Enhancement of Polymer-Free Carbon Nanotube Solar Cells via Transfer Matrix Modeling*, Advanced Energy Materials 2016, 6, 1501345.

(7) D. D. Tune, A. J. Blanch, C. J. Shearer, K. E. Moore, **M. Pfohl**, J. G. Shapter, B. S. Flavel, *Aligned Carbon Nanotube Thin Films from Liquid Crystal Polyelectrolyte Inks*, ACS Appl. Mater. Interfaces 2015, 7, 25857

(8) K. E. Moore, **M. Pfohl**, D. D. Tune, F. Hennrich, S. Dehm, V. S. K. Chakradhanula, C. Kübel, R. Krupke, B. S. Flavel, *Sorting of Double-Walled Carbon Nanotubes According to Their Outer Wall Electronic Type via a Gel Permeation Method*, ACS Nano 2015, 9, 3849

(9) K. E. Moore, **M. Pfohl**, F. Hennrich, V. S. K. Chakradhanula, C. Kübel, M. M. Kappes, J. G. Shapter, R. Krupke, B. S. Flavel, *Separation of Double-Walled Carbon Nanotubes by Size Exclusion Column Chromatography*, ACS Nano 2014, 8, 6756

(10) B. S. Flavel, K. E. Moore, **M. Pfohl**, M. M. Kappes, F. Hennrich, *Separation of Single-Walled Carbon Nanotubes with a Gel Permeation Chromatography System*, *ACS Nano* 2014, 8, 1817

List of Abbreviations

AFM	Atomic Force Microscopy
a.u.	Arbitrary Unit
BCP	Bathocuproine
BHJ	Bulk Heterojunction
BSE	Bethe-Salpeter Equation
C_{60}	Fullerene Out Of 60 Carbon Atoms
CoMoCAT	CO Disproportionation on Co-Mo Catalyst
cps	Counts per Second
CSA	Chlorosulfonic Acid
CVD	Chemical Vapour Deposition
d	Diameter
D	Dispersion
DFG	Deutsche Forschungsgemeinschaft
DGU	Density Gradient Ultracentrifugation
DMA	Dimethylacetamide
DOS	Density of States
DWCNT	Double Walled Carbon Nanotube
EDSA	Evaporation Driven Self-Assembly
EPS	Exciton Phonon Sideband
Eq	Equation
EQE	External Quantum Efficiency
FF	Fill Factor
FWHM	Full Width at Half Maximum
GO	Graphene Oxide
GPC	Gel Permeation Chromatography
GW	Many Body’s Green Function
HiPco	High Pressure Carbon Monoxide
HOMO	Highest Occupied Molecular Orbital
HWHM	Half Width at Half Maximum
IQE	Internal Quantum Efficiency
ISO	International Organization for Standardization

ITO	Indium Tin Oxide
JV	Current Voltage
LUMO	Lowest Occupied Molecular Orbital
MWCNT	Multi Walled Carbon Nanotube
nSSE	Normalized Sum of Squared Errors
OD	Optical Density
OPV	Organic Photovoltaics
P3HT	Poly(3-hexylthiophene)
PCBM	[6,6]-Phenyl C Butyric Acid Methyl Ester
PEDOT:PSS	Poly(3,4-ethylenedioxythiophene) Polystyrene Sulfonate
PESA	Photo-Electron Yield Spectroscopy in Air
PFO	Poly(9,9-dioctylfluorenyl-2,7diyl)
PL	Photoluminescence
PLE	Photoluminescence Excitation
PMMA	Poly(methyl methacrylate)
rGO	Reduced Graphene Oxide
rr-P3AT	Regioregular Poly(3-alkylthiophene)
SC	Sodium Cholate
SDS	Sodium Dodecyl Sulphate
SEM	Scanning Electron Microscope
SRH	Shockley-Read-Hall
SWCNT	Single Walled Carbon Nanotube
TA	Transient Absorbance
TEM	Transmission Electron Microscope
TMC	Transfer Matrix Calculation
VASE	Variable Angle Spectroscopic Ellipsometry
WL	White Light Spectroscopy
wt	Percentage by Mass (Weight)
XPS	X-Ray Photoelectron Spectroscopy

1. Introduction

Motivation

Faced with a growing world population, higher living standards and growing energy demands, humanity is challenged to address the destructive effects of global warming. Coupled with an emerging awareness of the need for clean energy with a low CO_2 footprint the search for efficient energy production is driving the development of the so called “renewable energies”. Despite many current technologies fulfilling this demand, they come with certain limitations: hydropower plants need to have a mountainous landscape to be efficient, wind energy parks are best suited off-shore and geothermal stations have certain geological prerequisites. Solar cells on the other hand can in principle be installed over the entire surface of the planet, even in space (e.g. on the International Space Station) and currently contribute 6 % of the total energy consumed in Germany (2015).(1) Extending the electricity generated by renewable energies from 30 % in 2015 to 100 % in 2050,(2) the German government has set a very ambitious goal. To achieve this, the scope of solar cells needs to be extended beyond that of traditional solar cells. Traditional solar cells (e.g. silicon solar cells) are currently being placed on roofs, fields or in concentrator parks, where the absorption of light in the visible spectrum is maximized. Due to their stiffness and high absorption in the visible, traditional solar cells cannot be used on the glass facades of houses or skyscrapers, in clothes or on top of cell phones. One way of exploiting energy production from these new locations is with the aid of organic photovoltaics (OPVs) that can be produced cheaply via roll-to-roll processing and offer flexibility and transparency.(3) In order to realize transparent photovoltaics new materials are needed that extend the limit of absorbing light in the visible of traditional solar cells to extract light from the infrared (IR). One possible material that is capable of absorbing light in the near infrared (NIR) and IR is carbon nanotubes (CNTs). CNTs have sharp absorption peaks that can be tailored by choosing the appropriate diameter. Carbon nanotubes not only allow for the light absorption of a solar cell to be precisely engineered but also come with highly desirable properties such as high charge carrier mobility along the nanotube axis and excellent stability toward degradation in ambient, humid, hot or high UV radiation conditions.(4) These properties make CNTs an attractive material for the active, light absorbing component in organic solar cells.

1.1 Carbon Nanotubes

Carbon nanotubes are long rods of carbon atoms that can either be single walled (SWCNT), double walled (DWCNT) or multi walled (MWCNTs). Since their first discovery in 1991,(5) their growth mechanism and ways to tailor their diameter range and electronic property were extensively studied. There are basically three different ways to grow carbon nanotubes: arc discharge, laser ablation and chemical vapor deposition (CVD).(6) All of these techniques share certain commonalities that can be used to tailor the length, diameter, purity and electronic type of the carbon nanotubes, i.e. high temperatures, a carbon source and catalytic particles that initialize the growth of carbon nanotubes. Arc discharge evaporation was the first method used to prepare MWCNTs, where a DC voltage is applied between two graphite rods and the anode is evaporated. At temperatures between 1000 – 2000 °C nanotubes form on the catalytic particles embedded in the graphite rod and precipitate on the cathode.(7) Upon controlling the temperature, composition and size of the catalytic particles, SWCNTs with diameters ranging from 1.2 – 1.7 nm can be produced with this method. A smaller diameter range can be obtained using laser ablation. The laser ablation method was developed in the group of R. Smalley in 1995 combining the evaporation of a graphite target in a heated reactor under inert atmosphere.(8) Using a nickel-cobalt mixture embedded in the graphite target and a temperature of 1200 °C, Thess et al. were able to fabricate SWCNT with a narrow diameter range around 1.4 nm.(9) Even smaller diameter ranges can only be obtained employing CVD, where the graphite rods and targets are replaced by a carbon feed gas, like acetylene or ethylene. The catalytic nanoparticles are placed on a substrate or feed in the gas stream directly into a tube furnace and initiate the decomposition of the hydrocarbon feed gas at lower temperatures than their decomposition temperature.(10) Upon diffusion of carbon into the metal, supersaturation takes place which initiates a tip (e.g. for nickel) or base (e.g for iron) growth of the carbon nanotube as indicated in Figure 1. Controlling the temperature (temperatures below 850 °C more likely yield MWCNTs due to the higher formation energy of SWCNTs) and particle size allows for growing either MWCNTs or SWCNTs, where the diameter of the SWCNTs is directly related to the size of the catalytic particles.(10) A modified CVD process utilizing high pressure carbon monoxide (HiPco) with iron carbon monoxide $Fe(CO)_5$ can be used to produce large amounts of defect free SWCNTs that have a diameter distribution between 0.6 nm and 1.3 nm.(11)

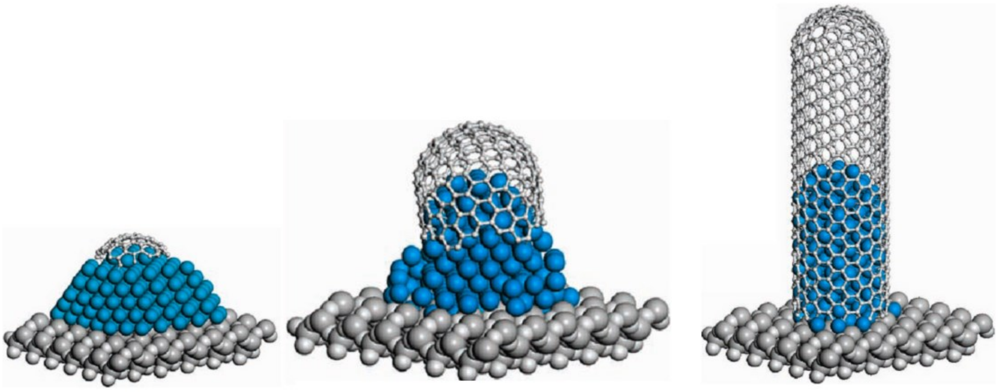

Figure 1. Schematic growth mechanism of carbon nanotubes. Upon supersaturation of a catalytic nanoparticle with carbon atoms, a cap is formed (left) that defines the chirality of the tube (center). The growth stops (right) as soon as all the carbon source particles are used or the uptake of new carbon atoms by the catalytic particle is blocked. The Schematic is reprinted (adapted) with permission from (12). Copyright (2007) American Chemical Society.

All of the methods to prepare carbon nanotubes share another commonality: they produce a mixture of semiconducting and metallic nanotubes in the ratio of about 2:1. To achieve the growth of individual chiralities with a yield of close to 100 % various strategies are currently pursued. For example the group of R. Fasel manufactured special designed carbon molecules, that serve as caps for SWCNTs that resulted in the growth of (6,6) only.(13) A different approach is the engineering of catalytic particles that favor the growth of a single chirality, e.g. (9,8) or (12,6).(14) A comprehensive overview of the current state of the art techniques and limitations in the field of growing chirality specific SWCNTs is given in the review from Yang et al.(15) However, all of the current techniques suffer from low yields and the need of further purification after growth. The only possibility to obtain high quality, single chirality SWCNTs is by sorting as prepared nanotube powder.

In the following sub-sections the structure and properties of carbon nanotubes will be discussed and methods to sort, characterize and prepare films will be reviewed.

1.1.1 *Structure and Properties*

Carbon nanotubes can be imagined as a sheet of graphene (honeycomb lattice of carbon atoms) that is rolled into a cylinder shaped tube. As there are countless ways to roll a cylinder from a sheet of graphene, there are numerous SWCNTs with vastly varying diameters and different electronic properties. Starting with the graphene unit cell and the vectors $\mathbf{a_1}$ and $\mathbf{a_2}$, as depicted in Figure 2, each individual tube can be described by forming the graphene lattice vector $\mathbf{c} = n \cdot \mathbf{a_1} + m \cdot \mathbf{a_2}$, which equally represents the circumference of the formed SWCNT.(16) Depending on the roll up vectors “n” and “m”, also called chiral indices “(n,m)”, the diameter d of the nanotube can be expressed as:(17)

$$d = \sqrt{(n^2 + m^2 + n \cdot m)} \cdot a_{C-C} \cdot \frac{\sqrt{3}}{\pi} \tag{1}$$

Where a_{C-C} is the carbon bond length of 0.142 nm.(17) The chiral indices can also be used to determine the electronic type of a specific SWCNT by calculating whether n-m is a multiple of 3 or 0 in which case the nanotube is metallic.(18) An example of the three different SWCNT types (chiral, armchair or zig-zag) is shown in Figure 2 along with a honeycomb lattice that illustrates the different (n,m) chiralities and their diameter.

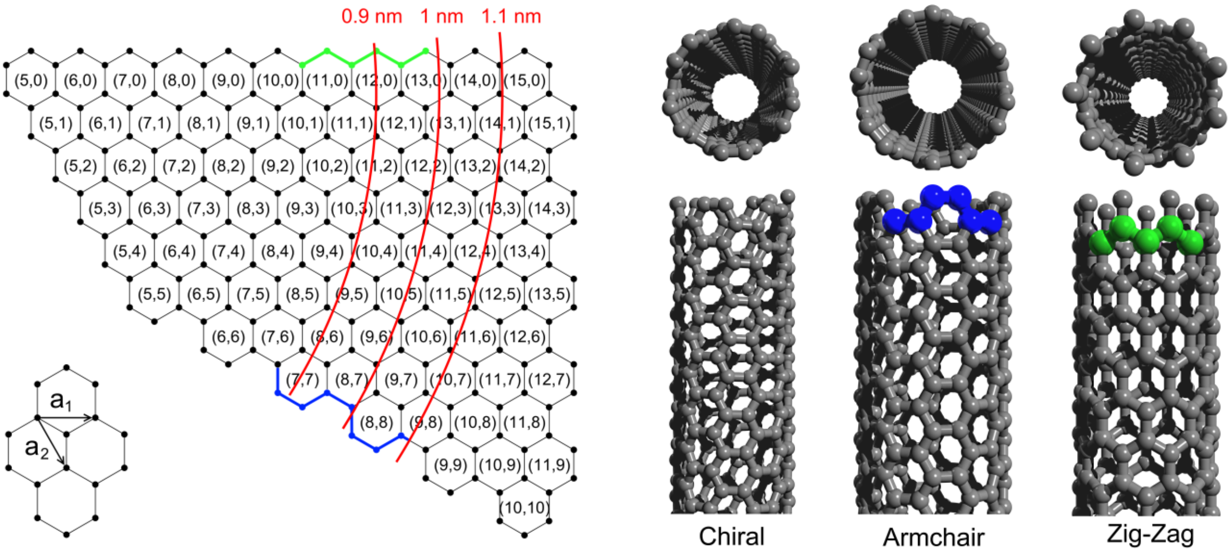

Figure 2. Honeycomb lattice of different (n,m) chiralities and their associated diameter (red line). The different shapes of armchair and zig-zag carbon nanotubes are indicated in blue and green, respectively. In the bottom left corner, the lattice vectors a_1 and a_2 are indicated.

Due to their high aspect ratio with nanometer diameters and lengths of micro- to centimeters, carbon nanotubes are considered as 1-D material. This narrow shape causes large confinement of the electrons and gives rise to unique material properties, like being either semiconducting or metallic in nature or having distinct absorption features. These properties can be derived by having a closer look at the Brillouin zone of the zero-gap semiconductor material graphene and the resulting band-folding structure.

The Brillouin zone is created from a hexagonal reciprocal lattice as shown in Figure 3a.(19) First, the nearest neighbors are connected (black lines) and the perpendicular bisectors of the sides are drawn (red). The red lines encompass an area that is called the Brillouin zone (orange) with the high-symmetry points Γ, K and M. Calculating the electronic band structure of graphene according to Reich et al.,(16) the so called “Fermi surface” of graphene can be obtained as shown in Figure

3b. The valence (orange) and conduction band (green) cross at the Fermi energy in the K-points of the Brillouin zone, causing graphene to be a semiconductor with zero bandgap.

For a carbon nanotube, the Brillouin zone represents the unit cell of the tube, i.e. the segment that is unique for each chirality, which is repeated over the entire length of the tube. Along the tube axis the wave vector of a quasi-particle, e.g. electron or phonon, is assumed to be continuous, whereas along the circumference of the nanotube, the wave vector $\boldsymbol{k}_{\perp}$ is quantized according to the following relations:(16)

$$u \cdot \lambda = |\boldsymbol{c}| = \pi \cdot d \tag{2}$$

$$k_u = \frac{2\pi}{\lambda} = \frac{2\pi}{|\boldsymbol{c}|} \cdot u = \frac{2}{d} \cdot u \tag{3}$$

In these relations u is an integer that can take the values –q/2+1,…,0,1,…,q/2 with 2q being the number of carbon atoms in a unit cell, d the diameter of the nanotube, λ is the wavelength and $\boldsymbol{c}$ is the circumference of the nanotube. The wave function of a quasi-particle must therefore have a phase shift of an integer multiple of 2π, otherwise the wavelength will vanish due to destructive interference.(16) Another outcome of the relation in Equation 3 is that there are $2 \cdot u$ nodes around the circumference of the nanotube. Plotting the wave vectors that obey Equation 3 onto the Brillouin zone of graphene, a set of parallel lines (Figure 3c) is obtained. For every SWCNT, in which the allowed, quantized wave vectors cross the K-point of the Brillouin zone, the nanotube is metallic.

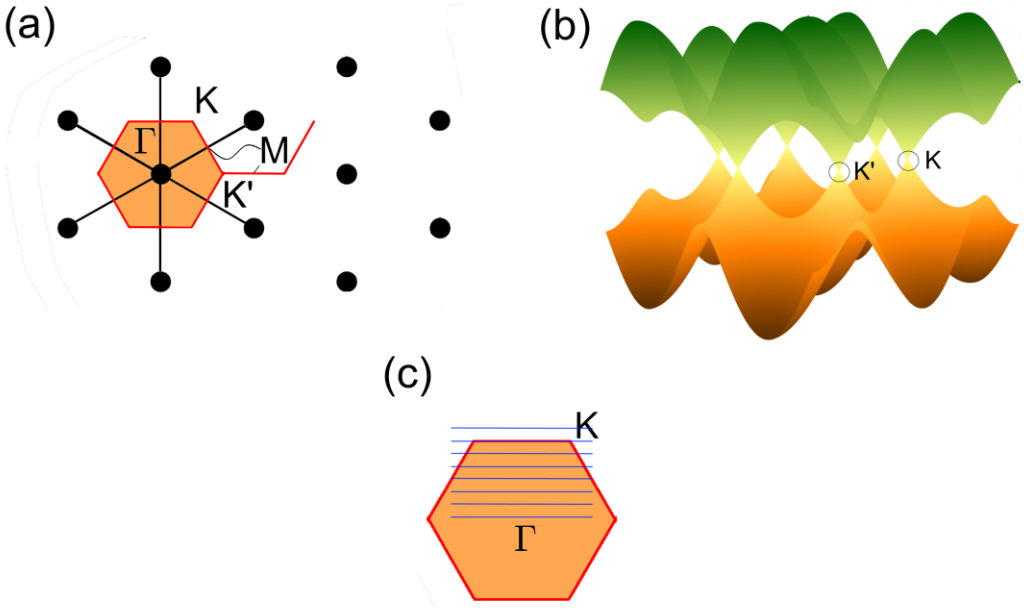

Figure 3. a) Construction of the Brillouin zone from a hexagonal reciprocal lattice. The area encompassed by the bisectors of the sides is called Brillouin zone and contains the high-symmetry points Γ, K, K′ and M. b) Fermi surface or electronic band structure of graphene. The conduction band (green) and valence band (orange) touch at the Fermi energy in the K and K' points of the Brillouin zone. c) According to Equation 3, the wave vector around the circumference of the nanotube is quantized. The allowed states can be pictured as parallel lines (blue).

The electronic and optical properties of a 1D material can be approximated using the concept and formation of density of states (DOS). DOS, or the number of available states to be occupied for a given energy interval, depend on the dimension of the system. For a 1-D system, it can be shown that the quantized energy values (E_p) around the circumference of the nanotube are equal to:(20)

$$E_p = \frac{2p}{d} \cdot a_{C-C} \cdot \gamma_0 \tag{4}$$

In Equation 4, p is equal to 1 for the nanotubes' first transition in the infrared (S_{11}), 2 for the second transition in the visible (S_{22}), 3 for the first transition of metallic SWCNTs (M_{11}), etc., γ_0 an empirical value that takes curvature effects into account and a_{C-C} the carbon-carbon bond length.(20, 21) The density of states is proportional to $|E|$ / $\sqrt{E^2 - E_p^2}$ for $|E|>|E_p|$ and 0 for $|E|<|E_p|$.(16) For E = E_p a singularity, also called van Hove singularity is obtained.(22) The plot of the density of states for a (6,6) and (6,5) SWCNT is shown in Figure 4.(23) It is apparent, that for metallic nanotubes the DOS around the Fermi energy ($Energy$ = 0) is larger than zero. For semiconducting tubes on the other hand, the Fermi energy is zero and a distinct gap between the valence and conduction band is visible that represents forbidden energy states.

The indicated transition energies between valence (orange) and conduction band (green) in Figure 4 are closely related to the optical absorption properties of the respective carbon nanotube. The probability of absorbing a photon is increased if the energy of the photon is matching the transition energy. Due to the inverse relation between nanotube diameter and allowed energy transition (see Equation 4), SWCNTs with increasing diameters absorb further and further in the infrared.

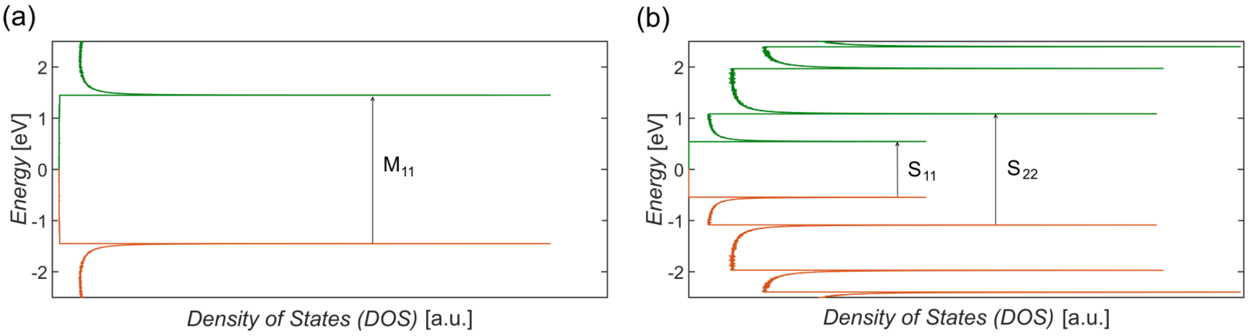

Figure 4. The Fermi level is set to be at 0 eV for both graphs. a) DOS of metallic (6,6) nanotubes that are not zero around the Fermi level, i.e. the valence (red) and conduction (green) band overlap. b) DOS of (6,5) nanotubes with the first and second (S_{11}, S_{22}, respectively) transitions indicated. At the Fermi level the DOS of valence and conduction band are both zero, i.e. they don't overlap and consequently there is a forbidden energy gap between the two bands which makes (6,5) a semiconducting SWCNT.

The direct relation of optical transition to excitation energy (E_{exc}) is known as one particle picture, which can be calculated using density functional theory or tight binding approximations.(16) However, this simple picture is not sufficient for describing the optical transition energies of the nanotubes and is known in literature as the “ratio-problem”.(24) According to Equation 4, the ratio of the energy for the second and first transition is expected to be two. In fact, photoluminescence excitation (PLE) measurements performed by Bachilo et al. indicated a ratio of 1.8 instead of 2.(25) This discrepancy can be explained by the large confinement of the nanotubes, which results in an exciton (electron-hole pair that is bound by a Coulomb interaction) binding energy (E_b) that can be in the order of ~1 eV.(24) Due to these large binding energies the optical transitions observed for carbon nanotubes must be described by an excitonic, rather than a one-particle picture. This excitonic picture not only includes the exciton binding energy but also considers the repulsion energy between electrons (E_{ee}) and the ground state energy derived by tight binding calculations (E_{ground}). The observed optical transition energy can therefore be expressed as:

$$E_{exc,ii} = E_{ground,ii} + E_{b,ii} - E_{ee,ii} \tag{5}$$

With ii = 11, 22, etc. The optical transition energies are calculated using the many-body Green’s function framework including one process for electron addition and removal (GW) and the Bethe-Salpeter equation (BSE) for electron-hole interactions.(26)

In order to accurately determine the optical transitions energies and being able to discuss the properties of excitons, the exciton binding energy needs to be determined. Capaz et al. proposed an analytically derived expression for the calculation of E_b as a function of the diameter d, ξ captures the chirality dependence, the chiral indices n and m and the constants A, B, C and D:(27)

$$E_b = \frac{1}{d}\left(A + \frac{B}{d} + C\xi + D\xi^2\right) \tag{6}$$

$$\xi = (-1)^{\mathrm{mod(n-m,3)}} \cdot \cos\left(\frac{3\theta}{d}\right) \tag{7}$$

$$\theta = \tan^{-1}\left(\frac{\sqrt{3}\cdot \mathrm{m}}{2\cdot \mathrm{n}+\mathrm{m}}\right) \cdot \frac{360}{2\pi} \tag{8}$$

According to the work of Perebeinos et al., the exciton binding energy in carbon nanotubes is strongly affected by the surrounding environment.(28) This relation can be expressed by $E_b \propto \varepsilon^{-1.4}$.(28) The larger the dielectric constant of the environment (ε) becomes, the smaller is the exciton binding energy. Capaz et al. used a value of 1.846 for their dielectric environment. Consequently, the exciton binding energy can be calculated for any given material by scaling to the appropriate dielectric constant of the environment.

An additional indication that the transitions in carbon nanotubes are excitonic in nature, are the so called “exciton phonon sidebands” (EPSs). It was proposed by Perebeinos et al.,(29) that the features located 200 meV above the excitonic transition (in both photoluminescence and optical absorption measurements) should be assigned to a resonance identified with the absorption of light to a bound exciton phonon state.(24) The intensity transferred from the S_{11} absorption ($I_{S_{11}}$) to the EPS (I_{EPS}) was found to scale inversely with the diameter of the nanotube:

$$\frac{I_{EPS}}{I_{S_{11}}} = 0.017 + \frac{0.1\,nm}{d} \tag{9}$$

1.1.2 *Separation*

The first step in any sorting approach is the suspension of CNTs in either aqueous or organic solvents resulting in individually suspended nanotubes. This can be achieved by either covalent (e.g. via acids)(30) or non-covalent (e.g. polymers or surfactants)(31, 32) modification of the outer wall of SWCNTs. In the following section the focus will be on non-covalent modifications of carbon nanotubes because they offer the advantage of preserving the nanotubes property and the selective removal of the dispersing agent. However, a comprehensive overview of nanotube functionalization can be found in the book from Hirsch et al.(33)

Dispersing nanotubes in an organic solution (e.g. toluene) with consecutive sorting is done within one step and was established in 2007 by Nish et al.(32) The raw nanotube powder is mixed with an aromatic polymer, e.g. poly(9,9-dioctylfluorenyl-2,7-diyl), also called “PFO” and the organic solvent and sonicated with an ultrasonic disintegrator. Following the ultrasonication, centrifugation is used to remove non-dispersed nanotubes and nanotube bundles.(32) The high selectivity toward semiconducting SWCNTs (> 99%) and the tunability of different polymers to wrap either near-monochiral or monochiral SWCNTs and even enantiomers of the same chirality,(34) makes polymer sorting a very attractive approach for many researchers. Even the removal of the polymer after sorting has seen several improvements over the past years.(35) However, it is widely accepted in the solar cell community that there is still a considerable amount of residue polymer on the sidewall of nanotubes and therefore in the final device, which affects film formation, exciton diffusion length and life time.(36) Also the yield is rather low, which limits the size of possible final devices and complicates large scale parameter studies.

Large amounts of chirality pure SWCNTs can be obtained using sorting methods that rely on aqueously dispersed carbon nanotubes. In order to disperse nanotubes in aqueous solutions, they are usually ultrasonicated in water containing different concentrations of sodium dodecyl sulphate (SDS) or mixtures of sodium cholate (SC) and SDS.(37) The wrapping of surfactant molecules around the nanotube is strongly dependent on the surfactant concentration, temperature, pH, the nanotube diameter and the electronic type of the nanotube.(38) For example the SDS concentration in solution favors either the formation of random networks at low concentrations or highly packed cylindrical micelles for increased concentrations.(39) Unlike SDS, the coverage of SC is assumed to be tighter.(40) Mixing SDS and SC therefore generates a loose packing around the nanotube that can be utilized e.g. for gel sorting. The coverage of SDS around the nanotube can also be controlled by the temperature. Lowering the temperature results in an increased SDS coverage due to a decreased SDS solubility, which causes an aggregation of SDS molecules on the nanotubes' sidewall.(38) Lowering the pH value, the micelle structure of SDS was reported to change from a continuous parallel semi-cylindrical structure to a herringbone pattern due to the incorporation of 1-dodecanol into the SDS micelle.(31, 41) This effect can be exploited in different sorting processes explained later on, e.g. density gradient ultracentrifugation (DGU) or gel based sorting.(31, 42) The smaller the diameter of a nanotube, the larger is the bond curvature. An increased bond curvature causes an increased energetic barrier for the SDS molecule due to bending.(43) Smaller diameter SWCNTs are therefore less covered with SDS which is of great importance for gel based sorting processed as explained later on. The different wrapping of SDS around metallic and semiconducting nanotubes can be explained by the higher polarizability of metallic SWCNTs and therefore an increased SDS coverage.(44) In addition to that, the SDS morphology around metallic nanotubes is believed to be relative rigid and therefore has a saturated coverage that cannot be tuned by changing the SDS concentration. For semiconducting nanotubes on the other hand, the SDS wrapping is more dynamic and therefore exhibit saturated morphologies at different SDS concentrations, which can be exploited for subsequent sorting techniques.(45)

One of these sorting techniques is density gradient ultracentrifugation (DGU).(46) Using DGU, surfactant wrapped CNTs are placed into a graded fluid medium with varying density within a centrifuge tube. Due to centripetal force inside the centrifuge tube, nanotubes accumulate in layers that resemble their respective buoyant densities and therefore spatially separate in the gradient medium.(47) These buoyant densities are determined by their surfactant encapsulation and can be tuned, e.g. by mixing SDS and SC, to result in an optimized electronic and chirality type sorting. Using DGU, not only electronic type sorting was demonstrated,(48) but also (n,m) specific sorting as well as the sorting of different enantiomers of the same chirality.(47, 49) Despite these remarkable results, DGU sorting is very time consuming and expensive due to multiple steps in dispersing the nanotubes, centrifugation and extraction. Furthermore the yield directly correlates to the size of the centrifuges and centrifuge tubes, which, except for large industrial facilities, is rather small.

A scalable and time saving approach to sort milligram quantities of (n,m) chirality enriched material without the need of a polymer is gel permeation chromatography (GPC). First described by Moshammer et al. in 2009,(50) gel sorting has been demonstrated to be capable of the separation of metallic and semiconducting species,(50) the sorting of (n,m) chirality enriched material (> 90 %),(31, 51) , as well as the sorting of semiconducting and metallic enantiomers.(52) In a first step, the nanotubes are dispersed in SDS or SC.(53) An optional step to remove bundles of nanotubes that were not dispersed in solution is centrifugation.(31) Being fully dispersed in solution the nanotubes are poured on a gel column. Several studies indicate that the nanotubes bind directly to the gel via a kinetically driven selective adsorption reaction, whereas the surfactant acts as mediator.(40, 45, 54) The SWCNTs with small interaction to the gel flow through and are collected for later experiments or disposed. The ones that got stuck on the gel can be eluted by different surfactant mixtures (SC and SDS) or solutions of different pH.(41, 51, 55)

1.1.3 *Characterization*

Having sorted carbon nanotubes based on their electronic type or their chirality, three different characterization methods can be used to analyze the nanotubes individual properties: optical, physical and electrical characterization tools.

Optical characterization

Optical characterization tools enable the analysis of the ratio of semiconducting to metallic tubes and the assignment of individual (n,m) chiralities in SWCNT solutions and films.

One of the most commonly used optical characterization techniques is absorption spectroscopy (UV/vis). If the nanotubes are still dispersed in solution, the typical range of the measurement is from the UV (~200 nm) up to the near infrared (NIR) (~1400 nm) in aqueous solutions and infrared (IR) (up to the detector limit) for organic solutions. Upon creating a film of nanotubes and placing it on a quartz or sapphire substrate, film absorption measurements from the UV to the IR are possible. The difficulties in analyzing absorption spectra are caused by a background that can be induced by metallic nanotubes, catalytic residue particles or carbonaceous impurities,(56) the convolution of many individual (n,m) species into broad absorption peaks (e.g. in the region from 450 – 600 nm where S_{22} and M_{11} overlaps), the shift of peaks due to different dielectric environments (e.g. from comparing a solution to a film measurement), associated exciton phonon sidebands or the choice of appropriate line profiles.

Another helpful tool in determining the semiconducting tubes in solution are photoluminescence (PL) measurements. Upon exciting an electron from the ground state to S_{22}, the electron relaxes to S_{11} by emitting a photon. Based on a 2D contour map, also called PL excitation (PLE) map, with the y-axis being the different excitation wavelengths and the x-axis the emission wavelengths, a detailed picture of the semiconducting nanotubes in solution can be drawn. Assigning the peaks in the contour map to individual nanotubes can be performed via a semi-empirical approach introduced by Bachilo et al.(25):

$$v_{11} = \frac{1x10^{7}cm^{-1}}{157.5+1066.9\cdot d} + \frac{A_1\cos(3\alpha)}{d^2} \tag{10}$$

$$v_{22} = \frac{1x10^{7}cm^{-1}}{145.6+575.7\cdot d} + \frac{A_1\cos(3\alpha)}{d^2} \tag{11}$$

With v_{11} and v_{22} being the first and second van Hove optical transition frequencies and A_1 an empirical parameter with varying values depending on whether $mod(n-m,3) = 1$ or 2. Due to the fact that metallic nanotubes have no bandgap, i.e. an overlapping valence and conduction band, recombination of excited carriers occurs non-radiative.

PLE and UV/vis are the ideal combination to determine the entire set of semiconducting SWCNTs in solution and film.(57) In order to detect and verify metallic nanotubes, Raman measurements can be used in combination with UV/vis.

Probing the vibrational modes via Raman scattering, it is possible to assign individual tubes, metallic and semiconducting ones, from the spectrum. The assignment of individual (n,m) species can be accomplished in two steps. First, by evaluating Equation 12 that relates the Raman shift of the radial breathing mode (RBM) to the diameter of the SWCNT:

$$\omega_{RBM} = \frac{c_1}{d} + c_2 \tag{12}$$

With c_1 and c_2 being empirical parameters, e.g. 223.5 ($nm\cdot cm^{-1}$) and 12.5 (cm^{-1}), respectively.(58) The RBM is a unique phonon mode that causes a bond-stretching and consequently a movement of all the carbon atoms in the radial direction.(59) Second, by the aids of the Kataura plot, which shows the tight binding calculated transition energies of different (n,m) species as a function of their diameter.(60) Choosing appropriate laser wavelengths, typically 488 nm, 514 nm, 633 nm and 785 nm,(61) to excite the nanotube solution or film and plotting the measured ω_{RBM} (or calculated d based on Equation 12) versus the laser energies, allows for specifying a large set of different (n,m) species and their electronic type.(59)

Physical characterization

Having characterized the electronic type and chiralities of a SWCNT solution and film, it is often important to further analyze the nanotube sample with respect to their length, bundle width, number of walls, orientation or even chirality, complementary to previously mentioned methods.

One of the physical characterization tools that allow the determination of different (n,m) chiralities is transmission electron microscopy (TEM). In TEM, the interaction of an electron beam with the sample is recorded and allows for atomic scale resolution. The interaction of the electrons with the carbon nanotube can also be used to generate an electronic diffraction pattern, where the interference pattern of electrons and carbon nanotube is unique for each chirality.(16) The high resolution of TEM is very helpful in determining the number of nanotube walls in case double walled or multi-walled carbon nanotubes are examined and therefore their diameters.(62)

A possible diameter distribution determined from TEM can be verified by performing atomic force microscopy (AFM). In AFM a sharp cantilever is used to analyze the height of different materials placed on a flat surface, e.g. SiO_2. In contact mode, the tip of the cantilever touches the surface whereas in tapping mode the cantilever is oscillating at resonance frequency. In close vicinity of the surface or any material placed upon, the frequency is slightly changed and monitored.(63) AFM can also be used to characterize film morphology, the length or bundle width of a given nanotube sample. The length distribution is best modeled with a log-normal distribution, as discussed by Wang et al. and can be helpful in understanding some fundamental aspects of sorting.(64) For example Thendie et al. observed a length separation using GPC whereas the longer tubes are washed out first and consequently have less interaction with the gel.(37) AFM can also be used to analyze film thicknesses within an error of a few nm, which is crucial for the exact determination of light distribution within a solar cell.(55)

Upon forming films of carbon nanotubes, their alignment, orientation and surface coverage can be accessed via scanning electron microscopy (SEM). In order to perform a SEM measurement, a focused beam of electrons is used that interacts with the electrons in the sample producing secondary electrons that are detected and used to restore the surface morphology of the sample.(65) Areas with a high accumulation of electrons are brighter than areas with a smaller electron loading. This effect can be used to verify whether a carbon nanotube successfully connects the electrodes of a transistor or if it was successfully cut, e.g. for the deposition of molecules in-between,(66) or unintentionally broke.(67)

Electrical characterization

As well as the physical characterization, the electrical characterization is also capable of analyzing single carbon nanotubes or films or large networks of CNTs. For example by implementing carbon nanotubes in a transistor, differentiation between semiconducting and metallic SWCNTs on a single nanotube level is possible. Furthermore, e.g. in the case of solar cells, it is of great importance to not only be certain about the electronic type of single nanotubes but also about their bandgap as an ensemble resembled by a dense or sparse film, as will be explained in Chapter 1.2.

In order to make use of the SWCNTs in a transistor, the nanotubes are used as channel material and deposited between two electrodes (source and drain) via dielectrophoresis.(68) Choosing the proper electrode geometry and applying high frequencies (>100 kHz) the group of R. Krupke demonstrated the assembly of single nanotube devices with an integration density of several millions per square centimeter.(69) Single nanotube devices are necessary to definitely distinguish between semiconducting and metallic nanotubes, whereas bundles of tubes can make the distinction impossible. Metallic nanotubes are easily identified by their linear current – voltage behavior and almost constant source-drain current (I_{SD}) for varying gate voltages. Semiconducting nanotubes on the other hand show a non-linear, almost S-shaped current – voltage characteristic due to the Schottky barrier at the contact side of the nanotube and electrode. They also show a strong gate dependence with I_{SD} On/Off ratios as high as 10^8.(70) Having millions of single nanotube devices and an automated measuring device, statistics about the semiconducting or metallic yield of the separation can be performed.

In addition to very small quantities of metallic SWCNTs, determining the exact energy levels of the semiconducting SWCNTs used as the light absorbing part in solar cells is crucial for estimating device performance. The method used in this study to determine the ionization potential (comparable to the conduction band for inorganic semiconductors) or highest occupied molecular orbital (HOMO) of the SWCNT film is called photo-electron yield spectroscopy in air (PESA) and was invented by M. Uda.(71) Using PESA, the film under investigation is irradiated with an UV beam of increasing intensity. If the ionization potential is reached, the excited electrons ionize the surrounding oxygen, which are accelerated towards the counting electrode. The cut-off point, i.e. the ionization potential, at which the electron count is increased can easily be determined by the intersection of two lines as shown in Figure 5 for a (6,5) nanotube film.

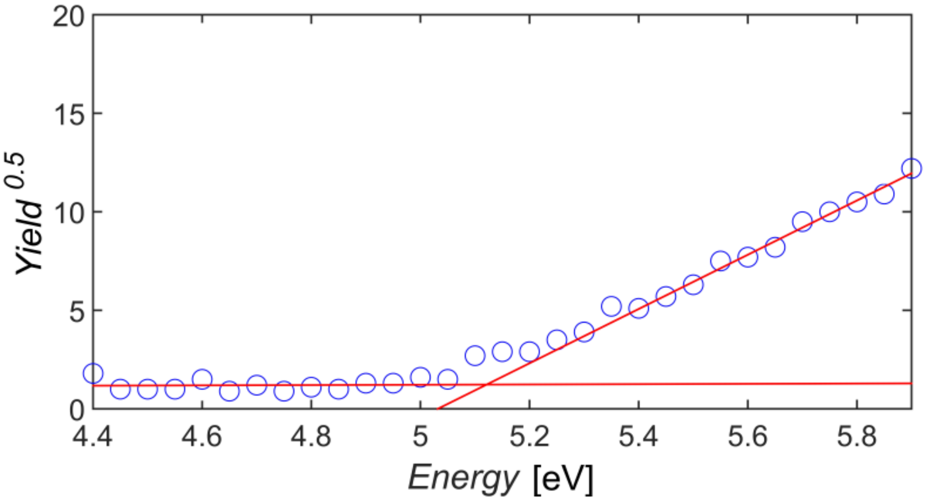

Figure 5. Photo-electron yield spectroscopy in air (PESA) measurement for a (6,5) film on glass. The intersection point at 5.1 eV of the two red lines marks the ionization potential or the highest occupied molecular orbital (HOMO) of the nanotube film. Image reproduced from (55).

1.1.4 *Film Preparation*

Subsequent to sorting and characterizing SWCNTs, they need to be incorporated into solar cells. A number of strategies were developed to reproducibly form films of controllable size, morphology and thickness. The keys to these parameters are SWCNT concentration and dispersant medium.

Demonstrating successful use of five different, polymer-wrapped SWCNTs as light sensitive material in solar cells for the first time in 2010, Bindl et al. used doctor blading to prepare dense and flat films from polymer wrapped nanotubes.(72) Using doctor blading, the SWCNT solution is placed between substrate and blade. By applying a constant movement the solution is spread and forms a film whose thickness can be controlled by the speed and the distance between blade and substrate. The prerequisite for this technique is a high concentration of SWCNTs in solution. Despite the high density and thinness, uniformity appears to be an issue which causes the active area of solar cells employing nanotube films fabricated with this method to be on the order of 0.008 – 0.04 cm^2. Remarkably larger, but less dense polymer wrapped (7,5) nanotube films were prepared using spray coating with an ultrasonic nozzle resulting in active areas of 0.101 cm^2.(73) Spray coating was demonstrated to be capable of uniformly coating hundreds of cm^2 with large diameter nanotubes in an aqueous solution.(74) Wang et al. demonstrated the applicability of spin coating to form SWCNT films of controllable size and thickness by controlling the rotation speed, amount of SWCNT solution and interval of casting a SWCNT drop onto the substrate.(75) As for the other methods, a high concentration of polymer-wrapped SWCNTs is needed to directly incorporate SWCNT films in solar cell devices that consist of hygroscopic layers.

Jain et al. were the first to prove that also polymer-free nanotubes can be used as light sensitive material in SWCNT:C_{60} solar cells in 2012.(76) The nanotube films were fabricated from highly enriched (6,5) nanotubes via vacuum filtration. In this method, the nanotube solution is filtered through an Alumina membrane which is dissolved in NaOH afterwards. By carefully replacing NaOH with deionized water the detached nanotube film floats on top of the water surface and can be picked up carefully. In this work, evaporation driven self assembly (EDSA) was applied to form randomly aligned, sparse nanotube films that uniformly covered areas of several square centimeters.(55, 57) This technique was inspired by the works of Engel et al.(77), Shastry et al.(78) and Li et al.(79) who produced stripes and closed film of randomly and parallel aligned SWCNTs by immersing the substrate vertically in the nanotube solution or in the work of Li et al.,(79) sandwich the nanotube solution horizontally between substrate and glass. In each case, the nanotube formation was driven by a dynamic slip-stick motion of the meniscus at the nanotube solution / substrate / air interface. As the solvent evaporates, capillary flow towards the contact lines causes the nanotubes to be deposited at the three phase interface. Controlling the concentration of surfactant and surrounding temperature, the film thickness and morphology (stripes or closed film) can be precisely engineered.

– This page intentionally left blank –

1.2 Organic Solar Cells

The most famous and widely spread solar cells are silicon based solar cells. Having a covalently bound crystal structure the working principle of silicon based (inorganic) solar cells can be described by consideration of the valence and conduction bands and their alignment at the contact sites of metals as well as at the interface of n-doped (electron) and p-doped (hole) semiconductors.(80) Unlike inorganic solar cells, organic solar cells have to be examined from the perspective of a molecular system that is weakly bound via van der Waals forces.(3) The working principle, device characteristics and layer thickness optimization will be discussed in the following sub-sections.

1.2.1 *Working Principle of Organic Solar Cells*

The prerequisite for organic molecules to exhibit semiconducting behavior is the presence of delocalized valence electrons. Recalling the simplified band model from Chapter 1.1, metallic behavior is expected when valence and conduction bands overlap and semiconducting behavior if there is a bandgap of 0.5 to 4 eV.(81) The valence band is completely filled with electrons at a temperature T approaching 0 K, whereas the conduction band is entirely empty at 0 K. For organic semiconductors, the picture of molecular orbitals is more precise than band structures. Returning to basic chemistry, a carbon nanotube is made up of a network of carbon atoms, where each carbon atom consists of six electrons of which four are valence electrons that can participate in chemical reactions. Being covalently bound, the outermost electrons are shared between the atoms. Upon forming a ring of six carbon atoms (benzene ring) an overlap of the innermost orbitals (s) and two outer orbitals (p_x and p_y) leads to a hybridization and the creation of three sp^2 orbitals with one remaining p_z orbital per carbon atom. The sp^2 bonds form so called σ-bonds whereas the p_z orbitals form π-bonds. The six circular arranged carbon atoms therefore form six π-bonds with different energies according to the arrangement of orbitals and “nodes” as indicated in Figure 6. Nodes are overlaps of wave functions, that create bonding (same phase and color) or anti-bonding (different phase and different color) states.(1) The six electrons fill the lowest energy π-orbitals forming the so called highest occupied molecular orbital (HOMO). The higher energy orbitals are unoccupied whereas the lowest unoccupied molecular orbital is abbreviated with “LUMO”. HOMO and LUMO states are the representation of valence and conduction band in an organic semiconductor.

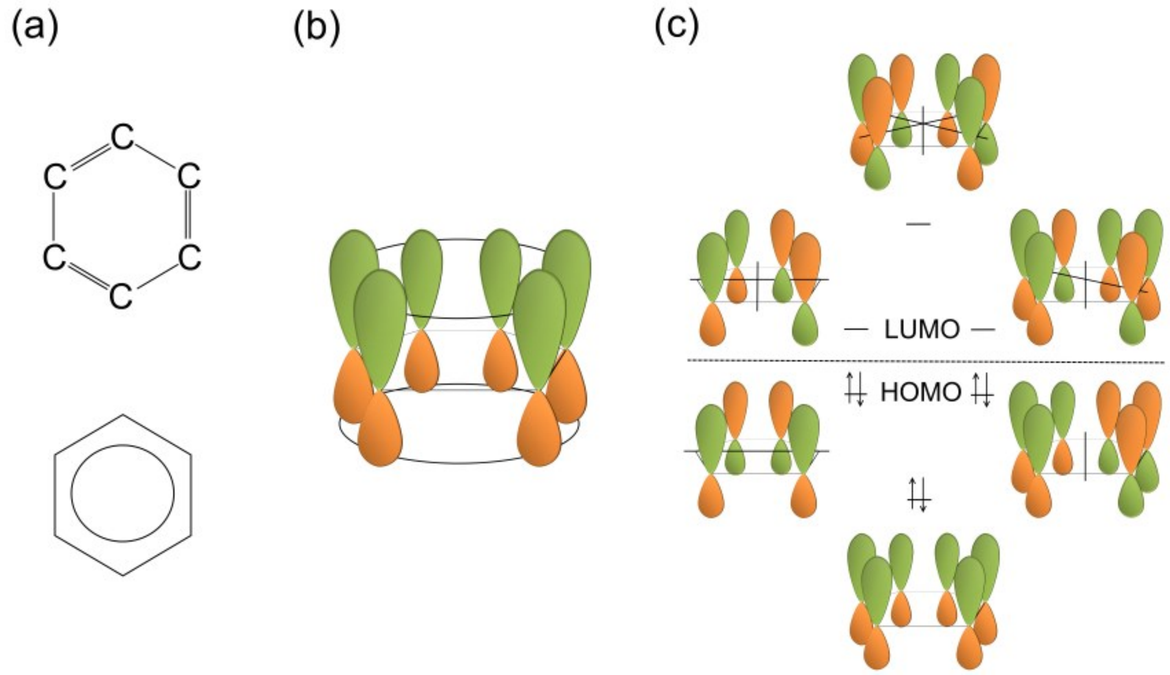

Figure 6. a) Benzene ring formed out of six carbon and six hydrogen (not shown) atoms. The delocalization of the electrons is indicated with a ring. b) Illustration of the lowest energy π-bond. c) The six possible π-bonds can be arranged in different ways, whereas anti-bonding orbitals inherit the higher energies (more nodes). The highest occupied molecular orbital (HOMO) indicates the highest energy level that is filled with electrons (arrows). The image was adapted from (3).

In organic solar cells, two materials with different HOMO and LUMO levels form the donor and acceptor pair responsible for charge generation. Upon the absorption of light, an electron is excited from the HOMO (hole conducting orbital) to the LUMO (electron conducting orbital) level in the donor material, forming a strongly bound exciton due to the confinement of electron and hole. Caused by diffusion, the exciton reaches the interface of the two materials. In order to split the exciton into separate charge carriers, the potentially large exciton binding energy has to be overcome. This exciton dissociation energy is provided by the LUMO offset of the donor and acceptor material, where the acceptor is more electronegative than the donor. The challenge in dissociating the exciton and forming charge carriers is the design of an appropriate LUMO offset between the different materials. A possible approach to derive the optimal LUMO offset is given by Marcus theory that combines the thermodynamic driving energy ΔG to the yield of charge carriers.(82) ΔG is defined as:

$$\Delta G = (HOMO_D - LUMO_A) - E_{exciton} \qquad (13)$$

With D and A being the energy levels of the donor and acceptor, respectively, and $E_{exciton}$ the energy of the bound exciton, which is only slightly smaller than the energy difference of the unbound electron $(LUMO_D)$ and hole $(LUMO_D)$.(83) Marcus demonstrated that there is an inverted region for which an increasing ΔG results in a decreased yield of charge carriers due to increased reorganization energy. Reorganization in organic semiconductors is comparable to thermalization in inorganic ones. In organic materials reorganization equals a loss in energy that is due to a vibrational or structural relaxation of an excited molecule which leads to dissipation of heat.(3) Ihly et al. determined the optimal ΔG and consequently the LUMO offset to be on the order of ~130 meV for SWCNT:Fullerene solar cells.(84) Upon successful charge separation, the electron is transported through the acceptor material, where the hole is conducted through the donor and the charge carriers are collected at the respective electrodes.(3)

In this chain from creation of an exciton up to the collection of charge carriers many different losses reducing efficiency and power of the solar cell can occur. An intrinsic loss to molecular organic semiconductors is the reorganization energy. Prior to a successful dissociation of an exciton the bound electron and hole can recombine; also called geminate recombination. It is therefore of great importance to supply a sufficient driving force to dissociate the exciton faster than the charge carriers recombine. Following the successful dissociation of an exciton the separated electron and hole can recombine either radiative (emitting a photon) or non-radiative. For radiative recombination an electron and hole recombine directly. Because both charge carriers are involved, this loss is often referred to as bimolecular recombination.(85) Non-radiative or monomolecular or Shockley-Read-Hall (SRH) losses involve two steps: first, the electron or hole becomes immobile in a trap state, which is lower, higher, respectively, in energy than the following states. In the second step, the emission of the electron into the HOMO level or the capture of a hole causes the annihilation of the charge carriers. Differentiating between bimolecular and SRH losses can be accomplished by light intensity dependent open circuit voltage (V_{OC}) measurements.

1.2.2 *Device Architecture*

In order to fabricate SWCNT based organic solar cells, there are basically two different device architectures: bulk heterojunctions (BHJ) where donor and acceptor molecules are mixed to increase the contact area and planar heterojunctions. For both architectures electrodes are needed that are highly reflective on the backside of the solar cell (in order to increase the light path through the solar cell) and a transparent front electrode, usually indium tin oxide (ITO). In order to prevent recombination of charge carriers at the ITO electrode and guide the hole transport poly(3,4-ethylenedioxythiophene) polystyrene sulfonate (PEDOT:PSS),(75) molybdenum oxide (MoO_x) or graphene oxide (GO) can be used.(86, 87) To guide the electrons on the back-electrode bathocuproine (BCP) or zinc oxide (ZnO) can be used.(87, 88) For the BHJ architecture, a small quantity of SWCNTs is mixed with an additional organic material, usually fullerene based derivatives like [6,6]-Phenyl C_{61} butyric acid methyl ester $PC_{61}BM$, and then spincoated to form films of controllable thickness by adjusting the rotational speed of the spincoater.(87) The nanotube content is usually rather low (< 10 wt%) in these mixtures, whereas the role of the carbon nanotubes can rather be described as improving the morphology of the different organic absorbers and hole collector, than being the dominant light absorbing part.

Pioneering the field of SWCNT based solar cells Bindl et al. were the first to fabricate planar and bulk heterojunction solar cells from polymer sorted SWCNTs in combination with C_{60} and $PC_{61}BM$, respectively.(72, 89) Jain et al. were the first to demonstrate the applicability of polymer-free SWCNTs as active elements in organic solar cells.(76) However, several questions regarding polymer-free SWCNTs in solar cells remained unanswered, like the actual differences to polymer wrapped SWCNTs regarding device performance and fundamental behavior, whether there is a diameter cut-off above which no current is generated by the nanotubes or the time scales of exciton dissociation and charge transport. A possible planar device architecture to address these questions is shown in Figure 7 along with the associated energy levels determined from PESA measurements.(55) BHJ solar cells employing inverted structures (electrons are collected via ITO, holes through silver) were used to fabricate SWCNT solar cells with currently record high efficiencies of 3.1 % with $PC_{71}BM$ by Gong et al.(87) Furthermore, the largest (0.5 cm^2) solar cells with SWCNT as light absorbing material were fabricated using the same inverted BHJ architecture by Shastry et al.(90) The main difference between state of the art planar and BHJ solar cells is the current contribution from SWCNTs that is much higher in planar devices than in BHJ ones.(87, 91)

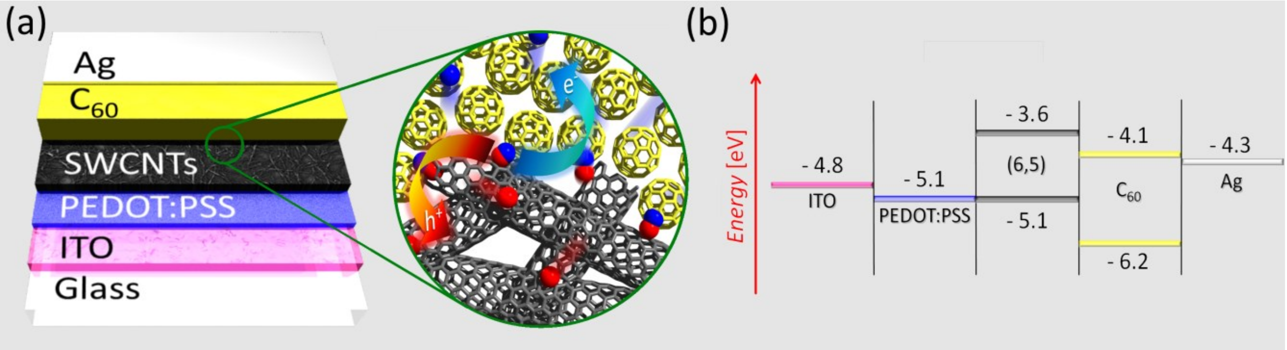

Figure 7. a) Schematic of the solar cell architecture with a close-up of the envisaged exciton dissociation at the SWCNT:C_{60} interface. Electrons (blue) migrate through C_{60} to the silver electrode while holes (red) are collected at the ITO in accordance with b) the energy-level diagram of the device stack. Image reproduced from (55).

1.2.3 *Device Characterization*

In order to represent the solar flux as accurately as possible, solar simulators are designed to resemble the AM1.5G spectrum of the sun or the solar irradiation at an angle of 48° on the earth surface (including absorbance losses in the atmosphere, e.g. water or ozone) taking diffusive light due to scattering and reflection into account and is called “1 sun illumination”.(3) The incident power on the solar cell is therefore set to be 100 mW / cm^2. Fulfilling this prerequisite, solar cells are usually characterized by current-voltage (*J*-*V*) curves, where a voltage sweep under 1 sun illumination is performed and the generated current is detected. The points at zero volts and zero current are called short circuit current (J_{SC}) and open circuit voltage (V_{OC}), respectively. One important device characteristic of each solar cell is the so called fill factor (*FF*), which gives the ratio of maximum power of the solar cell and the maximum power possible, as defined by J_{SC} and V_{OC}. The difference is illustrated in Figure 8 via the blue (max. actual power) and green (max. possible power) rectangle. The efficiency of the solar cell is given by the maximal actual power and the incident power of the solar simulator.

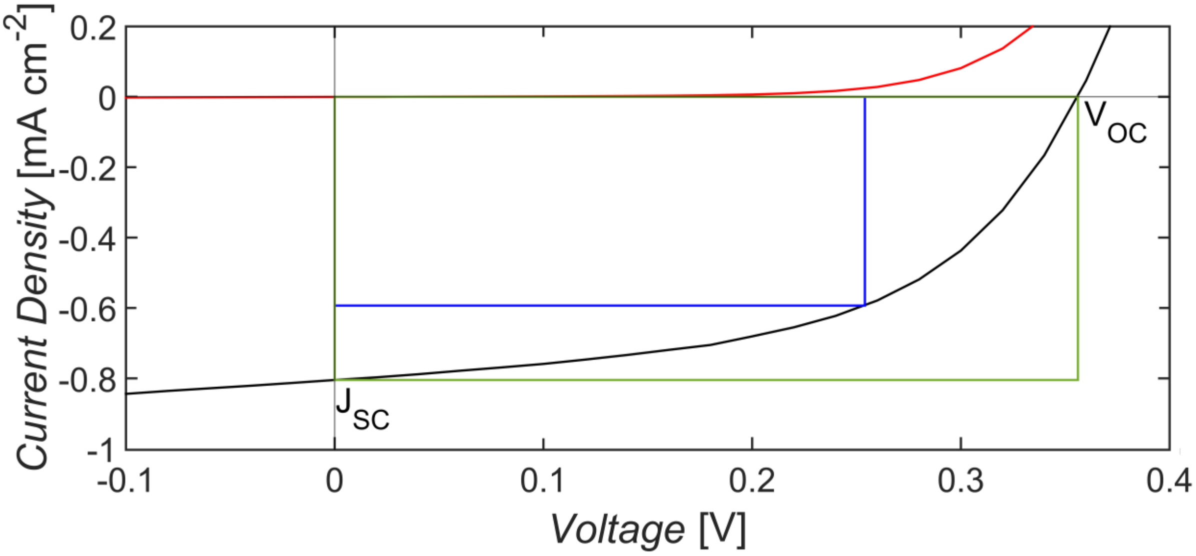

Figure 8. Current density vs. voltage plot (*J*-*V*) curve that was measured under 1 sun illumination (black) and in the dark (red). The intersection points are labeled with open circuit voltage (V_{OC}) and short circuit current (J_{SC}) and mark the corner points for the green rectangle that represents the maximum possible power generated by the solar cell. The blue rectangle indicates the actual maximum power generated by the solar cell. Dividing the area of the blue by the area of the green rectangle results in the fill factor (*FF*) of the solar cell.

The aforementioned recombination mechanisms can be tested by the aids of a light intensity dependent *J*-*V* measurement. According to Figure 8 there is no current flowing at open circuit conditions. Therefore all charge carriers that are created have to recombine in the absorbing materials,(3) which provides an opportunity to analyze the recombination behavior. According to Cowan et al.,(92) plotting the logarithm of light intensity vs V_{OC} the slope *S* of the curve is defined as:

$$S = \frac{X \cdot k_B \cdot T}{e} \tag{14}$$

Hereby, k_B is the Boltzmann constant, T is the room temperature (~296 K), e is the elementary charge and *X* is a pre-factor to adjust the slope of the curve. Having a pre-factor of *X*=1 is typical for bulk heterojunction solar cells that are dominated by bimolecular recombination. A pre-factor in the order of 2 or larger is typical for silicon solar cells and therefore SRH or trap assisted recombination.

Two further device characteristics that can be derived from the illuminated *J-V* curve are the shunt (R_{SH}) and series (R_S) resistance. Simplifying the solar cell behavior by assuming a built in potential (e.g. from the work function difference of the electrodes) and a diffusion driven forward current, it is possible to describe the solar cell behavior with the aids of an equivalent circuit as shown in Figure 9 with the following relations for R_S and $R_{SH:}$(80)

$$R_S = \left(\frac{dJ}{dV}\right)^{-1}\Bigg|_{V=V_{OC}} \tag{15}$$

$$R_{SH} = \left(\frac{dJ}{dV}\right)^{-1}\Bigg|_{V=0} \tag{16}$$

R_S should be as small as possible, whereas R_{SH} should be as large as possible to minimize voltage losses and a decrease of FF. (80) Physically, the series resistance is a macroscopic phenomenon that can be explained by contact resistances. The shunt resistance on the other hand can be explained by alternative current paths (pinholes) that cause internal shorts.

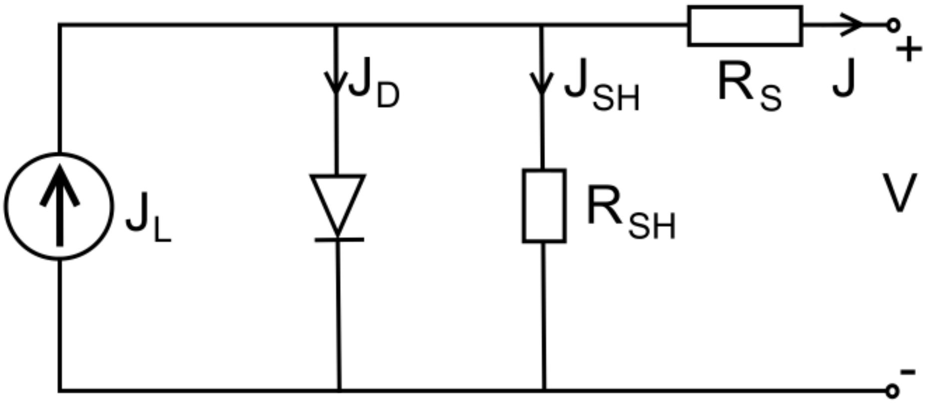

Figure 9. Equivalent circuit used to simulate solar cell behavior based on a light source (J_L), a diode (J_D), a shunt and a series resistance (R_{SH}, R_S, respectively).

The current J in the equivalent circuit in Figure 9 can be described as a function of the photocurrent (J_L), the diode current (J_D and the shunt current J_{SH}. The diode current itself can be expressed as a function of the Boltzmann's constant k_B, room temperature T, diode ideality factor n and elementary charge e:

$$J = J_L - J_D - J_{SH} = J_L - J_0 \cdot \left(e^{\frac{e\cdot(V+R_S\cdot J)}{n\cdot k_B\cdot T}} - 1\right) - \frac{V+R_SJ}{R_{SH}} \tag{17}$$

In the dark (no illumination) the *J-V* curve can be approximated via the diode equation whereas J_0 is the dark saturation current density, which should be as small at possible (measured at V=0):(93)

$$J = J_0 \cdot \left(e^{\frac{e \cdot V}{n \cdot k_B \cdot T}} - 1\right) \tag{18}$$

For V > k_B·T/e, the -1 term can be neglected, because the exponential term becomes much larger than 1. Taking the natural logarithm on both sides yields:

$$\ln(J) = \ln(J_0) + \frac{e \cdot V}{n \cdot k_B \cdot T} \tag{19}$$

Plotting $ln(J)$ as a function of V three different regions can be distinguished:(94) one is dominated by R_S ($V>V_{OC}$) one is dominated by R_{SH} ($V<<V_{OC}$) and the linear region in-between is dominated by recombination. For the latter region, the diode ideality factor can be extracted. For an ideal solar cell n equals 1. If n is calculated to be in the range of 1 to 2, trap charges might be a dominant recombination mechanism.(80)

In addition to *J-V* measurements, external quantum efficiency (EQE) measurements are mandatory to extract certain device characteristics. EQE is a measure of photons incident on the solar cell that actually generate charge carriers, which can be extracted at the electrodes. If every photon would result in an extractable charge carrier the EQE would be 100 %. EQE is measured by varying the wavelength and recording the photocurrent. The photon flux is calculated with the aids of a reference diode under the same illumination conditions. If no voltage bias is applied the integrated EQE curve (J_{EQE}) should be equal to the measured J_{SC} and can be calculated according to the following formula, where e is the elementary charge, h is Planck's constant and c is the speed of light:

$$J_{EQE} = \frac{e}{h \cdot c} \int_{\lambda_1}^{\lambda_2} \lambda \cdot EQE(\lambda) \cdot AM1.5G(\lambda) d\lambda \tag{20}$$

Closely related to EQE measurements are internal quantum efficiency (IQE) measurements, which are the ratio of EQE and film absorbance. If the EQE at a certain wavelength is 10 % and the film absorbance at the same wavelength is 20 %, the IQE consequently is 50 %. This means, that every second photon that was absorbed by the donor actually generated charge carriers that were extracted. The higher the IQE value the better the material is suited as donor in a solar cell.

1.2.4 *Light Management*

Having layer thicknesses in the order of the wavelength at which the materials absorb, it is necessary to consider interference effects in the solar cell stack. Furthermore, considering the distinct absorption features of SWCNTs, it is crucial to design the solar cell such that sufficient light is supplied at the wavelength of the nantoubes' first and/or second transition.(55, 73) A versatile and reliable method to do so is with transfer matrix calculations (TMCs). TMCs were introduced for organic solar cells in 1999 by Pettersson et al.(95) Assuming light is incident at 0° at the glass interface and at every interface of two different materials in the solar cell stack reflection and transmission is occurring, Pettersson et al. formulated an approach that related the incident electric field to the electric field at any given position within the multilayer stack. A detailed derivation of this approach including the concept of light as electromagnetic wave, laws of reflection and transmission (Fresnel equations) and the transfer matrix formalism can be found in Appendix 7.1. Briefly, the incoming and outgoing electric field E_0^+ and E_0^- at the front of the solar cell is related to the incoming and outgoing electric field on the backside of the solar cell via the transfer matrix S:

$$\begin{pmatrix} E_0^+ \\ E_0^- \end{pmatrix} = S \begin{pmatrix} E_{m+1}^+ \\ E_{m+1}^- \end{pmatrix} \tag{21}$$

The transfer matrix S itself contains the interface matrix (matrix of refraction) I_{jk} with t and r being transmission and reflection coefficient derived in Appendix 7.1 Equations 67 and 68:

$$I_{jk} = \frac{1}{t_{jk}} \begin{pmatrix} 1 & r_{jk} \\ r_{jk} & 1 \end{pmatrix} \tag{22}$$

and the layer matrix L_j that describes the propagation of light through the j-th layer:

$$L_j = \begin{pmatrix} e^{-i\xi_j d_j} & 0 \\ 0 & e^{i\xi_j d_j} \end{pmatrix} \tag{23}$$

$$\xi_j = \frac{2\pi(n+i\cdot k)}{\lambda} \tag{24}$$

With d_j being the thickness of the j-th layer and n and k the complex refractive index of the respective material.

Combining I and L, S can be expressed as follows:

$$S = \begin{pmatrix} S_{11} & S_{12} \\ S_{21} & S_{22} \end{pmatrix} = \left(\prod_{v=1}^{m} I_{(v-1)v} L_v\right) I_{m(m+1)} \tag{25}$$

In order to calculate the electric field in any layer "j" of the solar cell stack, a transfer matrix connecting the electric field on the front side to the j-th layer (S_j') and a transfer matrix connecting the electric field in the respective layer to the backside of solar cell (S_j'') is needed. A schematic of this approach is demonstrated in Figure 10.

It can be shown (Appendix 7.1 Equations 84 to 97) that the electric field in layer j is given as:

$$E_j(x) = \left(\frac{e^{-i\xi_j(d_j - x)} S''_{j11} + e^{i\xi_j(d_j - x)} S''_{j21}}{S'_{j11} e^{-i\xi_j d_j} S''_{j11} + S'_{j12} e^{i\xi_j d_j} S''_{j21}} \right) E_0^+ \tag{26}$$

With x being the actual position in j-th layer. Employing Equation 26, the electric field at any given position within the solar cell stack can be calculated with respect to the incoming electric field (usually the AM1.5G spectrum) and therefore engineered for an optimal light absorption by the SWCNTs.

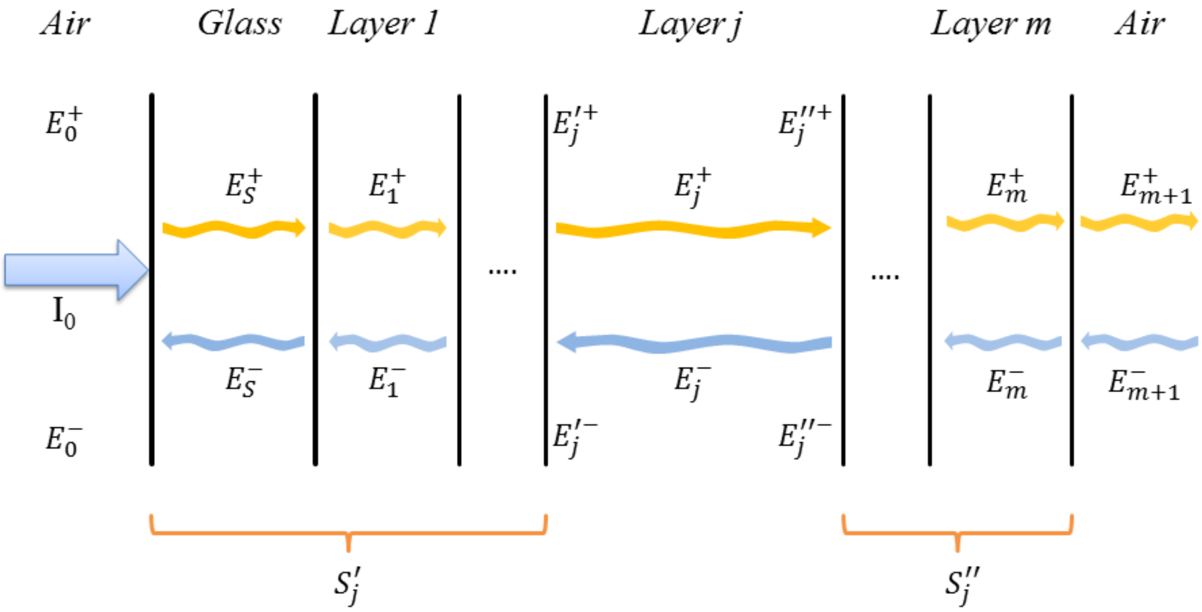

Figure 10. Schematic drawing of the multilayer stack of the solar cell. Incident light with intensity I_0 is coming in from the left hand side with an electric field entering the stack in forward direction (E_0^+) and one leaving the stack (E_0^-). The transfer matrix S can be used to relate the incident electric field with any layer in the solar cell, e.g. the incident electric field with the one entering and leaving the j-th layer on the left hand side (S_j') or the electric field entering and leaving to the right hand side of the j-th layer with the one on the back of the solar cell (S_j''). The schematic was adapted from (96).

– This page intentionally left blank –

1.3 References

(1) Bundesministerium für Wirtschaft und Energie (BMWi): Erneuerbare Energien auf einen Blick 2015, http://www.bmwi.de/DE/Themen/Energie/Erneuerbare-Energien/erneuerbare-energien-auf-einen-blick.html 2016.

(2) H. Lehmann, C. Herforth, *LIFIS ONLINE [11.01. 12], www. leibnizinstitut. de, ISSN* **1864**, 6972.

(3) W. Tress, in *Organic Solar Cells: Theory, Experiment, and Device Simulation*, Springer International Publishing, Cham **2014**, 67.

(4) G. Chen, T. M. Paronyan, E. M. Pigos, A. R. Harutyunyan, *Sci. Rep.* **2012**, 2, 343; T. Dürkop, S. A. Getty, E. Cobas, M. S. Fuhrer, *Nano Letters* **2003**, 4, 35; L. Yang, P. Kim, H. M. Meyer, S. Agnihotri, *Journal of Colloid and Interface Science* **2009**, 338, 128.

(5) S. Iijima, *Nature* **1991**, 354, 56.

(6) Y. Ando, X. Zhao, T. Sugai, M. Kumar, *Materials Today* **2004**, 7, 22.

(7) N. Arora, N. N. Sharma, *Diamond and Related Materials* **2014**, 50, 135.

(8) T. Guo, P. Nikolaev, A. G. Rinzler, D. Tomanek, D. T. Colbert, R. E. Smalley, *The Journal of Physical Chemistry* **1995**, 99, 10694; T. Guo, P. Nikolaev, A. Thess, D. T. Colbert, R. E. Smalley, *Chemical Physics Letters* **1995**, 243, 49.

(9) A. Thess, R. Lee, P. Nikolaev, H. Dai, P. Petit, J. Robert, C. Xu, Y. H. Lee, S. G. Kim, A. G. Rinzler, D. T. Colbert, G. E. Scuseria, D. Tománek, J. E. Fischer, R. E. Smalley, *Science* **1996**, 273, 483.

(10) M. Kumar, Y. Ando, *Journal of Nanoscience and Nanotechnology* **2010**, 10, 3739.

(11) M. J. Bronikowski, P. A. Willis, D. T. Colbert, K. A. Smith, R. E. Smalley, *Journal of Vacuum Science & Technology A* **2001**, 19, 1800.

(12) S. Hofmann, R. Sharma, C. Ducati, G. Du, C. Mattevi, C. Cepek, M. Cantoro, S. Pisana, A. Parvez, F. Cervantes-Sodi, A. C. Ferrari, R. Dunin-Borkowski, S. Lizzit, L. Petaccia, A. Goldoni, J. Robertson, *Nano Letters* **2007**, 7, 602.

(13) J. R. Sanchez-Valencia, T. Dienel, O. Groning, I. Shorubalko, A. Mueller, M. Jansen, K. Amsharov, P. Ruffieux, R. Fasel, *Nature* **2014**, 512, 61.

(14) F. Yang, X. Wang, D. Zhang, J. Yang, LuoDa, Z. Xu, J. Wei, J.-Q. Wang, Z. Xu, F. Peng, X. Li, R. Li, Y. Li, M. Li, X. Bai, F. Ding, Y. Li, *Nature* **2014**, 510, 522; M. He, H. Jiang, B. Liu, P. V. Fedotov, A. I. Chernov, E. D. Obraztsova, F. Cavalca, J. B. Wagner, T. W. Hansen, I. V. Anoshkin, E. A. Obraztsova, A. V. Belkin, E. Sairanen, A. G. Nasibulin, J. Lehtonen, E. I. Kauppinen, *Scientific Reports* **2013**, 3, 1460; H. Wang, L. Wei, F. Ren, Q. Wang, L. D. Pfefferle, G. L. Haller, Y. Chen, *ACS Nano* **2013**, 7, 614.

(15) F. Yang, X. Wang, M. Li, X. Liu, X. Zhao, D. Zhang, Y. Zhang, J. Yang, Y. Li, *Accounts of Chemical Research* **2016**, 49, 606.

(16) S. Reich, C. Thomsen, J. Maultzsch, *Carbon nanotubes: basic concepts and physical properties*, John Wiley & Sons, 2008.

(17) R. B. Pipes, S. Frankland, P. Hubert, E. Saether, *Composites Science and Technology* **2003**, 63, 1349.

(18) M. S. Dresselhaus, G. Dresselhaus, P. C. Eklund, in *Science of Fullerenes and Carbon Nanotubes*, Academic Press, San Diego **1996**, 464.

(19) C. Kittel, S. Hunklinger, *Einführung in die Festkörperphysik*, Oldenbourg Wissenschaftsverlag, München 2013.

(20) R. Saito, G. Dresselhaus, M. S. Dresselhaus, *Physical Review B* **2000**, 61, 2981.

(21) R. Saito, M. Fujita, G. Dresselhaus, M. S. Dresselhaus, *Physical Review B* **1992**, 46, 1804.

(22) L. Van Hove, *Physical Review* **1953**, 89, 1189.

(23) S. Maruyama, DOS for each chirality, http://www.photon.t.u-tokyo.ac.jp/~maruyama/kataura/kataura.html#DOS 2002.

(24) M. S. Dresselhaus, G. Dresselhaus, R. Saito, A. Jorio, *Annu. Rev. Phys. Chem.* **2007**, 58, 719.

(25) S. M. Bachilo, M. S. Strano, C. Kittrell, R. H. Hauge, R. E. Smalley, R. B. Weisman, *Science* **2002**, 298, 2361.

(26) C. D. Spataru, S. Ismail-Beigi, L. X. Benedict, S. G. Louie, *Physical Review Letters* **2004**, 92, 077402.

(27) R. B. Capaz, C. D. Spataru, S. Ismail-Beigi, S. G. Louie, *Physical Review B* **2006**, 74, 121401.

(28) V. Perebeinos, J. Tersoff, P. Avouris, *Physical review letters* **2004**, 92, 257402.

(29) V. Perebeinos, J. Tersoff, P. Avouris, *Physical review letters* **2005**, 94, 027402.

(30) S. Deng, Y. Zhang, A. H. Brozena, M. L. Mayes, P. Banerjee, W.-A. Chiou, G. W. Rubloff, G. C. Schatz, Y. Wang, *Nat Commun* **2011**, 2, 382.

(31) B. S. Flavel, K. E. Moore, M. Pfohl, M. M. Kappes, F. Hennrich, *ACS Nano* **2014**, 8, 1817.

(32) A. Nish, J.-Y. Hwang, J. Doig, R. J. Nicholas, *Nat Nano* **2007**, 2, 640.

(33) A. Hirsch, O. Vostrowsky, in *Functional Molecular Nanostructures: -/-*, (Ed: A. D. Schlüter), Springer Berlin Heidelberg, Berlin, Heidelberg **2005**, 193.

(34) D. J. Bindl, M. Y. Wu, F. C. Prehn, M. S. Arnold, *Nano Lett* **2011**, 11, 455; A. Graf, Y. Zakharko, S. P. Schießl, C. Backes, M. Pfohl, B. S. Flavel, J. Zaumseil, *Carbon* **2016**, 105, 593; K. Akazaki, F. Toshimitsu, H. Ozawa, T. Fujigaya, N. Nakashima, *Journal of the American Chemical Society* **2012**, 134, 12700.

(35) Y. Joo, G. J. Brady, M. J. Shea, M. B. Oviedo, C. Kanimozhi, S. K. Schmitt, B. M. Wong, M. S. Arnold, P. Gopalan, *ACS Nano* **2015**, 9, 10203; I. Pochorovski, H. Wang, J. I. Feldblyum, X. Zhang, A. L. Antaris, Z. Bao, *Journal of the American Chemical Society* **2015**, 137, 4328;

J. Han, Q. Ji, H. Li, G. Li, S. Qiu, H.-B. Li, Q. Zhang, H. Jin, Q. Li, J. Zhang, *Chemical Communications* **2016**, 52, 7683.

(36) D. J. Bindl, A. J. Ferguson, M.-Y. Wu, N. Kopidakis, J. L. Blackburn, M. S. Arnold, *The Journal of Physical Chemistry Letters* **2013**, 4, 3550.

(37) B. Thendie, Y. Miyata, R. Kitaura, Y. Miyauchi, K. Matsuda, H. Shinohara, *Applied Physics Express* **2013**, 6, 065101.

(38) H. Liu, T. Tanaka, Y. Urabe, H. Kataura, *Nano Lett* **2013**, 13, 1996.

(39) Z. Xu, X. Yang, Z. Yang, *Nano Letters* **2010**, 10, 985.

(40) R. M. Jain, M. Ben-Naim, M. P. Landry, M. S. Strano, *The Journal of Physical Chemistry C* **2015**, 119, 22737.

(41) B. S. Flavel, M. M. Kappes, R. Krupke, F. Hennrich, *ACS Nano* **2013**, 7, 3557.

(42) W. G. Reis, R. T. Weitz, M. Kettner, A. Kraus, M. G. Schwab, Ž. Tomović, R. Krupke, J. Mikhael, *Scientific Reports* **2016**, 6, 26259.

(43) N. R. Tummala, A. Striolo, *ACS Nano* **2009**, 3, 595.

(44) K. E. Moore, D. D. Tune, B. S. Flavel, *Advanced Materials* **2015**, 27, 3105.

(45) R. M. Jain, K. Tvrdy, R. Han, Z. Ulissi, M. S. Strano, *ACS Nano* **2014**, 8, 3367.

(46) M. S. Arnold, S. I. Stupp, M. C. Hersam, *Nano Letters* **2005**, 5, 713.

(47) M. S. Arnold, A. A. Green, J. F. Hulvat, S. I. Stupp, M. C. Hersam, *Nat Nano* **2006**, 1, 60.

(48) A. L. Antaris, J.-W. T. Seo, R. E. Brock, J. E. Herriman, M. J. Born, A. A. Green, M. C. Hersam, *The Journal of Physical Chemistry C* **2012**, 116, 20103.

(49) S. Ghosh, S. M. Bachilo, R. B. Weisman, *Nat Nano* **2010**, 5, 443; A. Green, M. Duch, M. Hersam, *Nano Research* **2009**, 2, 69.

(50) K. Moshammer, F. Hennrich, M. Kappes, *Nano Research* **2009**, 2, 599.

(51) H. Liu, D. Nishide, T. Tanaka, H. Kataura, *Nat Commun* **2011**, 2, 309.

(52) H. Liu, T. Tanaka, H. Kataura, *Nano Letters* **2014**, 14, 6237; T. Tanaka, Y. Urabe, T. Hirakawa, H. Kataura, *Analytical Chemistry* **2015**, 87, 9467.

(53) J. Zhang, H. Gui, B. Liu, J. Liu, C. Zhou, *Nano Research* **2013**, 6, 906.

(54) C. A. Silvera-Batista, D. C. Scott, S. M. McLeod, K. J. Ziegler, *The Journal of Physical Chemistry C* **2011**, 115, 9361; J. G. Clar, C. A. Silvera Batista, S. Youn, J.-C. J. Bonzongo, K. J. Ziegler, *Journal of the American Chemical Society* **2013**, 135, 17758; K. Tvrdy, R. M. Jain, R. Han, A. J. Hilmer, T. P. McNicholas, M. S. Strano, *ACS Nano* **2013**, 7, 1779.

(55) M. Pfohl, K. Glaser, J. Ludwig, D. D. Tune, S. Dehm, C. Kayser, A. Colsmann, R. Krupke, B. S. Flavel, *Advanced Energy Materials* **2016**, 6, 1501345.

(56) A. V. Naumov, S. Ghosh, D. A. Tsyboulski, S. M. Bachilo, R. B. Weisman, *ACS Nano* **2011**, 5, 1639.

(57) M. Pfohl, K. Glaser, A. Graf, A. Mertens, D. D. Tune, T. Puerckhauer, A. Alam, L. Wei, Y. Chen, J. Zaumseil, A. Colsmann, R. Krupke, B. S. Flavel, *Advanced Energy Materials* **2016**, 1600890.

(58) M. S. Strano, S. K. Doorn, E. H. Haroz, C. Kittrell, R. H. Hauge, R. E. Smalley, *Nano Letters* **2003**, 3, 1091.

(59) M. S. Dresselhaus, G. Dresselhaus, R. Saito, A. Jorio, *Physics Reports* **2005**, 409, 47.

(60) H. Kataura, Y. Kumazawa, Y. Maniwa, I. Umezu, S. Suzuki, Y. Ohtsuka, Y. Achiba, *Synthetic Metals* **1999**, 103, 2555.

(61) L. Qu, F. Du, L. Dai, *Nano Letters* **2008**, 8, 2682.

(62) K. E. Moore, M. Pfohl, F. Hennrich, V. S. K. Chakradhanula, C. Kuebel, M. M. Kappes, J. G. Shapter, R. Krupke, B. S. Flavel, *ACS Nano* **2014**, 8, 6756.

(63) J. Maultzsch, C. Thomsen, in *Carbon Nanotube Devices*, Wiley-VCH Verlag GmbH & Co. KGaA, **2008**, 125.

(64) S. Wang, Z. Liang, B. Wang, C. Zhang, *Nanotechnology* **2006**, 17, 634.

(65) R. F. Egerton, in *Physical Principles of Electron Microscopy: An Introduction to TEM, SEM, and AEM*, Springer US, Boston, MA **2005**, 125.

(66) C. Thiele, H. Vieker, A. Beyer, B. S. Flavel, F. Hennrich, D. Muñoz Torres, T. R. Eaton, M. Mayor, M. M. Kappes, A. Gölzhäuser, H. v. Löhneysen, R. Krupke, *Applied Physics Letters* **2014**, 104, 103102.

(67) K. E. Moore, M. Pfohl, D. D. Tune, F. Hennrich, S. Dehm, V. S. K. Chakradhanula, C. Kübel, R. Krupke, B. S. Flavel, *ACS Nano* **2015**, 9, 3849.

(68) R. Krupke, F. Hennrich, H. v. Löhneysen, M. M. Kappes, *Science* **2003**, 301, 344.

(69) A. Vijayaraghavan, S. Blatt, D. Weissenberger, M. Oron-Carl, F. Hennrich, D. Gerthsen, H. Hahn, R. Krupke, *Nano Letters* **2007**, 7, 1556.

(70) V. Derenskyi, W. Gomulya, J. M. S. Rios, M. Fritsch, N. Fröhlich, S. Jung, S. Allard, S. Z. Bisri, P. Gordiichuk, A. Herrmann, U. Scherf, M. A. Loi, *Advanced Materials* **2014**, 26, 5969.

(71) M. Uda, *Japanese Journal of Applied Physics Part 1-Regular Papers Short Notes & Review Papers* **1985**, 24, 284.

(72) D. J. Bindl, N. S. Safron, M. S. Arnold, *ACS Nano* **2010**, 4, 5657.

(73) S. L. Guillot, K. S. Mistry, A. D. Avery, J. Richard, A. M. Dowgiallo, P. F. Ndione, J. van de Lagemaat, M. O. Reese, J. L. Blackburn, *Nanoscale* **2015**, 7, 6556.

(74) R. C. Tenent, T. M. Barnes, J. D. Bergeson, A. J. Ferguson, B. To, L. M. Gedvilas, M. J. Heben, J. L. Blackburn, *Advanced materials* **2009**, 21, 3210.

(75) H. Wang, G. I. Koleilat, P. Liu, G. Jimenez-Oses, Y. C. Lai, M. Vosgueritchian, Y. Fang, S. Park, K. N. Houk, Z. Bao, *ACS Nano* **2014**, 8, 2609.

(76) R. M. Jain, R. Howden, K. Tvrdy, S. Shimizu, A. J. Hilmer, T. P. McNicholas, K. K. Gleason, M. S. Strano, *Adv Mater* **2012**, 24, 4436.

(77) M. Engel, J. P. Small, M. Steiner, M. Freitag, A. A. Green, M. C. Hersam, P. Avouris, *ACS Nano* **2008**, 2, 2445.

(78) T. A. Shastry, J.-W. T. Seo, J. J. Lopez, H. N. Arnold, J. Z. Kelter, V. K. Sangwan, L. J. Lauhon, T. J. Marks, M. C. Hersam, *Small* **2013**, 9, 45.

(79) H. Li, T. C. Hain, A. Muzha, F. Schöppler, T. Hertel, *ACS Nano* **2014**, 8, 6417.

(80) J. L. Gray, in *Handbook of Photovoltaic Science and Engineering*, John Wiley & Sons, Ltd, **2011**, 82.

(81) W. Tress, in *Organic Solar Cells: Theory, Experiment, and Device Simulation*, Springer International Publishing, Cham **2014**, 15.

(82) R. A. Marcus, *Annual Review of Physical Chemistry* **1964**, 15, 155.

(83) M. S. Arnold, J. L. Blackburn, J. J. Crochet, S. K. Doorn, J. G. Duque, A. Mohite, H. Telg, *Physical Chemistry Chemical Physics* **2013**, 15, 14896.

(84) R. Ihly, K. S. Mistry, A. J. Ferguson, T. T. Clikeman, B. W. Larson, O. Reid, O. V. Boltalina, S. H. Strauss, G. Rumbles, J. L. Blackburn, *Nat Chem* **2016**, 8, 603.

(85) J. D. Servaites, M. A. Ratner, T. J. Marks, *Energy & Environmental Science* **2011**, 4, 4410.

(86) M. Gong, T. A. Shastry, Q. Cui, R. R. Kohlmeyer, K. A. Luck, A. Rowberg, T. J. Marks, M. F. Durstock, H. Zhao, M. C. Hersam, S. Ren, *ACS Applied Materials & Interfaces* **2015**, 7, 7428.

(87) M. Gong, T. A. Shastry, Y. Xie, M. Bernardi, D. Jasion, K. A. Luck, T. J. Marks, J. C. Grossman, S. Ren, M. C. Hersam, *Nano Letters* **2014**, 14, 5308.

(88) ; D. J. Bindl, M. S. Arnold, *The Journal of Physical Chemistry C* **2013**, 117, 2390.

(89) D. J. Bindl, A. S. Brewer, M. S. Arnold, *Nano Research* **2011**, 4, 1174.

(90) T. A. Shastry, S. C. Clark, A. J. E. Rowberg, K. A. Luck, K.-S. Chen, T. J. Marks, M. C. Hersam, *Advanced Energy Materials* **2016**, 6, 1501466.

(91) M. J. Shea, M. S. Arnold, *Applied Physics Letters* **2013**, 102, 243101.

(92) S. R. Cowan, A. Roy, A. J. Heeger, *Physical Review B* **2010**, 82, 245207.

(93) S. K. Cheung, N. W. Cheung, *Applied Physics Letters* **1986**, 49, 85.

(94) B. Qi, J. Wang, *Physical Chemistry Chemical Physics* **2013**, 15, 8972.

(95) L. A. A. Pettersson, L. S. Roman, O. Inganäs, *Journal of Applied Physics* **1999**, 86, 487.

(96) Y. Li, *Three Dimensional Solar Cells Based on Optical Confinement Geometries*, Springer Science & Business Media, 2012.

– This page intentionally left blank –

2. Fitting Single Walled Carbon Nanotube Optical Spectra

The following Chapter was reproduced with permission from ACS Omega:

Fitting Single Walled Carbon Nanotube Optical Spectra
Moritz Pfohl, Daniel D. Tune, Arko Graf, Jana Zaumseil, Ralph Krupke, and Benjamin S. Flavel
ACS Omega. 2017, 1163
DOI: 10.1021/acsomega.6b00468

Abstract

In this chapter, a comprehensive methodology for the fitting of single walled carbon nanotube absorption spectra is presented. Different approaches to background subtraction, choice of line profile, and calculation of full width at half maximum are discussed both in the context of previous literature and in contemporary understanding of carbon nanotube photophysics. The fitting is improved by the inclusion of exciton-phonon sidebands, and new techniques to improve individualization of overlapped nanotube spectra by exploiting correlations between the first and second order optical transitions and the exciton-phonon sidebands are presented. Consideration of metallic nanotubes allows an analysis of the metallic/semiconducting content and a process of constraining the fit of highly congested spectra of carbon nanotube solid films according the spectral weights of each (n,m) species in solution is also presented, allowing for more reliable resolving overlapping peaks into single (n,m) species contributions.

Contribution

MP and BSF designed the experiments. AG and JZ performed optical characterizations of the different nanotube dispersions and prepared polymer sorted solutions and films. MP wrote the MATLAB® code. DDT and MP wrote the LabView® based graphical user interface. MP, DDT, RK and BSF analysed the results. MP, DDT and BSF drafted the manuscript.

– This page intentionally left blank –

ACS OMEGA
Article
http://pubs.acs.org/journal/acsodf

Fitting Single-Walled Carbon Nanotube Optical Spectra

Moritz Pfohl,[†,‡] Daniel D. Tune,[†,§] Arko Graf,[∥] Jana Zaumseil,[∥] Ralph Krupke,[†,‡] and Benjamin S. Flavel*,[†]

[†]Institute of Nanotechnology, Karlsruhe Institute of Technology (KIT), P.O. Box 3640, 76021 Karlsruhe, Germany
[‡]Institute of Materials Science, Technische Universität Darmstadt, Jovanka-Bontschits-Str. 2, 64287 Darmstadt, Germany
[§]Centre for Nanoscale Science and Technology, Flinders University, GPO Box 2100, 5042 Adelaide, Australia
[∥]Institute for Physical Chemistry, Universität Heidelberg, Im Neuenheimer Feld 253, 69120 Heidelberg, Germany

Supporting Information

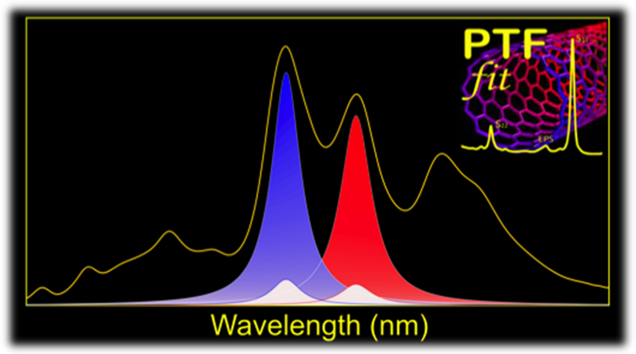

ABSTRACT: In this work, a comprehensive methodology for the fitting of single-walled carbon nanotube absorption spectra is presented. Different approaches to background subtraction, choice of line profile, and calculation of full width at half-maximum are discussed both in the context of previous literature and the contemporary understanding of carbon nanotube photophysics. The fitting is improved by the inclusion of exciton−phonon sidebands, and new techniques to improve the individualization of overlapped nanotube spectra by exploiting correlations between the first- and second-order optical transitions and the exciton−phonon sidebands are presented. Consideration of metallic nanotubes allows an analysis of the metallic/semiconducting content, and a process of constraining the fit of highly congested spectra of carbon nanotube solid films according to the spectral weights of each (*n*, *m*) species in solution is also presented, allowing for more reliable resolution of overlapping peaks into single (*n*, *m*) species contributions.

INTRODUCTION

Single-walled carbon nanotubes (SWCNTs) are an intensively studied nanomaterial and our fundamental understanding of their unique electronic, physical, chemical, and optical properties has steadily increased over the past 2 decades.[1] This has been accompanied by an explosion of applications-based research into SWCNTs in all fields of science from photonics,[2−4] telecommunications,[5] solar cells,[6,7] batteries,[8] fuel cells,[9] high-frequency transistors,[10] biosensors,[11] and novel memory devices,[12] through to sports equipment and cancer research.[7,13−15] Amongst other characteristics, it is their structure-dependent optical properties that make SWCNTs such an interesting material. Optical absorption spectroscopy of SWCNTs reveals sets of diameter-dependent absorption bands in the infrared, visible, and ultraviolet wavelength regimes, corresponding to the discrete energetic transitions of this one-dimensional nanomaterial. These are labeled the first (S_{11}), second (S_{22}), and third (S_{33}) transitions of a (semiconducting) SWCNT and were originally modeled using the single particle approximation.[16] However, two-photon excitation experiments have since revealed the excitonic nature of SWCNT optical transitions and theoretical models have been modified to include confined electron−electron interactions and exciton binding energies by solving the Bethe−Salpeter equation.[17,18] Distinctions have been made between dissimilar SWCNTs based on their chirality, as indicated by the (*n*, *m*) indices, with each semiconducting chirality possessing a unique set of S_{11}, S_{22}, and S_{33} transition energies, and where small changes in the chiral angle and diameter can cause large changes in the optical and electronic properties of a nanotube. Many different (*n*, *m*) species and electronic types of SWCNTs (metallic and semiconducting) are present within as-grown nanotubes, and theoretical calculations, verified by experimental observations, have established databases of the unique optical "fingerprint" associated with each species.[19]

In the case of semiconducting SWCNTs, photoluminescence (PL) spectroscopy, and the ability to measure two-dimensional PL contour maps, has allowed for further experimental verification of each nanotube's optical fingerprint and has provided an essential tool in the qualitative determination of the (*n*, *m*) distribution of as-grown SWCNT powders.[20] However, the insensitivity of PL measurements to metallic SWCNTs, and the strongly varying quantum yield between (*n*, *m*) species, especially for zig-zag nanotubes,[21−23] has resulted in a PL-based quantitative assessment of the (*n*, *m*) distribution remaining elaborate and difficult. Despite this, advances in the physical information that can be obtained with this technique continue to be made and the level of finesse with

Received: December 6, 2016
Accepted: March 9, 2017
Published: March 27, 2017

DOI: 10.1021/acsomega.6b00468
ACS Omega 2017, 2, 1163−1171

which PL spectra can be individualized into single (n, m) contributions and analyzed is improving.[24−27] Raman spectral mapping may offer an alternative solution in the future but currently suffers from the need for elaborate tunable excitation sources. In addition to that, highly structure-dependent and unknown sensitivity factors exacerbate the interpretation of the measurement data.[28] A much newer addition to the toolbox of spectroscopic probes of carbon nanotubes is variance spectroscopy.[29] This is a fluorescence-based technique that can provide excellent quantitative information on the (n, m) distribution of a polychiral material, as well as extract single-species spectra from such mixtures, and which will no doubt have a significant research impact as the required equipment and software become more prevalent. However, due in part to its broad applicability beyond the realm of carbon nanotubes, optical absorption spectroscopy will remain the most widely available and easily accessible technique in the near future and is still considered the preferred method for concentration, electronic purity, and (n, m) determination.[30]

The extraction of physical information from simple optical measurements has allowed for the rapid development of chirality-enriched growth techniques[31] and sorting processes, such as gel permeation,[32,33] density-gradient ultracentrifugation,[34] phase extraction,[35] and polymer wrapping.[36] All of these sorting techniques have been shown to produce single chirality SWCNTs, in some cases up to milligram quantities, and this new availability of material has in turn led to a further increase in applications-based research with SWCNTs. As single chirality SWCNTs move from being an exotic nanomaterial that is available in only a few research laboratories to something commonly available from commercial suppliers, it is imperative that methods of standardization are developed. Indeed, to this end, the ISO Technical Specification ISO/TS 10868:2011 (currently under revision)[37] establishes broad guidelines for the optical characterization of SWCNTs and the US-based National Institute of Standards and Technology (NIST) has released (6, 5) SWCNTs grown from the CoMoCat process and prepared under standardized conditions, as well as a basic "How-To Guide" for near infrared measurements of large diameter, arc discharge SWCNTs.[38]

Throughout the work in our laboratories, we have repeatedly found the need to reliably decongest the optical absorption spectra of single-/few-chirality, as well as polychiral, SWCNT samples and have, thus endeavored to develop a practical, yet robust, system of doing so. Of course, there are several software packages available for the generic fitting of multipeak spectra, each with a plethora of options for how the peaks should be approximated. However, the resultant fitting output rapidly loses physical significance as the number of peaks and their degree of congestion becomes excessive. Factors such as the type of background subtraction employed and the line shape used to approximate the various peaks are critical in obtaining accurate information from the decongestion process. Naturally, one can generate the "best" fit by simply using the largest number of adjustable parameters; however, each of these parameters should have its origin in real physical processes or the reliability, reproducibility, and usefulness of the obtained information are questionable.

Therefore, in the present work, a significantly improved method for decongesting carbon nanotube optical absorption spectra is provided that is grounded in the underlying physical processes and takes advantage of several unique characteristics of the material to markedly improve the quality and accuracy of the obtained information, particularly in the case of the polychiral and highly overlapped spectra that those in the carbon nanotube research community are routinely faced with, for example, in the development of new sorting or growth processes in which the (n, m) distribution can sometimes be large and unknown.[39] The common background subtraction procedures reported in the literature, the various line profiles that have been used, and (n, m) specific absorption databases have been combined with the current state-of-the-art in understanding of carbon nanotube photophysics to develop a comprehensive methodology for the quantitative characterization and (n, m) assignment of SWCNT spectra. Values of interest such as the (n, m) distribution and semiconducting purity can be determined quickly and reproducibly from the spectra of a polychiral material.

In the simplest case, the S_{11} and/or S_{22} regions of a spectrum can be fitted independently using one of several methods as previously reported. To this, we add the new ability to also consider the well-established, and in some cases very significant, contribution of the exciton−phonon sideband (EPS) to the spectra. The inclusion of this nanotube-specific, real-world constraint should significantly improve the accuracy and relevance of the output, particularly in the case of polychiral spectra. This work then takes the fitting process a step further by providing the option to fit the entire spectrum simultaneously, including the S_{11} and S_{22} peaks, and their respective EPS contributions. Such a heavily constrained fitting is only possible in this case because of the well-defined relationships that exist between the physical processes underlying the features observed in carbon nanotube optical absorption spectra, and the existence of complete databases and formulae of the measured energies/wavelengths, and goes beyond anything that can be achieved using generic multipeak fitting software packages. As a further useful addition, in the common case of a polychiral nanotube suspension being used to prepare a solid film, the initial (n, m) assignment and spectral weight data obtained from a fit of the solution spectrum can be used to constrain the fitting of the film's much more heavily congested spectrum, for which the real-world relevance of any fitting procedure would otherwise be questionable. Naturally, as with any decongestion and fitting procedure, there are limitations to the minimum degree of uncertainty that can be obtained, as discussed later. Throughout this work, we have attempted to bring together the theoretical framework and understanding underlying carbon nanotube optical absorption spectra into a single, accessible resource for researchers who need to deal with such spectra, as well as to provide a useful, practical, and robust fitting tool for both expert and novice alike. The work is structured such that the article gives an overview of the theory and review of the literature, as well as some important examples, the Supporting Information file provides more detailed and specific descriptions of fitting processes and mathematical derivations, and the MATLAB code and LabVIEW-based graphical user interface allow readers to implement the entire fitting process in their own work.

■ RESULTS AND DISCUSSION

In the decongestion of carbon nanotube absorption spectra into individual (n, m) contributions, and the determination of the spectral weight of each species and metallic content, the analyst is faced with many decisions regarding the appropriate model to best approximate their measured data. These decisions include: determination of the spectral regions associated with

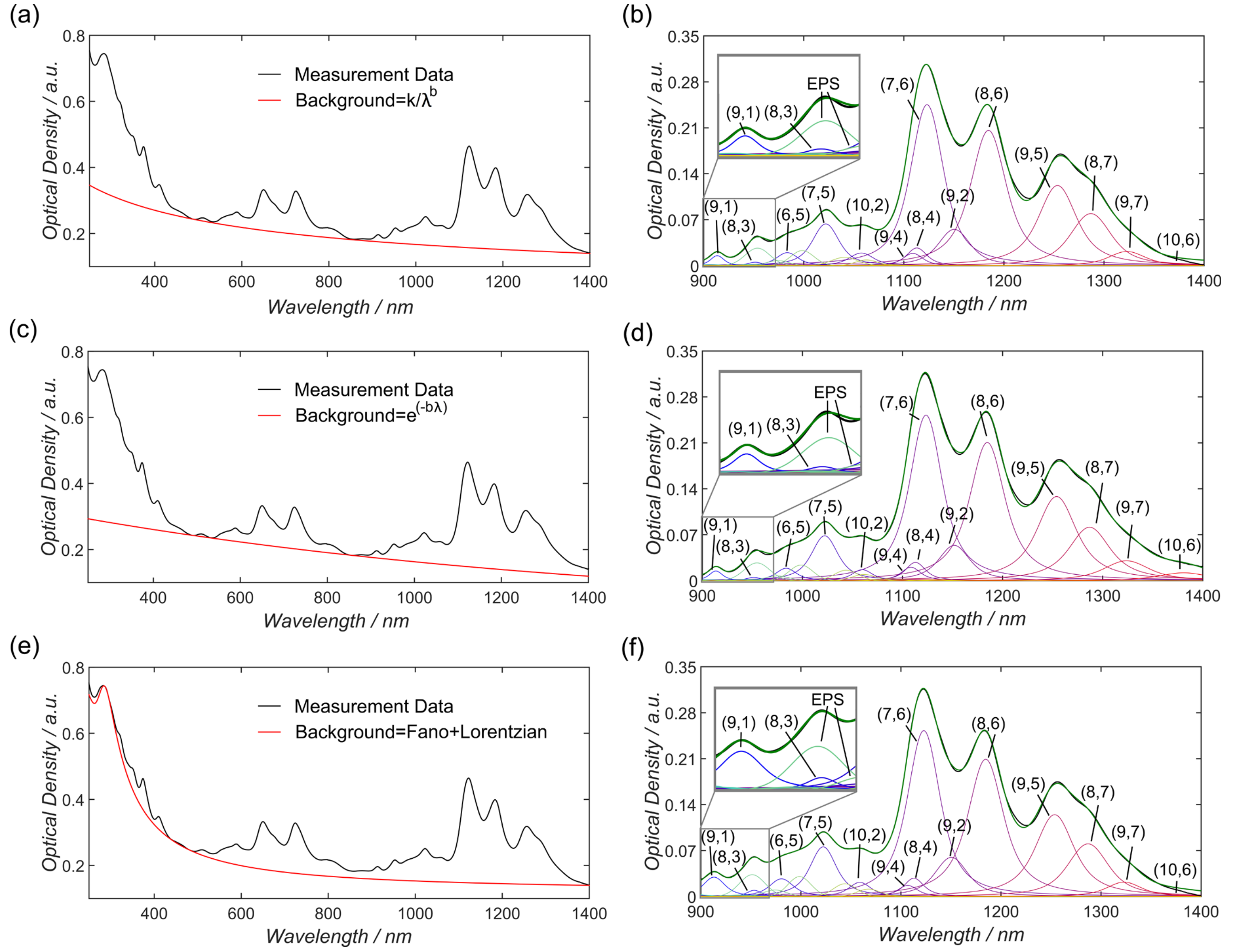

Figure 1. Three different background subtraction methods proposed by Nair et al. (a), Naumov et al. (c), and Tian et al. (e).[39−41] The measured absorption spectra are shown in black and the background profiles in red. The different background subtraction techniques result in comparable (n, m) distributions for shorter wavelengths in (b) and (d) but clearly deviate for (f). Above 1300 nm, (b) and (f) are comparable, whereas (d) clearly deviates, e.g., in the contribution of (9, 7) or (10, 6). A representative PL measurement is shown in Figure S1.

metallic or semiconducting nanotubes and their respective (n, m) dependent optical transitions, the spectral line shape, the full width at half-maximum (FWHM) and whether this is a fixed or variable parameter amongst (n, m) species, the appropriate S_{11} to S_{22} height or area ratio, consideration of EPS contributions and their proper magnitude relative to the main peaks, and, before any of this can be done, what type of background subtraction, if any, should be applied to the spectra. In the following discussion, we will first address the theoretical basis and implications of these factors and then demonstrate their application and some important considerations in their results.

Background Subtraction. The initial decision regarding background subtraction is extremely important as it affects all of the subsequent steps in the fitting process and can result in markedly different (n, m) distributions being calculated. The background in carbon nanotube absorption spectra emerges from a high-energy component often attributed to a π−plasmon interaction and overall scattering from carbonaceous materials, catalyst particles, and bundled or defected nanotubes.[40,41] For aqueous suspensions of SWCNTs, Nair et al.,[40] Naumov et al.,[41] and Ohmori et al.[42] have all presented different approaches to deal with the absorption background. With the aid of sequential centrifugation and difference spectra, Ohmori et al. were able to almost completely remove the contribution from the scattering background in SWCNT spectra and were left with only the high-energy π−plasmon interaction, which they fitted with a Lorentzian.[42] Naumov et al. provided additional experimental evidence that the shape of the background is dependent on metallic nanotube content, chemical modification, defect level, and the formation of bundles.[41] In their work, a background profile in the form $Ae^{(-b\lambda)}$ was found to best accommodate this contribution, with A being the Beer Law proportionality constant, which depends linearly on concentration. Alternatively, Nair et al. empirically determined the form k/λ^b, based on the work of Ryabenko et al.,[43] to best approximate their spectra of highly functionalized carbon nanotubes.[40] In a recent publication, Tian et al. proposed a new routine for background subtraction of carbon nanotube films based on an overlap of Fano and Lorentzian line shapes.[39] The Fano component models the strong coupling of an exciton around the M saddle point of the graphene lattice Brillouin zone (~4.5 eV) to an underlying free electron−hole pair continuum and is very sensitive to bundling.[44] The

DOI: 10.1021/acsomega.6b00468
ACS Omega 2017, 2, 1163−1171

Lorentzian component models the π-plasmon resonance (~5.3 eV), as suggested by Landi et al.[45] The Fano profile is proportional to $(a + \varepsilon)^2/(1 + \varepsilon^2)$ with "a" being a fitting parameter and $\varepsilon = (E - E_{\mathrm{res}})/(\Gamma/2)$, where E is the energy, E_{res} the peak position of the Fano profile, and Γ its FWHM.[46] To exemplify the critical importance of background subtraction, Figure 1 compares the approaches outlined by (a) Nair, (c) Naumov, and (e) Tian, showing how the corresponding (n, m) distributions subsequently calculated can differ considerably, particularly at the edges of the wavelength region, that is, for the (n, m) species (9, 7) (2.56, 4.22, and 2.36% for the methods based on Nair et al., Naumov et al., and Tian et al., respectively) and (10, 6) (0.08, 1.83, and 0.08% for the methods based on Nair et al., Naumov et al., and Tian et al., respectively) on the long wavelength side, and (9, 1) (0.25, 0.22, and 0.44% for the methods based on Nair et al., Naumov et al., and Tian et al., respectively) on the short wavelength side, as listed in Table S1 in the Supporting Information. The result of these considerations is that irrespective of the background subtraction method employed the degree of uncertainty in any quantitative information obtained for (n, m) species near the edges of the considered wavelength range will always be greater than that for those in the middle of the range. In addition, it must be mentioned that the issue of "correct" background shape and the various parameters contributing to it are still under investigation and debate. The large number of different nanotube preparation methods and media available for their suspension, means that a one size-fits-all approach to background subtraction is unlikely to be possible and the backgrounds found in the literature can only serve as a guide. Therefore, in the included code in the Supporting Information it is possible to not only use the background shapes defined in the literature but also to input any arbitrary reference plot data as the background. We hope that this feature will provide the flexibility to analyze a broad spectrum of different nanotube suspensions and enable the further study of background shapes in the future.

Spectral Line Shape. The choice of correct line shape to be used for the individual (n, m) species fitting has varied in the literature. However, it is accepted that a symmetric line shape can be used to fit optical absorption measurements.[47] Luo et al.[21] and Ohmori et al.[42] used Lorentzian line shapes, whereas Nair et al.,[40] Naumov et al.,[41] and Hagen et al.[48] used Voigtian line shapes, and Lolli et al.[49] fitted their data using Gaussian line profiles. In theory, the Voigt function is best suited to fully capture the underlying physical processes that give rise to SWCNT absorption spectra, that is, a convolution of a single finite excited state lifetime (Lorentzian)[50,51] and a random distribution of transition frequencies from heterogeneous environments (Gaussian), including thermal effects that might play a minor role.[52] Or, to put it briefly, the shape is essentially Lorentzian, but with variable Gaussian broadening.[52] Detailed descriptions of the Voigt, Lorentz, and Gauss expressions used in this work can be found in the Supporting Information.

FWHM. Following the selection of line shape, the FWHM must be defined. Similar to the choice of line profile, different empirical approaches for estimating the FWHM have been presented in the literature. Nair et al. divided their absorption spectra into three regions: S_{11}, S_{22}, and M_{11} for metallic SWCNTs,[40] and for each region they assumed a fixed FWHM in energy space. A related approach was carried out by Hagen et al., who assumed a fixed FWHM for S_{11} transitions below 1.4 eV.[53] Lolli et al. and Naumov et al. assumed a constant FWHM in wavenumber units.[41,49] On the basis of the fitting data provided by Ohmori et al.,[42] Tune et al., as well as Liu et al., proposed a linear increase in FWHM with increasing nanotube diameter (in energy space).[54,55] Recently, Kadria-Villi et al. suggested a diameter-dependent FWHM in cm^{-1} for PL measurements.[56] In the examples provided in the main text, the FWHM of Lorentzian and Gaussian functions were modeled on the values provided by Nair et al. as they were found to provide the best fit for our particular nanotube suspensions.[40] For comparison, Figure S2 shows both the initial and fitted FWHM values for a constant FWHM in eV and in nm,[40] or with a diameter dependent,[56] or E_{11} dependence.[55] The initial value in energy space was converted into wavelength and allowed to vary between 80% and 130%. These boundary conditions were determined based on numerous absorption spectra of monochiral, (n, m) enriched, and polychiral nanotube dispersions in aqueous and organic solutions. Nevertheless, in the code provided in the Supporting Information, it is possible to change the boundary conditions or use any of the other approaches for FWHM estimation by defining an equation to estimate the start values.

The definition of an initial value for the FWHM of the Voigtian line shape is complicated by the fact that it is a convolution of a Gaussian and Lorentzian line profile. Nevertheless, Olivero et al. provided an analytic expression for the Voigtian FWHM as a function of the Lorentzian and Gaussian FWHM,[57] as shown in eq 1 and in eq S21−S26

$$\mathrm{FWHM}_{\mathrm{V}} = 0.5436 \cdot \mathrm{FWHM}_{\mathrm{L}} + \sqrt{0.2166 \cdot \mathrm{FWHM}_{\mathrm{L}}^2 + \mathrm{FWHM}_{\mathrm{G}}^2} \tag{1}$$

To calculate Voigtian line profiles, several different approaches have been proposed, including numerical approximations of the Faddeeva, and therefore complex error function (eqs S27 and S28),[58−60] Fourier transformations, and weighted sums of Lorentzian and Gaussian line shapes.[61−63] In the present work, the procedure outlined by Schreier[58] for the rapid approximation of the Faddeeva function was used in combination with the MATLAB implementations from Cherkasov.[64] Thus, the Voigtian function was expressed in terms of the complex error function, as shown in the Supporting Information.

Exciton−Phonon Sidebands. Being excitonic in nature, the analysis of the optical properties of carbon nanotubes has revealed sidebands that are assigned to resonances emerging from the absorption of light by a bound exciton−phonon state.[65,66] According to the work of Perebeinos et al., an EPS can be assigned to optical nanotube transitions and is located ~0.2 eV above the peak energy.[66] Dynamic effects lead to the transfer of a fraction of the spectral weight from the main nanotube peak to the EPS, and the magnitude of this transfer scales inversely with the diameter, as shown in eq S33.[66] It is, therefore, crucial to consider EPS contributions when analyzing absorption spectra, especially for monochiral or chirality-enriched suspensions, as pointed out by Berciaud et al.,[67] and demonstrated in Figure S4. For polychiral solutions, it may be reasonable to consider only the EPS of the most intense peaks, as any EPS of smaller peaks will have only a small effect on the overall fit. In analyzing PL spectra, Jones et al. and Rocha et al. proposed fitting the EPS with Lorentzian line profiles with a fixed FWHM of 18 meV (Jones), or twice the FWHM of the S_{11} peak (Rocha).[26,27] With its sharp onset and long tail toward higher energies, the EPS is asymmetric in nature.[66] However, in the present study, the EPS contribution was approximated with a symmetric line profile to simplify the computation. The decision was made to fit the sharp onset of the EPS peak with a Gaussian line shape to minimize interference with the modeling of the nanotube absorption, which would occur by fitting the broad tail. In this work the default initial FWHM of the EPS was empirically determined to be 40 nm.

Initial Peak Heights. One of the most crucial factors in obtaining a physically meaningful fit is the choice of the initial starting values of the peak heights of each (*n*, *m*) species. In the case of near-monochiral suspensions, the determination of the initial starting value is straightforward as it is given simply by the peak height in the absorption measurement. However, in the case of polychiral mixtures, the determination of starting values is complicated by spectral overlap. Nair et al. proposed a weighting scheme that is reliant on peaks being flanked by a valley to their right and left.[40] They provided an automated routine to determine these parameters and also offered the possibility to insert peaks and valleys manually. Tian et al. introduced a different weighting scheme based on the sum of the two-norm of the residuals and the spectral weight multiplied by a prefactor, which was obtained empirically.[68] Luo et al. and Wang et al. proposed a combined approach of correlating PL intensities and optical absorption spectra via an assumed log-normal distribution of the SWCNT diameters and an electron−phonon model that provided them with S_{22} absorption extinction coefficients.[21,69] On the basis of these absorption coefficients and the PL intensities, they calculated the peak intensities of each (*n*, *m*) species in the optical absorption. The pitfall in their approach is the low PL quantum yield of zig-zag nanotubes that might cause an underrepresentation of these tubes in the optical absorption spectrum and therefore an unphysical fit.[22] The approach used in the present study is shown in Figure 2, where the absorption value of the spectrum to be fitted, at the wavelength corresponding to each (*n*, *m*) species to be included, is taken as the starting value for the peak height of that species and is allowed to vary between 10 and 90%. This method is useful for broad, congested spectral features from many nanotubes. A further alternative method is shown in Figure S5 and is included as an option in the fitting routine provided.

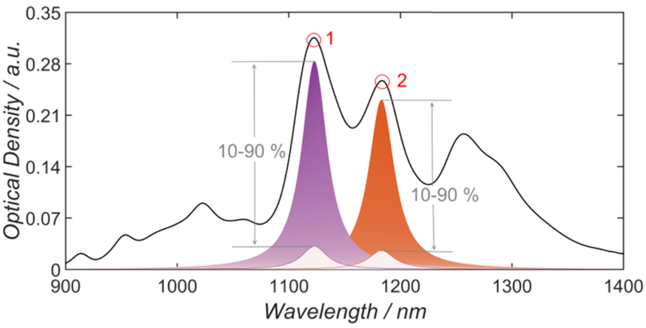

Figure 2. Schematic procedure of height assignment for peaks 1 and 2, where the height of the individual (*n*, *m*) species is allowed to vary between 10 and 90% of the initial height.

To make a quantitative comparison between fits of a particular spectrum, the quality of the fit can be determined by calculating the normalized sum of squared errors (nSSE), as described in eq 2, where y_{calc} is the fitted spectrum, y_{meas} is the absorption measurement, and $\overline{y_{\text{meas}}}$ is the mean value of the measurement. It is important to mention that the nSSE is equal to 1-R^2, where R^2[70] is a common measure of goodness of fit in regression analysis in statistics.[71] The numerator in eq 2 is equal to the sum of squared residuals or the sum of squared errors of prediction.[72] The denominator is the total sum of squares, indicating the deviation from the mean value and causing a normalization of the result. The closer the nSSE is to 0, the better the fit.

$$\text{nSSE} = \frac{\sum (y_{\text{meas}} - y_{\text{calc}})^2}{\sum (y_{\text{meas}} - \overline{y_{\text{meas}}})^2} \qquad (2)$$

A comparison of the different line profiles and their associated nSSE are shown in Figure S6.

Selection of (*n*, *m*) Species to Fit. The final, critical, consideration is that of the choice of (*n*, *m*) species to be fitted under a given spectrum. It is simply not possible to take a polychiral absorption spectrum and extract the (*n*, *m*) abundance by some kind of generic multipeak fitting procedure. However, with a good understanding of the underlying photophysics, and with databases of measured transition energies, combined with information from other characterization techniques such as PL or Raman measurement, it is possible to obtain useful information. In the examples in this work, PL was used to first qualitatively determine the (*n*, *m*) species to be included in the fit. The validity of this approach was verified by taking two different solutions enriched in (6, 5) and (7, 5), and mixing them in known ratios of 2:1, 1:1, and 1:2. By comparing the concentrations of (6, 5) and (7, 5) in the starting solutions to the measured and calculated concentrations in the mixtures, a relative error of 10.8 ± 2.5% was obtained, as shown in Figures S7 and S8. These experiments highlight the level of accuracy and internal consistency of the fitting routine used to determine the ratio of (6, 5):(7, 5) as it is reliant upon an accurate, reproducible spectral fit of the range between 900 and 1250 nm consisting of six different (*n*, *m*) species and their associated EPS.

Spectral Weight and (*n*, *m*) Distribution. Each (*n*, *m*) species has a different absorption cross section, and experimentally determined values can be found in the literature.[47,55,73] Although a full set of measured values is not yet available, Sanchez et al. provided an empirically derived formula for estimating the absorption cross section and molar absorptivity of different (*n*, *m*) species based on their diameter.[47] For the calculation of the (*n*, *m*) distribution, either the spectral weight (area under an individual peak, divided by the total area under the region of the spectrum considered) or the relative concentration based on the optical density and molar absorptivity (as shown in eq S35) can be employed. An example of the spectral weight and relative concentration calculated in the aforementioned ways is shown in Figure 3. Spectra of the polychiral mixtures that were used to generate these plots are shown for reference in Figure S9.

Constrained Fit of Entire Spectrum. A fit of the entire spectrum can be performed by dividing the absorption spectrum into different regions, as proposed by Nair et al.[40] However, such piecewise fitting of complete spectra has the potential to lead to nonphysical fits of the experimental data. For example, when a larger (*n*, *m*) distribution is required to fit S_{22} than is necessary for S_{11}, or vice versa. In reality, these spectral regimes are physically coupled and the (*n*, *m*) distribution must, therefore, remain the same, independent of the region of consideration. Ohmori et al. reported a ratio of 1.15 for S_{11}/S_{22}, whereas Miyata et al. reported a ratio of 1.2 for the integrated molar absorption coefficients.[42,74]

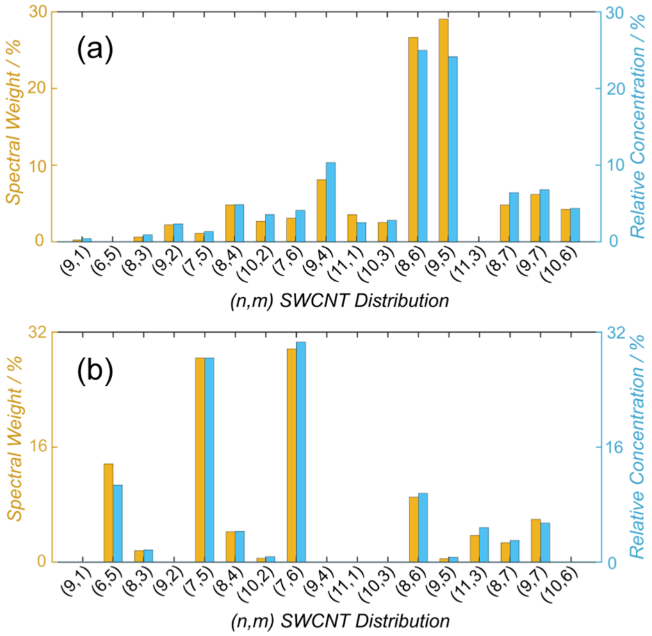

Figure 3. Histograms showing the (n, m) abundance of two different polychiral solutions (a) and (b), shown in Figure S9. The data is presented as both spectral weight and relative concentration.

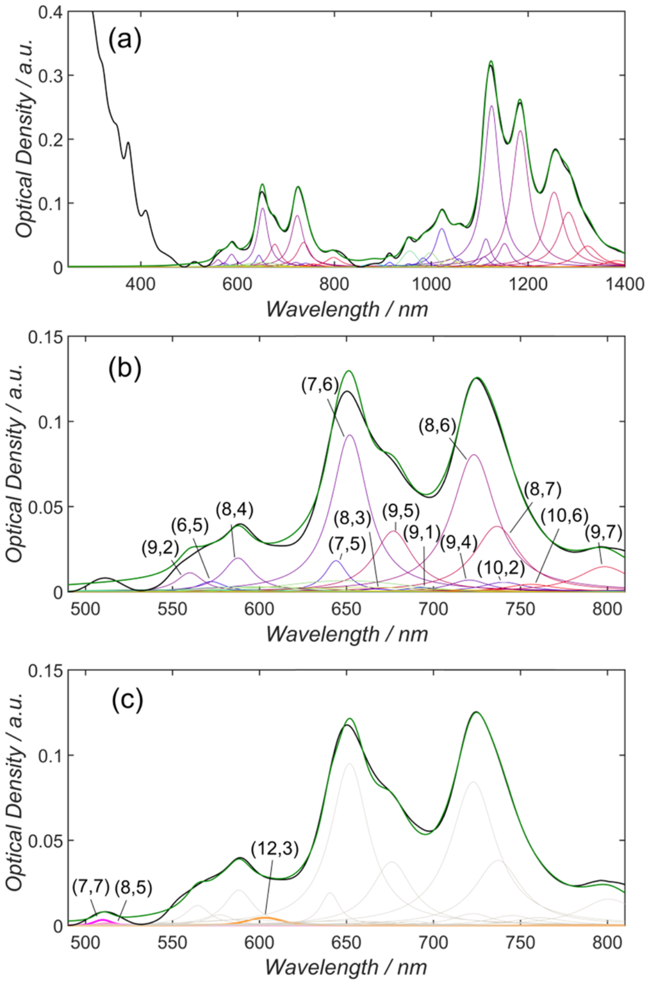

Figure 4. (a) Fit of entire spectral region that was background corrected according to Naumov et al.[41] The measured absorption spectrum is shown in black, and the calculated spectrum is shown in green. (b) Close-up of fit of S_{22} region that was constrained by the (n, m) species assigned to the S_{11} region with an intensity variation of S_{11}/S_{22} between 1 and 5. It can be seen in the region 500–620 nm that the experimental data has been poorly replicated. (c) Upon inclusion of three metallic species, the fit of the S_{22} region was significantly improved.

These values are overall estimates and a definite ratio could not be provided, neither in terms of intensity nor area, due to the spectral overlap and the assignment of one peak to multiple (n, m) species. Nair et al. reported that, for their fits, 30 out of 39 considered semiconducting SWCNTs had an S_{11}/S_{22} peak intensity ratio larger than one, thus 9 of the included SWCNTs had a larger peak intensity in S_{22} than they had in S_{11}.[40] In an ideal system without any doping effects, which might reduce S_{11} intensity, the absorption cross section of the second optical transition is smaller than that of the first one, which should always result in a smaller peak intensity of the S_{22} absorption.[73] Along with constraining the fit of the S_{22} region to only include those (n, m) species that were fitted in the S_{11} region, this assumption was used in the present study to also constrain the height of the peak in the S_{22} region to be a fraction of the S_{11} height, and the starting value for the fit was initially set to 4 $(S_{11,\text{height}}/S_{22,\text{height}} = 4)$, and allowed to vary between 1 and 5. All fractions $(S_{11,\text{height}}/S_{22,\text{height}}$ pair for each (n, m) species) were constrained to be within ±20% to guarantee for a comparable distribution of peak intensities. In this way, an S_{22} peak was prevented from becoming larger than its S_{11} counterpart. Additionally, the FWHM of the S_{22} peak was restricted to be smaller than the FWHM of the S_{11} counterpart to prevent not only the intensity but also the area of the of the (n, m) species in S_{11}, being smaller than that in S_{22}. An example of such a "constrained" fitting procedure is provided in Figure 4a.

As well as preventing nonphysical fits to the data, the great advantage of fitting the entire spectrum of a polychiral sample under such constrained conditions is that once all of the S_{22} peaks are removed, what is left in that region is predominantly due to absorption by metallic nanotubes, thereby providing some information about the metallic/semiconducting purity. However, care must be taken to ensure that a poor fit in S_{22} is not a result of missing (n, m) species in the fit of S_{11} (as shown in detail in Figure S10). Upon evaluating a close-up of the S_{22} region in Figure 4a, shown in Figure 4b, it is apparent that the wavelength regime between 500 and 620 nm was not properly fitted. As demonstrated in Figure 4c, by adding four additional metallic nanotubes to the absorption spectrum ((7,7), (8,5) and (12,3)), the quality of the fit is improved (nSSE = 2.87 × 10^{-3} compared to 3.30 × 10^{-3}). Table S2 summarizes the spectral weights of (n, m) species determined from the fits in Figure 4a,c. The spectral weight of the metallic tubes in solution was calculated to be 0.37% (total area of metallic nanotubes divided by the sum of the area of metallic and semiconducting S_{11} nanotubes).

Therefore, the semiconducting purity in S_{11}, according to spectral weight, of the solution is 99.63%, which is in good agreement with previously reported values for gel-sorted nanotube solutions.[75] However, due to a possible overlap of metallic nanotubes and the S_{22} phonon sideband, the metallic peak assignment is complicated. Likewise, the overlap of large diameter M_{11} peaks with smaller diameter S_{22} peaks makes assignment difficult and means that this method is best suited to fit nanotubes with a narrow diameter distribution.

The results of the solution fit can be used to fit film absorption measurements based on the spectral concentration of each (*n*, *m*) species. A detailed discussion on the film-fitting procedure and associated analysis of the effect of different backgrounds and possible fields of application is given in the Supporting Information.

■ CONCLUSIONS

A comprehensive and up-to-date methodology for fitting carbon nanotube absorption spectra was presented. The entire MATLAB code used in this work is provided in the Supporting Information, as well as a straightforward LabVIEW-based graphical user interface to improve accessibility for those less familiar with the MATLAB environment, but who would still like to employ the functionality of the algorithms in their work. The presented methodology provides the possibility of using different backgrounds for different experimental conditions, modeling of exciton−phonon sidebands, evaluation of the semiconducting purity of the sample by inclusion of metallic species, determination of concentration based on the spectral weight and absorption cross section of species, and the fitting of solid film absorption spectra based on the results of solution measurements. Although the processes used in this work, and made available in the MATLAB code and associated graphical user interface, are certainly an improvement over the use of generic peak fitting software for the specialized task of fitting carbon nanotube absorption spectra, the use of complementary techniques such as PL and Raman spectroscopy is still required to obtain physically significant data. In short, absorption spectroscopy alone should not be seen as the kind of "turnkey" solution that other techniques such as variance spectroscopy have the potential to be. However, we expect that the work presented herein will prove to be a useful resource and tool for those in the research community who employ optical absorption spectroscopy in their carbon nanotube work for a quantitative, yet reliable, analysis.

■ METHODS

Preparation of SWCNT Solutions. SWCNT dispersions were prepared from aqueous surfactant wrapped dispersions using sodium dodecylsulfate (SDS, Merck), sodium cholate (SC, ≥99%, Sigma-Aldrich), and co-surfactant mixtures thereof. Detailed experimental details can be found in previous publications.[14,32] In brief, small diameter HiPco (NanoIntegris) were suspended in 2 wt % SDS by sonication for 1 h followed by ultracentrifugation for 1 h at 64 206g (SW-40-TI rotor). The SDS concentration was then adjusted to 1.6 wt % SDS, and the sample was added to 40 mL of Sephacryl-S200 gel (Amersham Biosciences). Following the separation at 1.6 wt % SDS, the SDS concentration was gradually lowered in 0.2 wt % steps down to a concentration of 0.8 wt %. The absorption spectra shown in Figures 1, 2, and 4 were taken from SWCNT solutions with a starting concentration of 1 wt % SDS. The respective PL map is shown in Figure S1.

UV and PL Measurements. Optical absorption measurements of nanotube dispersions were performed on a Varian Cary 500 spectrophotometer. For the PLE maps of the SWCNT dispersion, the spectrally separated output of a WhiteLase SC400 supercontinuum laser source (Fianium Ltd.) was used for excitation and spectra were recorded with an Acton SpectraPro SP2358 (grating 150 lines/mm) spectrometer with an OMA-V InGaAs line camera (Princeton Instruments) and corrected for background and wavelength-dependent sensitivity/excitation power.

■ ASSOCIATED CONTENT

Supporting Information

The Supporting Information is available free of charge on the ACS Publications website at DOI: 10.1021/acsomega.6b00468.

MATLAB-based routines to fit solution and film absorption measurements (PDF)

A LabVIEW-based graphical user interface incorporating the MATLAB fitting routines (ZIP) (ZIP)

■ AUTHOR INFORMATION

Corresponding Author

*E-mail: benjamin.flavel@kit.edu.

ORCID

Daniel D. Tune: 0000-0002-8330-555X
Jana Zaumseil: 0000-0002-2048-217X
Benjamin S. Flavel: 0000-0002-8213-8673

Notes

The authors declare no competing financial interest.

■ ACKNOWLEDGMENTS

B.S.F. gratefully acknowledges support from the Deutsche Forschungsgemeinschaft (DFG) under grant numbers FL 834/1-1 and FL 834/2-1. R.K. acknowledges funding by the DFG under INST 163/354-1 FUGG. A.G. and J.Z. acknowledge financial support by European Research Council under the European Union's Seventh Framework Programme (FP/2007-2013)/ERC Grant Agreement No. 306298.

■ REFERENCES

(1) Jorio, A.; Dresselhaus, G.; Dresselhaus, M. S. *Carbon Nanotubes*; Springer: Berlin, 2008.

(2) Avouris, P.; Freitag, M.; Perebeinos, V. Carbon-nanotube photonics and optoelectronics. *Nat. Photonics* **2008**, *2*, 341−350.

(3) Pyatkov, F.; Fütterling, V.; Khasminskaya, S.; Flavel, B. S.; Hennrich, F.; Kappes, M. M.; Krupke, R.; Pernice, W. H. P. Cavity-enhanced light emission from electrically driven carbon nanotubes. *Nat. Photonics* **2016**, *10*, 420−427.

(4) Engel, M.; Moore, K. E.; Alam, A.; Dehm, S.; Krupke, R.; Flavel, B. S. Photocurrent Spectroscopy of (n, m) Sorted Solution-Processed Single-Walled Carbon Nanotubes. *ACS Nano* **2014**, *8*, 9324−9331.

(5) Tatsuura, S.; Furuki, M.; Sato, Y.; Iwasa, I.; Tian, M.; Mitsu, H. Semiconductor carbon nanotubes as ultrafast switching materials for optical telecommunications. *Adv. Mater.* **2003**, *15*, 534−537.

(6) Arnold, M. S.; Blackburn, J. L.; Crochet, J. J.; Doorn, S. K.; Duque, J. G.; Mohite, A.; Telg, H. Recent developments in the photophysics of single-walled carbon nanotubes for their use as active and passive material elements in thin film photovoltaics. *Phys. Chem. Chem. Phys.* **2013**, *15*, 14896−14918.

(7) Tune, D. D.; Hennrich, F.; Dehm, S.; Klein, M. F. G.; Glaser, K.; Colsmann, A.; Shapter, J. G.; Lemmer, U.; Kappes, M. M.; Krupke, R.; Flavel, B. S. The Role of Nanotubes in Carbon Nanotube−Silicon Solar Cells. *Adv. Energy Mater.* **2013**, *3*, 1091−1097.

(8) Landi, B. J.; Ganter, M. J.; Cress, C. D.; DiLeo, R. A.; Raffaelle, R. P. Carbon nanotubes for lithium ion batteries. *Energy Environ. Sci.* **2009**, *2*, 638−654.

(9) Varga, Á.; Pfohl, M.; Brunelli, N. A.; Schreier, M.; Giapis, K. P.; Haile, S. M. Carbon nanotubes as electronic interconnects in solid acid fuel cell electrodes. *Phys. Chem. Chem. Phys.* **2013**, *15*, 15470−15476.

(10) Steiner, M.; Engel, M.; Lin, Y.-M.; Wu, Y.; Jenkins, K.; Farmer, D. B.; Humes, J. J.; Yoder, N. L.; Seo, J.-W. T.; Green, A. A.; Hersam, M. C.; Krupke, R.; Avouris, P. High-frequency performance of scaled

carbon nanotube array field-effect transistors. *Appl. Phys. Lett.* **2012**, *101*, No. 053123.

(11) Wang, J. Carbon-Nanotube Based Electrochemical Biosensors: A Review. *Electroanalysis* **2005**, *17*, 7−14.

(12) Flavel, B. S.; Yu, J.; Shapter, J. G.; Quinton, J. S. Patterned ferrocenemethanol modified carbon nanotube electrodes on silane modified silicon. *J. Mater. Chem.* **2007**, *17*, 4757−4761.

(13) Yu, X.; Munge, B.; Patel, V.; Jensen, G.; Bhirde, A.; Gong, J. D.; Kim, S. N.; Gillespie, J.; Gutkind, J. S.; Papadimitrakopoulos, F.; Rusling, J. F. Carbon Nanotube Amplification Strategies for Highly Sensitive Immunodetection of Cancer Biomarkers. *J. Am. Chem. Soc.* **2006**, *128*, 11199−11205.

(14) Pfohl, M.; Glaser, K.; Ludwig, J.; Tune, D. D.; Dehm, S.; Kayser, C.; Colsmann, A.; Krupke, R.; Flavel, B. S. Performance Enhancement of Polymer-Free Carbon Nanotube Solar Cells via Transfer Matrix Modeling. *Adv. Energy Mater.* **2016**, *6*, No. 1501345.

(15) Bindl, D. J.; Safron, N. S.; Arnold, M. S. Dissociating Excitons Photogenerated in Semiconducting Carbon Nanotubes at Polymeric Photovoltaic Heterojunction Interfaces. *ACS Nano* **2010**, *4*, 5657−5664.

(16) Reich, S.; Thomsen, C.; Maultzsch, J. *Carbon Nanotubes: Basic Concepts and Physical Properties*; John Wiley & Sons, 2008.

(17) Maultzsch, J.; Pomraenke, R.; Reich, S.; Chang, E.; Prezzi, D.; Ruini, A.; Molinari, E.; Strano, M. S.; Thomsen, C.; Lienau, C. Exciton binding energies in carbon nanotubes from two-photon photoluminescence. *Phys. Rev. B* **2005**, *72*, No. 241402.

(18) Jiang, J.; Saito, R.; Samsonidze, G. G.; Jorio, A.; Chou, S. G.; Dresselhaus, G.; Dresselhaus, M. S. Chirality dependence of exciton effects in single-wall carbon nanotubes: Tight-binding model. *Phys. Rev. B* **2007**, *75*, No. 035407.

(19) Kataura, H.; Kumazawa, Y.; Maniwa, Y.; Umezu, I.; Suzuki, S.; Ohtsuka, Y.; Achiba, Y. Optical properties of single-wall carbon nanotubes. *Synth. Met.* **1999**, *103*, 2555−2558.

(20) Bachilo, S. M.; Strano, M. S.; Kittrell, C.; Hauge, R. H.; Smalley, R. E.; Weisman, R. B. Structure-Assigned Optical Spectra of Single-Walled Carbon Nanotubes. *Science* **2002**, *298*, 2361−2366.

(21) Luo, Z.; Pfefferle, L. D.; Haller, G. L.; Papadimitrakopoulos, F. (n,m) Abundance Evaluation of Single-Walled Carbon Nanotubes by Fluorescence and Absorption Spectroscopy. *J. Am. Chem. Soc.* **2006**, *128*, 15511−15516.

(22) Oyama, Y.; Saito, R.; Sato, K.; Jiang, J.; Samsonidze, G. G.; Grüneis, A.; Miyauchi, Y.; Maruyama, S.; Jorio, A.; Dresselhaus, G.; Dresselhaus, M. S. Photoluminescence intensity of single-wall carbon nanotubes. *Carbon* **2006**, *44*, 873−879.

(23) Tsyboulski, D. A.; Rocha, J.-D. R.; Bachilo, S. M.; Cognet, L.; Weisman, R. B. Structure-Dependent Fluorescence Efficiencies of Individual Single-Walled Carbon Nanotubes. *Nano Lett.* **2007**, *7*, 3080−3085.

(24) Cambré, S.; Campo, J.; Beirnaert, C.; Verlackt, C.; Cool, P.; Wenseleers, W. Asymmetric dyes align inside carbon nanotubes to yield a large nonlinear optical response. *Nat. Nanotechnol.* **2015**, *10*, 248−252.

(25) Cambré, S.; Santos, S. M.; Wenseleers, W.; Nugraha, A. R. T.; Saito, R.; Cognet, L.; Lounis, B. Luminescence Properties of Individual Empty and Water-Filled Single-Walled Carbon Nanotubes. *ACS Nano* **2012**, *6*, 2649−2655.

(26) Jones, M.; Engtrakul, C.; Metzger, W. K.; Ellingson, R. J.; Nozik, A. J.; Heben, M. J.; Rumbles, G. Analysis of photoluminescence from solubilized single-walled carbon nanotubes. *Phys. Rev. B: Condens. Matter Mater. Phys.* **2005**, *71*, No. 115426.

(27) Rocha, J.-D. R.; Bachilo, S. M.; Ghosh, S.; Arepalli, S.; Weisman, R. B. Efficient Spectrofluorimetric Analysis of Single-Walled Carbon Nanotube Samples. *Anal. Chem.* **2011**, *83*, 7431−7437.

(28) Lebedkin, S.; Arnold, K.; Kiowski, O.; Hennrich, F.; Kappes, M. M. Raman study of individually dispersed single-walled carbon nanotubes under pressure. *Phys. Rev. B: Condens. Matter Mater. Phys.* **2006**, *73*, No. 094109.

(29) Streit, J. K.; Bachilo, S. M.; Sanchez, S. R.; Lin, C.-W.; Weisman, R. B. Variance Spectroscopy. *J. Phys. Chem. Lett.* **2015**, *6*, 3976−3981.

(30) Itkis, M. E.; Perea, D. E.; Jung, R.; Niyogi, S.; Haddon, R. C. Comparison of Analytical Techniques for Purity Evaluation of Single-Walled Carbon Nanotubes. *J. Am. Chem. Soc.* **2005**, *127*, 3439−3448.

(31) He, M.; Jiang, H.; Liu, B.; Fedotov, P. V.; Chernov, A. I.; Obraztsova, E. D.; Cavalca, F.; Wagner, J. B.; Hansen, T. W.; Anoshkin, I. V.; Obraztsova, E. A.; Belkin, A. V.; Sairanen, E.; Nasibulin, A. G.; Lehtonen, J.; Kauppinen, E. I. Chiral-Selective Growth of Single-Walled Carbon Nanotubes on Lattice-Mismatched Epitaxial Cobalt Nanoparticles. *Sci. Rep.* **2013**, *3*, No. 1460.

(32) Flavel, B. S.; Moore, K. E.; Pfohl, M.; Kappes, M. M.; Hennrich, F. Separation of Single-Walled Carbon Nanotubes with a Gel Permeation Chromatography System. *ACS Nano* **2014**, *8*, 1817−1826.

(33) Liu, H.; Nishide, D.; Tanaka, T.; Kataura, H. Large-scale single-chirality separation of single-wall carbon nanotubes by simple gel chromatography. *Nat. Commun.* **2011**, *2*, No. 309.

(34) Arnold, M. S.; Green, A. A.; Hulvat, J. F.; Stupp, S. I.; Hersam, M. C. Sorting carbon nanotubes by electronic structure using density differentiation. *Nat. Nanotechnol.* **2006**, *1*, 60−65.

(35) Khripin, C. Y.; Fagan, J. A.; Zheng, M. Spontaneous Partition of Carbon Nanotubes in Polymer-Modified Aqueous Phases. *J. Am. Chem. Soc.* **2013**, *135*, 6822−6825.

(36) Nish, A.; Hwang, J.-Y.; Doig, J.; Nicholas, R. J. Highly selective dispersion of single-walled carbon nanotubes using aromatic polymers. *Nat. Nanotechnol.* **2007**, *2*, 640−646.

(37) ISO/TS 10868:2011. *Nanotechnologies — Characterization of Single-Wall Carbon Nanotubes Using Ultraviolet-Visible-Near Infrared (UV-vis-NIR) Absorption Spectroscopy*; International Organization for Standardization: Switzerland, 2011.

(38) Arepalli, S.; Freiman, S. W.; Hooker, S. A.; Migler, K. D. *Measurement Issues in Single-Wall Carbon Nanotubes*; Special Publication (NIST SP) - 960.19; NIST, 2008.

(39) Tian, Y.; Jiang, H.; Anoshkin, I. V.; Kauppinen, L. J. I.; Mustonen, K.; Nasibulin, A. G.; Kauppinen, E. I. A reference material of single-walled carbon nanotubes: quantitative chirality assessment using optical absorption spectroscopy. *RSC Adv.* **2015**, *5*, 102974−102980.

(40) Nair, N.; Usrey, M. L.; Kim, W.-J.; Braatz, R. D.; Strano, M. S. Estimation of the (n,m) Concentration Distribution of Single-Walled Carbon Nanotubes from Photoabsorption Spectra. *Anal. Chem.* **2006**, *78*, 7689−7696.

(41) Naumov, A. V.; Ghosh, S.; Tsyboulski, D. A.; Bachilo, S. M.; Weisman, R. B. Analyzing Absorption Backgrounds in Single-Walled Carbon Nanotube Spectra. *ACS Nano* **2011**, *5*, 1639−1648.

(42) Ohmori, S.; Saito, T.; Tange, M.; Shukla, B.; Okazaki, T.; Yumura, M.; Iijima, S. Fundamental Importance of Background Analysis in Precise Characterization of Single-Walled Carbon Nanotubes by Optical Absorption Spectroscopy. *J. Phys. Chem. C* **2010**, *114*, 10077−10081.

(43) Ryabenko, A. G.; Dorofeeva, T. V.; Zvereva, G. I. UV−VIS−NIR spectroscopy study of sensitivity of single-wall carbon nanotubes to chemical processing and Van-der-Waals SWNT/SWNT interaction. Verification of the SWNT content measurements by absorption spectroscopy. *Carbon* **2004**, *42*, 1523−1535.

(44) Crochet, J. J.; Hoseinkhani, S.; Lüer, L.; Hertel, T.; Doorn, S. K.; Lanzani, G. Free-Carrier Generation in Aggregates of Single-Wall Carbon Nanotubes by Photoexcitation in the Ultraviolet Regime. *Phys. Rev. Lett.* **2011**, *107*, No. 257402.

(45) Landi, B. J.; Ruf, H. J.; Evans, C. M.; Cress, C. D.; Raffaelle, R. P. Purity Assessment of Single-Wall Carbon Nanotubes, Using Optical Absorption Spectroscopy. *J. Phys. Chem. B* **2005**, *109*, 9952−9965.

(46) Fano, U. Effects of Configuration Interaction on Intensities and Phase Shifts. *Phys. Rev.* **1961**, *124*, 1866−1878.

(47) Sanchez, S. R.; Bachilo, S. M.; Kadria-Vili, Y.; Lin, C.-W.; Weisman, R. B. (n,m)-Specific Absorption Cross Sections of Single-Walled Carbon Nanotubes Measured by Variance Spectroscopy. *Nano Lett.* **2016**, *16*, 6903−6909.

(48) Hagen, A.; Moos, G.; Talalaev, V.; Hertel, T. Electronic structure and dynamics of optically excited single-wall carbon nanotubes. *Appl. Phys. A: Mater. Sci. Process.* **2004**, *78*, 1137−1145.

(49) Lolli, G.; Zhang, L.; Balzano, L.; Sakulchaicharoen, N.; Tan, Y.; Resasco, D. E. Tailoring (n,m) Structure of Single-Walled Carbon Nanotubes by Modifying Reaction Conditions and the Nature of the Support of CoMo Catalysts. *J. Phys. Chem. B* **2006**, *110*, 2108−2115.

(50) Hertel, V. I.; Schulz, C.-P. Linienbreiten, Multiphotonenprozesse und mehr. In *Atome, Moleküle und optische Physik 1: Atomphysik und Grundlagen der Spektroskopie*; Springer: Berlin, 2008; pp 157−193.

(51) Weisskopf, V.; Wigner, E. Berechnung der natürlichen Linienbreite auf Grund der Diracschen Lichttheorie. *Z. Phys.* **1930**, *63*, 54−73.

(52) Meier, R. J. On art and science in curve-fitting vibrational spectra. *Vib. Spectrosc.* **2005**, *39*, 266−269.

(53) Hagen, A.; Hertel, T. Quantitative Analysis of Optical Spectra from Individual Single-Wall Carbon Nanotubes. *Nano Lett.* **2003**, *3*, 383−388.

(54) Tune, D. D.; Shapter, J. G. The potential sunlight harvesting efficiency of carbon nanotube solar cells. *Energy Environ. Sci.* **2013**, *6*, 2572−2577.

(55) Liu, K.; Hong, X.; Choi, S.; Jin, C.; Capaz, R. B.; Kim, J.; Wang, W.; Bai, X.; Louie, S. G.; Wang, E.; Wang, F. Systematic determination of absolute absorption cross-section of individual carbon nanotubes. *Proc. Natl. Acad. Sci. U.S.A.* **2014**, *111*, 7564−7569.

(56) Kadria-Vili, Y.; Bachilo, S. M.; Blackburn, J. L.; Weisman, R. B. Photoluminescence Side Band Spectroscopy of Individual Single-Walled Carbon Nanotubes. *J. Phys. Chem. C* **2016**, *120*, 23898−23904.

(57) Olivero, J. J.; Longbothum, R. L. Empirical fits to the Voigt line width: A brief review. *J. Quant. Spectrosc. Radiat. Transfer* **1977**, *17*, 233−236.

(58) Schreier, F. Optimized implementations of rational approximations for the Voigt and complex error function. *J. Quant. Spectrosc. Radiat. Transfer* **2011**, *112*, 1010−1025.

(59) Humlíček, J. Optimized computation of the voigt and complex probability functions. *J. Quant. Spectrosc. Radiat. Transfer* **1982**, *27*, 437−444.

(60) Weideman, J. A. C. Computation of the Complex Error Function. *SIAM J. Numer. Anal.* **1994**, *31*, 1497−1518.

(61) Jian, H.; Chunmin, Z. The accurate calculation of the Fourier transform of the pure Voigt function. *J. Opt. A: Pure Appl. Opt.* **2005**, *7*, 613.

(62) Westberg, J.; Wang, J.; Axner, O. Fast and non-approximate methodology for calculation of wavelength-modulated Voigt lineshape functions suitable for real-time curve fitting. *J. Quant. Spectrosc. Radiat. Transfer* **2012**, *113*, 2049−2057.

(63) Liu, Y.; Lin, J.; Huang, G.; Guo, Y.; Duan, C. Simple empirical analytical approximation to the Voigt profile. *J. Opt. Soc. Am. B* **2001**, *18*, 666−672.

(64) Lukyanov, D. B.; Vazhnova, T.; Cherkasov, N.; Casci, J. L.; Birtill, J. J. Insights into Brønsted Acid Sites in the Zeolite Mordenite. *J. Phys. Chem. C* **2014**, *118*, 23918−23929.

(65) Dresselhaus, M. S.; Dresselhaus, G.; Saito, R.; Jorio, A. Exciton photophysics of carbon nanotubes. *Annu. Rev. Phys. Chem.* **2007**, *58*, 719−747.

(66) Perebeinos, V.; Tersoff, J.; Avouris, P. Effect of exciton-phonon coupling in the calculated optical absorption of carbon nanotubes. *Phys. Rev. Lett.* **2005**, *94*, No. 027402.

(67) Berciaud, S.; Cognet, L.; Poulin, P.; Weisman, R. B.; Lounis, B. Absorption Spectroscopy of Individual Single-Walled Carbon Nanotubes. *Nano Lett.* **2007**, *7*, 1203−1207.

(68) Tian, Y.; Jiang, H.; Pfaler, J. v.; Zhu, Z.; Nasibulin, A. G.; Nikitin, T.; Aitchison, B.; Khriachtchev, L.; Brown, D. P.; Kauppinen, E. I. Analysis of the Size Distribution of Single-Walled Carbon Nanotubes Using Optical Absorption Spectroscopy. *J. Phys. Chem. Lett.* **2010**, *1*, 1143−1148.

(69) Wang, B.; Poa, C. H. P.; Wei, L.; Li, L.-J.; Yang, Y.; Chen, Y. (n,m) Selectivity of Single-Walled Carbon Nanotubes by Different Carbon Precursors on Co−Mo Catalysts. *J. Am. Chem. Soc.* **2007**, *129*, 9014−9019.

(70) Hackl, P. *Einführung in die Ökonometrie*; Pearson Deutschland GmbH, 2008; Vol. *7118*.

(71) Mendenhall, W.; Beaver, R. J.; Beaver, B. M. *Introduction to Probability and Statistics*; Cengage Learning, 2012.

(72) Tsay, R. S. *Analysis of Financial Time Series*; John Wiley & Sons, 2005; Vol. *543*.

(73) Streit, J. K.; Bachilo, S. M.; Ghosh, S.; Lin, C.-W.; Weisman, R. B. Directly Measured Optical Absorption Cross Sections for Structure-Selected Single-Walled Carbon Nanotubes. *Nano Lett.* **2014**, *14*, 1530−1536.

(74) Miyata, Y.; Yanagi, K.; Maniwa, Y.; Kataura, H. Optical Evaluation of the Metal-to-Semiconductor Ratio of Single-Wall Carbon Nanotubes. *J. Phys. Chem. C* **2008**, *112*, 13187−13191.

(75) Tulevski, G. S.; Franklin, A. D.; Afzali, A. High Purity Isolation and Quantification of Semiconducting Carbon Nanotubes via Column Chromatography. *ACS Nano* **2013**, *7*, 2971−2976.

– This page intentionally left blank –

3. Performance Enhancement of Polymer-Free Carbon Nanotube Solar Cells via Transfer Matrix Modeling

The following Chapter is reproduced with the permission of John Wiley and Sons:

Performance Enhancement of Polymer-Free Carbon Nanotube Solar Cells via Transfer Matrix Modeling
Moritz Pfohl, Konstantin Glaser, Jens Ludwig, Daniel D. Tune, Simone Dehm, Christian Kayser, Alexander Colsmann, Ralph Krupke, Benjamin S. Flavel
Advanced Energy Materials, 2016, 6, 1501345
DOI: 10.1002/aenm.201501345

Abstract

Polymer-free (6,5) single-walled carbon nanotubes (SWCNTs) prepared using the gel permeation approach are integrated into SWCNT:C_{60} solar cells. Evaporation-driven self-assembly is used to form large-area SWCNT thin films from the surfactant-stabilized aqueous suspensions. The thicknesses of various layers within the solar cell are optimized by theoretical modeling using transfer matrix calculations, where the distribution of the electric field within the stack is matched to light absorption by the SWCNTs through either their primary (S_{11}) or secondary (S_{22}) absorption peaks, or a combination thereof. The validity of the model is verified experimentally through a detailed parameter study and then used to develop SWCNT:C_{60} solar cells with high open-circuit voltage (0.44 V) as well as a cutting-edge internal quantum efficiency of up to 86% through the nanotube S_{11} transition, over an active area of 0.105 cm^2.

Contribution

MP and BSF designed the experiments and prepared large amounts of highly enriched (6,5) SWCNT solutions. MP, SD and DDT performed AFM measurements to analyse different film thicknesses of C_{60}. CK, KG and JL performed DektakXT profiler measurements to evaluate the film thicknesses of PEDOT:PSS. MP, KG, JL, CK, DDT and BSF prepared and tested the solar cell devices. MP, DDT, AC, RK and BSF analysed the results. MP, DDT and BSF drafted the manuscript.

– This page intentionally left blank –

ADVANCED ENERGY MATERIALS
www.advenergymat.de

Performance Enhancement of Polymer-Free Carbon Nanotube Solar Cells via Transfer Matrix Modeling

*Moritz Pfohl, Konstantin Glaser, Jens Ludwig, Daniel D. Tune, Simone Dehm, Christian Kayser, Alexander Colsmann, Ralph Krupke, and Benjamin S. Flavel**

Polymer-free (6,5) single-walled carbon nanotubes (SWCNTs) prepared using the gel permeation approach are integrated into SWCNT:C_{60} solar cells. Evaporation-driven self-assembly is used to form large-area SWCNT thin films from the surfactant-stabilized aqueous suspensions. The thicknesses of various layers within the solar cell are optimized by theoretical modeling using transfer matrix calculations, where the distribution of the electric field within the stack is matched to light absorption by the SWCNTs through either their primary (S_{11}) or secondary (S_{22}) absorption peaks, or a combination thereof. The validity of the model is verified experimentally through a detailed parameter study and then used to develop SWCNT:C_{60} solar cells with high open-circuit voltage (0.44 V) as well as a cutting-edge internal quantum efficiency of up to 86% through the nanotube S_{11} transition, over an active area of 0.105 cm^2.

1. Introduction

Over the past 5 years, single-walled carbon nanotubes (SWCNTs) have attracted much attention in the organic solar cell community, from both a theoretical and practical point of view, as either a light sensitizing material, or in active layer composites.[1–7] This is due to such desirable characteristics as their high charge carrier mobility along the nanotube axis and excellent stability toward degradation in ambient, humid, hot or high UV radiation conditions.[8] As an active material, a key driver of this interest has been the desire to absorb the infrared light excluded by traditional organic sensitizers. In addition, the presence of multiple excitonic transitions within SWCNTs may allow for solar cells built from them to not only cover the infrared spectrum but also the visible and UV regimes. For example, small diameter (≈0.8–1.2 nm) semiconducting nanotubes have their first excitonic transition (S_{11}) in the NIR (900–1250 nm), the second (S_{22}) in the visible (550–900 nm), and the third (S_{33}) in the UV.[9] Due to the larger absorption cross section of the S_{11} transition compared to S_{22}, S_{33}, etc. most researchers have so far focused on the infrared regime. However, Bindl and Arnold have recently investigated the quantum efficiency from S_{11}, S_{22}, and even hot S_{11} + K transitions from (7,5) SWCNTs and found that the measured efficiencies correlated well with the expected absorption cross sections.[10]

The development of SWCNT solar cells capable of harvesting light across such a broad wavelength range introduces new questions regarding the ideal design of the layer stack such that there is adequate electric field intensity from the incoming light at the positions where the nanotubes absorb. To this end, transfer matrix calculations (TMCs) are particularly useful because it is possible to predict the optimal exciton generation rate in the nanotubes based on the normal squared electric field intensity ($|E|^2$) for any combination of layers in a solar cell stack.[11] By correlating $|E|^2$ calculations to the SWCNT absorption profile, we demonstrate control of the ratio of external quantum efficiency (EQE) due to S_{11}, S_{22}, and a combination thereof through variation of the stack design. This complements the work of Bindl and Arnold and Guillot et al. who used solar cell stack designs which resulted in electric fields distributed across either S_{22} and S_{11} or specifically across S_{11}.[1,2,6,10]

The preparation of semiconducting pure SWCNTs suitable for use in SWCNT:C_{60} solar cells can broadly be divided into two categories; first, via selective polymer wrapping in an organic medium,[12,13] or second, through aqueous surfactant-based methods such as gel permeation chromatography (GPC),[14,15] density gradient ultracentrifugation (DGU), or the newly developed phase transfer method.[16,17] In terms of industrial applicability, both methodologies have their advantages and disadvantages. For example polymer wrapping with poly(9,9-dioctylfluorenyl-2,7-diyl) (PFO) or regioregular poly(3-alkylthiophene)s (rr-P3ATs) has been shown to be highly

---

M. Pfohl, Dr. D. D. Tune, S. Dehm,
Prof. R. Krupke, Dr. B. S. Flavel
Institute of Nanotechnology
Karlsruhe Institute of Technology (KIT)
76021 Karlsruhe, Germany
E-mail: benjamin.flavel@kit.edu

M. Pfohl, Prof. R. Krupke
Institute of Materials Science
Technische Universität Darmstadt
64287 Darmstadt, Germany

K. Glaser, J. Ludwig, C. Kayser, Dr. A. Colsmann
Light Technology Institute
Karlsruhe Institute of Technology (KIT)
76131 Karlsruhe, Germany

Dr. D. D. Tune
Centre for Nanoscale Science and Technology
Flinders University
Adelaide 5042, Australia

DOI: 10.1002/aenm.201501345

selective to small diameter SWCNTs and capable of yielding extremely high semiconducting contents of >99%.[18] In the case of SWCNT solar cells this observed high selectivity is important as the absence of metallic species reduces the potential for interlayer shorts or the introduction of trap states.[19] Additionally, the processing of SWCNTs in an organic medium is often more amenable to flat, thin film fabrication, while still being compatible with the surrounding layers in the device stack, and techniques such as doctorblading,[1] spin-coating, and spray-coating have been used in the past.[4,6] It is likely for these reasons that most of the nanotube solar cell literature uses polymer-wrapped SWCNTs as the donor material. Pioneering the field in 2010, Bindl et al., used PFO-wrapped SWCNTs in combination with different electron and hole acceptor materials such as fullerene C_{60}, [6,6]-phenyl C_{61} butyric acid methyl ester ($PC_{61}BM$) or poly(3-hexylthiophene) (P3HT), respectively, and showed that the SWCNTs form a Type-II heterojunction with sufficient energetic offset to drive exciton dissociation and the generation of photocurrent.[1] Power conversion efficiencies of 1% with C_{60} and 3.1% with $PC_{71}BM$ were obtained using planar junctions and bulk heterojunction (BHJ) solar cells, respectively.[2,5] In the planar architecture, an EQE and internal quantum efficiency (IQE) of 40% and more than 85% were obtained at S_{11}.[2,10] Despite these remarkable results, new strategies to remove the excess polymer are required. As was later outlined by Bindl et al.,[20] residual PFO limits the intertube diffusion length to ≈8 nm and therefore restricts the usage of thicker nanotube films. However, the greatest limitation to polymer wrapping methodologies (at least for small diameters) is the low yield and expense of the polymer, which has likely contributed to the use of relatively small active areas of between 0.008 and 0.04 cm^2 until, recently, Guillot et al. fabricated solar cell devices with an active area of 0.101 cm^2 that were masked to 0.061 cm^2.[2,4,6,12] Although the use of small areas is convenient in the obtainment of statistics, increasing the active area is an important issue to address if carbon nanotube solar cells are to develop as a technology. Toward this end, Bao and co-workers have looked at the role of the polymer's alkyl side chains in increasing the yield of sorting small diameter nanotubes for solar cell applications.[4] Likewise, Blackburn and co-workers have demonstrated a spray-coating technique that is compatible with large area film fabrication.[21]

In contrast, the yield from surfactant-based methods is significantly higher; with our recently developed automated gel permeation system capable of routinely preparing mg amounts of (n,m) sorted material, albeit with higher metallic nanotube content compared to polymer wrapping. Although, as shown in the work of Tulevski et al.,[22] surfactant-based method can reach a semiconducting purity larger than 98%. The use of an aqueous suspension introduces new fabrication challenges due to the incompatibility of many common solar cells organic layers with water, which is probably a contributing factor in why the literature currently only provides one example of the use of surfactant-wrapped SWCNTs in these types of solar cells. In that work, Jain et al. prepared a SWCNT film via vacuum filtration of surfactant-stabilized (6,5) nanotubes and placed this in contact with C_{60} as an electron acceptor.[3] Despite having a 100 nm thick nanotube film, the current contribution from the nanotubes was only 0.5% in the EQE, with an overall power conversion efficiency of 0.1% and, although not reported, an evidently low IQE.

In our work, we have also investigated surfactant-wrapped (6,5) SWCNTs however, instead of vacuum filtration, we have used evaporation-driven self-assembly (EDSA) to form our nanotube films. In previous reports, this approach has yielded closed films and stripes of horizontally aligned nanotubes on silicon dioxide from surfactant wrapped, enriched (6,5) nanotube solutions in 0.1 and 1 wt% sodium dodecyl sulfate (SDS).[23,24] Recently, Li et al. published videos of SWCNT stripe formation via a "slip-stick" mechanism, demonstrating that the dynamic contact line pinning and SDS concentration are responsible for the horizontal alignment of nanotubes.[23] In this report, the stripe formation was suppressed by adjusting the evaporation speed of the nanotube solution and surfactant concentration to create thin (≈2 nm), homogenously closed films over large areas (≈2 cm^2). Similarly to the work of Wang et al., our design consists of the nanotube film sandwiched between a poly(3,4-ethylenedioxythiophene) polystyrene sulfonate (PEDOT:PSS) hole transport layer and a C_{60} electron acceptor and transport layer in a planar organic heterojunction solar cell.[4]

2. Results and Discussion

The solar cell architecture is shown in **Figure 1**a and a solution optical density spectrum and photoluminescence contour map of the (6,5) SWCNTs used in this work are shown in **Figure 2**a,b, respectively. Additional information regarding the peak fitting procedure used to determine (n,m) purity can be found in Figure S1 in the Supporting Information. Following the method of Ghosh et al.,[25] the purity of (6,5) was determined to be 93% with minor (6,4), (7,5), and (7,6)

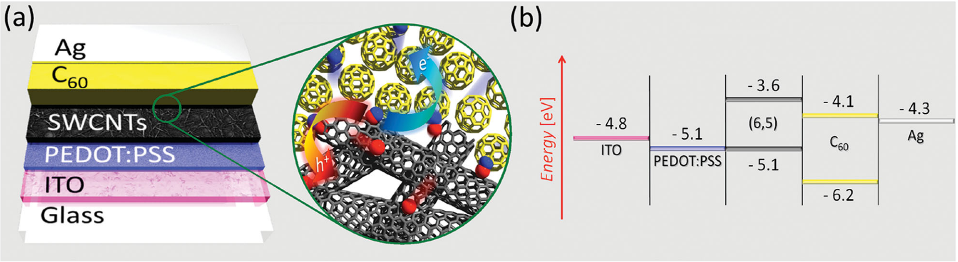

Figure 1. a) Schematic of the solar cell architecture with a close-up of the envisaged exciton dissociation at the SWCNT:C_{60} interface. Electrons (blue) migrate through C_{60} to the silver electrode while holes (red) are collected at the ITO in accordance with b) the energy-level diagram of the device stack.

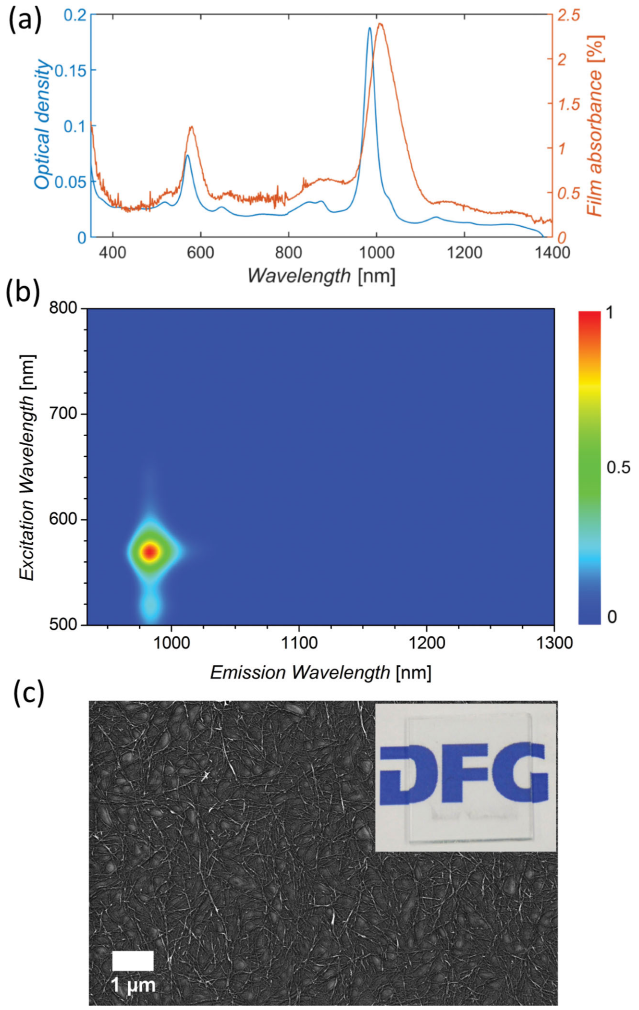

Figure 2. a) Optical density of the suspension measured with a 2 mm path length and film absorbance of (6,5) SWCNTs on glass, scaled by a factor of 3.1 to the mean absorbance determined from reflectance measurements in Figure S11 (Supporting Information), b) a normalized photoluminescence contour map of the SWCNTs in aqueous suspension, c) SEM image of the porous (6,5) nanotube film produced by evaporation-driven self-assembly. Inset shows a comparable film on glass to demonstrate the optical transparency.

impurities also present. The films made from this material are highly transparent, as seen in Figure 2a and the inset of Figure 2c. The nanotube films used in this work absorb ≈1.1% in the region of their S_{22} transition and ≈2.5% at S_{11}. As has been well documented in the literature, the absorption features of the nanotube films are red-shifted and broadened compared to those from the solution measurements, due to differences in the surrounding environment and to bundling of nanotubes.[26] This equates to a 10 nm shift for S_{22} (from 570 to 580 nm) and 24 nm for S_{11} (from 984 to 1008 nm). The morphology of a typical 2 cm^2 (6,5) film obtained by EDSA was also investigated and a representative scanning electron microscopy (SEM) image is shown in Figure 2c. The films are porous and disordered, consisting of bundles of nanotubes. As outlined in Figure S2, Supporting Information, the bundle height (SWCNT film thickness) is determined from atomic force microscopy (AFM) measurements to be a log normal distribution with an average of 2.1 ± 0.7 nm, and with a surface coverage of 60 ± 8%. Nevertheless, as will be shown later, these sub-monolayer thin films significantly outperform similar devices made from much thicker films (100 nm).[3]

The highest occupied molecular orbital (HOMO) energy of the nanotube films was determined by photo-electron yield spectroscopy in air (PESA) to be 5.10 ± 0.02 eV (Figure S3, Supporting Information), which was used to draw the energy band diagram shown in Figure 1b. The lowest unoccupied molecular orbital (LUMO) was calculated based on the work by Bindl et al. by adding the optical bandgap and exciton binding energy, determined by the works of Dukovic et al. and Perebeinos et al., to the HOMO.[27,28] In the work of Dukovic et al., a dielectric constant of 3 was used however in our work the dielectric environment is mostly determined by C_{60} with a dielectric constant of 4.4 and we have consequently scaled the exciton binding energy in accordance with Perebeinos et al.[29] The work functions and the energies of the HOMO and LUMO of all other materials were taken from literature or, in the case of C_{60}, from the works of Bindl et al.[27,30] The LUMOs of the nanotubes (−3.6 eV) and C_{60} (−4.05 eV) exhibit an energetic offset of 0.45 eV, which is more than the expected 0.25 eV exciton binding energy, that was previously reported by Wu et al.[19] After dissociation, the holes are collected through the nanotubes, PEDOT:PSS and indium tin oxide (ITO) electrode while electrons are collected by C_{60}/Ag.

Assuming that the thickness of the (6,5) SWCNT film, along with the glass, ITO and silver electrodes remain constant, varying the thickness of PEDOT:PSS (0 to 100 nm) and C_{60} (1 to 200 nm) in steps of 1 nm leads to more than 20 000 different possible combinations of layers in the solar cell design depicted in Figure 1a. Although it is not expected that 1 nm changes in thickness result in major differences in solar cell performance, such large data sets can easily be calculated with the aid of TMCs and are a helpful tool to optimize the layer thicknesses within the device such that absorption by the SWCNTs is maximized.

In the numerical modeling used in TMCs, it is important to precisely know the optical parameters of all layers. The complex refractive indices (n and k) of all materials in our devices except for the (6,5) SWCNTs are readily available in the literature (see Experimental Section and Supporting Information). The literature values of n and k are compared to the measured absorption profiles for C_{60} and PEDOT:PSS in Figure S4a,b (Supporting Information). Fagan et al. and Battie et al. have provided values of the complex refractive index of (6,5) films, which are plotted in Figure S4c, although they used different methods to obtain the film.[31] In Fagan's approach, DNA-wrapped (6,5) nanotubes were investigated based on their horizontal alignment in films whereas in Battie's approach, DGU was used to sort highly enriched (6,5) solutions. Unfortunately, not only do the two approaches yield different values, but neither of the absorption profiles calculated (Equation S2 to Equation S4, Supporting Information) using these different complex refractive indices, shown in Figure S4d, are in good agreement with that measured from the (6,5) nanotube films used in this study. Because of this lack of reliable values of the complex refractive index, and in light of the very high (>97%) transmittance of the films

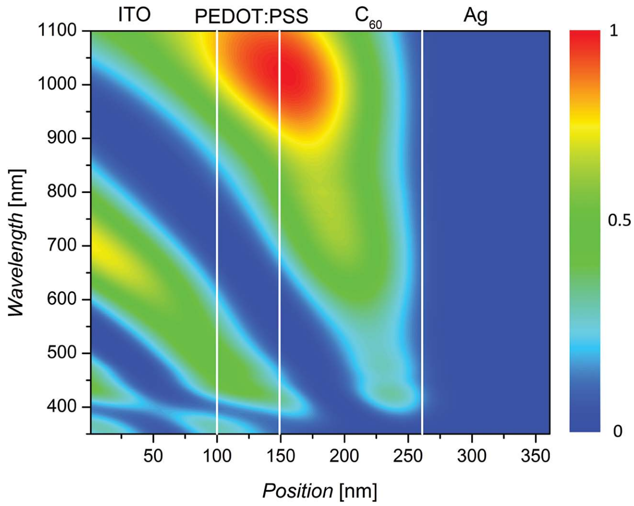

Figure 3. Normalized spatial distribution of the normalized squared electric field intensity, $|E|^2$, as a function of wavelength and position within the solar cell stack. Light is incident from the left, i.e., through the opaque ITO electrode. A layer stack consisting of 49 nm of PEDOT:PSS and 112 nm of C_{60} is shown and was calculated to maximize exciton generation rate through the S_{11} transition of the SWCNTs.

used herein, the influence of the SWCNT film on the position of the electric field intensity has been neglected. A similar approach of neglecting the nanotubes has previously shown qualitative agreement between $|E|^2$ and EQE for thin (<5 nm) PFO-wrapped (7,5) nanotube films, even with a light absorption at the nanotube's S_{11} transition of more than 50%.[2] In this way, the solar cells in the present study were optimized by maximizing $|E|^2$ where the (6,5) film is located at the interface of PEDOT:PSS and C_{60}. Rather than using TMCs to predict current densities or estimate EQE, they were employed in this study to estimate the exciton generation rate for all layer combinations and wavelength ranges. The exciton generation rate was calculated based on a (6,5) SWCNT film absorbance measurement, which was used instead of the product of absorption coefficient α and the real part of the complex refractive index n in Equation S3 (Supporting Information) and then employed in Equations S5,S7 (Supporting Information). A detailed approach and the formulas used are described in the Supporting Information. From these calculations, the optimum thickness combination for a maximized exciton generation rate from the SWCNTs through S_{11} was found to be at 49 nm of PEDOT:PSS and 112 nm of C_{60}. The corresponding normalized (to the incoming electric field $|E_0^+|$) $|E|^2$ can be visualized in a 2D plot as shown in **Figure 3**, where blue areas indicate low light intensity, and red areas represent high light intensity that holds the potential to be absorbed by the material.

The validity of the theoretical model was then tested experimentally in a parametric study varying the PEDOT:PSS and C_{60} layer thicknesses. For PEDOT:PSS, thicknesses of 11, 30, 41, 61, and 86 nm with an error of ±5 nm were used with a constant C_{60} thickness of 110 ± 5 nm and all combinations were made in triplicate (i.e., three substrates, each holding four separate solar-cell-active areas). The mean short-circuit current densities (J_{SC}, mA cm^{-2}), open-circuit voltages (V_{OC}, V), power conversion efficiencies (η, %) and fill factors (FF) of the corresponding devices are summarized in **Figure 4**a and depicted in

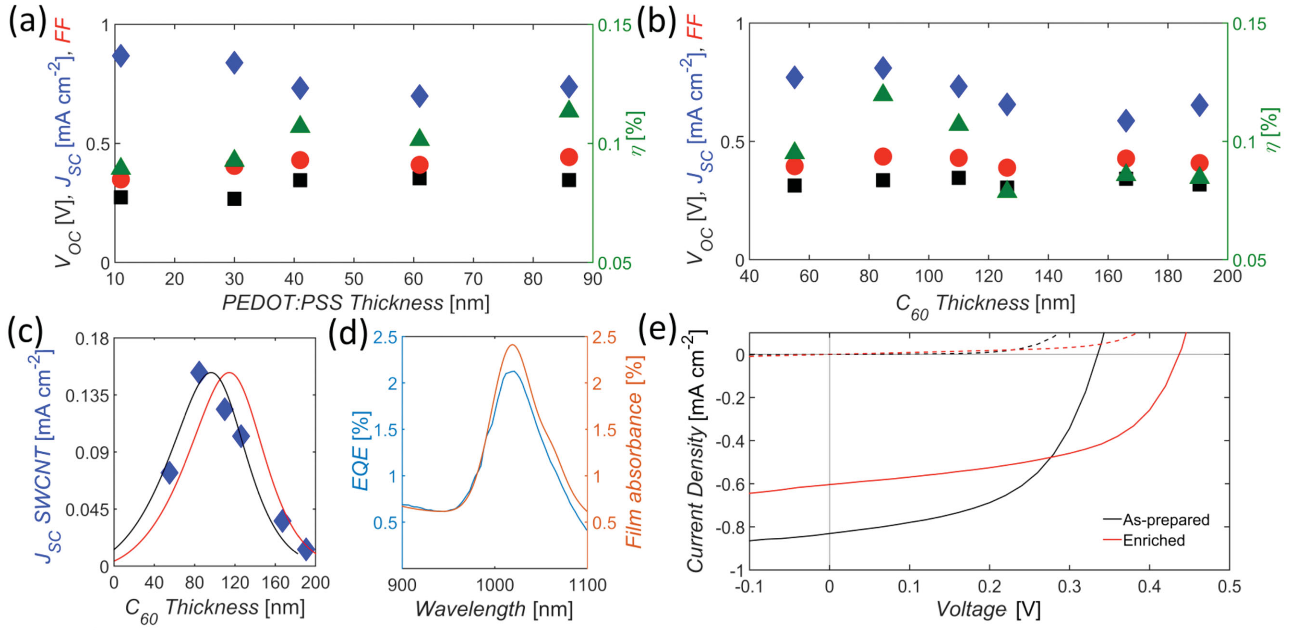

Figure 4. V_{oc}, J_{sc}, FF, and η values from parametric investigations of: a) PEDOT:PSS and b) C_{60} layer thicknesses. c) Correlation between the short circuit current density calculated to be due to the nanotube's S_{11} transition from 800 to 1100 nm (blue diamonds, Equation (1) and the theoretically predicted exciton generation rate-based on Equation S7 (Supporting Information) (red curve) normalized to the maximum current from the nanotubes for the same wavelength range. The black curve is the best fit of the exciton generation rate to the calculated current from the SWCNTs. d) Comparison between solar cell EQE and mean (6,5) nanotube film absorbance in the region of the nanotube's S_{11} transition. e) Light (solid line) and dark (dotted line) J–V measurements from solar cells made with as-prepared and (6,5) enriched SWCNTs.

more detail in Figures S5,S6 (Supporting Information). All cells without PEDOT:PSS failed (see Figure S7, Supporting Information), as well as some of the 11 nm ones. We attribute this to the porous nature of the SWCNT film that allows for direct contact of C_{60} with ITO in the absence of PEDOT:PSS or through pin holes in the case of thin films. Once the layer is sufficiently thick, the influence of PEDOT:PSS on the device current density is minor. Therefore, no immediate trend is clearly visible across all thicknesses. The FF and V_{OC} are approximately the same for all thicknesses and η is found to be largest for 41 and 86 nm. Having comparable J_{SC}, V_{OC}, and FF for these two thicknesses, 41 nm was chosen for the following C_{60} thickness study due to it being closer to the optimum of 49 nm predicted from the TMC model.

Solar cells with six different C_{60} layer thicknesses were tested: 55 ± 2, 85 ± 4, 110 ± 5, 126 ± 2, 167 ± 2, and 191 ± 2 nm and the results are plotted in Figure 4b. Once again, many devices from thin films failed (only two out of 12 possible devices worked for 55 nm of C_{60}), which in this case we attribute to electrical shorts between isolated rough regions of the nanotube film and the silver top electrode (one such isolated region has been highlighted in Figure S2d, Supporting Information). These regions in the SWCNT film likely consist of agglomerated bundles, impurities in the surfactant or catalytic particles from the nanotube growth process. For this reason, an additional physical buffer layer between C_{60} and silver can be beneficial.[2,6] Solar cells with 85 nm of C_{60} performed best with the highest J_{SC}, FF, and η. Any further increase of the C_{60} layer thickness resulted in a slight decrease of all parameters, as depicted in Figure 4b. However, the difference across devices with different C_{60} layer thicknesses is only small, likely due to C_{60} being significantly thicker compared to the SWCNTs, which means that its contribution is much larger, as visible in the EQE measurements from 300 to 800 nm shown in Figure S8 (Supporting Information). The relative contributions of C_{60} and SWCNTs to the photocurrent generation are also indicated in Figure S8 (Supporting Information) and calculated to be 82.9% for C_{60} and 17.1% for the S_{11} regime of (6,5) nanotubes (for 85 nm of C_{60}). For all different thicknesses of C_{60}, the interface with the nanotubes remains basically the same and with exciton diffusion lengths in C_{60} ranging from 6 to 35 nm, any increase in thickness beyond this value does not necessarily generate more current.[32] Hence, the lack of any significant variation in Figure 4b for increasing C_{60} layer thickness.

A much closer correlation between experiment and theoretical TMC calculations becomes obvious when comparing the photocurrent contribution from the (6,5) SWCNTs to the predicted exciton generation rate, as shown in Figure 4c for 41 nm of PEDOT:PSS. The current contribution from the nanotube film in the S_{11} region (800–1100 nm) was calculated from EQE using Equation (1):

$$J_{sc} = \frac{e}{hc}\int \lambda \cdot \mathrm{EQE}(\lambda) \cdot \phi(\lambda)\, d\lambda \qquad (1)$$

where e is the elementary charge, h is the Planck's constant, c is the speed of light, λ is the wavelength, and ϕ is the photon flux. In this calculation, only the S_{11} transition was considered due to an overlap of C_{60} with S_{22}, as seen in Figure S8 (Supporting Information). The optimum exciton generation rate for 41 nm of PEDOT:PSS was calculated to be at 114 nm of C_{60}. However, upon experimentally comparing the calculated exciton generation rate to the integrated photocurrent, a maximum of 96 nm of C_{60} was found. Qualitatively, this is in good agreement when considering that no nanotubes were assumed in the TMC model. Taking the nanotube contribution into account in future models will likely provide a closer agreement with experimental data.

Calculating the $|E|^2$ distribution throughout the solar cell and correlating this with the efficiency through the S_{11} transition of (6,5), we looked into tailoring the $|E|^2$ distribution such as to maximize photocurrent from S_{11}, S_{22}, or a combination of both. This approach is attractive in terms of light management in solar cells or toward transparent solar cells in which the nanotubes absorb only in the infrared. As shown in **Figure 5**a, comparing the calculated $|E|^2$ at the position of the nanotubes (interface of PEDOT:PSS and C_{60}) for different C_{60} thicknesses and a constant 41 nm thickness of PEDOT:PSS reveals the opportunity to maximize electric field intensity almost equally at both nanotube transitions (62 nm C_{60}), or primarily at S_{22} (200 nm of C_{60}), or almost exclusively at S_{11} (118 nm of C_{60}). In Figure 5b–d, these theoretical predictions are correlated with experimental EQE measurements, where the typical absorbance spectrum of a (6,5) film is also shown for reference. The EQE peak corresponding to the nanotube's S_{11} follows the electric field intensity well however, for S_{22}, the correlation is less clear due to the overlap of a peak centered at 620 nm, which has its origins in C_{60} being interfaced with other materials.[33] Nevertheless, a shoulder at 590 nm can still be clearly seen in the EQE spectrum and this we attribute to photocurrent generated through S_{22}. For 126 nm of C_{60}, a minimum in $|E|^2$ is predicted and neither the S_{22} feature at 590 nm nor the 620 nm peak associated with C_{60} is observed experimentally while, for 191 nm of C_{60}, the S_{22} region is obviously enhanced in line with the predictions. A comparison of $|E|^2$ throughout the solar cell stacks for calculated optima and experimentally prepared solar cells is shown in Figure S9 (Supporting Information). The exciton generation rate is shown as a function of C_{60} thickness and wavelength in Figure S10 (Supporting Information). The ability to predict and move the electric field intensity in SWCNT:C_{60} solar cells in this way is especially interesting in regard to designing future tandem solar cells or the use of large diameter nanotubes that absorb even further in the infrared than the (6,5) nanotubes used herein.

To gain an understanding of the scale and origin of internal losses, the IQE was also calculated for the optimal combination of PEDOT:PSS and C_{60}, as shown in Figure 4d. To eliminate the potential for artefacts and discrepancies due to inhomogeneity of the films, the absorbance of the active area was measured in situ at seven different locations. Further details, along with the raw and fitted data, are provided in Figure S11 of the Supporting Information. Based on an EQE at S_{11} of 2.1% and an average absorbance of ≈2.5% at the same wavelength, an overall IQE of 86 ± 12% at the S_{11} transition was calculated, which outperforms earlier work with an EQE at the S_{11} transition of 0.5% and corresponding absorbance of the film of 35%.[3] This is quite remarkable considering the large difference in nanotube film thickness of ≈2 nm (this work) and 100 nm (the earlier work). Exploiting the photocurrent

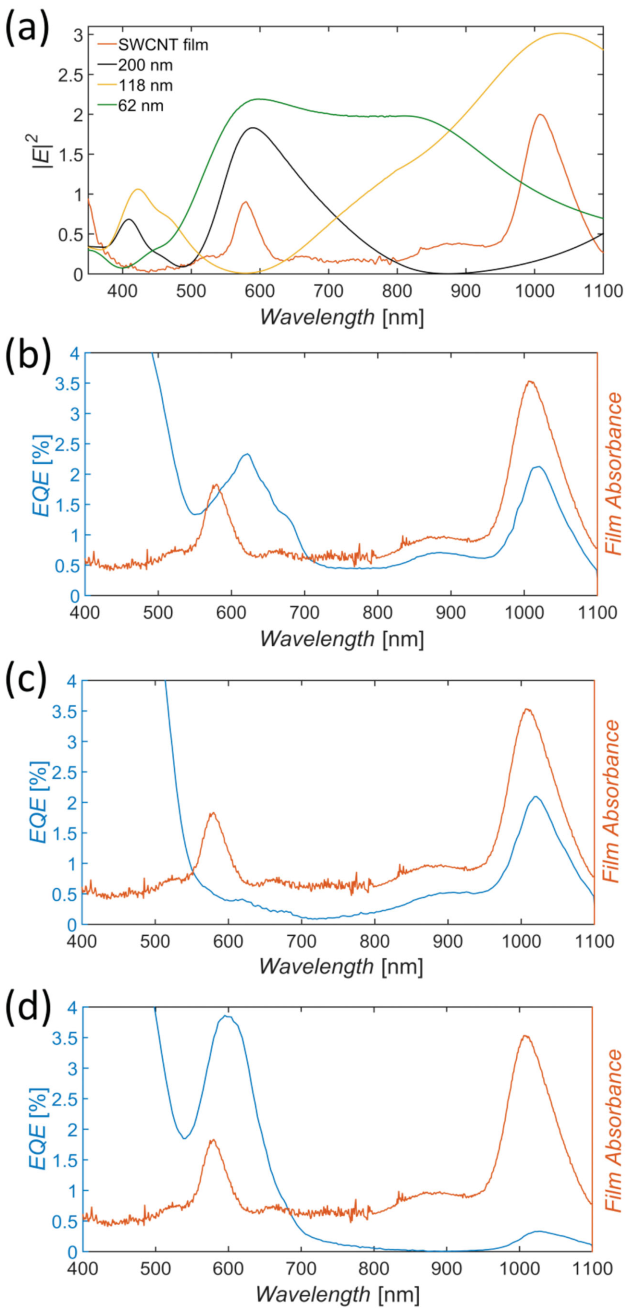

Figure 5. a) Variation in the electric field intensity, $|E|^2$, for different C_{60} layer thicknesses at a constant PEDOT:PSS thickness of 41 nm, b–d) show EQE spectra of solar cells with C_{60} thicknesses of 85, 126, and 191 nm, respectively. All plots show the normalized absorbance of a (6,5) nanotube film to guide the eye as to the positions of the S_{11} and S_{22} transitions of the nanotubes.

generation efficiency from the nanotubes to a degree of 86% is comparable to the best IQE values for polymer-wrapped nanotube solar cells that also used very thin nanotube films (≈7 nm) albeit with much higher absorption due to the use of denser films.[10,27] In the current polymer-free work, the limiting factor in terms of photocurrent generation and therefore power conversion efficiency is the high transmittance of the film. On the other hand, the porous nature of the films, which causes the high transmittance, has the advantage of preventing exciton quenching by metallic nanotubes, as would occur in denser and thicker films.[5] Having isolated bundles of SWCNTs also reduces the charge trapping influence of large diameter, smaller bandgap nanotubes.[3] It is for this reason that despite having equivalent IQE in our work the EQE remains low compared to the work of Guillot et al. and Bindl and Arnold who achieved values above 20% with much denser, polymer-wrapped films.[2,6,10]

With the goal of investigating possible improvements to device performance by increasing the semiconducting purity of the (6,5) suspension, we performed DGU, which is known to enrich the semiconducting purity and remove catalyst particles and bundles.[16] Absorption spectra of the enriched material obtained from DGU is shown in Figure S12 (Supporting Information) where a clear difference in the background, which is associated with metallic nanotubes, catalytic particles, and carbon residues, can be seen. In order to reduce the content of the DGU medium (iodixanol), the collected fraction was dialyzed, which resulted in a reduction in the nanotube concentration as measured by optical density (OD). Consequently, thin films formed from DGU enriched (6,5), henceforth referred to as "enriched (6,5)," were typically sparser than from the as-prepared material. The *J*–*V* curves of solar cells comprising as-prepared and enriched (6,5) nanotube films are shown in Figure 4e. The photocurrent is less from the enriched (6,5) films due to their lower density and there is only a slight increase in FF from 53% to 54% however, a significant improvement in V_{OC} was observed from 0.36 to 0.44 V. Important parameters are compared in **Table 1**. The shunt resistance (R_{sh}) was extracted from the slope of the *J*–*V* curve at V_{OC} and is 14% larger for solar cells comprising enriched (6,5) material than for as-prepared nanotubes, indicating a substantial decrease in alternative current paths, e.g., by the reduction of metallic tubes or trap states compared to the as-prepared solution. The series resistance (R_s) was extracted for as-prepared and enriched (6,5) from the illuminated *J*–*V* curve between 0.52 and 0.66 V and 0.54 to 0.66 V, respectively (see Figure S13, Supporting Information). The series resistance for the enriched (6,5) material is smaller but results only in a small increase in fill factor. The ideality factor was extracted from the slope of the dark current measurement ($dV\,d\ln(J)^{-1}$) in the linear region of 0.28 to 0.38 V and 0.4 to 0.5 V, for the as-prepared and enriched

Table 1. Key performance parameters for solar cells made from as-prepared and enriched (6,5) SWCNT films. Resistances were calculated from the *J*–*V* curves recorded under illumination.

	V_{OC} [V]	J_{SC} [mA cm^{-2}]	FF [%]	η [%]	J_0 [mA cm^{-2}]	R_{SH} [Ω cm^2]	R_S [Ω cm^2]	Ideality
As-prepared	0.34	0.83	52	0.15	7.6×10^{-4}	2112	28	1.6
Enriched	0.44	0.60	54	0.14	3.5×10^{-4}	2946	22	1.8

(6,5) material, respectively.[34] Reverse saturation current densities (J_0) are on the same order for both materials. Having an ideality factor between 1 and 2 indicates recombination losses due to Shockley-Read-Hall (SRH) recombination, also called "trap charges," at or near the interface of the SWCNTs and C_{60}.[34] Trap charges, or monomolecular recombination, occur if the electron hole pair is not dissociated fast enough upon being created.[35] Crucial for fast dissociation is a sufficient LUMO level offset between donor and acceptor material. Organic solar cells with energy offsets between 0.2 and 0.3 eV often suffer from suppressed quantum efficiencies and fill factors.[35] Similar effects can also be attributed to bimolecular recombination, which occurs when successfully dissociated electrons and holes collide at the diffusive interface of the two semiconductors. A clear differentiation between mono- and bimolecular recombination can be obtained by light intensity (I)-dependent V_{OC} measurements.[36] Based on the works of Cowan et al.,[37] the slope of the fitted V_{OC} to $ln(I)$ curve for BHJ solar cells should be equal to $k_BT\ e^{-1}$ (25.5 mV at room temperature, bimolecular recombination), whereas $2k_BT\ e^{-1}$ is expected for silicon solar cells (51 mV at room temperature, SRH/monomolecular recombination). Having slopes of $2.3k_BT\ e^{-1}$ (58 mV) for enriched material and $4.3k_BT\ e^{-1}$ (109 mV) for as-prepared (6,5) nanotubes (Figure S14a,b, Supporting Information, respectively) puts them in the regime of monomolecular recombination due to interface traps.[38] The increased slope for solar cells from as-prepared material is correlated with a reduction in V_{OC}.[38] Combining the increase in R_{SH} and the significantly smaller slope in the light-intensity-dependent V_{OC} measurements indicates a marked reduction in trap-assisted recombination in solar cells made from the enriched (6,5) material, likely due to a reduction of the content of metallic SWCNTs. The influence of metallic tubes on the J–V characteristics was additionally verified by comparing a solar cell with SWCNTs to a "C_{60}-only" solar cell without nanotubes in Figure S15 (Supporting Information). The absence of as-prepared SWCNTs in the solar cell stack resulted in a V_{OC} of 0.44 V, which is comparable to the V_{OC} obtained for enriched (6,5) solar cells. The negative impact of metallic SWCNTs on the quantum efficiency and exciton diffusion length was also verified in recent works by Gong et al.,[5] who similarly showed a dramatic increase in device efficiency upon increasing the semiconducting purity of their SWCNT films from 95% to 98%.

3. Conclusion

To conclude, SWCNT:C_{60} solar cells have been prepared using large area, highly transparent films of polymer-free (6,5)-enriched SWCNTs formed from aqueous solution with the aid of a novel evaporation-driven self-assembly. By theoretical modeling of the electric field intensity within the layer stack using extensive TMCs, light in the solar cells was effectively managed so as to maximize photocurrent output from the different optical transitions of the nanotubes. These results confirm the validity of this powerful modeling tool for predicting and tailoring light absorption in carbon nanotube solar cells, even when the contribution of the nanotube film is neglected in the model. With optimal layer thicknesses, SWCNT:C_{60} solar cells were constructed that showed V_{OC} of 0.44 V and IQE of 86%, which are the highest values so far reported for polymer-free variants of this design. This is despite the fact that, in contrast with earlier work, the nanotube films used were exceptionally thin, being sub-monolayer in terms of nanotube bundles, which provides a strong indication that very large improvements in overall power conversion efficiency could be obtained with appropriate multilayer and/or multijunction cell designs.

4. Experimental Section

ITO glass substrates (PGO, 20 ± 6 $\Omega\ \square^{-1}$, 1.0 ± 0.1 mm) were covered with a structured foil, etched with HCl (fuming 37%; Merck), rinsed with water and dried to form the bottom contact and afford an active area of 0.105 cm^2 together with a silver top contact. PEDOT:PSS (Al 4083, 500 to 5000 Ω cm; Ossila) was filtered (Millex-HV, 0.45 µm; Merck), mixed with ethanol (VWR) in ratios of 1:1 or 1:3 for thicknesses starting at 30 nm and below, respectively, and then sonicated (10 min). This was then spin coated (1000–5000 rpm for 60 s, to yield a series of different layer thicknesses) and baked in an inert atmosphere (250 °C, 10 min) before being covered with poly(methyl methacrylate) (40 nm, PMMA 950K 0.25 µm/4000 rpm; Allresist). The desired thickness of PMMA was achieved by mixing with anisole (Merck) in a 1:4 ratio and subsequent spin coating (5000 rpm, 60 s) followed by a baking step (160 °C, 10 min). The PMMA layer served to protect PEDOT:PSS from degradation during deposition of the SWCNT film and was removed prior to the evaporation of C_{60} and silver. (6,5) SWCNTs were prepared from HiPco raw material (NanoIntegris) as outlined previously using a GPC system.[14] Due to the high affinity of (6,5) to the Sephacryl-S200 gel (Amersham Biosciences) and their ability to displace other (n,m) species at 1.6 wt% SDS (Merck), 1 wt% sodium cholate (SC ≥ 99%; Sigma–Aldrich) was used as an eluent in a one-column approach without the use of a pH gradient. The simplicity of this approach allowed us to prepare large quantities of (6,5) and avoid device variations due to differences between suspensions. Films of (6,5) SWCNTs were first prepared on a "dummy" substrate before being transferred onto the solar cell. SiO_2 substrates were oxygen plasma treated (3 min, 200 W, 100 mTorr, 20 sccm) to increase the hydrophilicity of the surface prior to being covered with PMMA (200 nm). The hydrophilic surface activation of SiO_2 allowed for water to later penetrate between the SiO_2 and PMMA and thus assist transfer of the SWCNT film.[39] SWCNT films were prepared by evaporation driven self-assembly in an oven (60 °C, 6 h) by immersing the PMMA-coated SiO_2 substrate vertically in a 1 wt% SC suspension adjusted to an OD of 0.025 at S_{11}. Films were 2 cm^2 in size after evaporation. The SWCNT film was then scored into a rectangle ≈1.3 cm^2 in size and slowly immersed into water to detach the SWCNT-coated PMMA from the SiO_2. Prior to the final detachment of the film, the substrate was withdrawn from the water and re-immersed in glycerol (99.5%; VWR). The advantage of using glycerol is twofold: the PMMA/SWCNT film is less mobile on the glycerol surface, resulting in greater control over film alignment onto the active areas of the solar cell, and glycerol does not dissolve PEDOT:PSS. Following film transfer, the solar cell substrates were heated (120 °C, 15 min) in air to promote contact between nanotubes and the substrate. Remaining glycerol residues were then dissolved in ethanol. Finally, the PMMA was dissolved overnight in chloroform (≥99.8%; Sigma–Aldrich). Various thicknesses of C_{60} (99.9+%; Sigma–Aldrich) from 55 to 190 nm were then evaporated through a shadow mask with a Lesker SPECTROS (temperature range from 380 °C to 450 °C and pressure of $7–9 \times 10^{-7}$ Pa) with the layer thickness monitored by quartz crystals. In the final step, a 100 nm silver top electrode was evaporated.

Solution absorption measurements were carried out on a Varian Cary 500 spectrophotometer, whereas films were measured on a Bruker microscope (Vertex 80/Hyperion 2000 FTIR)). Film thicknesses were measured with a DektakXT profiler (Bruker) and an ICON AFM

(Bruker) using silicon cantilevers from Mikromasch (Mikromasch, USA, 325 kHz, 40 N m^{-1}). Nanotube films were additionally characterized using SEM (Zeiss Ultra Plus). The HOMO of (6,5) films, shown in Figure 1b, was measured on an ITO substrate by PESA (AC-2E, Riken Keiki) as shown in Figure S3 of the Supporting Information.[40] The solar cells were characterized with a Keithley 238 source meter under AM1.5G illumination from a Newport 300 W solar simulator. Following *J–V* characterization, EQE was measured with a 450 W Xenon light source, an optical chopper (84.7 Hz), a 300 mm monochromator (LOT-Oriel), a custom-designed current amplifier (DLPCA-S, Femto Messtechnik), and a digital lock-in amplifier (eLockin 203 Anfatec). Initial calibration was carried out with a calibrated UV-enhanced silicon diode (SM1PD2A, Thorlabs).

TMCs were performed using the MATLAB code available from the McGehee group at Stanford and as outlined by Burkhard et al. and Pettersson et al.[11,41] The complex refractive indices of glass, ITO, PEDOT:PSS, and C_{60} were included in the code and the electric field intensity and exciton generation rate were calculated for all layer combinations presented in this study.[11,41,42] Further information can also be found in the Supporting Information.

Supporting Information

Supporting Information is available from the Wiley Online Library or from the author.

Acknowledgements

B.S.F. gratefully acknowledges support from the Deutsche Forschungsgemeinschafts (DFG) Emmy Noether Program under grant number FL 834/1-1. R.K. acknowledges funding by the German Science Foundation INST 163/354-1 FUGG. K.G., C.K., and A.C. acknowledge funding by the German Federal Ministry for Education and Research (BMBF) under contract 03EK3504 (project TAURUS) and support by the DFG Center for Functional Nanostructures (CFN). M.P. acknowledges Tanja Puerckhauer for PESA measurements.

Received: July 6, 2015
Revised: September 25, 2015

---

[1] D. J. Bindl, N. S. Safron, M. S. Arnold, *ACS Nano* **2010**, *4*, 5657.
[2] M. J. Shea, M. S. Arnold, *Appl. Phys. Lett.* **2013**, *102*, 243101.
[3] R. M. Jain, R. Howden, K. Tvrdy, S. Shimizu, A. J. Hilmer, T. P. McNicholas, K. K. Gleason, M. S. Strano, *Adv. Mater.* **2012**, *24*, 4436.
[4] H. Wang, G. I. Koleilat, P. Liu, G. Jiménez-Osés, Y.-C. Lai, M. Vosgueritchian, Y. Fang, S. Park, K. N. Houk, Z. Bao, *ACS Nano* **2014**, *8*, 2609.
[5] M. Gong, T. A. Shastry, Y. Xie, M. Bernardi, D. Jasion, K. A. Luck, T. J. Marks, J. C. Grossman, S. Ren, M. C. Hersam, *Nano Lett.* **2014**, *14*, 5308.
[6] S. L. Guillot, K. S. Mistry, A. D. Avery, J. Richard, A.-M. Dowgiallo, P. F. Ndione, J. van de Lagemaat, M. O. Reese, J. L. Blackburn, *Nanoscale* **2015**, *7*, 6556.
[7] a) D. D. Tune, J. G. Shapter, *Energy Environ. Sci.* **2013**, *6*, 2572; b) D. O. Bellisario, R. M. Jain, Z. Ulissi, M. S. Strano, *Energy Environ. Sci.* **2014**, *7*, 3769; c) D. D. Tune, F. Hennrich, S. Dehm, M. F. G. Klein, K. Glaser, A. Colsmann, J. G. Shapter, U. Lemmer, M. M. Kappes, R. Krupke, B. S. Flavel, *Adv. Energy Mater.* **2013**, *3*, 1091; d) M. Engel, K. E. Moore, A. Alam, S. Dehm, R. Krupke, B. S. Flavel, *ACS Nano* **2014**, *8*, 9324.
[8] a) L. Yang, P. Kim, H. M. Meyer, S. Agnihotri, *J. Colloid Interface Sci.* **2009**, *338*, 128; b) G. Chen, T. M. Paronyan, E. M. Pigos, A. R. Harutyunyan, *Sci. Rep.* **2012**, *2*, 343; c) T. Dürkop, S. A. Getty, E. Cobas, M. S. Fuhrer, *Nano Lett.* **2003**, *4*, 35.
[9] a) H. Kataura, Y. Kumazawa, Y. Maniwa, I. Umezu, S. Suzuki, Y. Ohtsuka, Y. Achiba, *Synth. Met.* **1999**, *103*, 2555; b) R. B. Weisman, S. M. Bachilo, *Nano Lett.* **2003**, *3*, 1235; c) E. H. Haroz, S. M. Bachilo, R. B. Weisman, S. K. Doorn, *Phys. Rev. B* **2008**, *77*, 125405.
[10] D. J. Bindl, M. S. Arnold, *J. Phys. Chem. C* **2013**, *117*, 2390.
[11] L. A. A. Pettersson, L. S. Roman, O. Inganäs, *J. Appl. Phys.* **1999**, *86*, 487.
[12] A. Nish, J.-Y. Hwang, J. Doig, R. J. Nicholas, *Nat. Nano* **2007**, *2*, 640.
[13] F. Chen, B. Wang, Y. Chen, L.-J. Li, *Nano Lett.* **2007**, *7*, 3013.
[14] a) B. S. Flavel, M. M. Kappes, R. Krupke, F. Hennrich, *ACS Nano* **2013**, *7*, 3557; b) B. S. Flavel, K. E. Moore, M. Pfohl, M. M. Kappes, F. Hennrich, *ACS Nano* **2014**, *8*, 1817.
[15] a) K. Moshammer, F. Hennrich, M. Kappes, *Nano Res.* **2009**, *2*, 599; b) H. Liu, D. Nishide, T. Tanaka, H. Kataura, *Nat. Commun.* **2011**, *2*, 309.
[16] M. S. Arnold, A. A. Green, J. F. Hulvat, S. I. Stupp, M. C. Hersam, *Nat. Nano* **2006**, *1*, 60.
[17] C. Y. Khripin, J. A. Fagan, M. Zheng, *J. Am. Chem. Soc.* **2013**, *135*, 6822.
[18] K. S. Mistry, B. A. Larsen, J. L. Blackburn, *ACS Nano* **2013**, *7*, 2231.
[19] M.-Y. Wu, R. M. Jacobberger, M. S. Arnold, *J. Appl. Phys.* **2013**, *113*, 204504.
[20] D. J. Bindl, M. J. Shea, M. S. Arnold, *Chem. Phys.* **2013**, *413*, 29.
[21] R. C. Tenent, T. M. Barnes, J. D. Bergeson, A. J. Ferguson, B. To, L. M. Gedvilas, M. J. Heben, J. L. Blackburn, *Adv. Mater.* **2009**, *21*, 3210.
[22] G. S. Tulevski, A. D. Franklin, A. Afzali, *ACS Nano* **2013**, *7*, 2971.
[23] H. Li, T. C. Hain, A. Muzha, F. Schöppler, T. Hertel, *ACS Nano* **2014**, *8*, 6417.
[24] M. Engel, J. P. Small, M. Steiner, M. Freitag, A. A. Green, M. C. Hersam, P. Avouris, *ACS Nano* **2008**, *2*, 2445.
[25] S. Ghosh, S. M. Bachilo, R. B. Weisman, *Nat. Nano* **2010**, *5*, 443.
[26] a) M. J. O'Connell, S. M. Bachilo, C. B. Huffman, V. C. Moore, M. S. Strano, E. H. Haroz, K. L. Rialon, P. J. Boul, W. H. Noon, C. Kittrell, J. Ma, R. H. Hauge, R. B. Weisman, R. E. Smalley, *Science* **2002**, *297*, 593; b) S. Reich, C. Thomsen, P. Ordejón, *Phys. Rev. B* **2002**, *65*, 155411.
[27] D. J. Bindl, M. Y. Wu, F. C. Prehn, M. S. Arnold, *Nano Lett.* **2011**, *11*, 455.
[28] a) G. Dukovic, F. Wang, D. Song, M. Y. Sfeir, T. F. Heinz, L. E. Brus, *Nano Lett.* **2005**, *5*, 2314; b) V. Perebeinos, J. Tersoff, P. Avouris, *Phys. Rev. Lett.* **2004**, *92*, 257402.
[29] a) R. B. Capaz, C. D. Spataru, S. Ismail-Beigi, S. G. Louie, *Phys. Rev. B* **2006**, *74*, 121401; b) A. F. Hebard, R. C. Haddon, R. M. Fleming, A. R. Kortan, *Appl. Phys. Lett.* **1991**, *59*, 2109.
[30] a) J. Huang, P. F. Miller, J. S. Wilson, A. J. de Mello, J. C. de Mello, D. D. C. Bradley, *Adv. Funct. Mater.* **2005**, *15*, 290; b) S. Sapp, S. Luebben, Y. B. Losovyj, P. Jeppson, D. L. Schulz, A. N. Caruso, *Appl. Phys. Lett.* **2006**, *88*, 152107; c) A. W. Dweydari, C. H. B. Mee, *Phys. Status Solidi A* **1975**, *27*, 223.
[31] a) J. A. Fagan, J. R. Simpson, B. J. Landi, L. J. Richter, I. Mandelbaum, V. Bajpai, D. L. Ho, R. Raffaelle, A. R. H. Walker, B. J. Bauer, E. K. Hobbie, *Phys. Rev. Lett.* **2007**, *98*, 147402; b) Y. Battie, D. Jamon, A. En Naciri, J.-S. Lauret, A. Loiseau, *Appl. Phys. Lett.* **2013**, *102*, 091909.
[32] a) J. J. M. Halls, K. Pichler, R. H. Friend, S. C. Moratti, A. B. Holmes, *Appl. Phys. Lett.* **1996**, *68*, 3120; b) D. Qin, P. Gu, R. S. Dhar, S. G. Razavipour, D. Ban, *Phys. Status Solidi A* **2011**, *208*, 1967.
[33] F. Yan, X. M. Bao, X. W. Wu, H. L. Chen, *Appl. Phys. Lett.* **1995**, *67*, 3471.
[34] J. L. Gray, in *Handbook of Photovoltaic Science and Engineering*, John Wiley & Sons, Ltd., West Sussex, UK **2011**, p. 82.
[35] J. D. Servaites, M. A. Ratner, T. J. Marks, *Energy Environ. Sci.* **2011**, *4*, 4410.
[36] G. A. H. Wetzelaer, M. Kuik, M. Lenes, P. W. M. Blom, *Appl. Phys. Lett.* **2011**, *99*, 153506.

[37] S. R. Cowan, A. Roy, A. J. Heeger, *Phys. Rev. B* **2010**, *82*, 245207.

[38] M. Gong, T. A. Shastry, Q. Cui, R. R. Kohlmeyer, K. A. Luck, A. Rowberg, T. J. Marks, M. F. Durstock, H. Zhao, M. C. Hersam, S. Ren, *ACS Appl. Mater. Interfaces* **2015**, *7*, 7428.

[39] T. Suni, K. Henttinen, I. Suni, J. Mäkinen, *J. Electrochem. Soc.* **2002**, *149*, G348.

[40] M. Uda, *Jpn. J. Appl. Phys.* **1985**, *24*, 284.

[41] G. F. Burkhard, E. T. Hoke, M. D. McGehee, *Adv. Mater.* **2010**, *22*, 3293.

[42] a) S. L. Ren, Y. Wang, A. M. Rao, E. McRae, J. M. Holden, T. Hager, K. Wang, W. T. Lee, H. F. Ni, J. Selegue, P. C. Eklund, *Appl. Phys. Lett.* **1991**, *59*, 2678; b) E. D. Palik, *Handbook of Optical Constants of Solids*, Vol. *3*, Academic Press, Massachusetts, USA **1998**.

– This page intentionally left blank –

4. Probing the Diameter Limit of Single Walled Carbon Nanotubes in SWCNT:Fullerene Solar Cells

The following Chapter was reproduced with the permission of John Wiley and Sons:

Probing the Diameter Limit of Single Walled Carbon Nanotubes in SWCNT:Fullerene Solar Cells
Moritz Pfohl, Konstantin Glaser, Arko Graf, Adrian Mertens, Daniel D. Tune, Tanja Puerckhauer, Asiful Alam, Li Wei, Yuan Chen, Jana Zaumseil, Alexander Colsmann, Ralph Krupke, and Benjamin S. Flavel
Advanced Energy Materials, 2016, 1600890
DOI: 10.1002/aenm.201600890

Abstract

In this Chapter, for the first time, the diameter limit of surfactant wrapped single walled carbon nanotubes (SWCNTs) in SWCNT:C_{60} solar cells is determined through preparation of monochiral small and large diameter nanotube devices as well as those from polychiral mixtures. Through assignment of the different nanotube chiralities by photoluminescence and optical density measurements a diameter limit yielding 0% internal quantum efficiency (IQE) is determined. This Chapter provides insights into the required net driving energy for SWCNT exciton dissociation onto C_{60} and establishes a family of (n,m) species which can efficiently be utilized in polymer-free SWCNT:C_{60} solar cells. Using this approach the largest diameter nanotube with an IQE > 0% is found to be (8,6) with a diameter of 0.95 nm. Possible strategies to extend this diameter limit are then discussed.

Contribution

MP and BSF designed the experiments. YC and WL prepared large diameter single chirality (9,8) nanotubes. MP, AG, AA and JZ performed optical characterizations of the different nanotube dispersions. TP performed photo-electron yield spectroscopy in air (PESA). AM performed ellipsometry measurements. MP, KG, DDT and BSF prepared and tested the solar cell devices. MP, DDT, AC, RK and BSF analysed the results. MP, DDT and BSF drafted the manuscript.

– This page intentionally left blank –

Probing the Diameter Limit of Single Walled Carbon Nanotubes in SWCNT: Fullerene Solar Cells

*Moritz Pfohl, Konstantin Glaser, Arko Graf, Adrian Mertens, Daniel D. Tune, Tanja Puerckhauer, Asiful Alam, Li Wei, Yuan Chen, Jana Zaumseil, Alexander Colsmann, Ralph Krupke, and Benjamin S. Flavel**

In this work, for the first time, the diameter limit of surfactant wrapped single walled carbon nanotubes (SWCNTs) in SWCNT:C_{60} solar cells is determined through preparation of monochiral small and large diameter nanotube devices as well as those from polychiral mixtures. Through assignment of the different nanotube chiralities by photoluminescence and optical density measurements a diameter limit yielding 0% internal quantum efficiency (IQE) is determined. This work provides insights into the required net driving energy for SWCNT exciton dissociation onto C_{60} and establishes a family of (*n*,*m*) species which can efficiently be utilized in polymer-free SWCNT:C_{60} solar cells. Using this approach the largest diameter nanotube with an IQE > 0% is found to be (8,6) with a diameter of 0.95 nm. Possible strategies to extend this diameter limit are then discussed.

1. Introduction

Single walled carbon nanotubes (SWCNTs) are becoming an established, photoactive material for use in organic solar cells. Besides their large intrinsic mobility ($\approx 10^5$ cm^2 V^{-1} s^{-1}),[1] this is primarily due to their structurally dependent optical and electronic properties. In the literature, the analogy of 'rolling up' a sheet of graphene to form a SWCNT is often used, where the "(*n*,*m*)" chiral index determines not only whether the SWCNT is metallic or semiconducting but also its diameter and the magnitude of the optical transitions.[2] It is this ability to select SWCNTs with desired optical gaps,[3] along with the commercial availability of nanotubes with a range of diameters, that make SWCNTs an interesting material that also offers potential avenues to tailor or extend the light absorption within established solar cells.[4] For example, in the case of a SWCNT with ≈1 nm diameter, light is absorbed in the infrared (S_{11} optical transition), visible (S_{22}), and UV (S_{33}) regimes. Through careful combination of the appropriate (*n*,*m*) species a close match to the solar spectrum is possible.[5] Indeed, in the simulation work of Tune and Shapter, an idealized tandem solar cell consisting of four small diameter nanotube species ((6,4), (9,1), (7,3), and (7,5) with diameters of 0.69–0.76 nm) that absorb mostly in the visible and the near infrared (up to 1024 nm) was predicted to have a sunlight harvesting potential of up to 28%.[6] Likewise, by instead choosing large diameter nanotubes (1.01–1.47 nm), which almost exclusively absorb in the near infrared and infrared (793–1682 nm), a sunlight harvesting potential of up to 19% was predicted in a semi-transparent organic solar cell. The respective model considered only the spectroscopic overlap between the nanotubes' absorption spectra and the terrestrial solar spectrum (AM1.5G) and implicitly assumed that all nanotubes can be used in a solar cell. Actually, the realization of a fully transparent solar cell from SWCNTs seems unlikely, especially with common fullerene-based acceptors (either C_{60} or [6,6]-phenyl $C_{61/71}$ butyric acid methyl ester ($PC_{61/71}BM$)) absorbing light between 300 and 800 nm along with other hole and electron blocking layers such as poly(3,4-ethylenedioxythiophene):polystyrene sulfonate (PEDOT:PSS) or bathocuproine and also minor contributions from S_{33}, especially for large diameter nanotubes, as discussed by Tune and Shapter.[6]

More fundamental to this discussion is that theoretical and experimental studies predict the requirement of a minimum energetic offset between the lowest unoccupied molecular

---

M. Pfohl, Dr. D. D. Tune, A. Alam, Prof. R. Krupke,
Dr. B. S. Flavel
Institute of Nanotechnology
Karlsruhe Institute of Technology (KIT)
76021 Karlsruhe, Germany
E-mail: benjamin.flavel@kit.edu

M. Pfohl, A. Alam, Prof. R. Krupke
Institute of Materials Science
Technische Universität Darmstadt
64287 Darmstadt, Germany

K. Glaser, A. Mertens, T. Puerckhauer, Dr. A. Colsmann
Light Technology Institute
Karlsruhe Institute of Technology (KIT)
76131 Karlsruhe, Germany

A. Graf, Prof. J. Zaumseil
Institute for Physical Chemistry
Universität Heidelberg
69120 Heidelberg, Germany

Dr. D. D. Tune
Centre for Nanoscale Science and Technology
Flinders University
Adelaide 5042, Australia

Dr. L. Wei, Prof. Y. Chen
School of Chemical and Biomolecular Engineering
The University of Sydney
NSW 2006, Australia

DOI: 10.1002/aenm.201600890

orbital (LUMO) of the nanotube and that of the acceptor, that is necessary for exciton dissociation at the interface. The diameter dependent bandgap of SWCNTs therefore restricts the combination of (*n*,*m*) species or diameters that can be used for any specific acceptor molecule with fixed LUMO. In practice, the position of the LUMO in the SWCNT is calculated by adding the optical bandgap and exciton binding energy, which can be determined by the experimental findings of Dukovic et al.,[7] the analytic formula given by Capaz et al. and the scaling law proposed by Perebeinos et al.,[8,9] to the highest occupied molecular orbital (HOMO) of the nanotube.[10,11] In this way, the LUMO is approximated to the free carrier level. However, both the optical gap and the exciton binding energy are highly dependent on the surrounding dielectric environment. Therefore, in evaluating the actual diameter limit, it is important to distinguish between the two different SWCNT device architectures known from the literature, either a planar heterojunction or a bulk heterojunction (BHJ), but also between the two methods of preparation of the nanotubes. For BHJ solar cells, the SWCNTs are usually mixed with an acceptor with nanotube content below 10 wt% to reduce the probability of nanotube bundling and eventual trap states in the device. In this case, the surrounding dielectric environment can be assumed to be predominately defined by the acceptor molecule. Whereas, for planar solar cell designs, thin films of nanotubes are formed that can be either sparse, with 2%–3% light absorption, or dense, with more than 40% light absorption at the S_{11} transition for a 7 nm thick film.[12,13] In such a device layout the surrounding environment becomes a product of the film density, inter-tube interactions, and the adjacent layers on either side of the SWCNT film. The strength of these interactions is also dependent upon the method of nanotube preparation, be it through selective polymer wrapping or aqueous surfactant based routes. In the case of polymer wrapped SWCNT solar cells, despite efforts to remove the polymer after sorting, it is widely accepted that residual polymer remains on the sidewalls and therefore in the final device.[14] However, different strategies are now being developed to completely remove the polymer after sorting.[15] In the extreme case of high polymer content, this would afford a surrounding dielectric constant, ε, of approximately 3,[7] compared to 4.4 in the case of unwrapped nanotubes surrounded by C_{60} as an acceptor (SWCNT dielectric constant of ≥4).[9] This would in turn see the exciton binding energy in the nanotubes vary between 0.41 ($\varepsilon = 3$) and 0.24 eV ($\varepsilon = 4.4$) for (6,5) nanotubes with a diameter, $d_t = 0.75$ nm, or between 0.28 and 0.16 eV for (9,7) with $d_t = 1.09$ nm.[16]

For planar heterojunction solar cells of polymer wrapped (poly(9,9-dioctylfluorene) (PFO)) SWCNTs in conjunction with C_{60}, Bindl et al. pioneered the field and in 2010 they correlated the internal quantum efficiency (IQE) of five different nanotubes (7,5), (7,6), (8,6), (8,7), and (9,7) to the calculated exciton dissociation energy of the SWCNT:C_{60} interface.[10,17] Based on a reduction of IQE from 91% for the small diameter species of (7,5) to below 30% for the larger diameter (9,7), the authors concluded that above a nanotube diameter of 1 nm the excitons are no longer efficiently dissociated. However, the use of PFO in combination with the HiPco raw material that was used, provided the authors with only a narrow selection of (*n*,*m*) species. This prevented them from extending their measurement to larger diameters and identification of a cut-off point in the diameter range at which IQE is reduced to 0%. Wang et al. also investigated polymer wrapped SWCNTs (using regioregular poly(3-dodecylthiophene-2,5-diyl) (rr-P3DDT)) in planar solar cells but with the even smaller diameter CoMoCAT material (diameter distribution of 0.6–0.9 nm).[18] Although not specifically stated by the authors, it is apparent from comparing film absorption to external quantum efficiency measurements that nanotubes with an S_{11} optical transition greater than 1400 nm produce little, if any, photocurrent. For rr-P3DDT wrapped nanotubes in contact with C_{60} in a planar solar cell, the upper limit in terms of nanotubes with diameters still being able to dissociate excitons, should therefore be around 1.2 nm.

Bernardi et al. were the first to investigate the diameter cut-off in BHJ solar cells and suggested a diameter of 1.2 nm in combination with $PC_{61/71}BM$.[19] However, SWCNTs with a diameter of 1.2 nm would have S_{11} transitions up to 1500 nm (i.e., (12,5) with a diameter of 1.20 nm) and EQE data was only presented up to 1250 nm (diameter of ≈1 nm), which hinders the interpretation of the results. Likewise, Isborn et al. prepared BHJ solar cells consisting of SWCNT:C_{60} mixtures wrapped in graphene oxide and in contact with $PC_{61}BM$.[20] The authors tested the three different chiralities of (9,7), (7,6), and (6,5) and showed a decreasing short circuit current density (J_{SC}) for increasing diameters, which they interpreted to be a result of the decreasing efficiency of exciton dissociation. The findings were complemented by density functional theory (DFT) calculations. Despite solar cells consisting of (9,7) nanotubes outputting lower current and voltage, no EQE/IQE data was provided to clarify the question of whether (9,7) works less efficiently than (7,6) or (6,5), or even if (9,7) works at all (since it is possible to measure some photovoltaic output from similar SWCNT:C_{60} solar cells even in the absence of the SWCNTs. See discussion of exciting S_{22} of large diameter nanotubes at the end of this study). Most recently, Shastry et al. fabricated BHJ solar cells employing a mixture of $PC_{71}BM$, poly(3-hexylthiophene) (P3HT) and SWCNTs and demonstrated an increase in J_{SC} due to the broader absorption of polychiral nanotubes compared to monochiral devices, and showed a clear EQE signal from (8,7)-enriched SWCNTs at 1350 nm, which would correspond to a diameter of 1.02 nm.[21]

In recent work by Guillot et al. and by ourselves, transfer matrix calculations (TMCs) were used to evaluate the electric field intensity, $|E|^2$, within the solar cell stack, and changes in the acceptor layer thickness were shown to strongly modulate the EQE of devices due to resultant variation of $|E|^2$ at the plane of the nanotube film.[12,22] Following from these works, the conclusion can be drawn that for any investigation into a diameter cut-off not only is it important to consider the surrounding dielectric environment of the nanotubes, but also to ensure that the measurement reflects a true reduction in exciton dissociation and not an effect of decreasing electric field intensity at the wavelength of interest. In this work, we prepare planar SWCNT:C_{60} solar cells from polymer-free, monochiral SWCNTs of small ((6,5) and (7,5)) and large (9,8) diameter, along with polychiral mixtures of increasing diameter from the HiPco and arc discharge processes, with the aim of determining the diameter cut-off in polymer-free planar solar cell devices. In all cases, the nanotubes were prepared with surfactant-based methods. In the case of using aqueous preparation processes, it is possible to have water filled and un-filled carbon nanotubes,[23] which due to the high dielectric constant of water ($\varepsilon = 80$)[24] might be expected to drastically increase the overall dielectric constant of the nanotube and in turn decrease the exciton binding energies. However, as calculated by Cambre et al.,[25] the presence of endohedral water only changes the effective dielectric constant up to 20% compared to the unfilled case. Regardless of whether the nanotubes are water filled or not, the use of sequential surfactant-based sorting has the advantage of maintaining the same dielectric environment across all devices and does not rely on different polymer systems to achieve the same richness in diameter range.

2. Results and Discussion

Throughout this work, a solar cell architecture consisting of a thin layer of SWCNTs (2–3 nm) in contact with C_{60} (115–127 nm) with a layer of PEDOT:PSS (41 ± 5 nm) as a hole transport layer and ITO front and silver back contacts were used. The device architecture is illustrated in **Figure 1**a and is similar to our previous work with polymer-free (6,5) SWCNT films.[12] However, unlike our previous work, the composition of the SWCNT film was varied from monochiral to polychiral dispersions with diameter distributions ranging from 0.7 to 1.8 nm. The optical absorption spectra of the aqueous dispersions and thin films were initially used to determine the (n,m) species distribution within each SWCNT film and were then compared to the EQE data, allowing an evaluation of the IQE for each nanotube type. In this way, a range of different (n,m) species and diameters were tested to determine which of them produces an IQE of 0%. The dispersions used for SWCNT films are shown in **Figure 2** and are labeled D1–D7 in order of increasing diameter. D1–D5 were obtained from the HiPco raw material and cover the diameter range 0.7–1.1 nm. D1 and D2 were monochiral suspensions of (6,5) and (7,5) with diameters of 0.75 and 0.82 nm, respectively. D3 was a near-monochiral suspension of (7,6) with a diameter of 0.88 nm. D4 and D5 were polychiral mixtures of nanotubes with mean diameters of 0.934 ± 0.006 and 0.939 ± 0.005 nm. Above this diameter range, monochiral suspensions of (9,8), with a diameter of 1.15 nm and labeled as D6, and polychiral dispersions from the arc discharge process, with a diameter range of 1.2–1.8 nm and labeled as D7, were used.

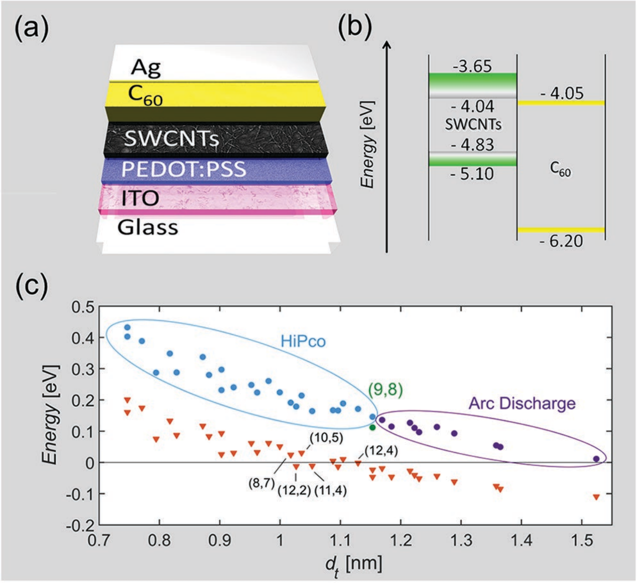

Figure 1. a) Schematic of the solar cell architecture. b) Energy diagram of SWCNTs with diameter between 0.7 and 1.8 nm and therefore variable bandgap, interfaced with C_{60}. Green bands indicate a sufficient energy offset between the LUMO HOMO ($Q = -1$) of the nanotubes and the LUMO ($Q = 0$) of C_{60}, according to the diagram shown in c), while white and grey indicate an insufficient energy offset. The net driving energy for exciton dissociation (triangles) is plotted in (c) along with the LUMO offset (dots) for SWCNTs with different diameters (d_t). Blue dots indicate nanotubes that are represented in dispersions from HiPco starting material while green and purple dots represent (9,8) enriched dispersions and dispersions from arc discharge starting material, respectively.

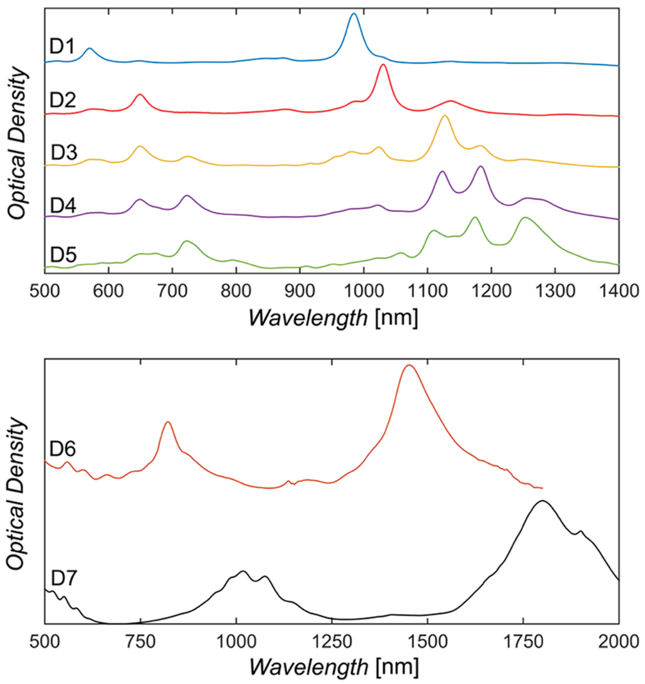

Figure 2. Optical density measurements on surfactant wrapped SWCNTs in dispersions made from HiPco (D1 to D5), (9,8) (D6) and arc discharge (D7) material.

Within the field of SWCNT:C_{60} solar cells it has become standard to discuss the HOMO/LUMO positions of the SWCNT, which, based on the LUMO offset to C_{60} and the exciton binding energy in the nanotubes, allows for a theoretical prediction to be made regarding the appropriate diameter range of SWCNTs for exciton dissociation at the C_{60} interface. In order to calculate the LUMO level of the SWCNTs, first photoelectron yield spectroscopy in air (PESA) was used to determine the HOMO energy of SWCNT films from all dispersions and a value of −4.83 eV for the arc discharge material through to −5.10 eV for (6,5) was measured. The PESA data can be found in Figure S1 in the Supporting Information. The HOMO energies of different nanotubes can also be calculated by assuming a Fermi level of −4.5 eV and adding half of the optical bandgap, itself determined by adding 40 nm to the wavelength of the S_{11} transition in solution to account for the red-shift observed in experiments, which is in good agreement with the experimental findings.[12,26] According to the works of Spartau et al. and Bindl et al. the energy of the optical gap and the exciton binding energy (determined from the works of Dukovic et al. and Perebeinos et al.) are then added to the HOMO level to yield what is often referred to as the "LUMO" position of the SWCNT.[7,9–11] In effect this calculation affords the free carrier energy level of the nanotube and should more appropriately be referred to as HOMO ($Q = -1$). In all cases a dielectric constant of 4.4 for C_{60} was assumed and the exciton binding energy in the nanotubes was scaled in accordance with the work of Perebeinos et al.[9]

The LUMO of C_{60} was assumed to be constant at −4.05 eV as proposed by Shirley and Louie.[27] Using this information, a bandgap diagram for different (n,m) species can be drawn as shown in Figure 1b and the LUMO offset between SWCNTs and C_{60} can be used to determine the potential energy inherent in the system. By subtracting the exciton binding energy from the LUMO offset, the net driving energy can be calculated and if it is larger than zero, exciton dissociation is expected. This is plotted in Figure 1c. According to this calculation, solar cells made with nanotubes having diameters larger than the (8,7) or (10,5) (1.02 and 1.04 nm, respectively) should not be able to dissociate excitons at the interface with C_{60}, and should thus have IQE of 0%.

Central to this work is the accurate determination of the different SWCNT species in the film under investigation. This was achieved through a combination of optical absorption measurements of the aqueous dispersions used to make the films and photoluminescence (PL) measurements of the parent dispersions they were obtained from. Fitting was performed as fully described in the experimental details. Briefly Lorentzian profiles were used to fit S_{11} peaks and Gaussian profiles for fitting the exciton phonon sideband (EPS). The initial height and full width at half maximum (FWHM) was determined for optical density measurements and allowed to vary, broaden, respectively, for film absorbance measurements. The relative concentration of each (n,m) species found for optical density measurements of dispersions was varied within ±10% for the film absorbance measurement. The results of the fitting procedure are shown in **Figure 3** with results for monochiral (6,5) dispersion shown in Figure S2 in the Supporting Information.

SWCNT films from D1–D7 were then integrated into SWCNT:C_{60} solar cells and TMCs were employed to ensure sufficient electric field intensity $|E|^2$ at the position of the nanotubes with increasing diameter. In agreement with previous work,[12] the complex refractive indices for the SWCNT were ignored due to the thinness of the film and $|E|^2$ at the interface of PEDOT:PSS and C_{60} was considered. For all devices, a constant PEDOT:PSS thickness of 41 ± 5 nm was used and the C_{60} thicknesses varied from 115 to 127 nm for D2 to D5, 170 nm for D6 and 240 nm for D7. Film thicknesses were confirmed with a Dektak XT profiler and atomic force microscopy (AFM). Corresponding J–V curves are shown in Figure S3 in the Supporting Information and typical solar cell performance parameters are summarized in Table S1 in the Supporting Information, with fill factors ranging from 25% (D6) to 43% (D5). The mean absolute film absorbance is plotted in **Figure 4** along with EQE and the calculated $|E|^2$. The mean absorbance of each film shown in Figure 4 was calculated from measurements of the internal reflectance, which is shown in detail for D5 in Figure S4 in the Supporting Information and is discussed later in reference to IQE. In Figure 4 and Figure S5 in the Supporting Information, the shape of the EQE follows that of the optical absorbance of the monochiral (7,5) and (6,5) films (D2, D1, respectively) and is in agreement with previous work.[12] However, for D3 and D4, at around 1000 nm the shape of the EQE is dramatically different to that of the films' absorbance spectra (blue vs green curve).

For D5, an EQE peak around 1310 nm is visible but does not appear in the EQE spectra of D2–D4 (which represent devices made from material taken earlier in the sequential sorting process). Either the relative concentration of those SWCNTs was too small in D2–D4 or the nanotubes causing the EQE signal were not present in those previous dispersions. In the case of solar cells made from (9,8) and arc discharge material (D6 and D7), a notable absence of any nanotube contribution to the EQE is apparent in both Figure S6 in the Supporting Information and the raw current signals from all EQE measurements in this study, summarized in Figure S7 in the Supporting Information. It suggests that the diameter regime of 1.15–1.8 nm is above the cut-off point.

In order to quantify the contribution of each kind of nanotube to the solar cell performance, the measured EQE was fitted based on the predetermined (n,m) distribution in the film. In this case, the fitting procedure was kept rigid; the FWHM was not allowed to vary from the FWHM of the film and the peak position was constrained to be within −5 to +15 nm from the film to account for a changed dielectric environment (caused by nanotubes being sandwiched between air and glass compared to being sandwiched between PEDOT:PSS and C_{60}). The magnitude of each EQE peak was then allowed to vary freely between 0 and 100%. The results of the EQE fit are shown alongside the film absorbance spectra and calculated $|E|^2$ in Figure 4. It is apparent that the contribution to the EQE from small diameter SWCNTs such as (6,5) and (8,3) (0.75–0.77 nm) is stronger than expected from their concentration in the film, which is already a first indication of more efficient exciton dissociation for these SWCNTs. Although there are some contributions from (8,4) and (8,6) nanotubes detectable in optical density and PL measurements for D2, they do not show up in the fit of the EQE result. As the EQE contribution of each peak is allowed to vary freely, overlapping tube contributions, especially if some chiralities are only represented in minor quantities, can lead to neglecting tubes that should have a contribution to the overall EQE. Therefore we investigated solar cells with varying mixtures of different chiralities to draw a reliable conclusion on which nanotube is the last working one in the increasing diameter series of polymer-free SWCNT:C_{60} solar cells. By directly comparing the contribution of (9,5) and (8,7) to the EQE in Figure 4, we conclude that their contribution is either negligible or nonexistent. The same can also be observed for (9,7) and (10,6) in D4 and D5.

In order to eventually determine the cut-off of nanotube diameter/chirality beyond which exciton dissociation is not possible, in situ reflectance measurements were performed to

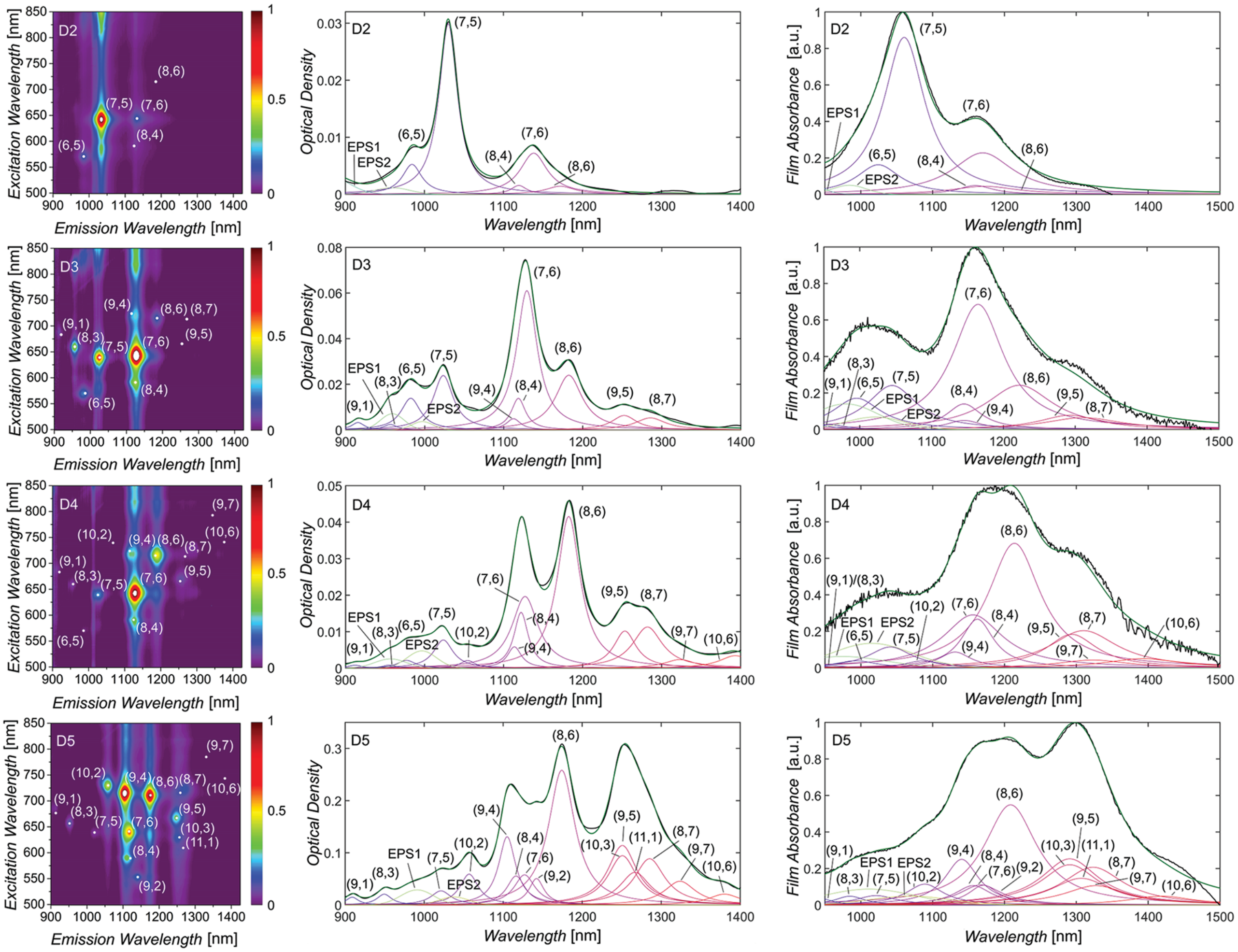

Figure 3. Photoluminescence contour map, corresponding optical density (measured with a 2 mm path length) and film absorbance measurements of SWCNT dispersions and films prepared from HiPco material. The sum of the Lorentzian S_{11} fits and the Gaussian shaped EPS is plotted in green, while the original optical density and film absorbance measurements are shown in black.

determine the absolute absorbance of the different nanotube films. From this, the IQE of all nanotubes under investigation was calculated. A scatter plot of the IQE of individual SWCNTs along with an exponential fit of the form $A \cdot e^{(b \cdot dt)}$ is shown in **Figure 5**. Compared to previous reported values on polymer-free, monochiral (6,5) SWCNT:C_{60} solar cells,[12] the IQE of the (6,5) nanotubes in the polychiral solar cell has decreased from 86% to 43%. This was partly attributed to the generation of trap states when interfacing large bandgap nanotubes and small bandgap nanotubes, and partly to intertube energy transfer amongst S_{11} transitions as outlined by Mehlenbacher et al.[28] Exciton dissociation at the SWCNT:C_{60} interface occurs on roughly the same time scale as the redistribution of energy to other S_{11} states (120 fs compared to ≈60 fs),[28,29] an increase in the number of alternative energy pathways likely causes a reduction in the total amount of excitons being dissociated at small diameter tubes and, consequently, the IQE of those junctions. Additionally, considering the comparable time scales, it becomes very difficult to distinguish between the generation of charge carriers from excitons being generated at the large diameter nanotubes and those that were generated from excitons being created on large band gap nanotubes and transferred onto small bandgap SWCNTs. Nevertheless, the recent study from Ihly et al. demonstrated an optimum LUMO offset between donor (SWCNTs) and acceptor (C_{60}) of ≈130 meV which is satisfied for small diameter (large bandgap) nanotubes, like (8,3), (9,1) or (6,5).[30] For larger or smaller LUMO offsets the relative carrier yield at the interface of donor and acceptor is clearly reduced and therefore the IQE of large diameter nanotubes. From these results we suggest an absolute upper bound diameter limit of 0.95 nm, corresponding to the (8,6) species. Beyond this diameter the required exciton dissociation energy is larger than that provided by the LUMO offset.

Upon comparing this finding to the cut-off values reported in the literature for polymer-wrapped nanotubes, the question arises why a significantly smaller diameter cut-off was obtained for polymer-free nanotubes (0.95 nm compared to up to 1.2 nm for polymer-wrapped nanotubes). Returning to the discussion about the net driving energy required for exciton dissociation at the SWCNT:C_{60} interface, the following set of equations can be used:

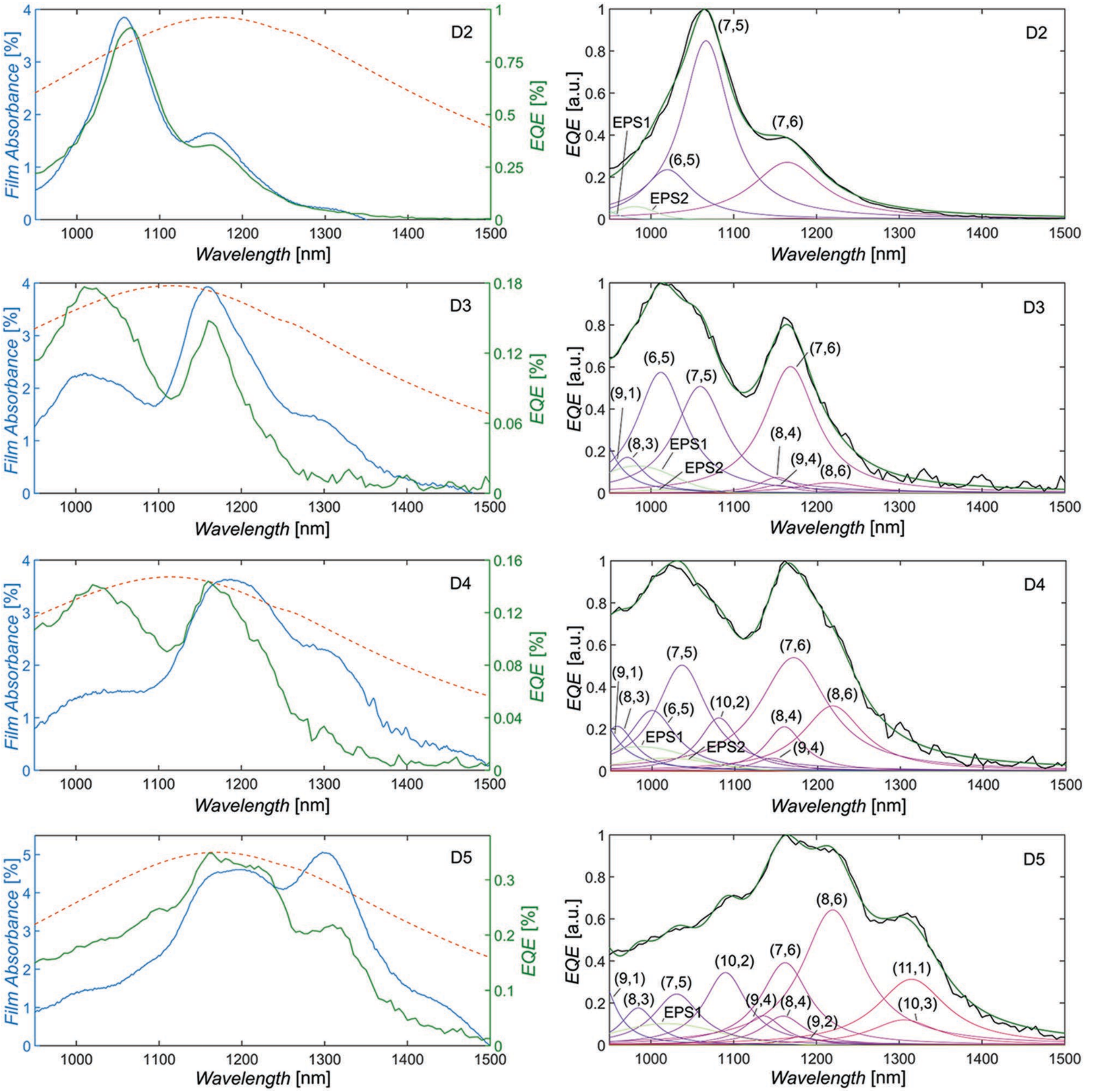

Figure 4. Mean film absorbance (blue), EQE (green) and $|E|^2$ (red) for solar cells prepared from HiPco material D2–D5 are shown in the left column. $|E|^2$ was scaled to the maximum film absorbance to guide the eye and to verify sufficient light intensity at the absorption of the nanotube film. In the right column the fit of the EQE is shown in green and the original measurement is shown in black.

$$\mathrm{LUMO}_{\mathrm{SWCNT}} - \mathrm{LUMO}_{\mathrm{C}_{60}} - E_{\mathrm{bind}} \geq 0 \tag{1}$$

$$\mathrm{HOMO}_{\mathrm{SWCNT}} + E_{\mathrm{S}_{11}} + E_{\mathrm{bind}} - \mathrm{LUMO}_{\mathrm{C}_{60}} - E_{\mathrm{bind}} \geq 0 \tag{2}$$

$$\mathrm{HOMO}_{\mathrm{SWCNT}} + E_{\mathrm{S}_{11}} - \mathrm{LUMO}_{\mathrm{C}_{60}} \geq 0 \tag{3}$$

According to Equation (3) it seems, that in determining the net driving energy, the binding energy of excitons E_{bind} in the SWCNTs cancels out. Thus, it may at first appear that changes in the dielectric environment of the nanotubes caused by the presence of the polymer wrapping and its effect on the exciton binding energy can be ruled out as an explanation for the observed difference in cut-off. However, the E_{S11} optical gaps of the nanotubes are themselves dependent on the dielectric environment since the optical gap is dependent on the electron–electron repulsion or self-energy and the binding energy, and both vary with the dielectric environment.[9,31] The net effect is that as the dielectric constant of the environment decreases, the optical gap increases. This can be readily seen when comparing the red-shifts of the optical gaps observed in solar cells versus those measured in solution. In the case of devices prepared

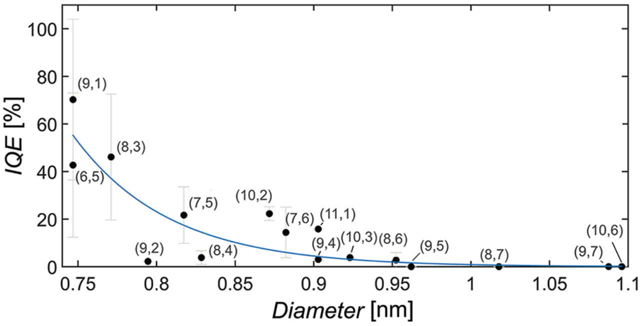

Figure 5. IQE values for nanotubes with different diameters (black dots). The best fit was obtained by an exponential function of the form $A{\cdot}\exp(b{\cdot}d_t)$ with $A = 11.26{\cdot}10^4$ and $b = -16.37$.

from polymer wrapped SWCNTs the red shift is around 6 meV (for a 7 nm thick film of (7,5) nanotubes reported by Bindl et al.,[32] that is even reduced upon increasing nanotube film thickness)[33] compared to around 42 meV for the same nanotubes, without the polymer, as used in this study and others.[34] A smaller red shift equates to a larger optical gap and therefore a larger net driving energy, as per Equation (3). Additionally, as shown in the work by Crochet et al., in the case of aggregated bundles of polymer-free SWCNTs the observed red-shift is not entirely captured by changes in the dielectric environment (increased screened Coulomb interaction between electron and holes) but also by a tunnelling induced splitting of the degenerate intertube conduction and valence bands that ultimately leads to delocalized excitons.[35] In summary, when going from polymer wrapped to polymer-free SWCNTs the optical gap decreases, which means that the net driving energy possessed by the junction decreases and therefore the maximum diameter (minimum gap) nanotube that will have a positive driving force for exciton separation at the junction decreases (required gap increases). A complicating factor in this analysis is that the binding energy, and thus LUMO energy, of the C_{60} is similarly dependent on the dielectric environment and is presumably thus also affected by the presence or absence of the polymer at the junction. Furthermore, the LUMO value for C_{60} used in Figure 1b does not take the free carrier state into account and is effectively a LUMO $Q = 0$ state. Therefore, the unrealistic comparison of a HOMO $Q = -1$ state in the SWCNT to a LUMO $Q = 0$ state in C_{60} is being made. Based on Shirley et al. the HOMO $Q = -1$ state in C_{60} can be calculated (based on the literature accepted HOMO value of −6.2 eV) to be −3.2 eV, which, in reference to Figure 1b, would result in none of the (n,m) species within the HiPco material contributing to the photocurrent.[12,17,27,34] As this is clearly not the case, the LUMO level used in this work must closely match reality and the HOMO level of the C_{60} must be different to the value often used in the SWCNT:C_{60} community. Using the HOMO/LUMO gap reported by Shirley et al., the HOMO level of C_{60} can be calculated to lie at around −7.05 eV.[27] However, the HOMO/LUMO gap of C_{60} has also been reported to vary between 2.6–3 eV and highlights the importance of measuring these values in situ in a SWCNT:C_{60} solar cell in the future.[36]

Considering the 0.95 nm diameter cut-off observed in this work (equivalent to a maximum wavelength of 1315 nm in the EQE), the ability to truly take advantage of the IR absorption properties of SWCNTs appears limited and the question arises as to what can be done to gain access to these larger diameters. One way to circumvent this limitation is to wrap the larger diameter nanotubes with a polymer such as the aforementioned rr-P3DDT, allowing the cut-off to be shifted to ≈1.2 nm (equivalent to a wavelength of 1500 nm). An alternative strategy was presented by Bernardi et al. for BHJ solar cells.[19] By introducing reduced graphene oxide (rGO), a highly disordered amorphous semiconductor with quasi metallic properties, in-between $PC_{61/71}BM$ and large diameter (>1.2 nm) SWCNTs, contributions to the photocurrent from nanotubes in the wavelength range from 1300 nm up to 1530 nm were demonstrated in the EQE data. With a dielectric constant for rGO of ≈30,[37] this clearly cannot be understood in terms of the dielectric environment model already described (which would predict the maximum accessible wavelength to decrease). However, they explained their finding in reference to the formation of large Schottky barriers for electrons between PCBM and rGO and therefore an energetically favoured hole transport from PCBM to rGO and finally onto SWCNTs. Perhaps the most obvious strategy is to change the acceptor to a material with a lower (more negative) LUMO energy than C_{60}. Often, fullerene derivatives like $PC_{61}BM$ or $PC_{71}BM$, with higher LUMO energies (at −3.96,[38] −3.95 eV,[39] respectively) are used as C_{60} alternatives. However, comparing the net driving energy of these acceptors to C_{60}, shown in **Figure 6**, would actually further decrease the number of available SWCNTs. Lowering the LUMO energy would cause a decrease in energy offset between the HOMO of the SWCNTs and the LUMO of acceptor, which is believed to reduce the V_{OC},[40] but by accessing the lower energy portion of the solar spectrum the available photon current could be significantly increased.[41] Clearly, if solar cells that operate further into the IR regime are desired, then new acceptor molecules with lower LUMO energies should be investigated. One alternative to C_{60} would be C_{70} (−4.09 eV).[42] This decrease in LUMO energy already shifts the net driving up so that larger diameter nanotubes up to (10,8) with a diameter of 1.23 nm are accessible. In order to successfully dissociate excitons from the full set of HiPco, (9,8) and arc discharge prepared SWCNTs, the LUMO level needs to be lowered even further. Two possibilities are C_{84} and $PC_{85}BM$,[39,42] (−4.44 and −4.31 eV, respectively, as outlined

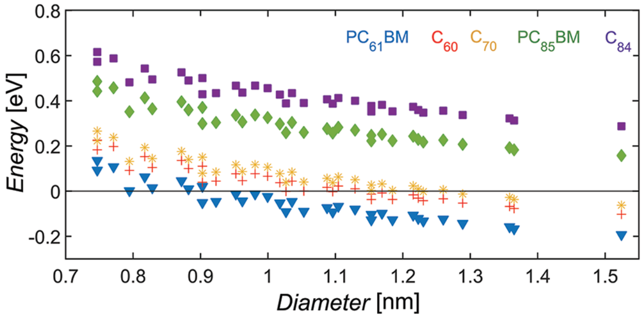

Figure 6. Net driving energy for different acceptor materials in contact with SWCNTs. The more negative the LUMO (highest value for $PC_{61}BM$ and smallest for C_{84}) the further the cut-off diameter shifts toward larger diameter/smaller bandgap nanotubes.

in the Supporting Information) which could, in theory, allow access to those nanotubes with diameters ≫ 1.5 nm as shown in Figure 6. Experimental evidence supporting this concept has previously been shown in solution experiments by Hilmer et al. through quenching of the nanotube PL by $PC_{85}BM$.[43] However, Ihly et al. demonstrated that increasing the LUMO offset (lowering the LUMO level of the acceptor) beyond the optimum of 130 meV, results in a decreasing carrier generation at the interface of SWCNTs and acceptor molecules.[30] In order to efficiently generate charge carriers in a SWCNT solar cell, different acceptors have therefore to be employed for different nanotube bandgap and diameter ranges. It seems as if the only way to exploit the full diameter range of HiPco and arc discharge SWCNTs in a solar cell is a tandem architecture with different acceptor molecules that ensure a LUMO offset being in the range of 130 meV.

An additional question that arises, particularly in the case of large diameter SWCNTs which do not possess a large enough bandgap to contribute to photocurrent generation via their fundamental S_{11} transition, is the possibility of photocurrent generation through the second optical transition (S_{22}). In the case of small diameter polymer-free and polymer wrapped SWCNTs, photocurrent has previously been shown to be generated from S_{22}.[5,12,22] In the case of large diameter SWCNTs such as those in D6 and D7, the bandgap of S_{22} should be large enough to provide a sufficient LUMO energy offset to C_{60}. We investigated this by first changing the C_{60} thickness to 124 nm to ensure high electric field intensity at the position of the S_{22} of D6 and D7, then measuring the EQE spectra. As shown in Figure S8c,f in the Supporting Information no photocurrent was observed from SWCNTs in the wavelength regime above 800 nm, corresponding to S_{22} of (9,8). According to the work of Lüer et al. and Mehlenbacher et al.,[44,45] excitons relax from S_{22} to S_{11} within ≈40 fs. Using two dimensional white light spectroscopy (2D-WL), Mehlenbacher et al. furthermore verified that energy is redistributed among S_{22} states on comparable time scales, and is about as fast as energy transfer among S_{11} states.[28,45] For the latter case, they stated that in mixed SWCNT chirality films, energy transfer from the smallest tube to the largest nanotube is equally likely as the transfer amongst nanotubes with almost equal diameters.[45] Dowgiallo et al. investigated the time scales of exciton dissociation and charge transfer from the S_{11} state of purified (6,5) SWCNTs onto C_{60}.[29] According to their findings, electrons are transferred from nanotubes to C_{60} within less than 120 fs. Comparing the different timescales, it is likely that the energy relaxation from S_{22} to S_{11} is happening faster than the exciton dissociation between S_{22} and C_{60} and that the S_{11} position of the nanotube determines whether there is an energy transfer from S_{22} to C_{60}. This idea is further supported by the higher binding energy for S_{22}, calculated by Ando,[46] despite a 2.4 times higher free carrier quantum yield for S_{22} excitons compared to S_{11} was shown by Park et al.[47]

3. Conclusions

To conclude, solar cells comprising SWCNT films with varying contents of small and large diameters were prepared and used in SWCNT:C_{60} solar cells. By careful assignment of the different component chiralities to PL measurements and subsequent fits to the optical spectra of dispersions, the distribution of nanotubes in each dispersion used in this study was derived. Employing these unique chirality distributions for subsequent fits to the optical spectra of SWCNT films made from these dispersions, and for EQE measurements of the corresponding solar cells, a direct assignment of each nanotube seen in EQE was possible. As a result, the largest polymer-free SWCNT to generate photocurrent in planar SWCNT:C_{60} solar cells has been determined to be the (8,6) nanotube with a diameter of 0.95 nm. The difference in diameter cut-off between the polymer-free nanotubes used in this study and the polymer wrapped nanotubes used in previous studies can be explained by a larger red-shift of the S_{11} optical transition in the polymer-free nanotubes, which can in turn be understood by considering the differences in dielectric environment in both cases. Additionally, the possibility of obtaining photocurrent by instead exciting the S_{22} transition of nanotubes with a diameter larger than the cut-off was ruled out in this study. As well as defining an upper limit of nanotube diameters that could be used in high efficiency SWCNT:C_{60} solar cells absorbing in the UV through to NIR, these results hold relevance in regards to the possibility of building solar cells from polymer-free SWCNTs that are (semi) transparent in the visible regime (400–800 nm) with the outcome being that to access the correct nanotube chiralities for that application, they must be interfaced with a different acceptor than C_{60}.

4. Experimental Section

Preparation of SWCNT Dispersions: SWCNT dispersions were prepared from aqueous surfactant wrapped dispersions using sodium dodecylsulfate (SDS, Merck), sodium cholate (SC ≥ 99%, Sigma Aldrich) and co-surfactant mixtures thereof. Detailed experimental details can be found in previous publications.[12,48] In brief small diameter HiPco (NanoIntegris) were suspended in 2 wt% SDS by sonication for 1 h followed by ultracentrifugation for 1 h at 64206·g (SW-40-TI rotor). The SDS concentration was then adjusted to 1.6 wt% SDS and added to 40 mL of Sephacryl-S200 gel (Amersham Biosciences). At 1.6 wt% SDS predominately (6,5) remained adsorbed to the gel and could be eluted with 1 wt% SC to afford dispersion D1. Following the separation of (6,5) the SDS concentration was gradually lowered in 0.2 wt% steps down to a concentration of 0.8 wt% and the process repeated to afford dispersions D2 to D5. In the case of large diameter nanotube dispersions, arc discharge material was obtained commercially (P2, Carbon Solutions) and (9,8) was selectively grown utilizing a sulfate-promoted catalyst approach in a chemical vapor deposition (CVD) process.[49] Semiconducting fractions of large diameter species were then prepared following the recent description for double walled carbon nanotubes (DWCNTs) by suspension in 1 wt% SC and the subsequent addition to a sephacryl column under 1 wt% SDS.[50] Dispersion absorption measurements were performed on a Varian Cary 500 spectrophotometer. For the (photoluminescence excitation) PLE maps of the SWCNT dispersion the spectrally separated output of a WhiteLase SC400 supercontinuum laser source (Fianium Ltd.) was used for excitation and spectra were recorded with an Acton SpectraPro SP2358 (grating 150 lines mm^{-1}) spectrometer with an OMA-V InGaAs line camera (Princeton Instruments) and corrected for background and wavelength-dependent sensitivity/excitation power.

Preparation of SWCNT Films: SWCNT films were prepared via the method of EDSA.[12] Briefly, silicon oxide (SiO_2) wafers were covered with poly(methyl methacrylate) (PMMA 950K 0.25 μm $(4000\ rpm)^{-1}$, Allresist), baked (160 °C, 30 min) and immersed vertically in the SWCNT dispersion in an oven (60 °C, 6 h). Copious washing with deionized water was used to remove any residual surfactant on the nanotubes. The SWCNT film was then scored into a rectangle (≈1.3 cm^2 in size) and slowly immersed into water to detach the SWCNT coated PMMA from the SiO$_2$. Prior to the final detachment of the film, the substrate was withdrawn from the water, re-immersed in glycerol (99.5%, VWR), and transferred onto glass for characterization. Scanning electron microscopy (SEM) (Zeiss Ultra Plus), AFM (Bruker Dimension Icon) using silicon cantilevers (Mikromasch, 325 kHz, 40 Nm^{-1}), and film absorbance measurements (Varian Cary 500 spectrophotometer) were taken to characterize the nanotube films. The HOMO level of all films were measured on a glass substrate at 800 nW by PESA (AC-2E, Riken Keiki).[51]

Detailed Fitting Procedure: Assignment of the (n,m) species in a PL contour map was performed using a modified approach from Bachilo et al. by individually fitting the parameters a1 to a3 and b1 to b3 for mod(n − m) = 1 and mod(n − m) = 2 SWCNTs for each dispersion to calculate the first (ν_{11}) and second (ν_{22}) van Hove transition frequencies, as proposed by Cambré et al.[52,53] Fitting was performed with an unconstrained, non-linear least square solver, "lsqnonlin," using MATLAB R2014b:

$$\nu_{11} = \frac{1\times10^{7}\ \text{cm}^{-1}}{a_1 + a_2 \times d_\text{t}} + \frac{a_3 \times \cos(3\alpha)}{d_\text{t}^2} \tag{4}$$

$$\nu_{22} = \frac{1\times10^{7}\ \text{cm}^{-1}}{b_1 + b_2 \times d_\text{t}} + \frac{b_3 \times \cos(3\alpha)}{d_\text{t}^2} \tag{5}$$

The transition frequencies in Equations (4) and (5) depend on the diameter (d_t) and the chiral angle (α) of the individual SWCNT. Each diameter and chiral angle was calculated based on the formulas given by Pipes et al., assuming a C–C bond length of 0.142 nm.[54] The results of these assignments are shown in Figure 3. Using the assignment from photoluminescence contour maps, the S$_{11}$ regions of the dispersion absorption measurements were fitted with Lorentzian functions after subtracting a background as described by Nair et al.[55] Fitting was again performed with a constrained, non-linear least square solver, "lsqnonlin," using MATLAB R2014b. The quality of the fit of a nonlinear equation strongly depends on the starting values of the fit. Therefore, the initial FWHM of each (n,m) species was calculated based on the position of S$_{11}$ in the units of eV ($E^{(n,m)}{}_{11}$) as proposed empirically by Tune and Shapter:[6]

$$\text{FWHM}_{(n,m)} = 0.067 \times E_{11}^{(n,m)} - 0.02 \tag{6}$$

This initial FWHM was divided by a factor of two to match the measurements and was converted into wavelength and allowed to increase or decrease during fitting within ± 20% for SWCNTs with an S$_{11}$ smaller or equal to 1050 nm. For nanotubes with S$_{11}$ transitions larger than 1050 nm, an increase in FWHM of 20% was not sufficient for an accurate fit. The upper limit of Lorentzian broadening was therefore allowed to increase up to 60% of the initial FWHM. The initial peak position was based on the set of S$_{11}$ positions for HiPco SWCNTs provided by Bachilo et al.[52] Employing the built in MATLAB function "findpeaks," local maxima of the optical density plots were detected. The position of these peaks was then compared to the data set of initial S$_{11}$ positions for HiPco SWCNTs and assigned to specific (n,m) chiralities. All peak positions that could be assigned this way were allowed to vary within ±5 nm during the fitting. Remaining nanotubes, that could not be detected automatically, were allowed to vary between −5 and +20 nm of their recorded S$_{11}$ position. Also the height of the peaks was allowed to vary during fitting. The lower limit was set to be 10% of the initial peak height, while the upper limit was set case sensitive: for dispersions with only a few chiralities, one peak usually represented one tube. For mixed chiralities a peak can represent a convolution of many different (n,m) species with unknown spectral weight and therefore unknown height. Based on this observation, the upper bound of the peak height was set to 95% of the initial peak height for dispersions with only a few nanotubes and to 90% for dispersions with mixed chiralities. Additionally, a Gaussian curve for the exciton phonon side band (EPS) was introduced with a starting FWHM of 40 nm, which was allowed to vary between 50% and 200% (20–80 nm). The spectral weight transfer of S$_{11}$ to the phonon side band was also modeled based on the diameter dependence suggested by Perebeinos et al in Equation (7):[56]

$$\frac{I_\text{EPS}}{I_{\text{S}_{11}}} = 0.017 + \frac{0.1\ \text{nm}}{d_t} + f_1 \tag{7}$$

whereas I_EPS is the spectral weight of the exciton phonon side band and I_S11 is the spectral weight of the first optical transition. The correction factor f_1 was introduced in this study to account for a modified weight transfer due to changes in dielectric environment or an increase in bundling and was allowed to vary during fitting between ±0.07. The necessity of the correction factor f_1 is verified in Figure S9 in the Supporting Information. The position of the EPS was set to be 0.200 eV above the S$_{11}$ transition and allowed to vary within ±0.005 eV. The results of this fitting procedure are shown in Figure 3. Additionally the relative concentration of each (n,m) species was determined by dividing the area of a specific tube by the sum of all areas and is tabulated along with the center and FWHM of each nanotube in Table S2 to Table S4 in the Supporting Information.

As described in the previous work,[12] evaporation driven self-assembly (EDSA) was used to prepare the thin SWCNTs films from dispersions D1–D7. Representative SEM images of SWCNT films can be found in Figure S10 in the Supporting Information, where sparse films with optical densities of 2%–5% are depicted. In the next step, film absorbance measurements were fitted based on the (n,m) distribution determined from dispersion. Prior to fitting the film, the background was subtracted following the procedure outlined by Tian et al.[57] The sum of a Fano and Lorentzian profile was used to account for inter-band electronic transition at the M saddle point of the Brillouin zone (≈4.5 eV) and the π Plasmon resonance (≈5.3 eV), respectively. An example of the background subtraction procedure for both the dispersion and thin film measurements is provided in Figure S11 in the Supporting Information. In accordance with previous reports a broadening and red-shift of all peaks was observed and was accounted for by applying a constant factor between 1 and 2.5 to the FWHM of all Lorentzian and 1 to 3 for all Gaussians.[58]

The red-shift itself was modeled to vary between 0 and +40 nm with an initial guess of +30 nm. The relative concentration of each nanotube was also allowed to vary between ±10% compared to the relative concentration calculated for dispersion measurements. This deviation was necessary to compensate uncertainties introduced by film formation and subsequent background subtraction. For the EPS, Equation (7) was used to calculate f_1 and was allowed to vary between −0.05 and 0.1. These higher upper boundary conditions were set to reflect the larger part of the spectral weight to be transferred from S$_{11}$ onto the EPS in a film of mixed chiralities. For the measurements of D1 and D2, nearly monochiral (6,5), (7,5), a smaller part of the spectral weight as proposed by Perebeinos et al. was transferred in the film fitting, as confirmed by the fitting results listed in Table S5 in the Supporting Information. For mixed chiralities a smaller part (negative f_1) was transferred for solution fits, but a larger one for film measurements.

Solar Cell Preparation: PEDOT:PSS (Al 4083, Ossila) was filtered (Millex-HV, 0.45 µm, Merck) and mixed with ethanol (absolute, VWR) in ratios of 1:1 before sonication for 10 min. This mixture was then spin coated (40 µL at 2200 rpm for 60 s, yielding a thickness of 41 ± 5 nm) and baked in inert atmosphere (250 °C, 10 min) before being covered with PMMA (40 nm). SWCNT films floating on glycerol were subsequently transferred onto the sample and left in chloroform (≥99.8%, Sigma-Aldrich) over night. Following electric field intensity calculations, different thicknesses of C$_{60}$ (99.9+%, Sigma Aldrich) were evaporated at 380–450 °C through a shadow mask in a Lesker SPECTROS Evaporation System (base pressure: 7–9 × 10^{-7} Pa) with the layer thickness monitored by quartz crystals. A 100 nm silver top electrode was evaporated to complete the fabrication of solar cells with areas of 0.105 cm^2. Internal reflectance measurements were carried out on a Bruker microscope (Vertex 80/Hyperion 2000 FTIR). Film thicknesses were measured with a DektakXT profiler (Bruker) and an AFM (Bruker Dimension Icon) using silicon cantilevers (Mikromasch, 325 kHz, 40 Nm^{-1}).

Solar Cell Characterization: The solar cells were characterized with a Keithley 238 source meter under AM1.5G illumination from a Newport 300 W solar simulator (M-91160). The solar simulator was calibrated using a silicon reference cell (91150-KG5, Newport). Following *J–V* characterization, the EQE was measured with a 450 W Xenon light source, an optical chopper (473.5 Hz), a 300 mm monochromator (LOT-Oriel), a custom designed current amplifier (DLPCA-S, Femto Messtechnik) and a digital lock-in amplifier (eLockin 203 Anfatec). Initial calibration was carried out with a calibrated UV-enhanced silicon (SM1PD2A, Thorlabs) and germanium diode (FDG03-CAL, Thorlabs).

Transfer Matrix Calculations: Transfer matrix calculations were performed using a modified MATLAB code available from the McGehee group at Stanford and as outlined by Burkhard et al. and Pettersson et al.[59] The complex refractive indices of glass, ITO, PEDOT:PSS and C_{60} were determined with a LOT Woolam Vaiable Angle Spectroscopic Ellipsometry (VASE) Ellipsometer and included in the code. The electric field intensity was calculated for all solar cells presented in this study.

Supporting Information

Supporting Information is available from the Wiley Online Library or from the author.

Acknowledgements

B.S.F. gratefully acknowledges support from the Deutsche Forschungsgemeinschaft (DFG) under grant numbers FL 834/1-1 and FL 834/2-1. R.K. acknowledges funding by the DFG under INST 163/354-1 FUGG. K.G., A.M., T.P., and A.C. acknowledge funding by the German Federal Ministry for Education and Research (BMBF) under contract 03EK3504 (project TAURUS) and support by the DFG Centre for Functional Nanostructures (CFN). A.G. and J.Z. acknowledge financial support by European Research Council under the European Union's Seventh Framework Programme (FP/2007-2013)/ERC Grant Agreement No. 306298. Y.C. acknowledges support from the Faculty of Engineering and Information Technologies, The University of Sydney, under the Faculty Research Cluster Program. R.K., B.S.F., Y.C., and W.L. acknowledge support from the Singaporean–German Researcher Mobility Scheme. The views expressed herein are those of the authors and are not necessarily those of the Faculty.

Received: April 28, 2016
Revised: July 6, 2016
Published online:

---

[1] T. Dürkop, S. A. Getty, E. Cobas, M. S. Fuhrer, *Nano Lett.* **2003**, *4*, 35.
[2] a) M. S. Dresselhaus, G. Dresselhaus, R. Saito, A. Jorio, *Phys. Rep.* **2005**, *409*, 47; b) H. Kataura, Y. Kumazawa, Y. Maniwa, I. Umezu, S. Suzuki, Y. Ohtsuka, Y. Achiba, *Synth. Metals* **1999**, *103*, 2555.
[3] M. Engel, K. E. Moore, A. Alam, S. Dehm, R. Krupke, B. S. Flavel, *ACS Nano* **2014**, *8*, 9324.
[4] D. D. Tune, F. Hennrich, S. Dehm, M. F. G. Klein, K. Glaser, A. Colsmann, J. G. Shapter, U. Lemmer, M. M. Kappes, R. Krupke, B. S. Flavel, *Adv. Energy Mater.* **2013**, *3*, 1091.
[5] D. J. Bindl, M. S. Arnold, *J. Phys. Chem. C* **2013**, *117*, 2390.
[6] D. D. Tune, J. G. Shapter, *Energy Environ. Sci.* **2013**, *6*, 2572.
[7] G. Dukovic, F. Wang, D. Song, M. Y. Sfeir, T. F. Heinz, L. E. Brus, *Nano Lett.* **2005**, *5*, 2314.
[8] R. B. Capaz, C. D. Spataru, S. Ismail-Beigi, S. G. Louie, *Phys. Rev. B* **2006**, *74*, 121401.
[9] V. Perebeinos, J. Tersoff, P. Avouris, *Phys. Rev. Lett.* **2004**, *92*, 257402.
[10] D. J. Bindl, M. Y. Wu, F. C. Prehn, M. S. Arnold, *Nano Lett.* **2011**, *11*, 455.
[11] C. D. Spataru, S. Ismail-Beigi, L. X. Benedict, S. G. Louie, *Phys. Rev. Lett.* **2004**, *92*, 077402.
[12] M. Pfohl, K. Glaser, J. Ludwig, D. D. Tune, S. Dehm, C. Kayser, A. Colsmann, R. Krupke, B. S. Flavel, unpublished.
[13] M. J. Shea, M. S. Arnold, *Appl. Phys. Lett.* **2013**, *102*, 243101.
[14] D. J. Bindl, M. J. Shea, M. S. Arnold, *Chem. Phys.* **2013**, *413*, 29.
[15] a) Y. Joo, G. J. Brady, M. J. Shea, M. B. Oviedo, C. Kanimozhi, S. K. Schmitt, B. M. Wong, M. S. Arnold, P. Gopalan, *ACS Nano* **2015**, *9*, 10203; b) I. Pochorovski, H. Wang, J. I. Feldblyum, X. Zhang, A. L. Antaris, Z. Bao, *J. Am. Chem. Soc.* **2015**, *137*, 4328; c) J. Han, Q. Ji, H. Li, G. Li, S. Qiu, H.-B. Li, Q. Zhang, H. Jin, Q. Li, J. Zhang, *Chem. Commun.* **2016**, *52*, 7683.
[16] A. F. Hebard, R. C. Haddon, R. M. Fleming, A. R. Kortan, *Appl. Phys. Lett.* **1991**, *59*, 2109.
[17] D. J. Bindl, N. S. Safron, M. S. Arnold, *ACS Nano* **2010**, *4*, 5657.
[18] H. Wang, G. I. Koleilat, P. Liu, G. Jiménez-Osés, Y.-C. Lai, M. Vosgueritchian, Y. Fang, S. Park, K. N. Houk, Z. Bao, *ACS Nano* **2014**, *8*, 2609.
[19] M. Bernardi, J. Lohrman, P. V. Kumar, A. Kirkeminde, N. Ferralis, J. C. Grossman, S. Ren, *ACS Nano* **2012**, *6*, 8896.
[20] C. M. Isborn, C. Tang, A. Martini, E. R. Johnson, A. Otero-de-la-Roza, V. C. Tung, *J. Phys. Chem. Lett.* **2013**, *4*, 2914.
[21] T. A. Shastry, S. C. Clark, A. J. E. Rowberg, K. A. Luck, K.-S. Chen, T. J. Marks, M. C. Hersam, unpublished.
[22] S. L. Guillot, K. S. Mistry, A. D. Avery, J. Richard, A.-M. Dowgiallo, P. F. Ndione, J. van de Lagemaat, M. O. Reese, J. L. Blackburn, *Nanoscale* **2015**, *7*, 6556.
[23] a) S. Cambré, B. Schoeters, S. Luyckx, E. Goovaerts, W. Wenseleers, *Phys. Rev. Lett.* **2010**, *104*, 207401; b) J. A. Fagan, J. Y. Huh, J. R. Simpson, J. L. Blackburn, J. M. Holt, B. A. Larsen, A. R. H. Walker, *ACS Nano* **2011**, *5*, 3943.
[24] C. G. Malmberg, A. A. Maryott, *J. Res. Natl. Bur. Stand.* **1956**, *56*, 1.
[25] S. Cambré, S. M. Santos, W. Wenseleers, A. R. T. Nugraha, R. Saito, L. Cognet, B. Lounis, *ACS Nano* **2012**, *6*, 2649.
[26] V. Barone, J. E. Peralta, J. Uddin, G. E. Scuseria, *J. Chem. Phys.* **2006**, *124*, 024709.
[27] E. L. Shirley, S. G. Louie, *Phys. Rev. Lett.* **1993**, *71*, 133.
[28] R. D. Mehlenbacher, J. Wang, N. M. Kearns, M. J. Shea, J. T. Flach, T. J. McDonough, M.-Y. Wu, M. S. Arnold, M. T. Zanni, *J. Phys. Chem. Lett.* **2016**, *7*, 2024.
[29] A.-M. Dowgiallo, K. S. Mistry, J. C. Johnson, J. L. Blackburn, *ACS Nano* **2014**, *8*, 8573.
[30] R. Ihly, K. S. Mistry, A. J. Ferguson, T. T. Clikeman, B. W. Larson, O. Reid, O. V. Boltalina, S. H. Strauss, G. Rumbles, J. L. Blackburn, *Nat. Chem.* **2016**, *8*, 603.
[31] J. Jiang, R. Saito, G. G. Samsonidze, A. Jorio, S. G. Chou, G. Dresselhaus, M. S. Dresselhaus, *Phys. Rev. B* **2007**, *75*, 035407.
[32] D. J. Bindl, A. J. Ferguson, M.-Y. Wu, N. Kopidakis, J. L. Blackburn, M. S. Arnold, *J. Phys. Chem. Lett.* **2013**, *4*, 3550.
[33] A. J. Ferguson, A.-M. Dowgiallo, D. J. Bindl, K. S. Mistry, O. G. Reid, N. Kopidakis, M. S. Arnold, J. L. Blackburn, *Phys. Rev. B* **2015**, *91*, 245311.
[34] R. M. Jain, R. Howden, K. Tvrdy, S. Shimizu, A. J. Hilmer, T. P. McNicholas, K. K. Gleason, M. S. Strano, *Adv. Mater.* **2012**, *24*, 4436.

[35] J. J. Crochet, J. D. Sau, J. G. Duque, S. K. Doorn, M. L. Cohen, *ACS Nano* **2011**, *5*, 2611.

[36] M. S. Dresselhaus, G. Dresselhaus, P. C. Eklund, in *Science of Fullerenes and Carbon Nanotubes*, Academic Press, San Diego, **1996**, 464.

[37] J. Y. Kim, T. Kim, J. W. Suk, H. Chou, J. H. Jang, J. H. Lee, I. N. Kholmanov, D. Akinwande, R. S. Ruoff, *Small* **2014**, *10*, 3405.

[38] B. W. Larson, J. B. Whitaker, X.-B. Wang, A. A. Popov, G. Rumbles, N. Kopidakis, S. H. Strauss, O. V. Boltalina, *J. Phys. Chem. C* **2013**, *117*, 14958.

[39] F. B. Kooistra, V. D. Mihailetchi, L. M. Popescu, D. Kronholm, P. W. M. Blom, J. C. Hummelen, *Chem. Mater.* **2006**, *18*, 3068.

[40] N. K. Elumalai, A. Uddin, *Energy Environ. Sci.* **2016**, *9*, 391.

[41] S. Rühle, *Solar Energy* **2016**, *130*, 139.

[42] Y. Yang, F. Arias, L. Echegoyen, L. P. F. Chibante, S. Flanagan, A. Robertson, L. J. Wilson, *J. Am. Chem. Soc.* **1995**, *117*, 7801.

[43] A. J. Hilmer, K. Tvrdy, J. Zhang, M. S. Strano, *J. Am. Chem. Soc.* **2013**, *135*, 11901.

[44] L. Lüer, J. Crochet, T. Hertel, G. Cerullo, G. Lanzani, *ACS Nano* **2010**, *4*, 4265.

[45] R. D. Mehlenbacher, T. J. McDonough, M. Grechko, M.-Y. Wu, M. S. Arnold, M. T. Zanni, *Nat. Commun.* **2015**, *6*, 6732.

[46] T. Ando, *J. Phys. Soc. Jpn.* **2004**, *73*, 3351.

[47] J. Park, O. G. Reid, J. L. Blackburn, G. Rumbles, *Nat. Commun.* **2015**, *6*, 8809.

[48] B. S. Flavel, K. E. Moore, M. Pfohl, M. M. Kappes, F. Hennrich, *ACS Nano* **2014**, *8*, 1817.

[49] a) H. Wang, B. Wang, X.-Y. Quek, L. Wei, J. Zhao, L.-J. Li, M. B. Chan-Park, Y. Yang, Y. Chen, *J. Am. Chem. Soc.* **2010**, *132*, 16747; b) H. Wang, L. Wei, F. Ren, Q. Wang, L. D. Pfefferle, G. L. Haller, Y. Chen, *ACS Nano* **2013**, *7*, 614.

[50] K. E. Moore, M. Pfohl, D. D. Tune, F. Hennrich, S. Dehm, V. S. K. Chakradhanula, C. Kübel, R. Krupke, B. S. Flavel, *ACS Nano* **2015**, *9*, 3849.

[51] M. Uda, *Jpn. J. Appl. Phys.* **1985**, *24*, 284.

[52] S. M. Bachilo, M. S. Strano, C. Kittrell, R. H. Hauge, R. E. Smalley, R. B. Weisman, *Science* **2002**, *298*, 2361.

[53] S. Cambré, W. Wenseleers, *Angew. Chem. Int. Ed.* **2011**, *50*, 2764.

[54] a) M. S. Dresselhaus, G. Dresselhaus, R. Saito, *Carbon* **1995**, *33*, 883; b) R. B. Pipes, S. Frankland, P. Hubert, E. Saether, *Comp. Sci. Technol.* **2003**, *63*, 1349.

[55] N. Nair, M. L. Usrey, W.-J. Kim, R. D. Braatz, M. S. Strano, *Anal. Chem.* **2006**, *78*, 7689.

[56] V. Perebeinos, J. Tersoff, P. Avouris, *Phys. Rev. Lett.* **2005**, *94*, 027402.

[57] Y. Tian, H. Jiang, I. V. Anoshkin, L. J. I. Kauppinen, K. Mustonen, A. G. Nasibulin, E. I. Kauppinen, *RSC Adv.* **2015**, *5*, 102974.

[58] a) M. J. O'Connell, S. M. Bachilo, C. B. Huffman, V. C. Moore, M. S. Strano, E. H. Haroz, K. L. Rialon, P. J. Boul, W. H. Noon, C. Kittrell, J. Ma, R. H. Hauge, R. B. Weisman, R. E. Smalley, *Science* **2002**, *297*, 593; b) S. Reich, C. Thomsen, P. Ordejón, *Phys. Rev. B* **2002**, *65*, 155411.

[59] a) G. F. Burkhard, E. T. Hoke, M. D. McGehee, *Adv. Mater.* **2010**, *22*, 3293; b) L. A. A. Pettersson, L. S. Roman, O. Inganäs, *J. Appl. Phys.* **1999**, *86*, 487.

– This page intentionally left blank –

5. Summary

The main topic and motivation of this thesis was the fabrication and investigation of polymer-free carbon nanotube solar cells. But prior to analyzing nanotube solutions and fabricating organic solar cells out of nanotube films, the necessary semiconducting and chirality enriched nanotube solutions needed to be prepared. In order to accomplish this task, raw nanotube powder was suspended in an aqueous solution of 2 wt% SDS. Employing gel permeation chromatography (GPC), the nanotubes adsorbed on the gel and were selectively washed off with 1 wt% SC. By controlling the SDS concentration and temperature of the gel and eluents, chirality pure solutions of (6,5), highly enriched solutions of (7,5), chirality enriched (7,6) and dispersions with increasing average nanotube diameter were obtained. PLE and UV/vis measurements were used to analyze the (n,m) distribution and semiconducting purity of the collected solutions. Especially for nanotube solution with many different chiralities, a reliable tool for deconvolution absorption spectra into individual (n,m) contributions was necessary. Throughout this thesis, a MATLAB® based tool was developed to subtract the background from UV/vis measurements, fit either S_{11} or S_{22} transitions or the entire spectrum with different line profiles and include metallic nanotubes in the fit. It was demonstrated in Chapter 2 that special caution has to be paid to the background subtraction. Changing the shape of the background can influence the spectral weight distribution and consequently alter the concentration of individual (n,m) SWCNTs for the same solution. Furthermore, a violation of the constraint that the S_{11} intensities have to be larger than their S_{22} counterparts (due to the larger absorption cross section) can be an indication of doping (shift of the Fermi level into the first optical transitions and therefore a reduction in intensity). The proposed constraint of fitting SWCNT films based on the spectral weight distribution obtained for previously fitted nanotube solutions proofed itself to be of great importance for the analysis of EQE spectra and consequently for the analysis of the nanotube diameter cut-off in SWCNT:C_{60} solar cells.

Having sorted large amounts of (6,5) SWCNTs and verified their high semiconducting purity, EDSA was used to manufacture morphologically comparable, thin and sparse films over large areas within 6 hours; resulting in active solar cell areas of 0.105 cm^2 compared to 0.101 cm^2 for planar polymer-wrapped SWCNT solar cells.(1) By carefully adjusting the layer thicknesses of PEDOT:PSS and C_{60}, IQE values of around 86 % were obtained at the S_{11} absorption of (6,5) proofing that polymer-free SWCNTs can be of equal efficiency in terms of light conversion as their polymer-wrapped counterparts. The performance limiting factors were determined to be the low light absorption (~2.4 %) and recombination due to trap charges which could be an indication of minor residues of metallic and/or large diameter nanotubes in the solution and film; a drawback compared to polymer-wrapped nanotube films that prevented the use of thicker and denser films that could have increased the light absorption. However, one advantage of sparse nanotube films was the applicability of transfer matrix calculations without having to measure the complex refractive index for different (n,m) chiralities. TMCs prooved to be a powerful and reliable tool that was used to modulate light absorption via individual or both nanotube transitions. A possible extension of these calculations could be in tandem solar cells were different transitions are optimized in each sub-cell.

Being able to manufacture highly efficient and optically almost transparent polymer-free SWCNT films, the question was raised whether or not transparent solar cells from large diameter tubes could be prepared. Solar cells employing nanotube films with increasing average diameter were prepared to test this hypothesis. By carefully fitting EQE spectra based on the SWCNT film fits that had the same spectral (n,m) distribution as in solution, the largest diameter nanotube contributing to the current generation was found to be (8,6) with a diameter of 0.95 nm. In order to employ larger diameter SWCNTs in solar cells two different strategies were proposed: first, the thickness of C_{60} should be changed in order to excite the nanotubes' second transition (LUMO offset to C_{60} is sufficient). Second, a different acceptor material should be used. Exciting the second transition of large diameter nanotubes (1.2 to 1.5 nm) did not result in a measurable current in EQE measurements. Therefore the exciton was assumed to relax faster to S_{11}, where the LUMO offset is too small to dissociate the exciton, than it is dissociated at the C_{60} interface. Consequently, the S_{11} position of a nanotube determines whether an exciton can be dissociated or not. Calculations of the net driving energy (LUMO difference of nanotube and acceptor minus binding energy of an exciton) for different acceptors, including C_{60} and higher fullerenes, indicated that it should be possible to split excitons and collect charge carriers from large diameter SWCNTs. Comparing the absorption of C_{60} and higher fullerenes, the onset of absorption is successively shifted to larger wavelengths for an increasing number of carbon atoms.(2) Therefore, transparent solar cells employing large diameter nanotubes in combination with these higher fullerenes are unlikely to be possible. Instead, semi-transparent solar cells could be realizable with nanotubes absorbing exclusively in the infrared. Another finding of this study was the fact, that different acceptors are needed for different diameter ranges of nanotubes. According to the LUMO offsets between different acceptors and the nanotubes, C_{60} is suitable for small diameter nanotubes up to 0.95 nm, C_{84} could be suitable for diameters above 1.4 nm and C_{76} or C_{78} for the diameter range in-between. A possible realization of these design strategies could be in a tandem solar cell employing nanotube films with increasing diameter and fullerenes with higher order. In addition, the electric field could be tuned such that the peak position of the intensity is maximized at the nanotubes S_{11} absorption for each sub-cell.

References

(1) S. L. Guillot, K. S. Mistry, A. D. Avery, J. Richard, A. M. Dowgiallo, P. F. Ndione, J. van de Lagemaat, M. O. Reese, J. L. Blackburn, *Nanoscale* **2015**, 7, 6556.

(2) F. Diederich, R. L. Whetten, *Accounts of Chemical Research* **1992**, 25, 119.

– This page intentionally left blank –

6. Outlook

In order to deepen the current understanding of SWCNT solar cells and increase the device performance several strategies could be pursued of which the most promising ones are listed here.

One way of gaining a deeper understanding of the transfer mechanism at the interface of carbon nanotubes and an acceptor molecule are transient absorbance (TA) measurement.(1) Using TA measurements, laser pulses are used to excite and probe the sample with a time resolution of several fs (10^{-15} s). It is therefore possible to probe the generation, transfer and decay of excitons and charge carriers at different time scales. TA measurements could especially be helpful for the investigation of the time scales of the charge transfer from S_{22} to an acceptor in order to understand the device properties at the SWCNT diameter cut-off even better.

A limiting factor of the solar cell device performance was found to be the low light absorption and minor contents of metallic and large diameter SWCNTs. Combining polymer sorting with a semiconducting purity of 99.99 % and doctor blading yielding dense, flat films Shea et al. fabricated SWCNT:C_{60} solar cells with 1 % efficiency.(2) Further increase in film thickness are not expected to increase the efficiency due to the limited exciton diffusion length of around 8 nm in polymer wrapped SWCNTs.(3) However, two different approaches to increase device performance are possible: first, building tandem solar cells from chirality enriched species where the acceptor material is adjusted to fit the LUMO level of the SWCNTs. In order to maximize the light absorption at the distinct absorption of each chirality in the sub-cells, transfer matrix calculations are needed employing the complex refractive index of the SWCNTs. Using tandem architectures of heterojunctions in combination with an optimized light distribution, an absolute upper limit of device performance could be derived. The second approach is focused on preparing porous 3D structures of SWCNTs in order to fabricate a bulk heterojunction (BHJ) solar cell. Unlike the work of the Hersam group,(4) where SWCNTs contribute only little to the overall current generation, a well manufactured device structure with engineered pore size could exploit the high intrinsic mobility of the SWCNTs along the tubes without the need of exciton hopping. A possible realization of such device architectures could be aerogels. Ye et al. fabricated a SWCNT aerogel with the aids of PMMA resulting in increased device efficiencies of 1.7 %.(5) However, possible residues of PMMA around the nanotubes might have reduced the exciton diffusion length and prevented the realization of even higher device efficiencies. Clearly, this is a promising start but more effort and time needs to be spent in order to realize highly efficient, BHJ SWCNT solar cells.

A different approach to increase device performance could be the usage of dyes, like zinc phthalocyanine (ZnPc). ZnPc in combination with C_{60} was demonstrated to yield device efficiencies larger than 2 %.(6) However, preliminary experiments were performed, placing the dye in-between the interface of SWCNT and C_{60}. If the dye-concentration is too large, the current signal from the nanotubes in EQE is vanishing. Most likely the dye is blocking the contact sites of SWCNTs and C_{60}. A different approach could be the filling of large diameter nanotubes with the dye molecule as demonstrated by Cambre et al.(7) Using an appropriate acceptor that offers a sufficient LUMO offset to the large diameter SWCNTs (e.g. C_{84}) this material combination could offer a large, tunable absorption in the visible and infrared.

References

(1) A.-M. Dowgiallo, K. S. Mistry, J. C. Johnson, J. L. Blackburn, *ACS Nano* **2014**, 8, 8573.

(2) M. J. Shea, M. S. Arnold, *Applied Physics Letters* **2013**, 102, 243101.

(3) D. J. Bindl, A. J. Ferguson, M.-Y. Wu, N. Kopidakis, J. L. Blackburn, M. S. Arnold, *The Journal of Physical Chemistry Letters* **2013**, 4, 3550.

(4) M. Gong, T. A. Shastry, Q. Cui, R. R. Kohlmeyer, K. A. Luck, A. Rowberg, T. J. Marks, M. F. Durstock, H. Zhao, M. C. Hersam, S. Ren, *ACS Applied Materials & Interfaces* **2015**, 7, 7428; M. Gong, T. A. Shastry, Y. Xie, M. Bernardi, D. Jasion, K. A. Luck, T. J. Marks, J. C. Grossman, S. Ren, M. C. Hersam, *Nano Letters* **2014**, 14, 5308; T. A. Shastry, S. C. Clark, A. J. E. Rowberg, K. A. Luck, K.-S. Chen, T. J. Marks, M. C. Hersam, *Advanced Energy Materials* **2016**, 6, 1501466.

(5) Y. Ye, D. J. Bindl, R. M. Jacobberger, M.-Y. Wu, S. S. Roy, M. S. Arnold, *Small* **2014**, 10, 3299.

(6) W. Tress, S. Pfuetzner, K. Leo, M. Riede, *Journal of Photonics for Energy* **2011**, 1, 011114.

(7) S. Cambré, J. Campo, C. Beirnaert, C. Verlackt, P. Cool, W. Wenseleers, *Nat Nano* **2015**, 10, 248.

– This page intentionally left blank –

7. Appendix

The following sub-chapters contain additional material, e.g. derivations, measurements or explanations, which might be helpful in understanding some passages in Chapters 1 – 4. The first sub-section is intended to give a comprehensive derivation of the transfer matrix formalism, including the basic equations for the propagation of light and the laws of reflection and transmission.

The numbering of Equations and Figures in each sub-section starts from 1 in order to be consistent with their reference in the papers reproduced in Chapters 2 – 4.

– This page intentionally left blank –

7.1 Derivation of Transfer Matrix Calculations

7.1.1 *Deriving the Wave Equation*

In order to derive the necessary equations describing the distribution and intensity of light in a solar cell stack, the wave equations of light and light matter interactions have to be derived and described. The starting point of deriving the wave equation of light is the famous Maxwell equations. A short revision of the mathematical operators “gradient” (∇), “divergence” (∇ ·) and “curl” (∇x) is given in Equations 1 to 3:

Gradient: $$\nabla \mathbf{F} = \mathrm{grad}(\mathbf{F}) = \begin{pmatrix} \frac{\partial F_1}{\partial x_1} \\ \frac{\partial F_2}{\partial x_2} \\ \frac{\partial F_3}{\partial x_3} \end{pmatrix} = \frac{\partial F_1}{\partial x_1}\mathbf{e}_1 + \frac{\partial F_2}{\partial x_2}\mathbf{e}_2 + \frac{\partial F_3}{\partial x_3}\mathbf{e}_3 \tag{1}$$

Divergence: $$\nabla \cdot \mathbf{F} = \mathrm{div}(\mathbf{F}) = \frac{\partial F_1}{\partial x_1} + \frac{\partial F_2}{\partial x_2} + \frac{\partial F_3}{\partial x_3} \tag{2}$$

Curl: $$\nabla \times \mathbf{F} = \mathrm{rot}(\mathbf{F}) = \begin{pmatrix} \frac{\partial F_3}{\partial x_2} - \frac{\partial F_2}{\partial x_3} \\ \frac{\partial F_1}{\partial x_3} - \frac{\partial F_3}{\partial x_1} \\ \frac{\partial F_2}{\partial x_1} - \frac{\partial F_1}{\partial x_2} \end{pmatrix} =$$

$$= \left(\frac{\partial F_3}{\partial x_2} - \frac{\partial F_2}{\partial x_3}\right)\mathbf{e}_1 + \left(\frac{\partial F_1}{\partial x_3} - \frac{\partial F_3}{\partial x_1}\right)\mathbf{e}_2 + \left(\frac{\partial F_2}{\partial x_1} - \frac{\partial F_1}{\partial x_2}\right)\mathbf{e}_3 \tag{3}$$

In Equation 1 to 3, $\mathbf{e}_1$ to $\mathbf{e}_3$ represent the unit vectors in a three dimensional coordinate system. Starting with the Maxwell equations:

$$\nabla \cdot \boldsymbol{E} = \frac{\rho}{\varepsilon_0} \tag{4}$$

$$\nabla \cdot \mathbf{B} = 0 \tag{5}$$

$$\nabla \times \mathbf{E} = -\frac{\partial \mathbf{B}}{\partial t} \tag{6}$$

$$\nabla \times \mathbf{B} = \mu_0 \mathbf{j} + \mu_0 \varepsilon_0 \frac{\partial \mathbf{E}}{\partial t} \tag{7}$$

In Equation 4, ρ is the charge density that creates the electric field ***E***. In the same equation, ε_0 is the vacuum permittivity. Equation 5 can be read such, that the magnetic field ***B*** is source free or, in other words, there are no magnetic monopoles. Equation 6 describes how a changing magnetic flux induces a circulating electric field. A similar relation as for Equation 6 can be found for changes in the electric field that cause a circulating magnetic field, as described in Equation 7. Hereby, μ_0 is the vacuum permeability and ***j*** is the current density.

Assuming there are no free charges (ρ=0) or currents ($\boldsymbol{j}$=0), e.g. in vacuum, Equation 4 and Equation 7 can be rewritten:

$$\nabla \cdot \boldsymbol{E} = 0 \tag{4b}$$

$$\nabla \times \mathbf{B} = \mu_0 \varepsilon_0 \frac{\partial \mathbf{E}}{\partial \mathrm{t}} \tag{7b}$$

In order to derive an expression for the wave equation, the curl of Equation 6 is calculated. Applying the curl operation on the left hand side of Equation 6 and applying Equation 4b, the following expression is derived:

$$\nabla \times (\nabla \times \mathbf{E}) = \nabla (\nabla \cdot \mathbf{E}) - \Delta \mathbf{E} = \nabla(0) - \Delta \mathbf{E} = -\Delta \mathbf{E} \tag{6a}$$

With $\Delta = \frac{\partial^2}{\partial \mathrm{x}^2} + \frac{\partial^2}{\partial \mathrm{y}^2} + \frac{\partial^2}{\partial \mathrm{z}^2}$ being the Laplace operator for the Cartesian coordinate system. Applying the curl operation on the right hand side of Equation 6 and employing Equation 7b, it follows:

$$\nabla \times \left(-\frac{\partial \mathbf{B}}{\partial \mathrm{t}}\right) = -\frac{\partial}{\partial \mathrm{t}} (\nabla \times \mathbf{B}) = -\mu_0 \varepsilon_0 \frac{\partial^2 \boldsymbol{E}}{\partial t^2} \tag{6b}$$

Recombining Equation 6a and 6b, the following expression for the electric field is given:

$$\frac{\partial^2 \boldsymbol{E}}{\partial t^2} = v^2 \Delta \boldsymbol{E} \tag{8}$$

with $v^2 = \frac{1}{\mu_0 \varepsilon_0}$ being the square of the velocity. Equation 8 represents a homogenous wave equation. Each component of ***E*** in x-, y- and z-direction, has its own wave equation. For simplicity, the following derivation will focus on only one component in space.

7.1.2 *Solving the Wave Equation*

It is well known, that equations of the form presented in Equation 8 can be solved with a sinusoidal approach. Using wave number k that propagates in direction x with an amplitude E_0:

$$E(x,t)|_{t=0} = E(x) = E_0 \cdot \sin(kx) \tag{9}$$

A propagating wave in time is described by replacing x with $(x - v \cdot t)$:

$$E(x,t) = E_0 \cdot \sin(k(x - v \cdot t)) \tag{10}$$

Employing the relationship of k, the period τ, the frequency f and the angular frequency ω:

$$k = \frac{2\pi}{\lambda} \tag{11}$$

$$\tau = \frac{\lambda}{v} \tag{12}$$

$$f = \frac{1}{\tau} \tag{13}$$

$$\omega = \frac{2\pi}{\tau} = 2\pi f \tag{14}$$

Equation (10) can be rewritten by using the following relation:

$$v = \frac{\lambda}{\tau} = \lambda \cdot f = \frac{\lambda \cdot \omega}{2\pi} = \frac{\omega}{k} \tag{15}$$

By inserting the expression derived in Equation 15 in Equation 10, the wave equation is expressed in terms of the angular frequency instead of velocity:

$$E(x,t) = E_0 \cdot \sin(kx - k \cdot vt) = E_0 \cdot \sin(kx - \omega t) \tag{16}$$

A relation between the electric field E and the magnetic field B can be derived by inserting Equation (16) in Equation (6):

$$\nabla \times E = \nabla \times (E_0 \cdot \sin(kx - \omega t)) = E_0 \cdot k \cdot \cos(kx - \omega t) = -\frac{\partial B}{\partial t} \tag{17}$$

Integrating both sides in Equation 17 with respect to time yields:

$$B = -\int E_0 \cdot k \cdot \cos(kx - \omega t)\, dt = -E_0 \cdot k \cdot \left(-\frac{1}{\omega}\right) \cdot \sin(kx - \omega t) = \frac{E_0}{v} \cdot \sin(kx - \omega t) \tag{18}$$

Comparing Equation 18 with Equation 16 it is obvious, that:

$$E(x,t) = B(x,t) \cdot v \tag{19}$$

With $v = c$, the speed of light, in vacuum.

In the general case the phase (kx - ωt) is unknown. In order to account for this the starting phase ε is added. For the ease of derivation of the transfer matrix equations, one can rewrite the sine to a cosine function by:

$$E(x,t) = E_0 \cdot \cos\left(kx - \omega t - \frac{\pi}{2}\right) = E_0 \cdot \cos(kx - \omega t + \varepsilon) \tag{20}$$

Using Euler's equation:

$$e^{i\theta} = \cos(\theta) + i\sin(\theta) \tag{21}$$

Equation (20) becomes:

$$E(x,t) = Re(E_0 \cdot e^{i(kx-wt+\varepsilon)}) \tag{22}$$

In order to link the expression from Equation 22 to the actual speed of light in a medium, the complex refractive index ñ has to be used. The complex refractive index $ñ = (n + i \cdot \kappa)$ is defined as the reduction of velocity of the speed of light:

$$ñ = \frac{c}{v} \tag{23}$$

Using the relation employed in Equation (15), Equation (23) can be rewritten to yield an expression for the complex wave number $\tilde{k}$:

$$ñ = \frac{c}{\omega/_{\tilde{k}}} <=> \tilde{k} = \frac{ñ \cdot \omega}{c} = \frac{ñ}{c} \cdot \frac{2\pi \cdot c}{\lambda} = \frac{2\pi}{\lambda}(n + i \cdot \kappa) \tag{24}$$

Inserting the relation derived in Equation (24) back into Equation (22), the electric field can be described as a function of the material parameters n and κ:

$$\begin{aligned} E(x,t) = Re\left(E_0 \cdot e^{i\left(\frac{2\pi}{\lambda}(n+i\cdot\kappa)x-wt+\varepsilon\right)}\right) &= Re\left(E_0 \cdot e^{i\left(\frac{2\pi}{\lambda}nx-wt+\varepsilon\right)-\frac{2\pi\kappa}{\lambda}x}\right) = \\ &= E_0 \cdot e^{-\frac{2\pi\kappa}{\lambda}x} Re\left(e^{i\left(\frac{2\pi}{\lambda}nx-wt+\varepsilon\right)}\right) \end{aligned} \tag{25}$$

The expression $E_0 \cdot e^{-\frac{2\pi\kappa}{\lambda}x}$ describes the damping of the electric field intensity while the real part of $e^{i\left(\frac{2\pi}{\lambda}nx-wt+\varepsilon\right)}$ describes refraction in the medium.

7.1.3 *Light Intensity Derivation*

An important concept for deriving the light intensity is described by Poynting's Theorem, which describes the energy transport of an electromagnetic wave.(1) Assuming a plane wave is travelling through a cylinder with an area A at a velocity c within a time dt. The energy u is distributed continuously across the wave and has two components: one from the electric and one from the magnetic field of the wave (according to Equations 6 and 7, a changing electric/magnetic field induces a magnetic/electric field, respectively). The Poynting vector S therefore can be described as energy in a certain volume that is transported through an area in a certain time and has the unit Watts/m^2:

$$S = \frac{u \cdot c \cdot \Delta t \cdot A}{\Delta t \cdot A} = u \cdot c \tag{26}$$

The energy of an electric field can be written as:(2)

$$u_E = \frac{1}{2} \cdot \varepsilon_0 \cdot E^2 \tag{27}$$

The energy stored in a magnetic field can be written as:(2)

$$u_B = \frac{1}{2} \cdot \frac{1}{\mu_0} \cdot B^2 \tag{28}$$

Employing the expression found in Equation 8, $c^2 = \frac{1}{\varepsilon_0 \cdot \mu_0}$ and Equation 19, it can be shown that the energy stored in an electric field is equal to the energy stored in a magnetic field. The overall energy of an electromagnetic wave u can therefore be written as:

$$u = u_E + u_B = \varepsilon_0 \cdot E^2 = \frac{1}{\mu_0} \cdot B^2 = \frac{1}{\mu_0 \cdot c} \cdot E \cdot B \tag{29}$$

Therefore the Equation 26 can be rewritten to:

$$S = c \cdot \frac{1}{\mu_0 \cdot c} \cdot E \cdot B = \frac{1}{\mu_0} \cdot E \cdot B \tag{30}$$

Written in terms of $\boldsymbol{E}$ and $\boldsymbol{B}$ being vectors, the Poynting vector $\boldsymbol{S}$ reads as follows:

$$\boldsymbol{S} = \boldsymbol{E} \times \frac{\boldsymbol{B}}{\mu_0} \tag{31}$$

Due to the short wavelengths of light (hundreds of nm) and the resulting frequencies (according to Equation 12 and 13) in the range of 10^{15} Hz, the time averaged values, denoted as $\langle \boldsymbol{S} \rangle_T$, of the Poynting vector, also called “Intensity” I are of interest. Time averaging the square of a complex function is rather straight forward by recalling the following relation:(3)

$$sin^2(\theta) + cos^2(\theta) = 1 \tag{32}$$

Over a complete cycle, the average of sin^2 and cos^2 are the same and therefore:

$$\langle sin^2 \rangle_T = \langle cos^2 \rangle_T = \frac{1}{2} \tag{33}$$

Considering again a planar wave in x-direction, the intensity I can be described as:

$$I = \langle S \rangle_T = \langle \frac{1}{\mu_0} \cdot E \cdot B \rangle_T \tag{34}$$

Employing Equation 25 and the relation formulated in Equation 19, Equation 34 can be formulated as follows:

$$I = \langle S \rangle_T = \langle \frac{1}{\mu_0} \cdot E \cdot \frac{E}{v} \rangle_T = \frac{1}{v \cdot \mu_0} \langle E^2 \rangle = \frac{1}{v \cdot \mu_0} \langle E_0^2 \cdot e^{-\frac{4\pi\kappa}{\lambda}x} Re\left(e^{2i\left(\frac{2\pi}{\lambda}nx - wt + \varepsilon\right)}\right) \rangle_T =$$

$$= \frac{1}{v \cdot \mu_0} \cdot E_0^2 \cdot e^{-\frac{4\pi\kappa}{\lambda}x} \langle Re\left(e^{2i\left(\frac{2\pi}{\lambda}nx - wt + \varepsilon\right)}\right) \rangle_T \tag{35}$$

Using the relation formulated in Equation 33, Equation 35 can be simplified to:

$$I = \langle S \rangle_T = \frac{1}{2 \cdot v \cdot \mu_0} \cdot E_0^2 \cdot e^{-\frac{4\pi\kappa}{\lambda}x} \tag{36}$$

The velocity v in Equation 36 can be replaced with the definition of the refractive index n of a medium:(4)

$$v = \frac{c}{n} \tag{37}$$

The intensity can therefore be expressed as a function of the refractive index n and κ:

$$I = \langle S \rangle_T = \frac{1}{2 \cdot c \cdot \mu_0} \cdot n \cdot E_0^2 \cdot e^{-\frac{4\pi\kappa}{\lambda}x} = \frac{1}{2} \cdot \varepsilon_0 \cdot c \cdot n \cdot E_0^2 \cdot e^{-\frac{4\pi\kappa}{\lambda}x} \tag{38}$$

Comparing Equation 38 to the formulation of the Beer-Lambert law, which describes the reduction of intensity due to absorption in the respective material:

$$I = I_0 \cdot e^{-\alpha \cdot d} \tag{39}$$

Where I_0 is the incoming light intensity, d the thickness of the material and α the absorption coefficient, it is apparent that the absorption coefficient can be described as:

$$\alpha = \frac{4\pi\kappa}{\lambda} \tag{40}$$

And the incoming light intensity I_0 as:

$$I_0 = \frac{1}{2} \cdot \varepsilon_0 \cdot c \cdot n \cdot E_0^2 \tag{41}$$

For solar cell applications, I_0 can be regarded as the AM1.5G solar irradiation if n=1. The conservation of energy Q(x) or the time averaged local energy flow absorption per time at the point x can be described as:

$$Q(x) = \langle -\nabla S \rangle_T \tag{42}$$

Differentiating S with respect to x and keeping in mind that the time average of sin(ωt) and cos(ωt) equals zero, the following expression for Q(x) is deduced, assuming $cc = \frac{2\pi}{\lambda}nx - wt + \varepsilon$:

$$\begin{aligned} Q(x) &= \langle -\nabla \left(\frac{1}{v \cdot \mu_0} \cdot E_0^2 \cdot e^{-\frac{4\pi\kappa}{\lambda}x} \cdot Re\left(e^{2i(cc)}\right) \right) \rangle_T = \\ &= \langle -\frac{1}{v \cdot \mu_0} \cdot E_0^2 \cdot \left(-\frac{4\pi\kappa}{\lambda} \cdot e^{-\frac{4\pi\kappa}{\lambda}x} \cdot Re\left(e^{2i(cc)}\right) - \left(e^{-\frac{4\pi\kappa}{\lambda}x} \cdot cos(cc) \cdot sin(cc) \cdot \frac{2\pi}{\lambda} n \right) \right) \rangle_T = \\ &= \frac{1}{v \cdot \mu_0} \cdot \frac{4\pi\kappa}{\lambda} \cdot E_0^2 \cdot e^{-\frac{4\pi\kappa}{\lambda}x} \cdot \langle Re\left(e^{2i(cc)}\right) - \left(e^{-\frac{4\pi\kappa}{\lambda}x} \cdot cos(cc) \cdot sin(cc) \cdot \frac{2\pi}{\lambda} n \right) \rangle_T = \\ &= \frac{1}{2} \cdot c \cdot \varepsilon_0 \cdot n \cdot \alpha \cdot E_0^2 \cdot e^{-\frac{4\pi\kappa}{\lambda}x} \end{aligned} \tag{43}$$

7.1.4 *Fresnel Equations*

In general, if the angle of incidence is not normal, one has to distinguish two different cases: the electric field is normal to the plane of incidence or parallel. Following the derivation from Hecht et al.,(5) the unit vector û, the electric and magnetic field $\boldsymbol{E}$ and $\boldsymbol{B}$ follow:

$$\hat{u} \times \boldsymbol{E} = v\boldsymbol{B} \tag{44}$$

and $\hat{u} \cdot \boldsymbol{E} = 0$. In order to derive relations for the reflected and transmitted electric field one has to understand the boundary conditions for electric fields at interfaces first. Applying Faraday's law:(2)

$$\oint_C \boldsymbol{E} \cdot dl = -\frac{\partial}{\partial t} \int_S \boldsymbol{B} \cdot \hat{\boldsymbol{n}}\, da \tag{45}$$

to a rectangle depictured in Figure 1, and assuming the rectangle is small enough that the fields on either side of the half rectangle are uniform, the left hand side of Equation 45 equals:

$$\oint \boldsymbol{E} \cdot dl = E_{1\perp} l_1 + E_{1\parallel} d - E_{1\perp} l_1 - E_{2\perp} l_2 - E_{2\parallel} d + E_{2\perp} l_2 = d(E_{1\parallel} - E_{2\parallel}) \tag{46}$$

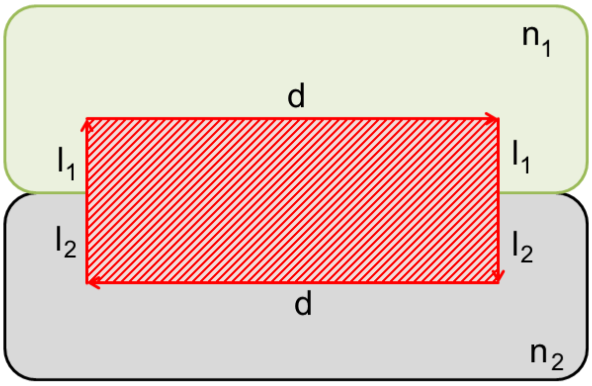

Figure 1. Interface of two different materials. Adapted from (2).

If the rectangle is shrunk by reducing l_1 and l_2 to 0, the surface of the rectangle and therefore the right hand side of Faraday's law equal 0. Therefore the parallel components of the electric field are the same at any material interface:

$$E_{1\parallel} = E_{2\parallel} \tag{47}$$

Considering the situation depictured in Figure 2b, the electric field is parallel to the surface. The incident (index i) and reflected (index r) light travels in the same medium. Therefore, the relation between the incident, reflected and transmitted electric field at the interface of the two materials can be written as:

$$\boldsymbol{E}_{0i} + \boldsymbol{E}_{0r} = \boldsymbol{E}_{0t} \tag{48}$$

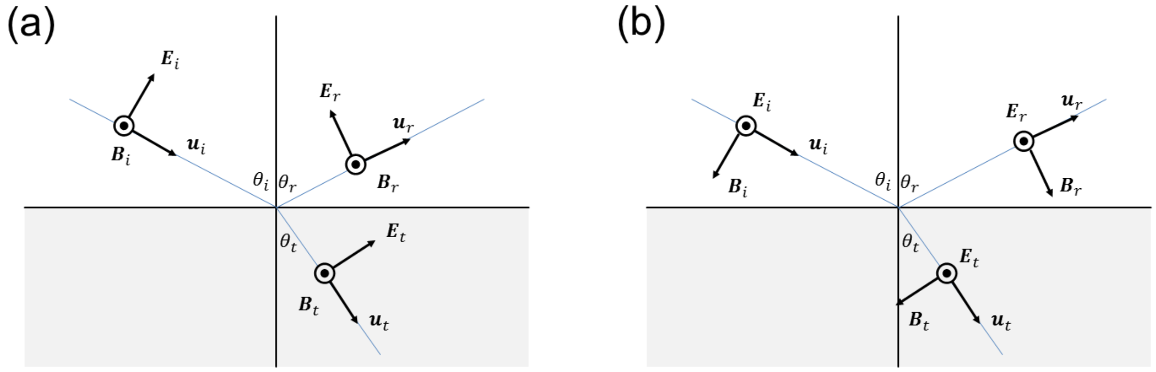

Figure 2. a) Incoming light with the magnetic field B being parallel to the surface. b) Incoming light with the electric field E being parallel to the surface. Adapted from (5).

A similar relation as for the electric field can be derived for the magnetic field strength H considering the magnetic field is parallel to the surface as depictured in Figure 2a. Based on Ampere's law:

$$\oint_C \boldsymbol{H} \cdot dl = \mu_0 \int_S (\boldsymbol{J} + \boldsymbol{\varepsilon_0} \frac{\partial \boldsymbol{E}}{\partial t}) \cdot \hat{\boldsymbol{n}}\, da \tag{49}$$

As for the electric field, the same rectangle can be used to calculate the path integral of the left hand side of Equation 49:

$$\oint \boldsymbol{H} \cdot dl = H_{1\perp} l_1 + H_{1\parallel} d - H_{1\perp} l_1 - H_{2\perp} l_2 - H_{2\parallel} d + H_{2\perp} l_2 = d(H_{1\parallel} - H_{2\parallel}) \tag{50}$$

Again, by shrinking l_1 and l_2 to 0, the right hand side of Equation 50 equals 0 and therefore:

$$H_{1\parallel} = H_{2\parallel} \tag{51}$$

With $H = \frac{B}{\mu}$ the relation in Equation 51 becomes:

$$\frac{B_{1\parallel}}{\mu_1} = \frac{B_{2\parallel}}{\mu_2} \tag{52}$$

In terms of an incoming electric field that is parallel to the surface (Figure 2b), the parallel components of the magnetic field are related by:

$$-\frac{B_i}{\mu_i}\cos(\theta_i) + \frac{B_r}{\mu_r}\cos(\theta_r) = -\frac{B_t}{\mu_t}\cos(\theta_t) \tag{53}$$

In order to continue deriving Fresnel's Equations, the law of reflection has to be employed. Following Fermat's principle, light is always traveling the fastest possible way from point S to point P.(5) This relation becomes clear by considering Figure 3. The total time to travel from point S to O and finally to P can be expressed as:

$$t = \frac{\overline{SO}}{v_i} + \frac{\overline{OP}}{v_t} \tag{54}$$

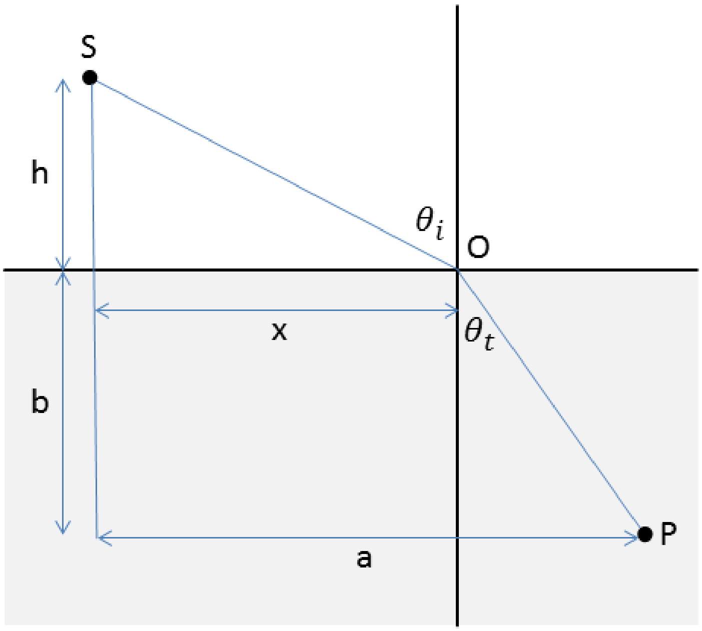

Figure 3. Illustration of Fermat's principle; adapted from (5).

With v_i and v_t being the speed in each material. Equation 54 can also be expressed in terms of x. Whereas a change in x shifts the point O and therefore affects the total time needed to travel from S to P:

$$t(x) = \frac{\sqrt{h^2+x^2}}{v_i} + \frac{\sqrt{b^2+(a-x)^2}}{v_t} \tag{55}$$

Finding the fastest way possible resembles the minimum of $t(x)$ and therefore:

$$\frac{dt}{dx} = \frac{x}{v_i\sqrt{h^2+x^2}} - \frac{(a-x)}{v_t\sqrt{b^2+(a-x)^2}} = 0 \tag{56}$$

Employing the following relations:

$$\sin(\theta_i) = \frac{x}{\overline{SO}} \tag{57}$$

$$\sin(\theta_t) = \frac{a-x}{\overline{OP}} \tag{58}$$

Equation 56 becomes:

$$\frac{\sin(\theta_i)}{v_i} = \frac{\sin(\theta_t)}{v_t} \tag{59}$$

This relation is called Snell's law. If the points S and P are in the same medium, the velocities are the same and consequently are the angles $\theta_i = \theta_r$. This result is called the law of reflection and is needed for the further simplification of Equation 53. Replacing B with the correlation from

Equation 44 and the fact that the incoming and reflected waves travel in the same medium and therefore with the same speed and under the same angle, Equation 53 becomes:

$$-\frac{E_i}{\mu_i v_i}\cos(\theta_i) + \frac{E_r}{\mu_r v_r}\cos(\theta_r) = -\frac{E_t}{\mu_t v_t}\cos(\theta_t) \tag{60}$$

$$\frac{1}{\mu_i v_i}(E_i - E_r)\cos(\theta_i) = \frac{E_t}{\mu_t v_t}\cos(\theta_t) \tag{61}$$

Multiplying Equation 61 with c, using the relation from Equation 23, resulting relation becomes:

$$\frac{\tilde{n}_i}{\mu_i}(E_{0i} - E_{0r})\cos(\theta_i) = \frac{\tilde{n}_t}{\mu_t}E_{0t}\cos(\theta_t) \tag{62}$$

Replacing E_{0t} with the relation formulated in Equation 48 and dividing both sides of Equation 62 with E_{0i}:

$$\frac{\tilde{n}_i}{\mu_i}\cos(\theta_i) - \frac{E_{0r}}{E_{0i}}\frac{\tilde{n}_i}{\mu_i}\cos(\theta_i) = \frac{\tilde{n}_t}{\mu_t}\cos(\theta_t) + \frac{E_{0r}}{E_{0i}}\frac{\tilde{n}_t}{\mu_t}\cos(\theta_t) \tag{63}$$

$$\frac{E_{0r}}{E_{0i}} = \frac{\frac{\tilde{n}_i}{\mu_i}\cos(\theta_i) - \frac{\tilde{n}_t}{\mu_t}\cos(\theta_t)}{\frac{\tilde{n}_i}{\mu_i}\cos(\theta_i) + \frac{\tilde{n}_t}{\mu_t}\cos(\theta_t)} \tag{64}$$

Replacing E_{0r} with Equation 48 and again dividing both sides by E_{0i}:

$$2\frac{\tilde{n}_i}{\mu_i}\cos(\theta_i) - \frac{E_{0t}}{E_{0i}}\frac{\tilde{n}_i}{\mu_i}\cos(\theta_i) = \frac{E_{0r}}{E_{0i}}\frac{\tilde{n}_t}{\mu_t}\cos(\theta_t) \tag{65}$$

$$\frac{E_{0t}}{E_{0i}} = \frac{2\frac{\tilde{n}_i}{\mu_i}\cos(\theta_i)}{\frac{\tilde{n}_i}{\mu_i}\cos(\theta_i) + \frac{\tilde{n}_t}{\mu_t}\cos(\theta_t)} \tag{66}$$

If the materials under consideration are dielectrics, $\mu_i \approx \mu_t \approx \mu_0$, and the angle of incidence is 0°, Equation 64 and Equation 66, which are called the Fresnel equations, can be expressed in terms of reflection and transmission coefficient r and t, respectively:

$$r = \frac{E_{0r}}{E_{0i}} = \frac{\tilde{n}_i - \tilde{n}_t}{\tilde{n}_i + \tilde{n}_t} \tag{67}$$

$$t = \frac{E_{0t}}{E_{0i}} = \frac{2\tilde{n}_i}{\tilde{n}_i + \tilde{n}_t} \tag{68}$$

Finally, the reflection and transmission coefficient can be used to describe the reflectance R and transmittance T. First, a beam of light with an area A that is reflected on a surface has to be imagined. The energy of the beam is described by its intensity and was already determined in Equation 38. The reflectance is defined as ratio of reflected and incoming intensity. Considering the law of reflection and the fact that incoming and reflected light travel in the same medium, the reflectance equals:

$$R = \frac{I_r A\cos(\theta_r)}{I_i A\cos(\theta_i)} = \frac{I_r}{I_i} = \frac{v_r \varepsilon_r E_{0r}^2}{v_i \varepsilon_i E_{0i}^2} = \left(\frac{E_{0r}}{E_{0i}}\right)^2 = r^2 \tag{69}$$

The transmittance is defined in a similar way as the reflectance, except now the transmitted intensity is considered:

$$T = \frac{I_t A \cos(\theta_t)}{I_i A \cos(\theta_i)} = \frac{I_t \cos(\theta_t)}{I_i \cos(\theta_i)} = \frac{v_t \varepsilon_t E_{0t}^2 \cos(\theta_t)}{v_i \varepsilon_i E_{0i}^2 \cos(\theta_i)} \tag{70}$$

Employing the relation $v^2 = \frac{1}{\mu_0 \varepsilon_0}$, Equation 70 becomes:

$$T = \frac{v_t \varepsilon_t E_{0t}^2 \cos(\theta_t)}{v_i \varepsilon_i E_{0i}^2 \cos(\theta_i)} = \frac{v_t}{v_i} \cdot \frac{1}{v_t^2 \mu_t} \cdot v_i^2 \mu_i \cdot \frac{E_{0t}^2 \cos(\theta_t)}{E_{0i}^2 \cos(\theta_i)} \tag{71}$$

Further assuming a dielectric material, $\mu_i \approx \mu_t \approx \mu_0$, and Equation 23, T becomes:

$$T = \frac{v_i}{v_t} \cdot \frac{c}{c} \cdot \frac{E_{0t}^2 \cos(\theta_t)}{E_{0i}^2 \cos(\theta_i)} = \frac{\tilde{n}_t E_{0t}^2 \cos(\theta_t)}{\tilde{n}_i E_{0i}^2 \cos(\theta_i)} = \frac{\tilde{n}_t \cos(\theta_t)}{\tilde{n}_i \cos(\theta_i)} \left(\frac{E_{0t}}{E_{0i}}\right)^2 = \frac{\tilde{n}_t \cos(\theta_t)}{\tilde{n}_i \cos(\theta_i)} t^2 \tag{72}$$

For vertical, incident light, reflectance and transmission can be expressed in terms of their complex refractive indices:

$$R = \left(\frac{\tilde{n}_i - \tilde{n}_t}{\tilde{n}_i + \tilde{n}_t}\right)^2 \tag{73}$$

$$T = \frac{\tilde{n}_t}{\tilde{n}_i} \cdot \frac{4\tilde{n}_i^{\,2}}{(\tilde{n}_i + \tilde{n}_t)^2} = \frac{4\tilde{n}_i \tilde{n}_t}{(\tilde{n}_i + \tilde{n}_t)^2} \tag{74}$$

7.1.5 *Transfer Matrix Relations*

The transfer matrix formalism was developed in 1999 by Pettersson et al.(6) and summarized comprehensively by Li.(7) The following derivation is therefore based on the procedure of the two aforementioned works.

In the previous section the concept of reflection and transmission was introduced. In order to derive the electric field distribution inside a planar solar cell stack, we assume that the incident light has an angle of 0° to the surface; a reasonable assumption considering a standard solar cell testing device. Each layer has a certain thickness d_i, with an electric field in the forward ($^+$) and backward ($^-$) direction. Indices “S” and “m” indicate the substrate (usually glass) and the metallic back electrode. An illustration of this scheme is given in Figure 4.

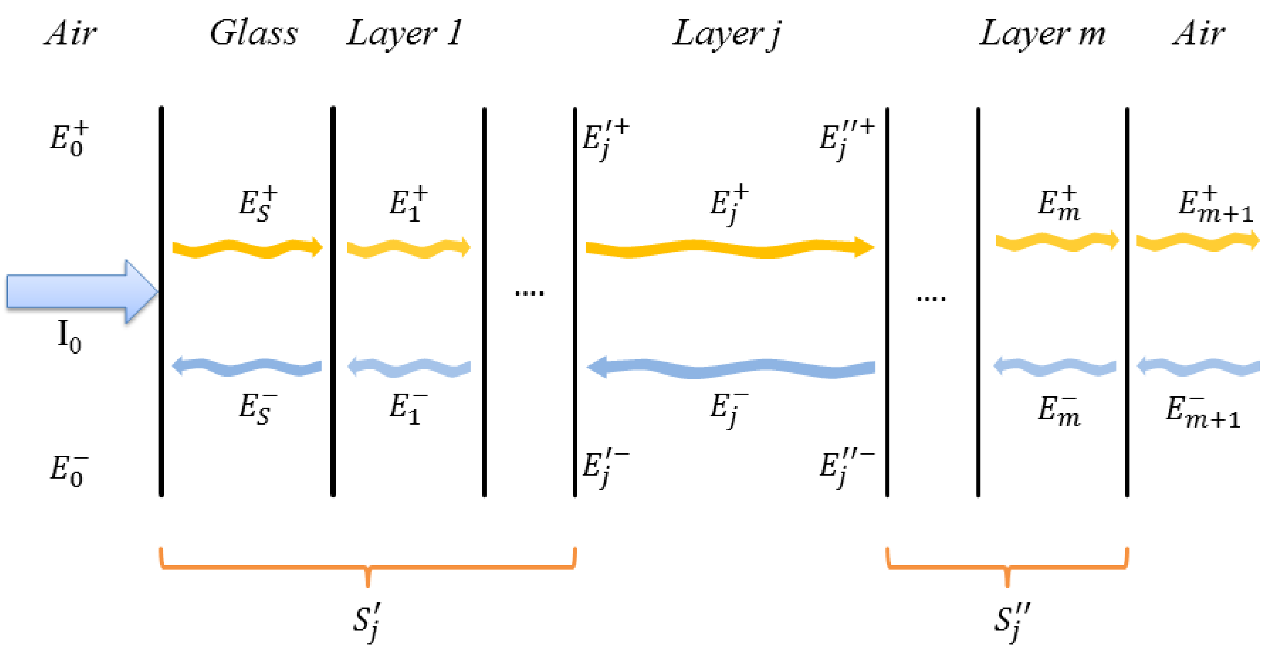

Figure 4. Schematic drawing of the multilayer stack of the solar cell. Incident light with intensity I₀ is coming in from the left hand side with an electric field entering the stack in forward direction (E_0^+) and one leaving the stack (E_0^-). The transfer matrix S can be used to relate the incident electric field with any layer in the solar cell, e.g. the incident electric field with the one entering and leaving the j-th layer on the left hand side (S_j') or the electric field entering and leaving to the right hand side of the j-th layer with the one on the back of the solar cell (S_j''). The schematic was adapted from (7).

The thickness of the substrate is assumed to be in the order of millimeters compared to nanometers of the solar cell stack. Due to this thickness difference the reflected and transmitted light through the glass substrate was derived by a geometric series. A geometric series has the form:

$$a + a \cdot r + a \cdot r^2 + \ldots + a \cdot r^n = \frac{a}{1-r} \quad (75)$$

for |r| < 1. Based on Figure 5 the overall reflected intensity R_{tot} from the solar cell is calculated based on the reflectance and transmission r and t and the incoming light intensity I_0 by:

$$R_{tot} = I_0 \cdot r_1 + I_0 \cdot t_1^2 \cdot r_2 + I_0 \cdot t_1^2 \cdot r_1 \cdot r_2^2 + \ldots + I_0 \cdot t_1^2 \cdot r_1^n \cdot r_2^{n+1} = I_0 \cdot r_1 + \frac{I_0 \cdot t_1^2 \cdot r_2}{1 - r_1 \cdot r_2} \quad (76)$$

Hereby r_1, r_2 and t_1 denote the reflectance from glass, the multilayer stack and the transmission through glass, respectively. In the same way as the total reflected intensity, the transmitted intensity T through the glass substrate can be calculated for the position right at the interface of glass and multilayer:

$$T = I_0 \cdot t_1 + I_0 \cdot t_1 \cdot r_1 \cdot r_2 + I_0 \cdot t_1 \cdot r_1^2 \cdot r_2^2 + \ldots + I_0 \cdot t_1 \cdot r_1^n \cdot r_2^n = \frac{I_0 \cdot t_1}{1 - r_1 r_2} \quad (77)$$

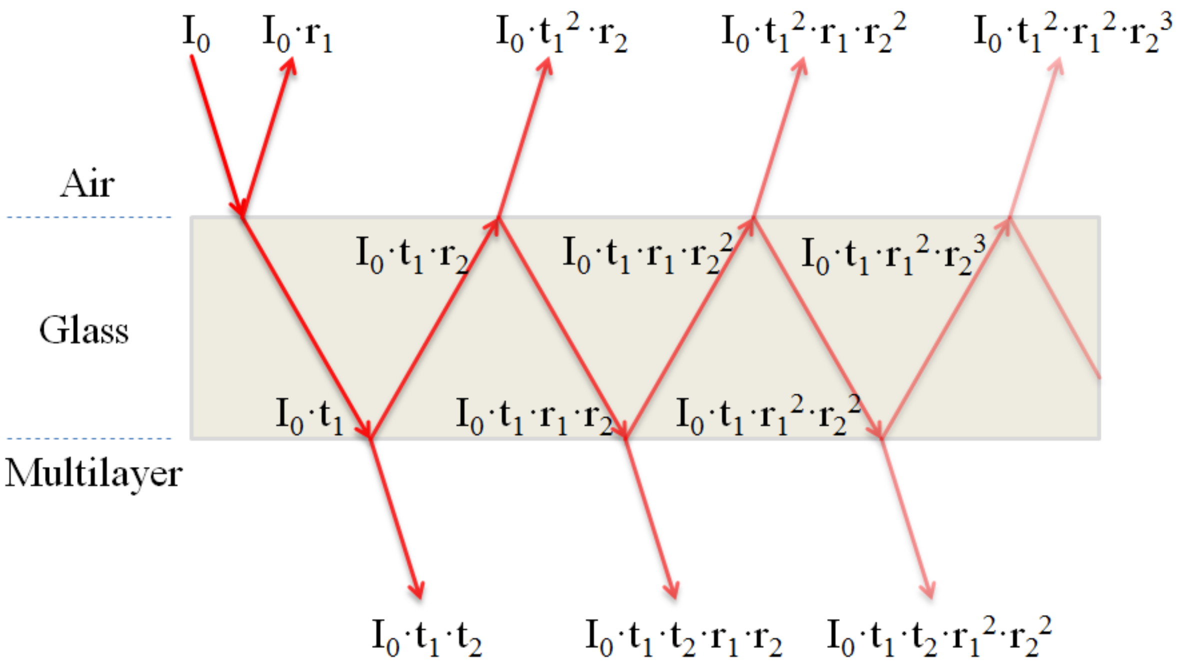

Figure 5. Illustration of the derivation of the geometric series for reflectance and transmission through a glass substrate.

From Equation 77 we derive the amplitude of the electric field at the interface of glass and multilayer. With the notation introduced in Figure 4 the magnitude of the electric field entering the multilayer stack $\left|E''^{+}_{S}\right|$ can be written as:

$$|E''^{+}_{S}|^2 = \frac{t_1}{1-r_1 r_2}\cdot|E_0^+|^2 \Leftrightarrow \left|E''^{+}_{S}\right| = \sqrt{\frac{t_1}{1-r_1 r_2}}\cdot|E_0^+| \tag{78}$$

The concept of transfer matrix calculations is to connect the incident electric field E_0^+, which we can relate to the AM1.5G spectrum via Equation 41, to the electric field at each position in forward and backward direction and the complex refractive index of the respective layer. The electric field at a given position x away from the glass substrate inside the multilayer stack can be given as:

$$E_j(x) = E_j^+(x) + E_j^-(x) \tag{79}$$

The connection between the incoming light and the light at the back of the solar cell is given by a transfer matrix S:

$$\begin{pmatrix} E_0^+ \\ E_0^- \end{pmatrix} = S \begin{pmatrix} E_{m+1}^+ \\ E_{m+1}^- \end{pmatrix} \tag{80}$$

The matrix S itself contains the interface matrix (matrix of refraction) I_{jk} with t and r being transmission and reflection coefficient derived in Equations 67 and 68:

$$I_{jk} = \frac{1}{t_{jk}} \begin{pmatrix} 1 & r_{jk} \\ r_{jk} & 1 \end{pmatrix} \tag{81}$$

and the layer matrix L_j that describes the propagation of light through the j-th layer with $\xi_j = \frac{2\pi\widetilde{n_j}}{\lambda}$:

$$L_j = \begin{pmatrix} e^{-i\xi_j d_j} & 0 \\ 0 & e^{i\xi_j d_j} \end{pmatrix} \tag{82}$$

Combining I and L, S can be expressed as follows:

$$S = \begin{pmatrix} S_{11} & S_{12} \\ S_{21} & S_{22} \end{pmatrix} = \left(\prod_{v=1}^{m} I_{(v-1)v} L_v\right) I_{m(m+1)} \tag{83}$$

In order to calculate the electric field in layer j, the transfer matrix S needs to be split up in a part left of the j-th layer (S'_j) and one to the right of the j-th layer (S''_j). Together with the layer matrix L_j, S can be described as:

$$S'_j = \left(\prod_{v=1}^{j-1} I_{(v-1)v} L_v\right) I_{(j-1)j} \tag{84}$$

$$S''_j = \left(\prod_{v=j+1}^{m} I_{(v-1)v} L_v\right) I_{m(m+1)} \tag{85}$$

$$S = S'_j L_j S''_j \tag{86}$$

As it was previously stated, the electric field in layer j needs to be related to the incoming electric field and the one leaving the solar cell. Having a detailed description of S all that is left to do are three steps. First, relate the incident incoming and reflected electric field to the one entering and leaving the j-th layer on the left hand side. In the second step, the electric field entering and leaving the j-th layer on the right hand side needs to be related to the one on the back of the solar cell. Finally, employing the layer matrix L, the electric fields entering and leaving on both sides of the j-th layer are correlated. Starting with step one:

$$\begin{pmatrix} E_0^+ \\ E_0^- \end{pmatrix} = S'_j \begin{pmatrix} E'^+_j \\ E'^-_j \end{pmatrix} = \begin{pmatrix} S'_{j11} E'^+_j + S'_{j12} E'^-_j \\ S'_{j21} E'^+_j + S'_{j22} E'^-_j \end{pmatrix} \tag{87}$$

Step two can be expressed as follows:

$$\begin{pmatrix} E''^+_j \\ E''^-_j \end{pmatrix} = S''_j \begin{pmatrix} E^+_{m+1} \\ E^-_{m+1} \end{pmatrix} = \begin{pmatrix} S''_{j11} E^+_{m+1} + S''_{j12} E^-_{m+1} \\ S''_{j21} E^+_{m+1} + S''_{j22} E^-_{m+1} \end{pmatrix} \tag{88}$$

Finally, employing Equation 82, the third steps yields the following relation:

$$\begin{pmatrix} E'^+_j \\ E'^-_j \end{pmatrix} = L_j \begin{pmatrix} E''^+_j \\ E''^-_j \end{pmatrix} = \begin{pmatrix} e^{-i\xi_j d_j} E''^+_j \\ e^{i\xi_j d_j} E''^-_j \end{pmatrix} \tag{89}$$

According to Equation 79 the electric field at any position x within the j-th layer is the sum of the electric field in forward and backward direction. Using a similar relation as given in Equation 89, the electric field in forward and backward direction is given as:

$$\begin{pmatrix} E_j^+(x) \\ E_j^-(x) \end{pmatrix} = L_j(x) \begin{pmatrix} E''^+_j \\ E''^-_j \end{pmatrix} = \begin{pmatrix} e^{-i\xi_j(d_j-x)} E''^+_j \\ e^{i\xi_j(d_j-x)} E''^-_j \end{pmatrix} \tag{90}$$

In combination with Equation 79, the electric field at any position in layer j can be written as:

$$E_j(x) = E_j^+(x) + E_j^-(x) = e^{-i\xi_j(d_j-x)} E''^+_j + e^{i\xi_j(d_j-x)} E''^-_j \tag{91}$$

Since the m-th layer is metallic, it is assumed that $E^-_{m+1} = 0$. Substituting the relation established in Equation 88 into Equation 89 yields:

$$\begin{pmatrix} E'^+_j \\ E'^-_j \end{pmatrix} = \begin{pmatrix} e^{-i\xi_j d_j} E''^+_j \\ e^{i\xi_j d_j} E''^-_j \end{pmatrix} = \begin{pmatrix} e^{-i\xi_j d_j} S''_{j11} E^+_{m+1} \\ e^{i\xi_j d_j} S''_{j21} E^+_{m+1} \end{pmatrix} \tag{92}$$

Equation 92 can be used to establish a relationship between the incident electric field and the one on the back of the solar cell by inserting Equation 92 into Equation 87:

$$\begin{pmatrix} E_0^+ \\ E_0^- \end{pmatrix} = \begin{pmatrix} S'_{j11} E'^+_j + S'_{j12} E'^-_j \\ S'_{j21} E'^+_j + S'_{j22} E'^-_j \end{pmatrix} = \begin{pmatrix} S'_{j11} e^{-i\xi_j d_j} S''_{j11} E^+_{m+1} + S'_{j12} e^{i\xi_j d_j} S''_{j21} E^+_{m+1} \\ S'_{j21} e^{-i\xi_j d_j} S''_{j11} E^+_{m+1} + S'_{j22} e^{i\xi_j d_j} S''_{j21} E^+_{m+1} \end{pmatrix} \tag{93}$$

The first row of Equation 93 can be rearranged to give an expression for E^+_{m+1} as function of E_0^+:

$$E^+_{m+1} = \frac{E_0^+}{S'_{j11} e^{-i\xi_j d_j} S''_{j11} + S'_{j12} e^{i\xi_j d_j} S''_{j21}} \tag{94}$$

Resubstituting this expression into Equation 88 yields:

$$\begin{pmatrix} E''^+_j \\ E''^-_j \end{pmatrix} = \begin{pmatrix} S''_{j11} E^+_{m+1} \\ S''_{j21} E^+_{m+1} \end{pmatrix} = \begin{pmatrix} \dfrac{S''_{j11} E_0^+}{S'_{j11} e^{-i\xi_j d_j} S''_{j11} + S'_{j12} e^{i\xi_j d_j} S''_{j21}} \\ \dfrac{S''_{j21} E_0^+}{S'_{j11} e^{-i\xi_j d_j} S''_{j11} + S'_{j12} e^{i\xi_j d_j} S''_{j21}} \end{pmatrix} \tag{95}$$

Finally, this expression can be used to determine the electric field by substituting Equation 95 into Equation 91:

$$E_j(x) = e^{-i\xi_j(d_j-x)} E''^+_j + e^{i\xi_j(d_j-x)} E''^-_j = \frac{e^{-i\xi_j(d_j-x)} S''_{j11} E_0^+}{S'_{j11} e^{-i\xi_j d_j} S''_{j11} + S'_{j12} e^{i\xi_j d_j} S''_{j21}} + \frac{e^{i\xi_j(d_j-x)} S''_{j21} E_0^+}{S'_{j11} e^{-i\xi_j d_j} S''_{j11} + S'_{j12} e^{i\xi_j d_j} S''_{j21}} \tag{96}$$

Rearranging Equation 96 ultimately results in an expression for the electric field at any given position inside the multilayer stack as a function of the incoming electric field E_0^+:

$$E_j(x) = \left(\frac{e^{-i\xi_j(d_j-x)}S''_{j11}+e^{i\xi_j(d_j-x)}S''_{j21}}{S'_{j11}e^{-i\xi_j d_j}S''_{j11}+S'_{j12}e^{i\xi_j d_j}S''_{j21}}\right)E_0^+ \tag{97}$$

The reflectance from the multilayer stack (r_2) can be expressed in terms of Equation 69 and Equation 80:

$$r_2 = \left(\frac{E_0^-}{E_0^+}\right)^2 = \left(\frac{S_{21}}{S_{11}}\right)^2 \tag{98}$$

Combining Equation 78 and Equation 97 and inserting the expressions derived in Equation 98 and Equations 73 and 74 with the complex refractive index of air being $\widetilde{n_{air}} = 1$, the normalized transfer matrix formalism is derived, taking reflectance and transmission at the glass substrate into account:

$$E_j(x) = \left(\frac{e^{-i\xi_j(d_j-x)}S''_{j11}+e^{i\xi_j\left(d_j-x\right)}S''_{j21}}{S'_{j11}e^{-i\xi_j d_j}S''_{j11}+S'_{j12}e^{i\xi_j d_j}S''_{j21}}\right)\sqrt{\frac{t_1}{1-r_1r_2}} = \left(\frac{e^{-i\xi_j(d_j-x)}S''_{j11}+e^{i\xi_j(d_j-x)}S''_{j21}}{S'_{j11}e^{-i\xi_j d_j}S''_{j11}+S'_{j12}e^{i\xi_j d_j}S''_{j21}}\right)\sqrt{\frac{\frac{4\cdot 1\cdot n_{\widetilde{glass}}}{\left(1+n_{\widetilde{glass}}\right)^2}}{1-\left(\frac{1-n_{\widetilde{glass}}}{1+n_{\widetilde{glass}}}\right)^2\cdot\left(\frac{S_{21}}{S_{11}}\right)^2}} \tag{99}$$

7.2 Separation of SWCNTs

Using gel permeation chromatography and aqueous suspended SWCNTs, the electronic type and chirality sorting can be influenced by the surfactant concentration, temperature and eluent. In this thesis, SWCNTs were suspended in 2 wt% SDS. After sonication and ultracentrifugation they were poured on the gel at a certain temperature and selectively eluted with 1 wt% SC. The gel and the cholate eluent were kept at the same temperature as the SWCNTs. A detailed temperature study was performed for SWCNTs being initially dissolved in 2, 1.6 and 1.4 wt% SDS, where the SDS concentration was lowered subsequent to a separation step. The results of this temperature study are shown in Fig. 1a. A high purity of (6,4) SWCNTs was obtained at 17 °C but the overall concentration was too low to be processed and employed in solar cells. Having larger quantities of (6,4) and comparably small amounts of (6,5) at 21°C, this temperature was used to selectively extract (6,4) from the nanotube solution to increase the purity of the subsequent (6,5) separation by passing the solution three times through the gel. At a concentration of 1.6 wt% SDS and 21°C, hundreds of milliliters of highly enriched (6,5) solutions were obtained. Yielding the largest quantities at 21°C, as indicated in Fig. 1b, this temperature was also used to selectively extract (6,5) from solution to increase the purity of the subsequent (7,5) separation. By lowering the SDS concentration to 1.4 wt% and successively varying the temperature as shown in Fig. 1c, the highest purity of (7,5) in solution was obtained at 17°C. Lowering the SDS concentration further in 0.2 wt% steps did not result in chirality pure solutions but rather in an enrichment in (7,6) at 1.2 wt% SDS, an increased amount of (8,6) at 1.0 wt% SDS and (9,5) at 0.8 wt% SDS. As described in Chapter 4, for each reduction in SDS the average diameter of SWCNTs in solution was increased.

Films of varying thickness and density were prepared by dissolving highly enriched (6,5), (7,5) and metallic SWCNT powders in chlorosulfonic acid (CSA), as described by Tune et al.(8) In doing so, films with increased absorption compared to the sparse films used in this thesis were fabricated and the complex refractive index measured via ellipsometry as shown in Fig. 2. The extinction coefficient k is comparable to UV/vis film absorption measurements on glass and illustrates the broadening effect of the S_{11} transition due to bundle formation. The resulting complex refractive indices are essential for further studies on dense films of polymer-free SWCNTs in solar cells.

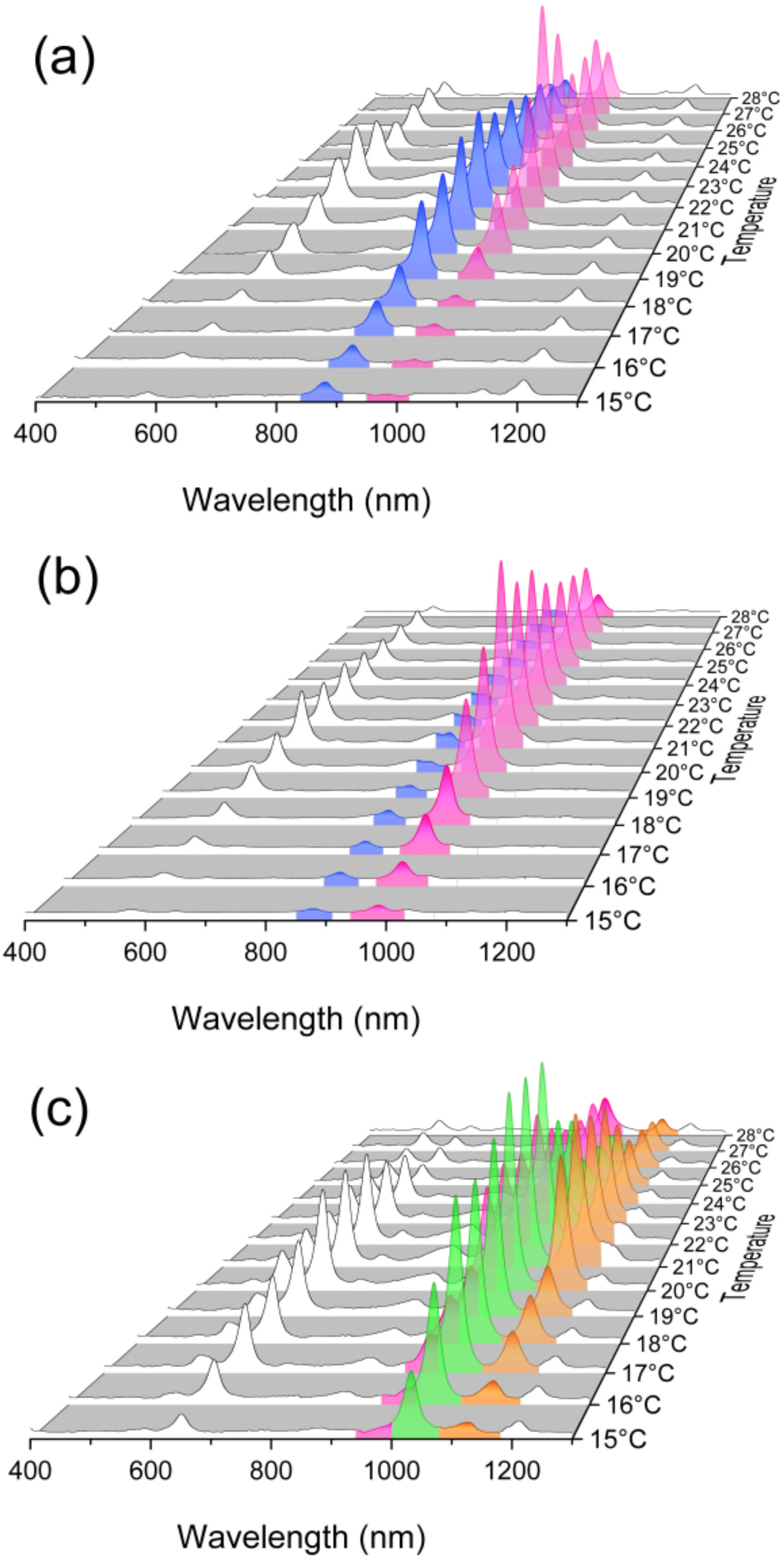

Fig. 1. Detailed temperature study for SWCNTs being suspended in 2 wt% SDS (a), 1.6 wt% SDS (b) and 1.4 wt% SDS (c). By choosing the appropriate temperatures and SDS concentrations, chirality pure (6,4) (blue), (6,5) (purple) and (7,5) (green) can be obtained. For the separation shown in (c) the purity of (7,5) is reduced by an increasing concentration of (7,6) (orange).

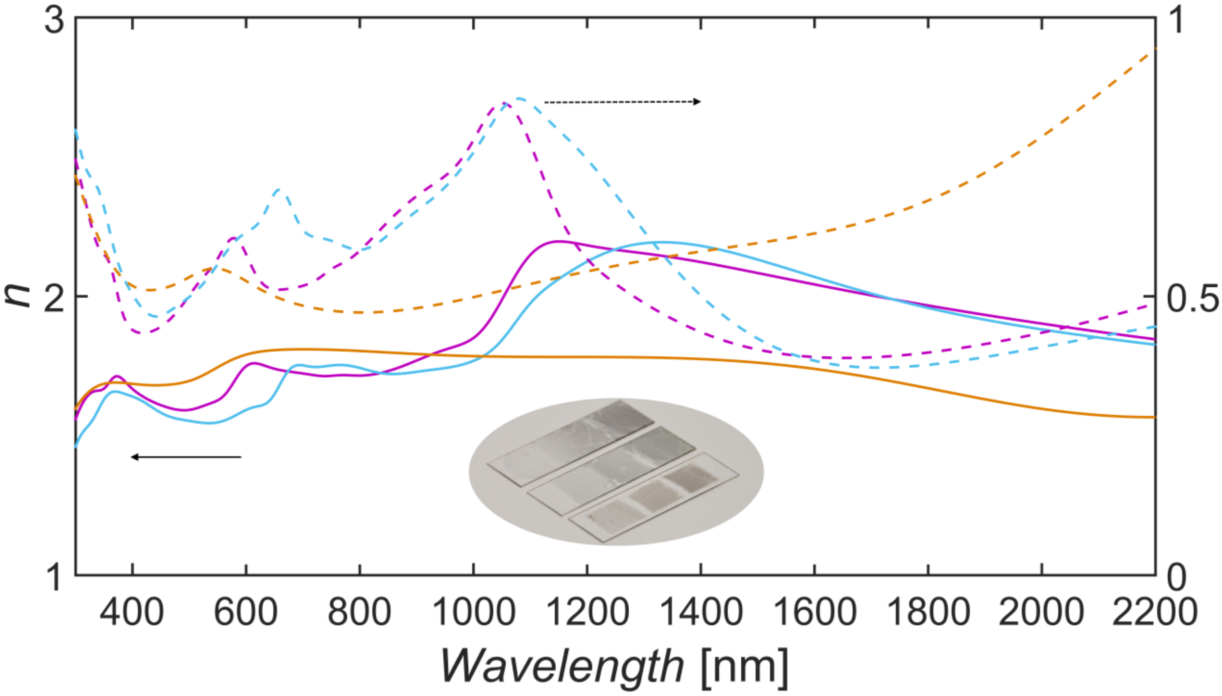

Fig. 2. Illustration of various n (solid line) and k (dotted line) values for (6,5) (purple, outer left films), (7,5) (blue, center films) and metallic enriched (brown, outer right films) nanotube films measured on a VASE ellipsometer. The nanotubes films were prepared via dry shear force alignment and stapled to vary the layer thickness between 5, 15 and 25 nm.

– This page intentionally left blank –

7.3 Supporting Information: Fitting Single Walled Carbon Nanotube Spectra

Photoluminescence measurement

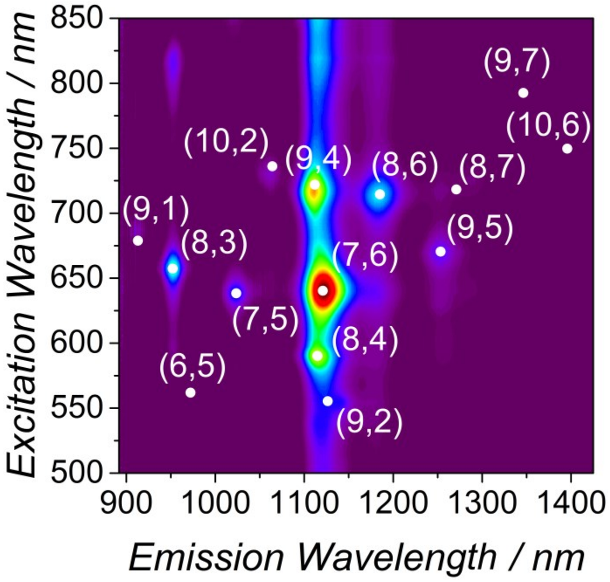

Fig. S1: Photoluminescence contour plot of the polychiral suspension used to obtain the absorption spectra shown in Figure 1, Figure 2 and Figure 4. The position of the individual (n,m) species was calculated as outlined previously.$^{(9-11)}$

(n,m) concentration for different background subtractions

Table S1: Spectral weight of different (n,m) species for different background subtraction methods.

	Spectral Weight (%)		
Background / SWCNT	k / λ^b (Nair et al.)	$Ae^{-b\lambda}$ (Naumov et al.)	Fano + Lorentzian (Tian et al.)
(7,6)	27.029	25.89	26.30
(8,6)	25.46	24.08	24.32
(9,5)	16.24	16.50	15.81
(7,5)	5.52	5.54	6.31
(8,3)	1.53	1.04	1.47
(9,1)	0.25	0.22	0.44
(6,5)	0.66	0.60	2.00
(10,2)	1.38	1.19	1.98
(9,4)	1.20	1.22	1.01
(8,4)	1.81	1.71	1.80
(9,2)	5.75	5.13	6.04
(8,7)	10.54	10.83	10.08
(9,7)	2.56	4.22	2.36
(10,6)	0.08	1.83	0.08

Gaussian and Lorentzian line shape

The Gaussian and Lorentzian line shapes can be defined based on their height or area as shown in eq S1 to S4. The relationship between area and height for Gaussian and Lorentzian line profiles can be determined by evaluating the area based function at the peak position λ_c, as demonstrated in eq S5 to S8:

$$y_{Gauss}(\lambda) = height \cdot e^{\left(-ln(2)\cdot\left(\frac{\lambda-\lambda_C}{0.5\cdot FWHM_G}\right)^2\right)} \tag{S1}$$

$$y_{Lorentz}(\lambda) = \frac{height}{1+\frac{\lambda-\lambda_C}{(0.5\cdot FWHM_L)^2}} \tag{S2}$$

$$y_{Gauss}(\lambda) = \sqrt{\frac{2\cdot ln(4)}{\pi}} \cdot \frac{area}{FWHM_G} \cdot e^{\left(-2\cdot ln(4)\cdot\left(\frac{\lambda-\lambda_C}{FWHM_G}\right)^2\right)} \tag{S3}$$

$$y_{Lorentz}(\lambda) = \frac{2\cdot area\cdot FWHM_L}{\pi} \cdot \frac{1}{4\cdot(\lambda-\lambda_c)^2+FWHM_L^2} \tag{S4}$$

$$y_{Gauss}(\lambda = \lambda_c) = height = \sqrt{\frac{2\cdot ln(4)}{\pi}} \cdot \frac{area}{FWHM_G} \cdot e^{\left(-2\cdot ln(4)\cdot\left(\frac{\lambda_C-\lambda_C}{FWHM_G}\right)^2\right)} \tag{S5}$$

$$height = \sqrt{\frac{2\cdot ln(4)}{\pi}} \cdot \frac{area}{FWHM_G} \tag{S6}$$

$$y_{Lorentz}(\lambda = \lambda_c) = height = \frac{2\cdot area\cdot FWHM_L}{\pi} \cdot \frac{1}{4\cdot(\lambda_c-\lambda_c)^2+FWHM_L^2} \tag{S7}$$

$$height = \frac{2\cdot area}{\pi\cdot FWHM_L} \tag{S8}$$

Derivation of Voigtian line-shape

The Voigtian function V(t) is defined as convolution$^{(12)}$ of a Gaussian (G) and Lorentzian (L) function:

$$V(t) = \int_{-\infty}^{+\infty} G(t')L(t-t')dt' \tag{S9}$$

In order to calculate the convolution integral, the Gaussian and Lorentzian functions are written as functions of “t” and “y” with t_c being the peak position:

$$G(y) = \sqrt{\frac{4 \cdot ln(2)}{\pi}} \cdot \frac{e^{\left(-\frac{4 \cdot ln(2)}{(FWHM_G)^2} \cdot y^2\right)}}{FWHM_G} \tag{S10}$$

$$L(t-y) = \frac{2 \cdot area \cdot FWHM_L}{\pi} \cdot \frac{1}{4 \cdot (t-t_c-y)^2 + FWHM_L^2} \tag{S11}$$

The exponent of the Gaussian function can then be re-written as function of t’:

$$\frac{4 \cdot ln(2)}{(FWHM_G)^2} \cdot y^2 = (t')^2 \tag{S12}$$

$$y = \frac{t' \cdot FWHM_G}{\sqrt{4 \cdot ln(2)}} \tag{S13}$$

Inserting the expression for y from eq S13 into the formalism of the Lorentzian function in eq S11 yields:

$$\begin{aligned} L(t-t') &= \frac{2 \cdot area \cdot FWHM_L}{\pi} \cdot \frac{1}{4 \cdot \left(t-t_c-\frac{t' \cdot FWHM_G}{\sqrt{4 \cdot ln(2)}}\right)^2 + FWHM_L^2} = \\ &= \frac{2 \cdot area \cdot FWHM_L}{\pi} \cdot \frac{1}{4 \cdot \left(\frac{\sqrt{4 \cdot ln(2)} \cdot (t-t_c) - t' \cdot FWHM_G}{\sqrt{4 \cdot ln(2)}}\right)^2 + FWHM_L^2} = \\ &= \frac{2 \cdot area \cdot FWHM_L}{\pi} \cdot \frac{1}{\frac{4 \cdot FWHM_G{}^2}{4 \cdot ln(2)} \cdot \left(\frac{\sqrt{4 \cdot ln(2)}}{FWHM_G} \cdot (t-t_c) - t'\right)^2 + FWHM_L^2} = \\ &= \frac{2 \cdot area \cdot FWHM_L}{\pi} \cdot \frac{ln(2)}{FWHM_G{}^2} \cdot \frac{1}{\left(\frac{\sqrt{4 \cdot ln(2)}}{FWHM_G} \cdot (t-t_c) - t'\right)^2 + \frac{FWHM_L^2}{FWHM_G{}^2} \cdot ln(2)} \end{aligned} \tag{S14}$$

In the last step the differential dy has to be expressed as a function of dt’, based on eq S13:

$$\frac{dy}{dt'} = \frac{FWHM_G}{\sqrt{4 \cdot ln(2)}} \tag{S15}$$

$$dy = \frac{FWHM_G}{\sqrt{4 \cdot ln(2)}} \cdot dt' \tag{S16}$$

Combining eq S12 with eq S10 and inserting it together with eq S14 and eq S16 into eq S9, the Voigtian function can be written in terms of its area:

$$V(t) = \int_{-\infty}^{+\infty} G(y)L(t-y)dy = \frac{FWHM_G}{\sqrt{4 \cdot ln(2)}} \cdot \int_{-\infty}^{+\infty} G(t')L(t-t')dt' =$$

$$= \frac{FWHM_G}{\sqrt{4 \cdot ln(2)}} \cdot \int_{-\infty}^{+\infty} \sqrt{\frac{4 \cdot ln(2)}{\pi}} \cdot \frac{e^{\left(-(t')^2\right)}}{FWHM_G} \cdot \frac{2 \cdot area \cdot FWHM_L}{\pi} \cdot \frac{ln(2)}{FWHM_G{}^2} \cdot \frac{1}{\left(\frac{\sqrt{4 \cdot ln(2)}}{FWHM_G} \cdot (t-t_c)-t'\right)^2 + \frac{FWHM_L^2}{FWHM_G{}^2} \cdot ln(2)} =$$

$$= area \cdot \frac{2 \cdot ln(2) \cdot FWHM_L}{\pi^{\frac{3}{2}} \cdot FWHM_G{}^2} \cdot \int_{-\infty}^{+\infty} \frac{e^{\left(-(t')^2\right)}}{\left(\frac{\sqrt{4 \cdot ln(2)}}{FWHM_G} \cdot (t-t_c)-t'\right)^2 + \frac{FWHM_L^2}{FWHM_G{}^2} \cdot ln(2)} dt' \qquad \text{(S17)}$$

Evaluating eq S17 at the peak position t_c yields:

$$V_{max}(t = t_c) = height = \ area \cdot \frac{2 \cdot ln(2) \cdot FWHM_L}{\pi^{\frac{3}{2}} \cdot FWHM_G{}^2} \cdot \int_{-\infty}^{+\infty} \frac{e^{\left(-(t')^2\right)}}{\left(\frac{\sqrt{4 \cdot ln(2)}}{FWHM_G} \cdot (t_c-t_c)-t'\right)^2 + \frac{FWHM_L^2}{FWHM_G{}^2} \cdot ln(2)} dt' =$$

$$= area \cdot \frac{2 \cdot ln(2) \cdot FWHM_L}{\pi^{\frac{3}{2}} \cdot FWHM_G{}^2} \cdot \int_{-\infty}^{+\infty} \frac{e^{\left(-(t')^2\right)}}{(-t')^2 + \frac{FWHM_L^2}{FWHM_G{}^2} \cdot ln(2)} dt' \qquad \text{(S18)}$$

A direct relation between peak height and area can then be proposed:

$$area \cdot \frac{2 \cdot ln(2) \cdot FWHM_L}{\pi^{\frac{3}{2}} \cdot FWHM_G{}^2} = \frac{height}{\int_{-\infty}^{+\infty} \frac{e^{\left(-(t')^2\right)}}{(-t')^2 + \frac{FWHM_L^2}{FWHM_G{}^2} \cdot ln(2)} dt'} \qquad \text{(S19)}$$

By applying the relationship given in eq S19 to eq S17, the Voigtian function can be expressed in terms of its height:

$$V(t) = height \cdot \frac{\int_{-\infty}^{+\infty} \frac{e^{\left(-(t')^2\right)}}{\left(\frac{\sqrt{4 \cdot \ln(2)}}{FWHM_G} \cdot (t-t_c)-t'\right)^2 + \frac{FWHM_L^2}{FWHM_G{}^2} \cdot \ln(2)} dt'}{\int_{-\infty}^{+\infty} \frac{e^{\left(-(t')^2\right)}}{(-t')^2 + \frac{FWHM_L^2}{FWHM_G{}^2} \cdot \ln(2)} dt'} \qquad \text{(S20)}$$

Deriving an expression for the Gaussian FWHM for Voigtian line-shsapes

The Voigtian FWHM was assumed to be constant (C_x, with x representing either the S_{11}, S_{22} or M_{11} region) in eV as per the work of Nair et al.(13) Based on eq S21 the FWHM was calculated in nm, with h being Planck's constant, c the speed of light and E_x the position of the peak absorption in the according region:

$$FWHM_V = \frac{C_x \cdot h \cdot c}{(E_x)^2 - \left(\frac{C_x}{2}\right)^2} \cdot 10^9 \tag{S21}$$

Olivero et al.(14) derived an analytical expression for the Voigtian FWHM:

$$FWHM_V = 0.5436 \cdot FWHM_L + \sqrt{0.2166 \cdot FWHM_L^2 + FWHM_G^2} \tag{S22}$$

Combining eq S21 and eq S22 it follows:

$$\frac{C_x \cdot h \cdot c}{(E_x)^2 - \left(\frac{C_x}{2}\right)^2} \cdot 10^9 = 0.5436 \cdot FWHM_L + \sqrt{0.2166 \cdot FWHM_L^2 + FWHM_G^2} \tag{S23}$$

The initial guess for the Lorentzian FWHM ($FWHM_L$) was calculated by assuming an equal contribution of Gaussian and Lorentzian FWHM to the Voigtian FWHM. Nevertheless, the supplied code offers the user the possibility to change this starting ratio (R) and the respective upper and lower boundaries of the ratio. However, all ratios are constrained to be within ± 20 % to be comparable; a constraint that can be changed to smaller or larger values by the user. The ratio is of Gaussian to Lorentzian FWHM is calculated by assuming the following:

$$\frac{FWHM_G}{FWHM_L} = R \tag{S24}$$

By resubstituting eq S24 into eq S23, it follows that:

$$\frac{C_x \cdot h \cdot c}{(E_x)^2 - \left(\frac{C_x}{2}\right)^2} \cdot 10^9 = 0.5436 \cdot FWHM_L + \sqrt{0.2166 \cdot FWHM_L^2 + FWHM_L^2 \cdot R^2} \tag{S25}$$

The Lorentzian FWHM can therefore be expressed as a function of E_{11} and R:

$$FWHM_L = \frac{C_x \cdot h \cdot c \cdot 10^9}{\left((E_x)^2 - \left(\frac{C_x}{2}\right)^2\right) \cdot \left(0.5436 + \sqrt{0.2166 + R^2}\right)} \tag{S26}$$

Voigtian and complex error function

The Voigtian function (in this case “K”, to differentiate from the previous expression “V”) represents the real part of the Faddeeva function (W) which, for y > 0, is identical to the complex error function (w):(15)

$$W(z) = K(x,y) + i \cdot L(x,y) = \frac{i}{\pi}\int_{-\infty}^{+\infty}\frac{e^{-t^2}}{z-t}dt \tag{S27}$$

$$w(z) = e^{-z^2}\left(1 + \frac{2i}{\sqrt{\pi}}\int_0^z e^{t^2}dt\right) = e^{-z^2}(1 - erf(-iz)) \tag{S28}$$

with the dimensionless variables x and y as defined in eq S29 and eq S30, respectively and z = x + i·y.

$$x = \sqrt{ln(2)} \cdot \frac{\lambda - \lambda_c}{HWHM_G} \tag{S29}$$

$$y = \sqrt{ln(2)} \cdot \frac{HWHM_L}{HWHM_G} \tag{S30}$$

The Voigt function K can be normalized to $\sqrt{\pi}$ and defined as shown in eq S31.

$$K(x,y) = \frac{y}{\pi}\int_{-\infty}^{+\infty}\frac{e^{-t^2}}{(x-t)^2 + y^2}dt \tag{S31}$$

For a Voigtian line shape; instead of the FWHM, the half width at half maximum (HWHM) is used for calculation and can be expressed as a function of height and the real part of eq S28:

$$y_{Voigt} = height \cdot \frac{Re(w(x,y))}{Re(w(0,y))} \tag{S32}$$

Fitting procedure

For the fitting demonstrated in the present work, the initial peak positions of all line profiles were obtained from the databases provided by Bachilo et al.(10) for semiconducting (n,m) species (an alternative set of semiconducting nanotubes was provided by Weisman et al.(16)) and Nair et al.(13) for metallic nanotubes, and were allowed to vary between 0 and +20 nm. These boundary conditions were chosen under the assumption that the reference peak position resembles the case of the highest transition energies for each (n,m) species. As stated, upon bundling, a change in dielectric environment or the creation of defects, e.g. via sonication, the absorption peaks tend to red-shift because of an increased dielectric screening and exciton tunneling.(17) A different pair of boundary conditions for the allowed peak shift was assumed in the case where a peak in the measured spectrum was manually assigned to an (n,m) species (i.e. a spectral feature was enforced to be a certain nanotube type). In this case, the allowed red/blue shift was set to ±5 nm of the peak position identified in the spectra.

The FWHM of the EPS was assumed to vary between 50 – 200 % of its initial value during the fit. The FWHM is always calculated for the (n,m) species with the largest EPS and the FWHM of all subsequent (n,m) species is allowed to deviate from this value by ±10 % to enforce a similar line shape amongst all the EPSs fitted to a sample. The peak area was modeled based on the spectral weight transfer from a peak, S_x (I_{S_x}) with x=11 or x=22, to its corresponding EPS (I_{EPS}), as described by Perebeinos et al. with an additional, diameter independent factor f_1 as introduced in our previous work:(9, 18)

$$\frac{I_{EPS}}{I_{S_x}} = 0.017 + \frac{0.1\,nm}{d_t} + f_1 \tag{S33}$$

The factor f_1 was allowed to vary during the fit between -0.07 and +0.07 to account for a marginally reduced or increased spectral weight transfer from S_x to the EPS.

Comparison of different FWHM starting values

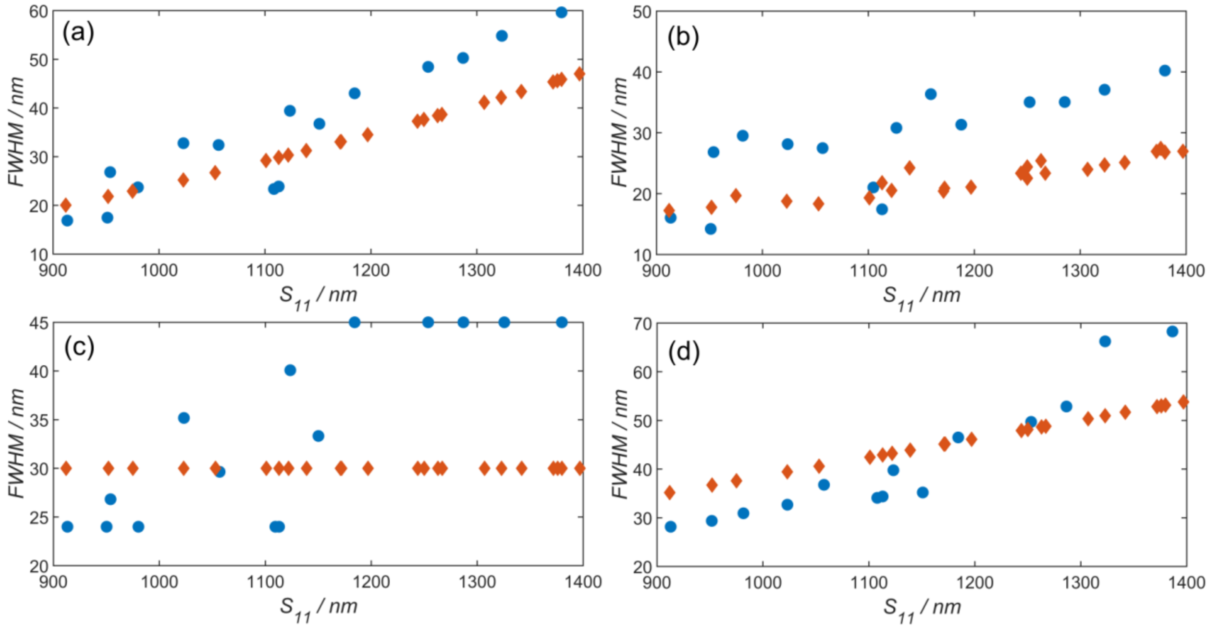

Fig. S2: Comparison of FWHM starting values (red diamonds) and fitted values (blue circles) for different methods of estimating the initial FWHM for the nanotube suspension used in the main text: (a) constant FWHM in energy space,$^{(13)}$ (b) diameter dependent in frequency space,$^{(19)}$ (c) constant in nanometer and (d) as function of E_{11} in energy space.$^{(20)}$ The FWHM for (b) and (c) was allowed to vary within 80 to 150 % of its initial starting value as compared to (a) and (d) where it was allowed to vary between 80 and 130 % of its initial value. Based on the nSSE value, method (a) provides the best fit for this particular nanotube suspension with $4.33 \cdot 10^{-4}$, compared to $1.0 \cdot 10^{-2}$, $5.60 \cdot 10^{-4}$ and $7.1 \cdot 10^{-4}$ for (b) to (d).

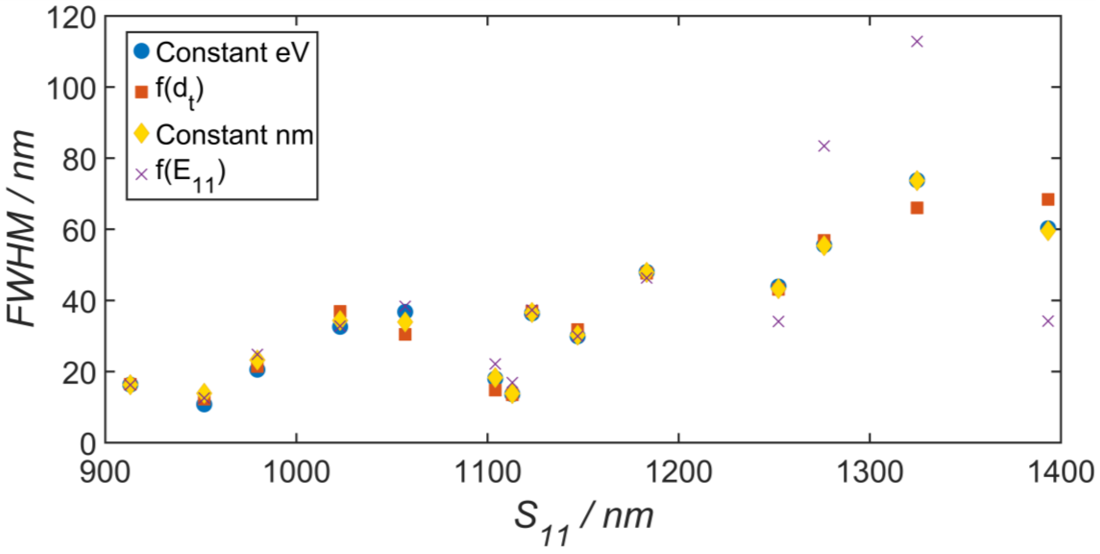

Fig. S3: Fitted FWHM values using the four different methods of initial FWHM estimation, shown in Fig. S2, where the FWHM is allowed to vary freely. Blue dots represent the method with a fixed FWHM in energy space,$^{(13)}$ red squares were calculated based on the nanotubes diameter,$^{(19)}$ yellow diamonds represent a constant FWHM in nm and purple crosses were initially calculated based on a linear function of the E_{11} absorption position.$^{(20)}$ Here it can be seen, that the FWHM obtained is the same, irrespective of the starting position. Nevertheless, good starting values allow for a more constrained and faster fit.

Importance of EPS

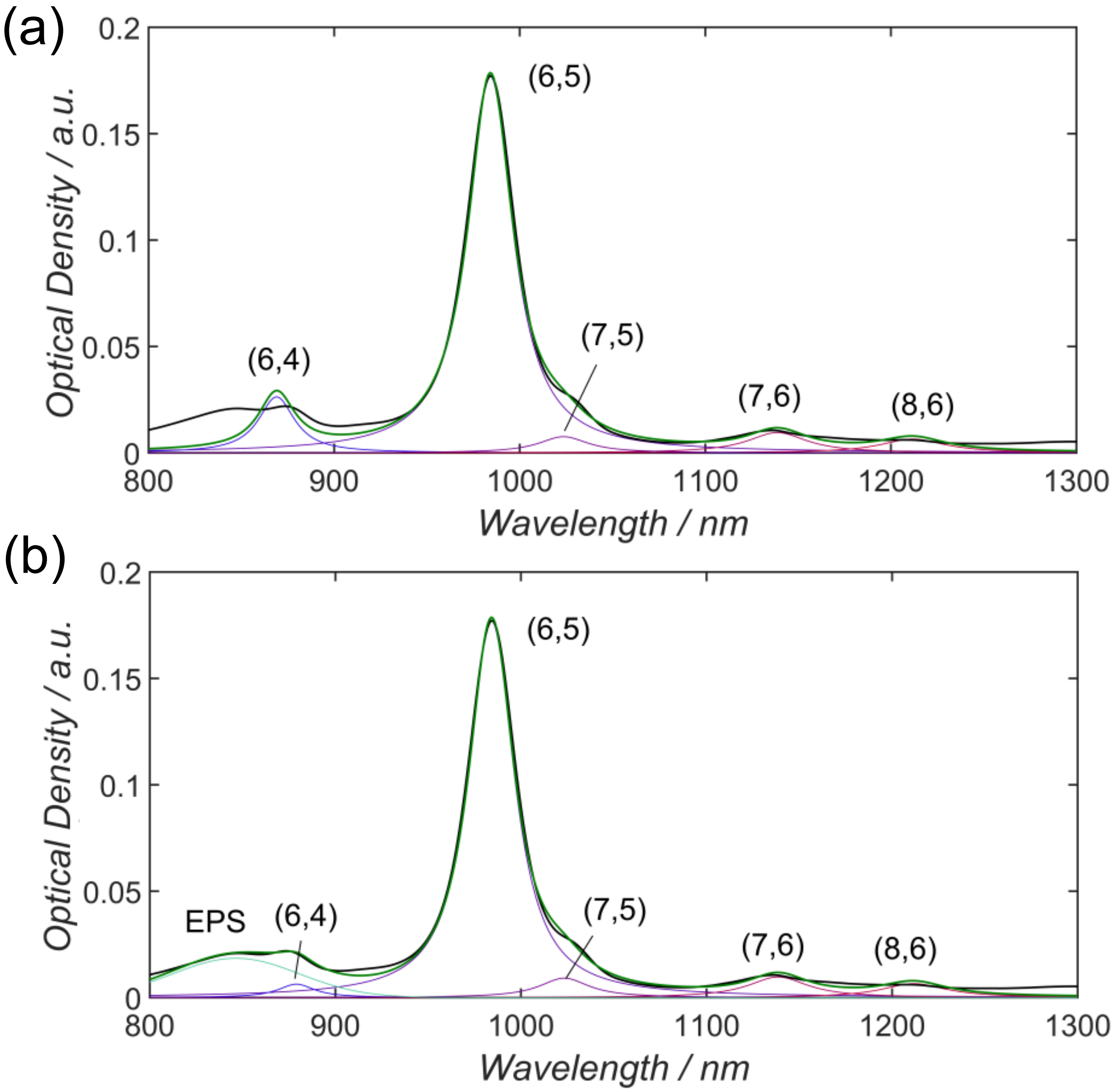

Fig. S4: Fit of (6,5) enriched SWCNT solution (black) without (a) and with (b) an associated exciton-phonon sideband (EPS). The quality of the fit between 800 – 900 nm is improved by inclusion of an EPS for (6,5).

Alternative method for height assignment

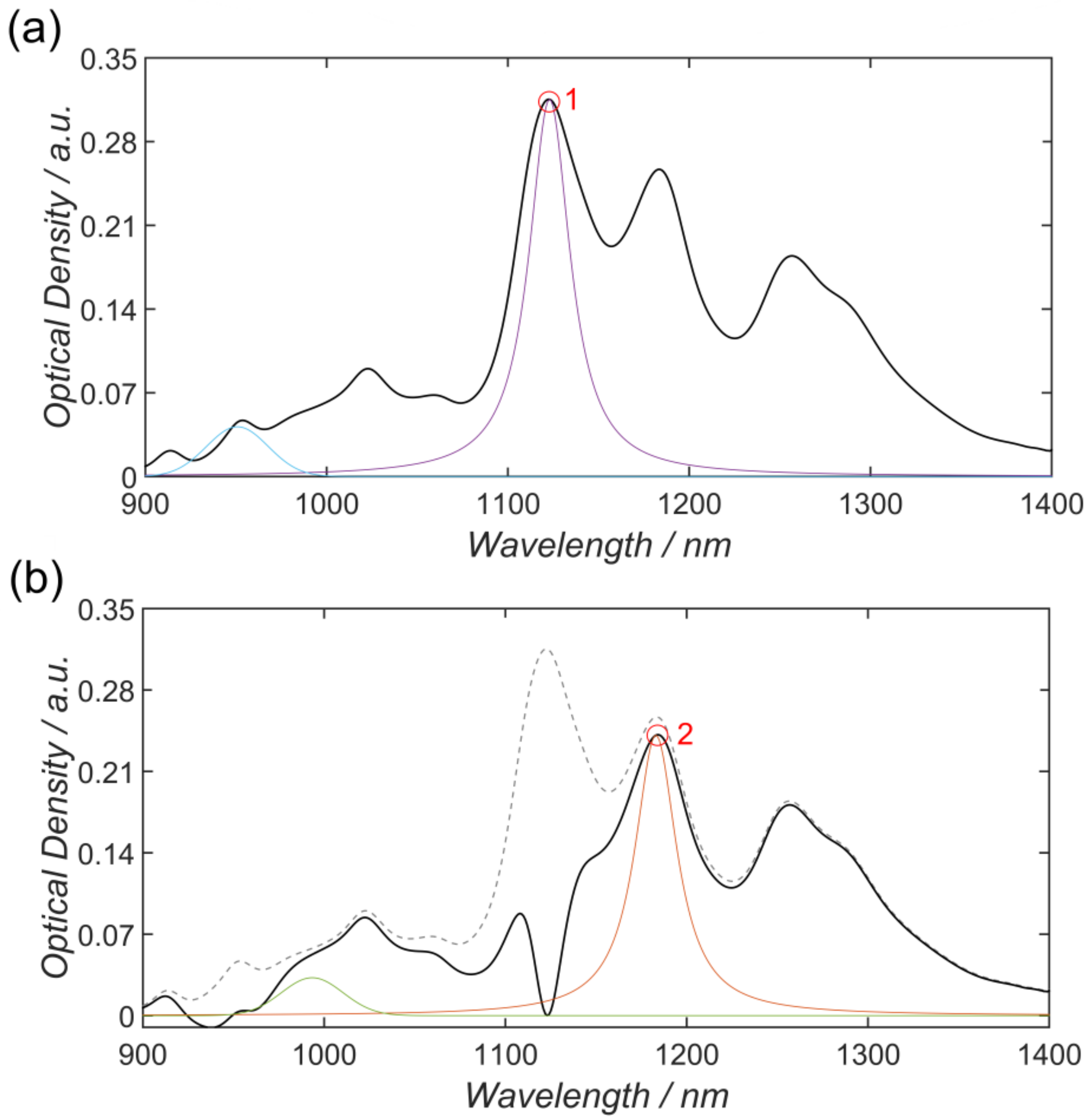

Fig. S5: The method shown in (a) and (b) and is based on the sequential subtraction of ab initio calculated line profiles. In this routine, the largest peak (labeled 1) is considered first and both the line profile of the nanotube and any associated EPS are subtracted from the original spectrum to yield a “corrected” absorption spectrum. From this corrected spectrum, the second most intense nanotube peak (labeled 2) is calculated and again subtracted to yield a new corrected spectrum. This procedure is repeated for all (n,m) species under consideration and the height of the individual (n,m) species is varied between 10 and 120 % of the peak intensity in the corrected spectrum. This approach is well suited for monochiral or (n,m) enriched SWCNT absorption spectra with clearly separated peaks and minor contributions from low concentration (n,m) species. Another approach would be the combination of the method presented in Figure 2 and Fig. S5 applied to the right and left, respectively, of a cut-off wavelength. However, it is possible to set this boundary condition to suitably high or low values such that the entire spectrum of interest is fitted with either of the methods shown in Figure 2 and Fig. S5.

Voigtian, Lorentzian and Gaussian line profiles

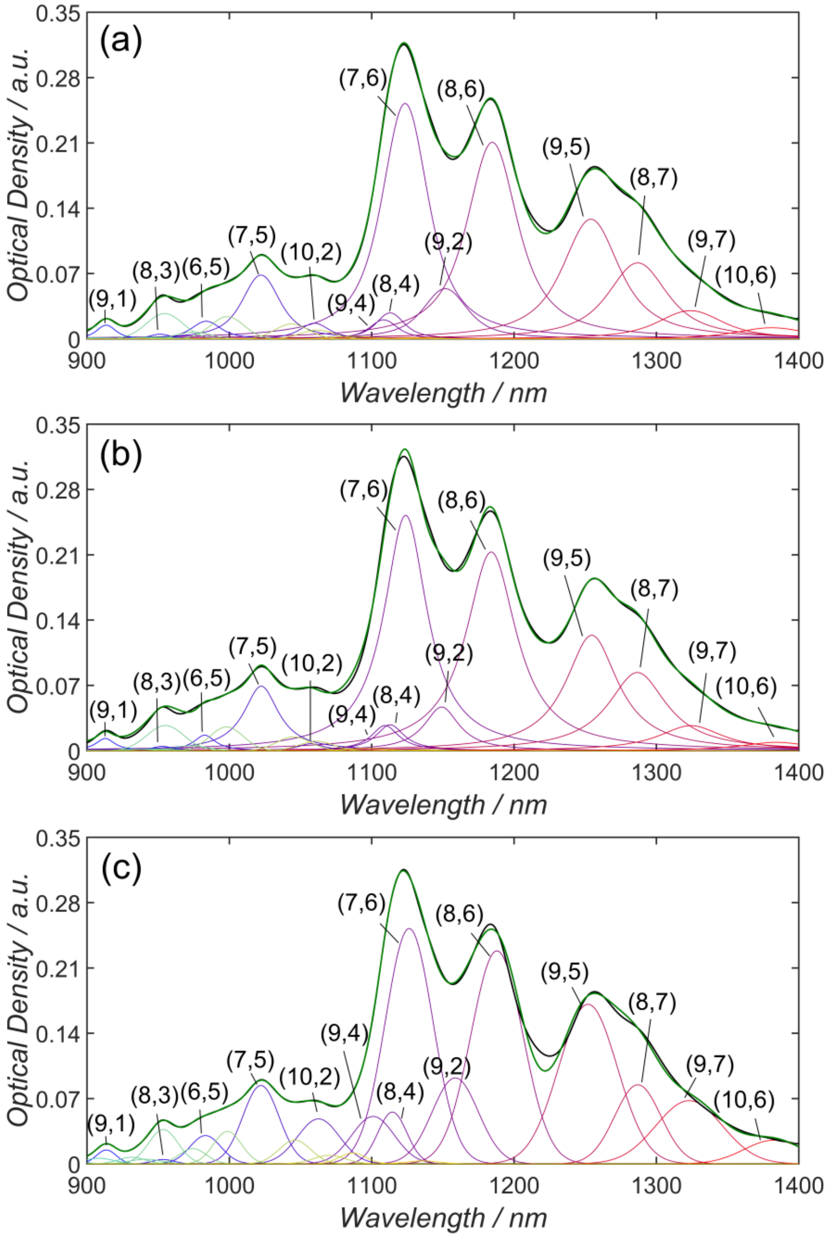

Fig. S6: (a) Fit of the polychiral SWCNT solution (black) shown in Figure 1 with Voigtian line profiles (calculated spectra is shown in green and a background based on Naumov et al.(21) was subtracted). (b) and (c) The same polychiral nanotube solution fitted with Lorentzian and Gaussian line profiles, respectively. The difference in (n,m) distribution is visible, e.g. by comparing the shape of (7,6) and (8,6) or the calculated spectrum above 1200 nm where the contribution of (9,5) and (9,7) vary significantly for Gaussian line profiles compared to the other two line shapes. Peaks that were not assigned to any nanotube are exciton phonon sidebands.

Voigtian, Lorentzian and Gaussian line profiles were used to fit the polychiral nanotube solution shown in Figure 1. Comparing the normalized sum of squared errors (nSSE) value of these fits ($4.33 \cdot 10^{-4}$, $1.05 \cdot 10^{-3}$ and $2.22 \cdot 10^{-3}$, respectively) the Voigtian and Lorentzian line profiles seem to be best suited for fitting aqueous dispersions of polychiral SWCNTs.

Decongestion of different mixtures with known ratios

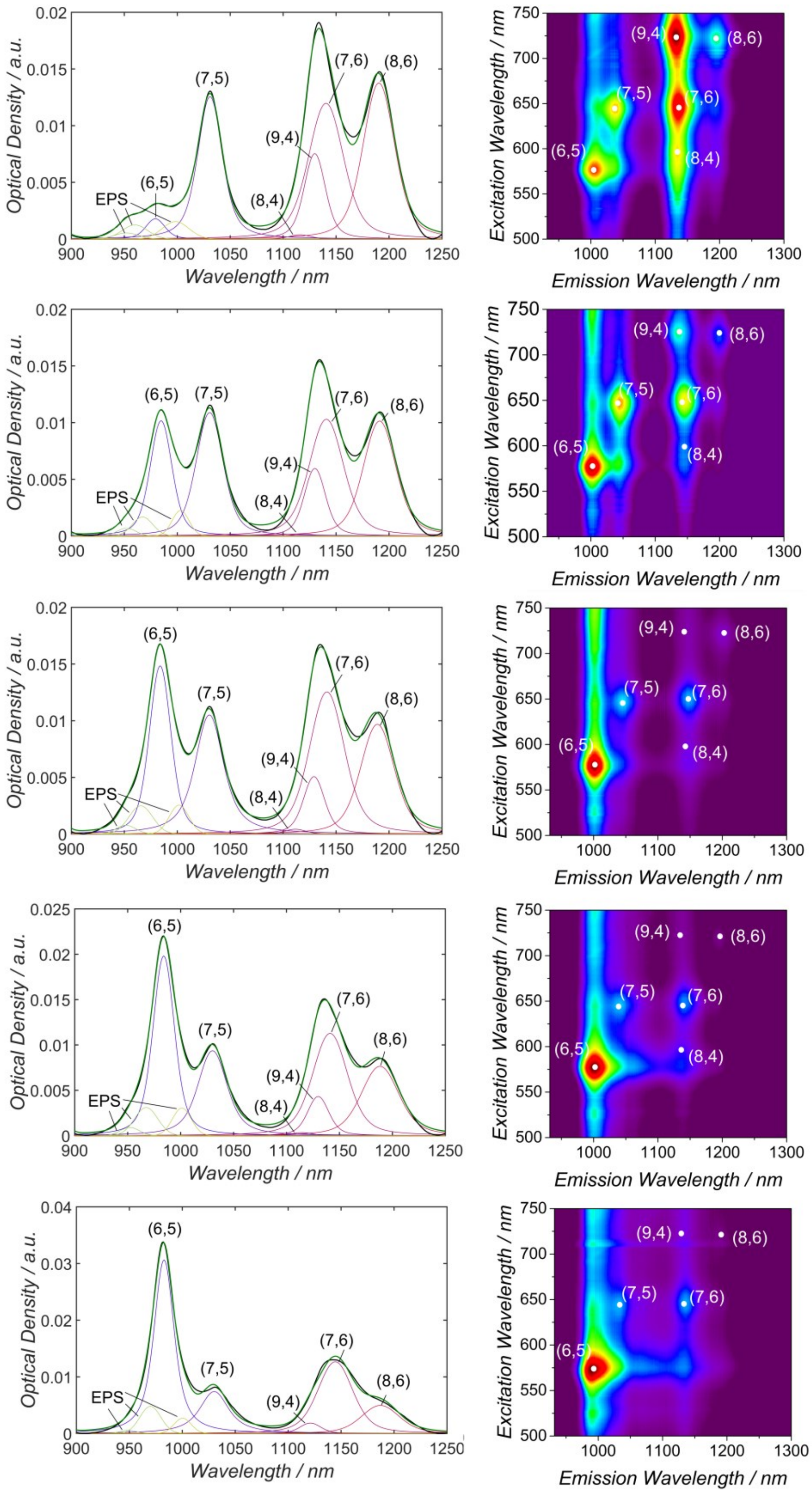

Fig. S7: In the left column the optical absorption data of solution 1 (bottom), solution 2 (top) and mixtures thereof in ratios of 2:1, 1:2 and 1:2 (from bottom to top) are shown. In the right column, the corresponding PL measurements are shown.

Calculating the concentration of (6,5) and (7,5) in solution 1 and 2, the expected concentration ratio can be calculated according to the following equation, where r1 is the ratio taken of solution 1 and r2 the ratio of solution 2:

$$Concentration\ Ratio = \frac{r1 \cdot conc_{65_{sol1}} + r2 \cdot conc_{65_{sol2}}}{r1 \cdot conc_{75_{sol1}} + r2 \cdot conc_{75_{sol2}}} \tag{S34}$$

The fitted concentration ratio can be determined from Fig. S7 by determining the concentration based on the optical density OD, cuvette path length l_{path} of 2 mm and the molar absorptivity ε calculated based on Sanchez et al.(22) for the different (n,m) species:

$$conc = \frac{OD}{l_{path} \cdot \varepsilon} \tag{S35}$$

The relative error between the measured concentration ratio in Figure S8 and the calculated one based on eq S34 was calculated to be 10.8 ± 2.5 %.

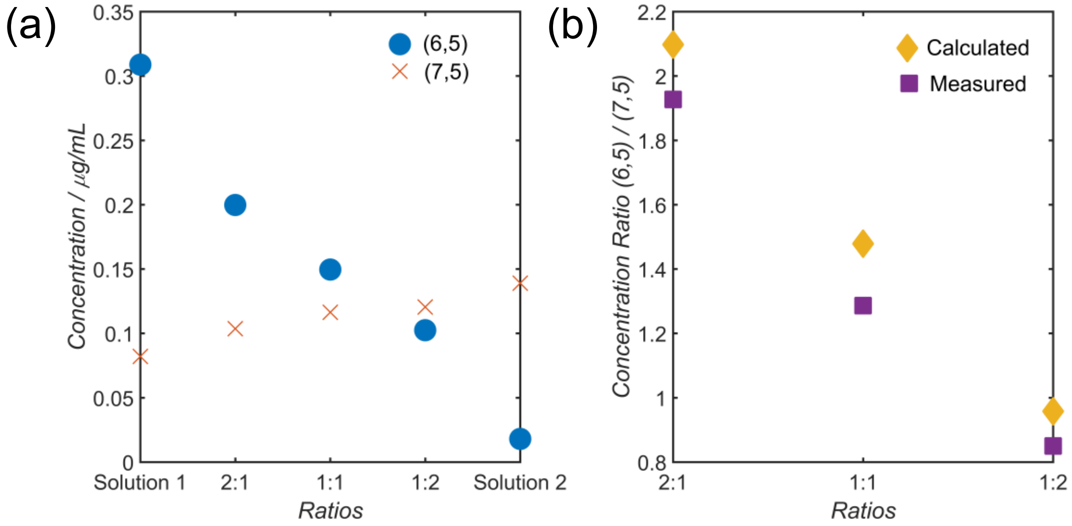

Fig. S8: The concentration of (6,5) and (7,5) in solution 1, solution 2 and different ratios thereof are shown in (a). The measured and calculated concentration ratio for different mixtures is shown in (b).

Polychiral suspensions for comparison of (n,m) abundance

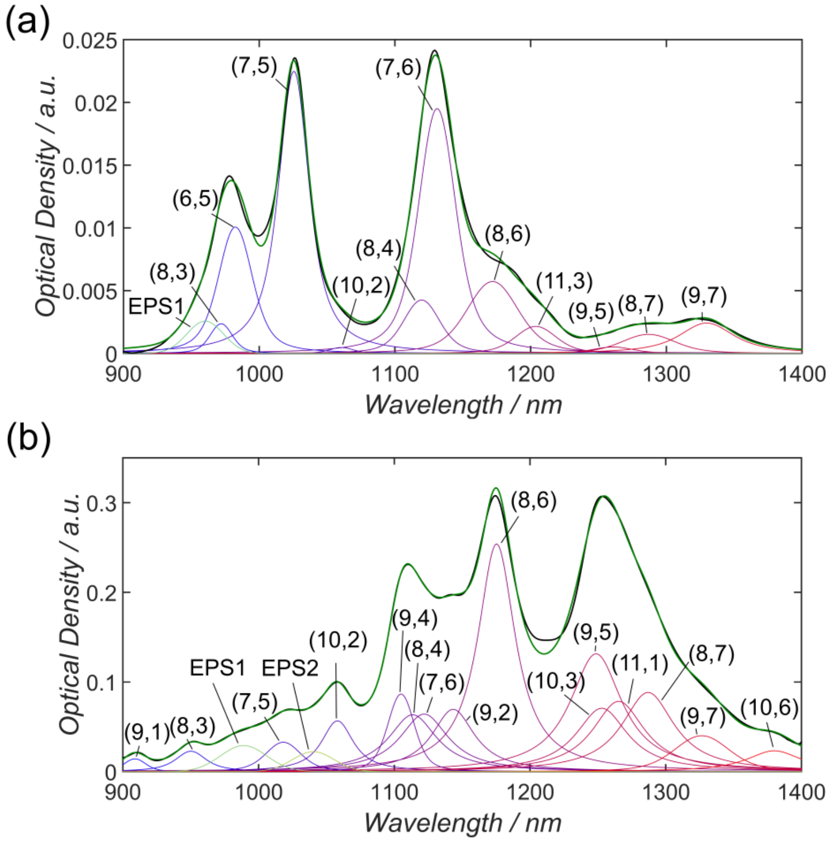

Fig. S9: Comparison of two different polychiral solutions (a and b). The background corrected spectrum (with the method presented by Naumov et al.(21)) is shown in black while the calculated spectrum is shown in green. Along with the different (n,m) species (using Voigtian line profiles), the exciton phonon sidebands (EPSs) were also considered during fitting.

Fit of polymer sorted (6,5)

Polymer sorted (6,5) solutions were fitted in the S_{11} region with three different line profiles: Gaussian (Fig. S10 (a)), Lorentzian (Fig. S10 (c)) and Voigtian (Fig. S10 (e)). Based on the S_{11} fit, the S_{22} region was fitted (Fig. S10 right column). Upon comparing the region around 600 nm for Lorentzian and Voigtian fits ((d) and (f)), it seems as if (6,4) is missing. Having a closer look at the wavelength regime from 700 to 800 nm, S_{22} of (10,2) needs be included for Lorentzian and Voigtian fits.

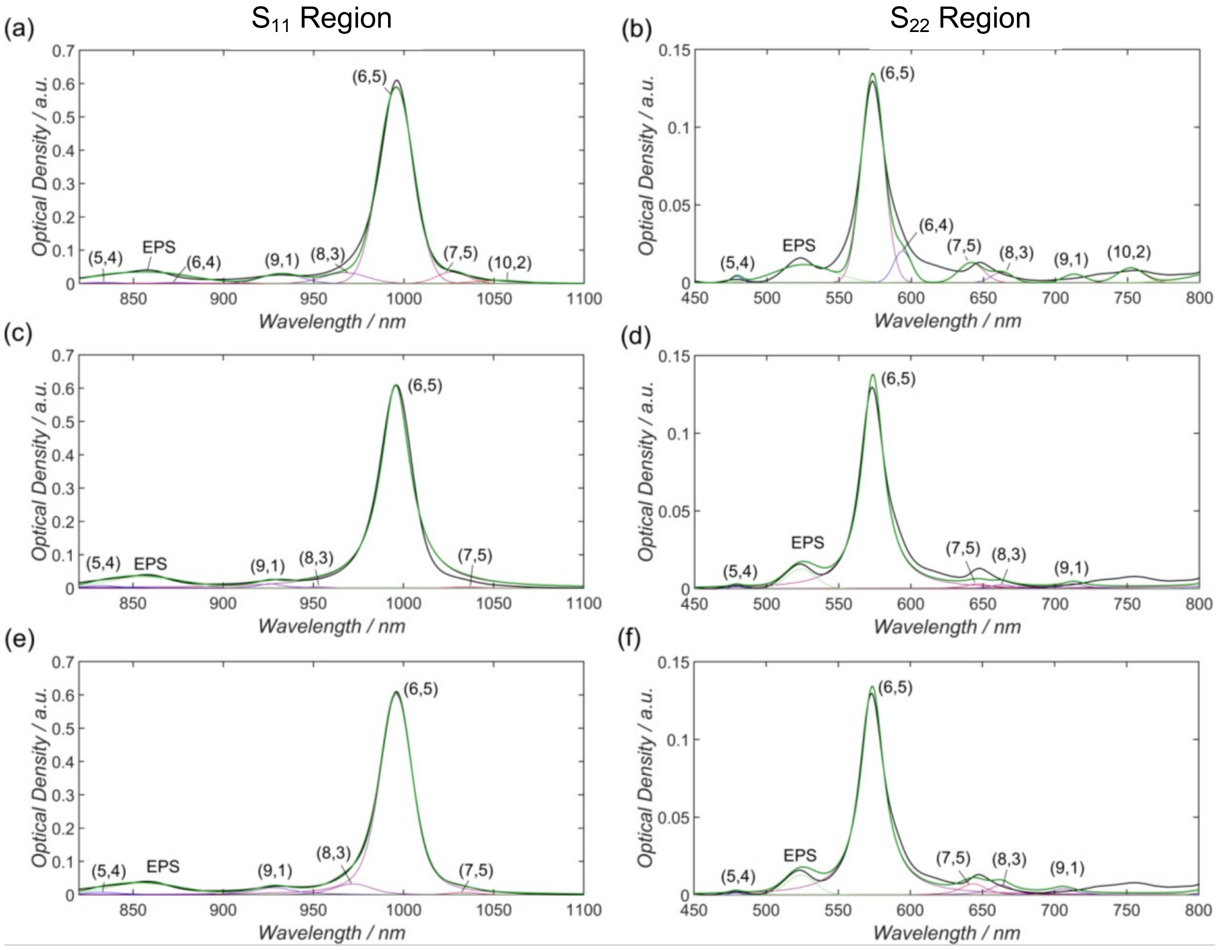

Fig. S10: (a) Gaussian, (c) Lorentzian and (e) Voigtian line profiles were used to fit the nearly monochiral (6,5) solution (black) in the S_{11} region. The calculated spectrum is shown in green with nSSE values of $4.02\text{x}10^{-3}$, $7.98\text{x}10^{-3}$ and $6.48\text{x}10^{-4}$ for Gaussian, Lorentzian and Voigtian fits, respectively. Based on this fit the S_{22} region was fitted (b), (d) and (f). The nSSE values for the entire region were calculated to be $7.52\text{x}10^{-3}$, $8.97\text{x}10^{-3}$ and $2.19\text{x}10^{-3}$ for Gaussian, Lorentzian and Voigtian profiles, respectively. For monochiral, polymer sorted SWCNT solutions Gaussian and Voigtian line profiles seem to be the best choice for fitting the absorption spectrum.

Fitting results

The fitting results of the solution absorption measurement shown in Figure 4 are listed in full detail in Table S2.

Table S2: Fitting results for different (n,m) species in their S11 (left column) S22 (right column) and M11 transition region.

SWCNT	Center (nm)		FWHM (nm)		Area		Spectral Weight (%)	
(7,6)	1125	652	38.80	26.36	15.10	3.89	26.88	25.82
(8,6)	1184	723	43.01	31.44	14.19	4.12	25.27	27.33
(9,5)	1254	676	46.39	28.10	8.40	1.63	14.95	10.82
(7,5)	1022	641	31.76	13.29	2.94	0.39	5.24	2.62
(10,2)	1057	745	25.80	31.76	0.51	0.29	0.90	1.92
(8,3)	953	668	17.48	21.12	0.13	0.05	0.24	0.36
(9,1)	914	688	16.05	23.04	0.18	0.09	0.32	0.62
(6,5)	983	577	21.01	18.91	0.46	0.18	0.82	1.23
(9,4)	1110	723	23.36	27.36	0.57	0.30	1.02	1.98
(8,4)	1113	588	24.00	20.14	1.63	0.65	2.89	4.31
(9,2)	1151	564	28.22	17.62	1.59	0.32	2.84	2.13
(8,7)	1284	737	50.18	32.88	6.64	1.95	11.82	12.93
(9,7)	1323	801	54.38	39.11	2.75	0.94	4.89	6.23
(10,6)	1383	761	58.09	35.83	0.88	0.26	1.57	1.71
(7,7)	510		11.80		$48.15\cdot10^{-3}$		0.086	
(8,5)	512		12.09		$19.51\cdot10^{-3}$		0.035	
(12,3)	608		24.34		0.14		0.25	

In Table S2 it can be seen that there are large variations in the FWHM, especially for (8,6), (9,5), (9,7) which are much larger than (8,3) or (9,1). This can be a result of starting values that wandered far astray from the 'correct' values or are an indication of missing (n,m) species in the fit. In our work we have used PL measurements to quantitatively determine the (n,m) species to be fitted and constrained the fit accordingly. For some users this might be an acceptable approach but will require the user to accept that some FWHM values might be significantly different to others. Alternatively, not seeing (n,m) species in PL is not necessarily confirmation that they do not exist in suspension and additional (n,m) species can be included in spectral regions with dramatically different FWHM values. In Figure S11 the same data has been fitted once again without constraining the (n,m) distribution by those species seen in PL. The reference data set extracted from Bachilo et al.(10) and a variation of the FWHM of ± 10 % was used. In this case the fitted FWHM follows to estimated FWHM trend closely, regardless of the initial estimation method used. However, once again for the suspension used in this analysis a fit based on a fixed FWHM in energy space is best.

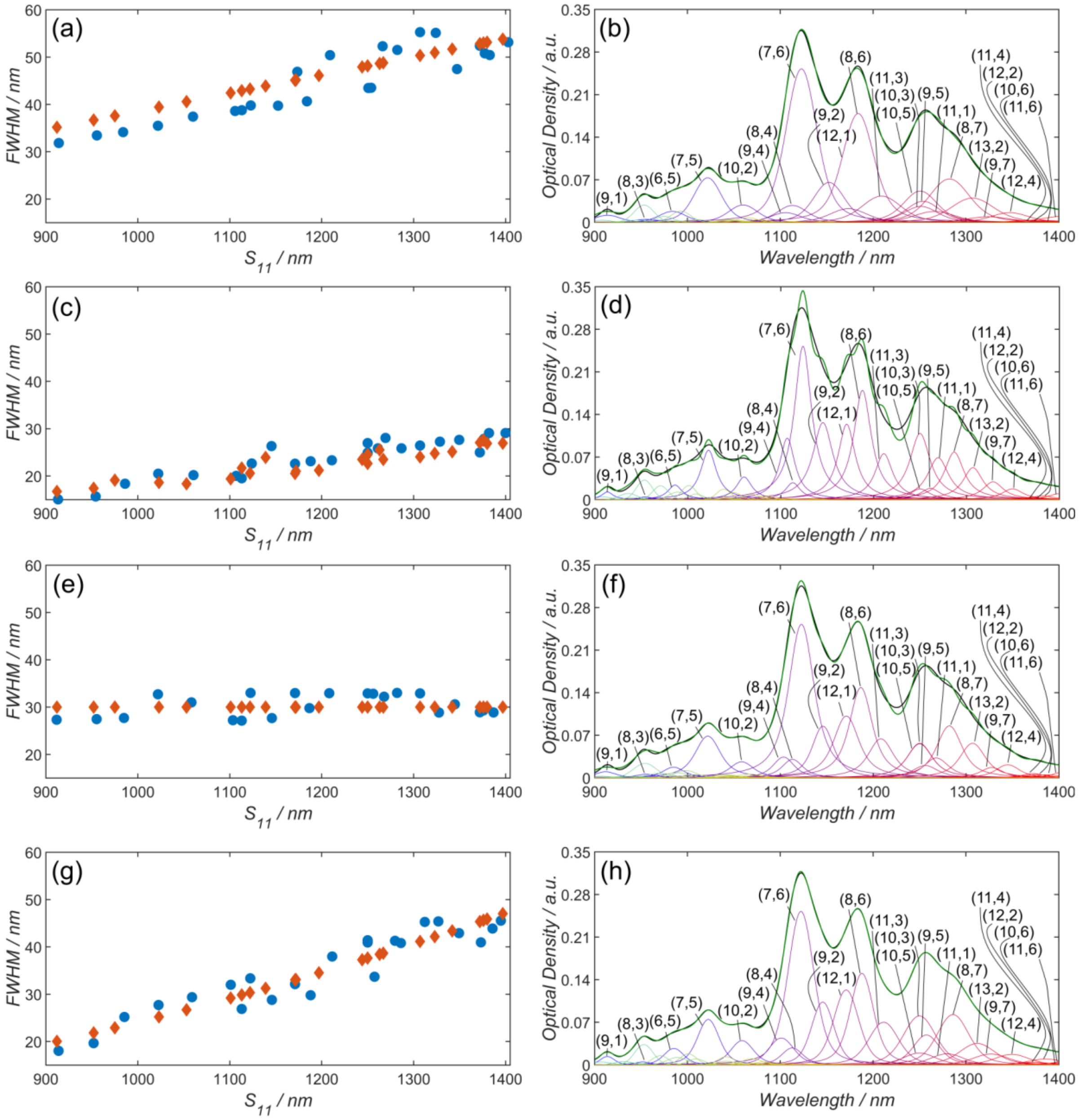

Fig. S11: Consideration of all (n,m) species provided by Bachilo et al.,(10) with a variation of the initial starting value for the FWHM of ± 10 %. The best fit was obtained for a FWHM constant in eV (g and h)(13) with a nSSE of $1.02\cdot10^{-4}$. Increasing nSSE values were obtained for fits based on FWHM calculated as a function of E_{11} (a and b),(20) a constant FWHM of 30 nm (e and f) and a diameter dependent FWHM (c and d)(19) with $6.33\cdot10^{-4}$, $1.73\cdot10^{-3}$ and $7.69\cdot10^{-3}$, respectively.

Constrained fitting of film spectra

Beyond spectroscopic characterization, SWCNTs are rarely used in solution but are rather incorporated into solid films, composites, fibers, etc. Upon forming a film of carbon nanotubes, the optical properties of the SWCNTs are commonly observed to red shift, the peaks become broader, and the contribution of scattering to the background as a result of bundling is significantly increased compared to solution absorption measurements.(23, 24) These effects result in greater spectral overlap which in turn increases the difficulty in accurately determining the (n,m) distribution within the film. Fitting film spectra of monochiral or chirality enriched SWCNTs can be straightforward as demonstrated by Berciaud et al.,(25) who used Lorentzian line profiles. For fitting polychiral film spectra, Tian et al. used Gaussian line profiles in their earlier work and Lorentzian line profiles in their later work, and assumed a constant FWHM (in eV).(26, 27) In combination with the aforementioned set of two norm equations, they obtained a set of linear equations that were easy to solve and then they verified the results of their fit using transmission electron microscopy (TEM). Since the formation of a solid film necessarily involves the filtration, deposition, capture, or otherwise extraction of nanotubes from a solution, a straightforward and reliable way of fitting a film spectrum is to constrain the spectral weights of each nanotube in the film fit to be very close to those determined from a fit of the solution that was used to fabricate the film. Hereby, the total area under the corresponding spectral region for the film ($\text{area}_{\text{total,Film}}$) is calculated using numerical integration and then multiplied by the concentration of each (n,m) species in solution to yield its corresponding area in the film using eq S36:

$$area_{i,Film} = area_{total,Film} \cdot c_{i,Solution} \cdot x_i \tag{S36}$$

In the examples which follow, the concentration was allowed to vary between ±10 %, with x_i being the correction factor for the concentration. Additionally, a maximum red-shift of each nanotube's peak position must be introduced, and can be varied depending on the expected shift. For example, an allowed peak shift of 0 – 40 nm for surfactant wrapped SWCNTs is in agreement with previous reports in the literature,(23) however, for polymer wrapped SWCNTs this value should be significantly smaller.(28) The FWHM of the nanotube peaks was allowed to broaden during fitting between a factor of 1 to 2.5 to account for nanotube bundling but the broadening factor was constrained to be the same for all nanotubes. Furthermore the EPS was allowed to broaden by a factor of 1 - 3 and was also constrained to be the same for all exciton phonon sidebands. The correction factor f_1 (eq S33) between (n,m) species was allowed to vary between -0.05 and 0.1 in agreement with our previous work.(9)

As stated for solution spectra and in accordance with Meier,(29) the shape of the background has a huge impact on the calculation of the absorption spectra. For film measurements on glass it is fairly easy to extend the measurement range beyond 1400 nm and therefore increase the long wavelength accuracy of the background correction methods of Tian et al. and Nair et al.(13, 26) Being able to constrain the fit based on a previous solution spectra and setting the change of the concentration to a reasonably small number therefore has two advantages: first, the fit of the film resembles the (n,m) distribution that was measured in solution previously. An example is provided in Fig. S12, where a Fano and Lorentzian shaped background results in the best fit using the (n,m) distribution determined from Figure 1 (d). Second, a bad agreement of measured and calculated film absorption spectra might be caused by an insufficient background correction and be corrected by the choice of a different background.

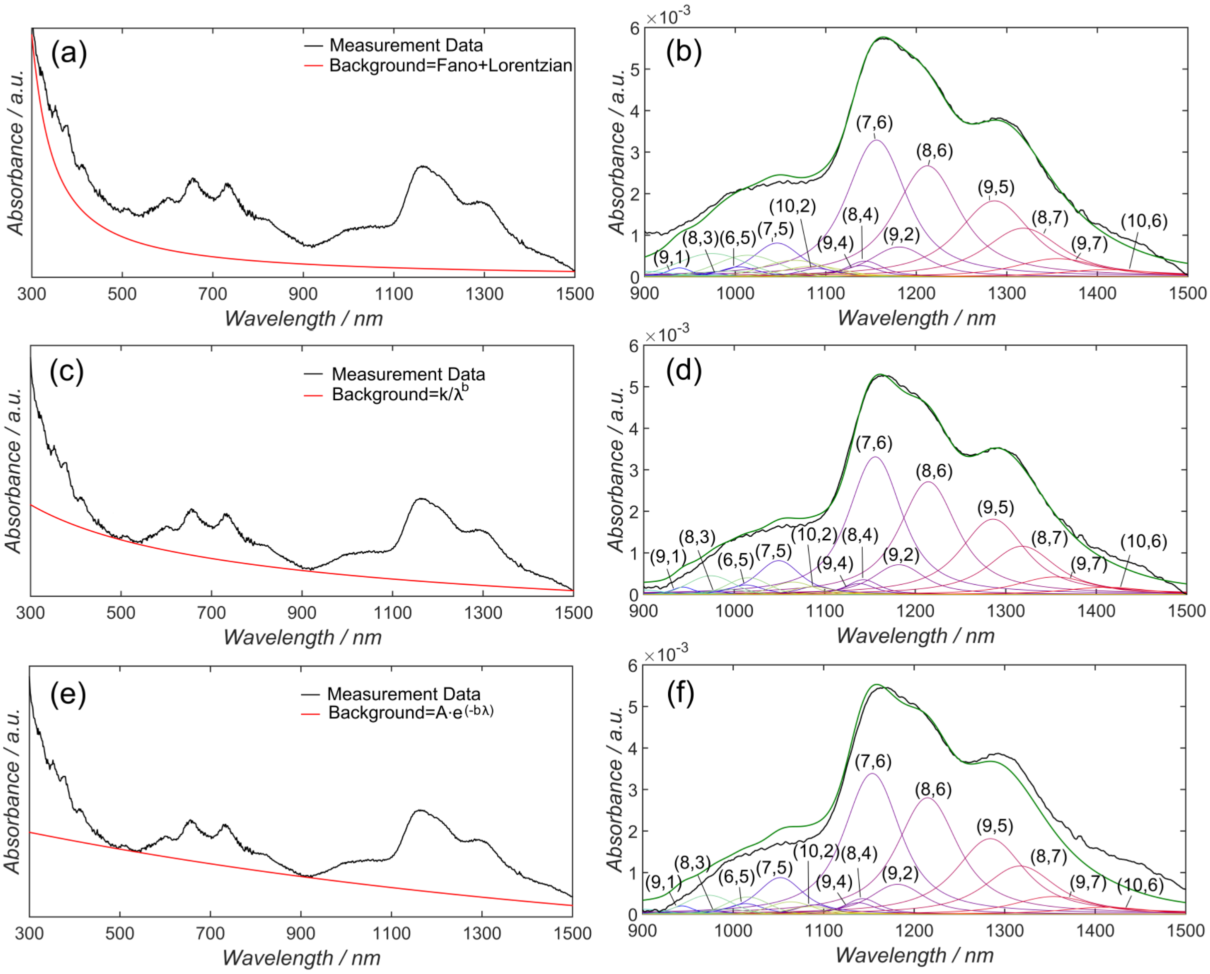

Fig. S12: The measured film absorption spectrum is shown in black and the different background subtraction methods in the left column (a, c and e) in red. In the right column, the calculated spectrum of the film is shown in green (b, d and f). The film fit is constrained by the solution fit shown in Figure 1 (d) by a relative (n,m) distribution change of ±10 %.

Although it is possible to improve the quality of the fit for these approaches, this would require an unreasonable increase of the relative concentration change. An example is shown in Fig. S13, where the relative concentration of each (n,m) species was allowed to vary ±100 % compared to the spectral concentration in solution. The effect of this improved fit quality on the spectral (n,m) concentrations in solution and film can also be seen in Table S3. In the case of Nair et al. (k/λ^b), a reduction in the concentration of (8,3) and (9,1) is apparent while for a background shape based on the work of Naumov et al. ($A\cdot e^{-\lambda\cdot b}$) the concentration of (6,5) is also drastically reduced and the spectral amounts of (9,7) and (10,6) are doubled. While small changes in the spectral area of species can occur due to (n,m) dependent differences in how the absorption properties alter during the bundling that occurs during film formation, or due to the absence of solvent, changes of ±100 % are most likely unphysical. This should be taken into account when adjusting parameters to obtain the best overall fit, and is one of the advantages of using the solution measurement to constrain the film fit.

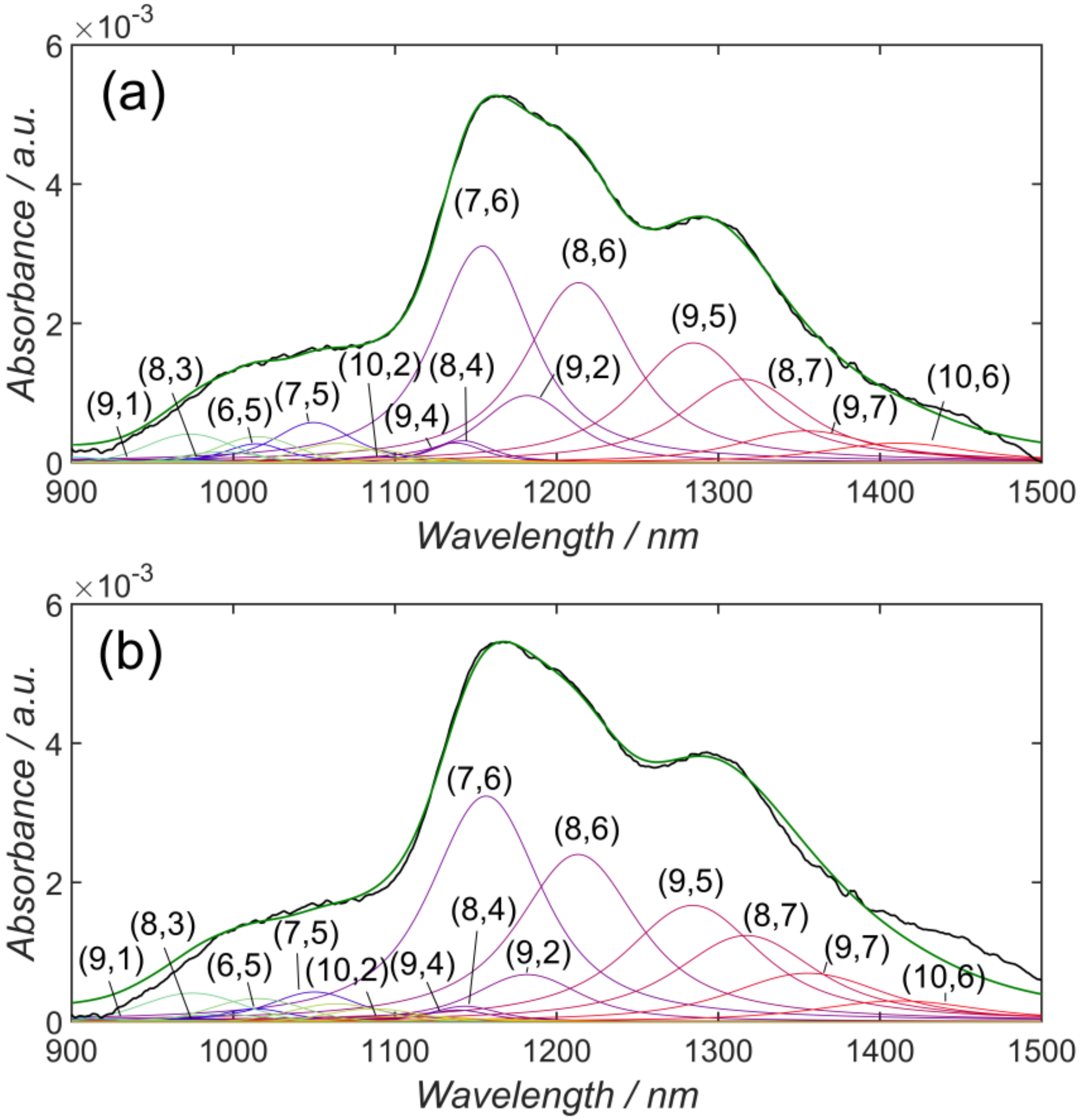

Fig. S13: Film absorption measurement (black) and calculated spectrum (green) for the background subtraction approaches of Nair et al. (a) and Naumov et al. (b) where the relative concentration change was set to vary within x_i = ± 100%.

The fitting of a film or solid spectrum may seem to be of little use when the spectral concentrations of nanotubes in the solution that was used to create it are already known. However, it becomes particularly important in the cases where the film is treated with some agent, or deposited on some material, that is also optically active (e.g., dyes, fluorescent markers, quantum dots, etc.), or when the embedding matrix is itself optically active (e.g., some polymers, glasses, etc.). In such cases, the ability to more reliably decongest the contributions of the nanotubes and the other material could be quite advantageous. In addition, surface induced doping can readily be seen, e.g. by a good fit of the S_{11} region and an underestimation of the S_{22} region. Another use, that pertains particularly to photovoltaics or light emitting devices wherein the nanotubes are (one of) the core light absorbing/emitting element(s), is in the calculation of quantum efficiency. For example, in our previous work we showed that it is possible to derive the (n,m)-resolved internal quantum efficiency of nanotubes in SWCNT/Fullerene-C_{60} solar cells even when there is very significant overlap in the spectra of both the optical absorption and the photocurrent.(9)

Variation of relative concentration change of (n,m) distribution for the fit of film absorption spectra

Table S3: Comparison of relative concentration of different (n,m) species in solution (left column) and film (right column) for different film absorption background subtractions and different concentration constraints (x_i).

	Spectral Weight (%)					
Background SWCNT	Fano + Lorentzian (x_i = ±10 %)		k / λ^b (x_i = ±100 %)		$A \cdot e^{-\lambda \cdot b}$ (x_i = ±100 %)	
(7,6)	25.89	25.37	25.89	24.60	25.89	26.26
(8,6)	24.08	22.92	24.08	22.76	24.08	21.68
(9,5)	16.50	17.66	16.50	17.03	16.50	16.97
(7,5)	5.54	4.92	5.54	3.57	5.54	2.71
(10,2)	1.04	0.92	1.04	0.412	1.04	0.17
(8,3)	0.22	0.23	0.22	0.14	0.22	0.15
(9,1)	0.60	0.65	0.60	0.01	0.60	0.04
(6,5)	1.19	1.11	1.19	1.29	1.19	0.89
(9,4)	1.22	1.19	1.22	1.28	1.22	0.77
(8,4)	1.71	1.72	1.71	1.46	1.71	1.06
(9,2)	5.13	5.12	5.13	7.06	5.13	5.08
(8,7)	10.83	11.66	10.83	12.24	10.83	12.98
(9,7)	4.22	4.55	4.22	4.87	4.22	7.65
(10,6)	1.83	1.97	1.83	3.28	1.83	3.60

Variables used during fitting

Table S4: List of all variables used during solution fitting.

Variable	Lower Limit	Starting Value	Upper Limit
Shift of center for any (n,m) species not assigned to a peak by the user (nm)	-5	0	20
Shift of center for any (n,m) assigned to a peak by the user (nm)	-5	0	5
Broadening of FWHM	0.8	1	1.3
Height guess	-	Method 1	-
Factor times most intense peak	0.8	0.95	1
Factor times height for Method 1	0.1	0.9	1
Factor times height for Method 2	0.1	1	1.2
Starting FWHM of Lorentzian for calculation of Voigitan FWHM (nm)	-	40	-
Ratio of Gaussian to Lorentzian FWHM for calculation of Voigtian FWHM	0.1	1	2
Change of ratio of Gaussian to Lorentzian FWHM	0.8	1	1.2
Cuvette path length for calculation of absolute concentration (cm)	-	0.2	-
Starting value for FWHM of Gaussian EPS (nm)	-	40	-
Broadening of initial FWHM of Gaussian EPS (nm)	0.5	1	2
Change of FWHM within different EPSs	0.9	1	1.1
Shift of EPS center position (eV)	-0.005	0	0.005
f_1 (in eq S33)	-0.07	0	0.07
Height ratio of S_{11}/S_{22}	1	4	5
Change of height within height ratios	0.8	1	1.2
Change of S_{22} height upon addition of metallic nanotubes	0.85	0.9	1.05
Change of S_{22} FWHM upon addition of metallic nanotubes	0.75	0.8	1.05
Change of EPS FWHM in S_{22} upon addition of metallic nanotubes	0.95	1	1.05
Change of EPS f_1 in S_{22} upon addition of metallic nanotubes	0.95	1	1.05
Change of ratio of Gaussian to Lorentzian FWHM upon addition of metallic nanotubes	0.95	1	1.05
Shift of metallic nanotube center position (nm)	-5	0	20
Broadening of initial FWHM for metallic nanotubes	0.6	1	1.3
Change of height for metallic nanotubes	0.1	1.2	1.6

Table S5: List of all variables used during film fitting.

Variable	Lower Limit	Starting Value	Upper Limit
Shift of center position (nm)	0	30	40
Concentration change ± (%)		10	
Broadening of FWHM	0.5	2	2.5
f_1 (in eq S33)	-0.05	0	0.1
Broadening of initial FWHM of Gaussian EPS (nm)	1	2	3
Consider surface doping?		Yes	

– This page intentionally left blank –

7.4 Supporting Information: Performance Enhancement of Polymer-Free Carbon Nanotube Solar Cells via Transfer Matrix Modeling

Characterization of the (6,5) SWCNT suspension

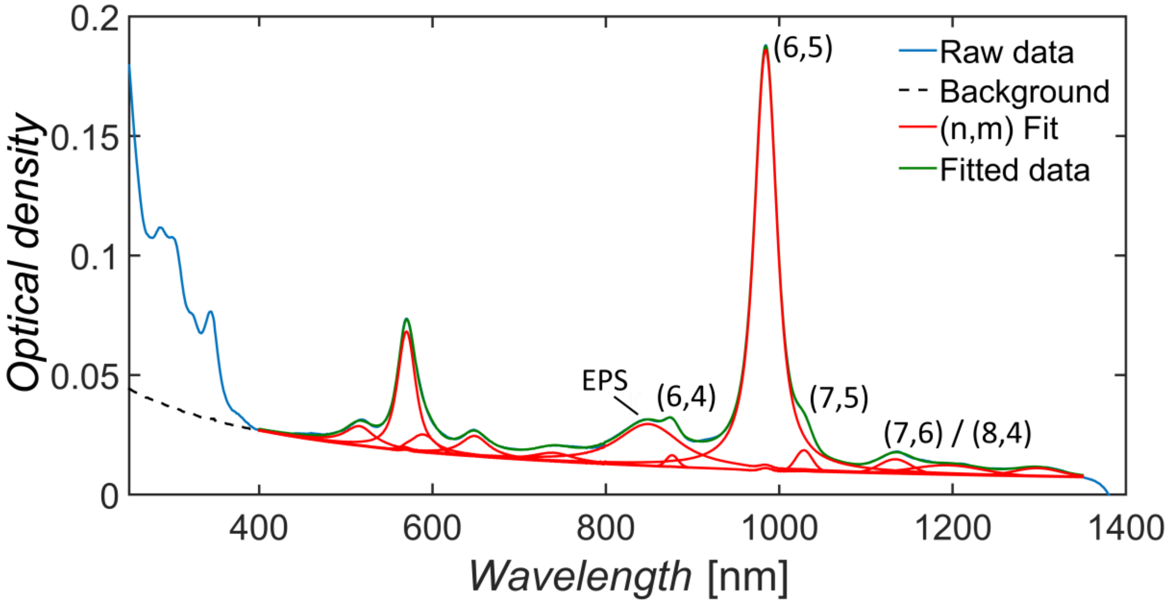

Figure S1. Absorption spectrum of the (6,5) SWCNT suspension in 1 wt % sodium cholate (SC) measured with a 2 mm path length, along with the background subtraction and peak fitting procedure used to determine purity. At 848 nm, the exciton-phonon sideband (EPS) is visible.

Using the procedure outline by Nair et al. the background was subtracted (black line) from the raw data (blue line).(13) Subsequently the software "Fityk" was used to fit Voigt functions to the (n,m) species in solution in the S_{11} (900 – 1300 nm) and S_{22} (550 – 900 nm) regions (red line) with peak positions provided in the literature so that the envelope of fitted peaks replicated the raw data with a mean χ^2 value of 3.95×10^{-5} (green line).(16) The peak at 848 nm is 0.2 eV shifted compared to the main S_{11} peak at 984 nm and therefore associated to a resonance effect emerging from absorption of light to a bound exciton-phonon state, as proposed by Perebeinos et al.(18) Using Equation S1 the purity of (6,5) was then calculated by taking only the S_{11} regime into account and assuming the absorbance cross section to be the same for all (n,m) species:

$$Purity\ (\%) = \frac{Area_{(6,5)}}{\sum_{i=1}^{\#(n,m)} Area_i} \tag{S1}$$

Characterization of the (6,5) SWCNT film

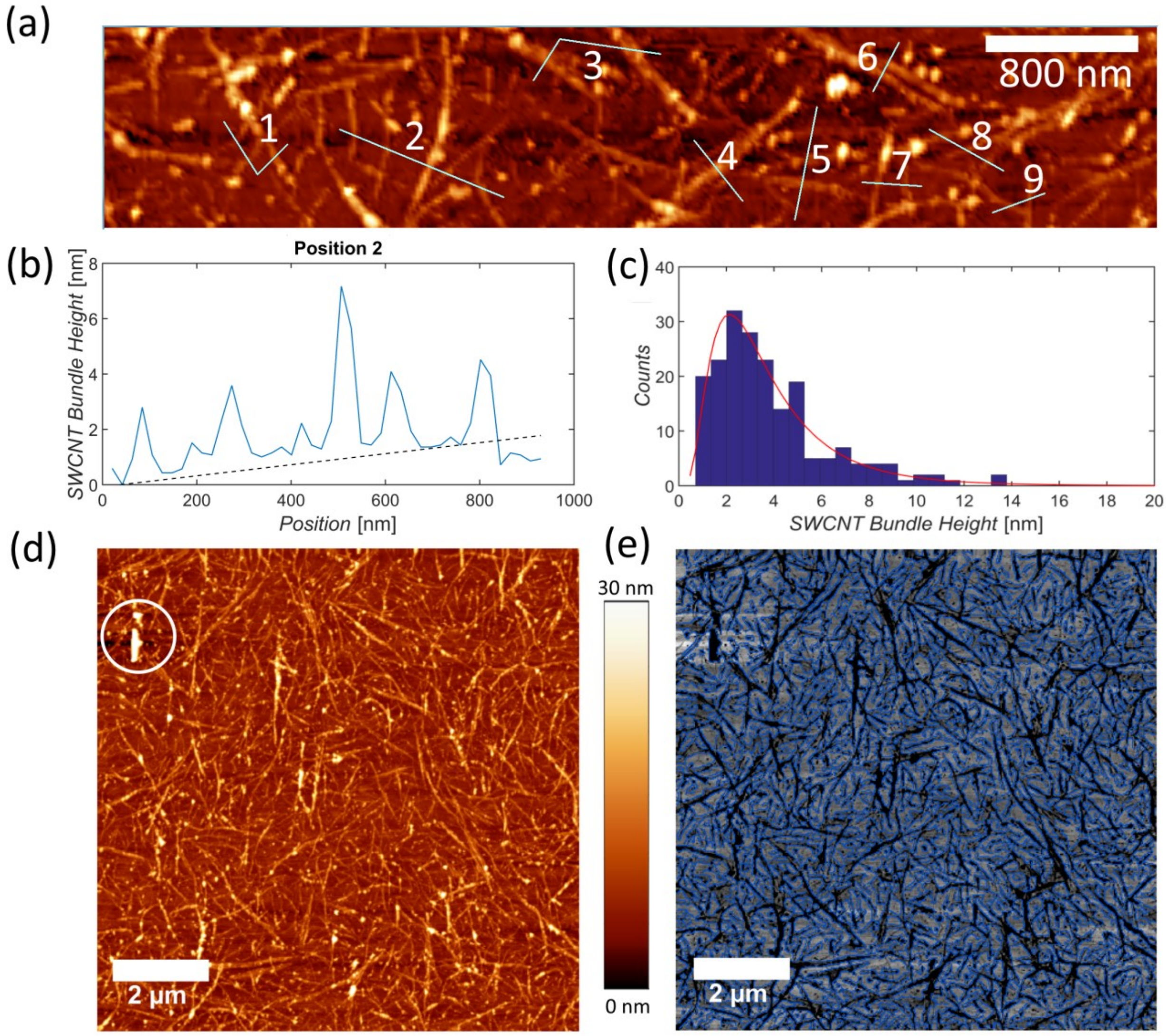

Figure S2. (a) The average bundle height was determined by cross-sectional analysis of 196 positions in the (6,5) SWCNT film. An example of the height analysis section and additional background subtraction (black dotted line) is shown in (b) and histogram in (c). SWCNT film coverage was calculated from 6 different AFM images taken from random spots across the film with a representative image shown in (d). Additionally highlighted in white circle is an object in the film with a height greater than 60 nm, as mentioned in the main text. Using the built in edge detection function “canny” in MATLAB® an overlay plot of the SWCNT edges and the original image was generated (e). This allowed the surface coverage to be calculated using the function “bwarea” to divide the number of SWCNT pixels by the total number in the image.

Photo-electron yield spectroscopy in air (PESA)

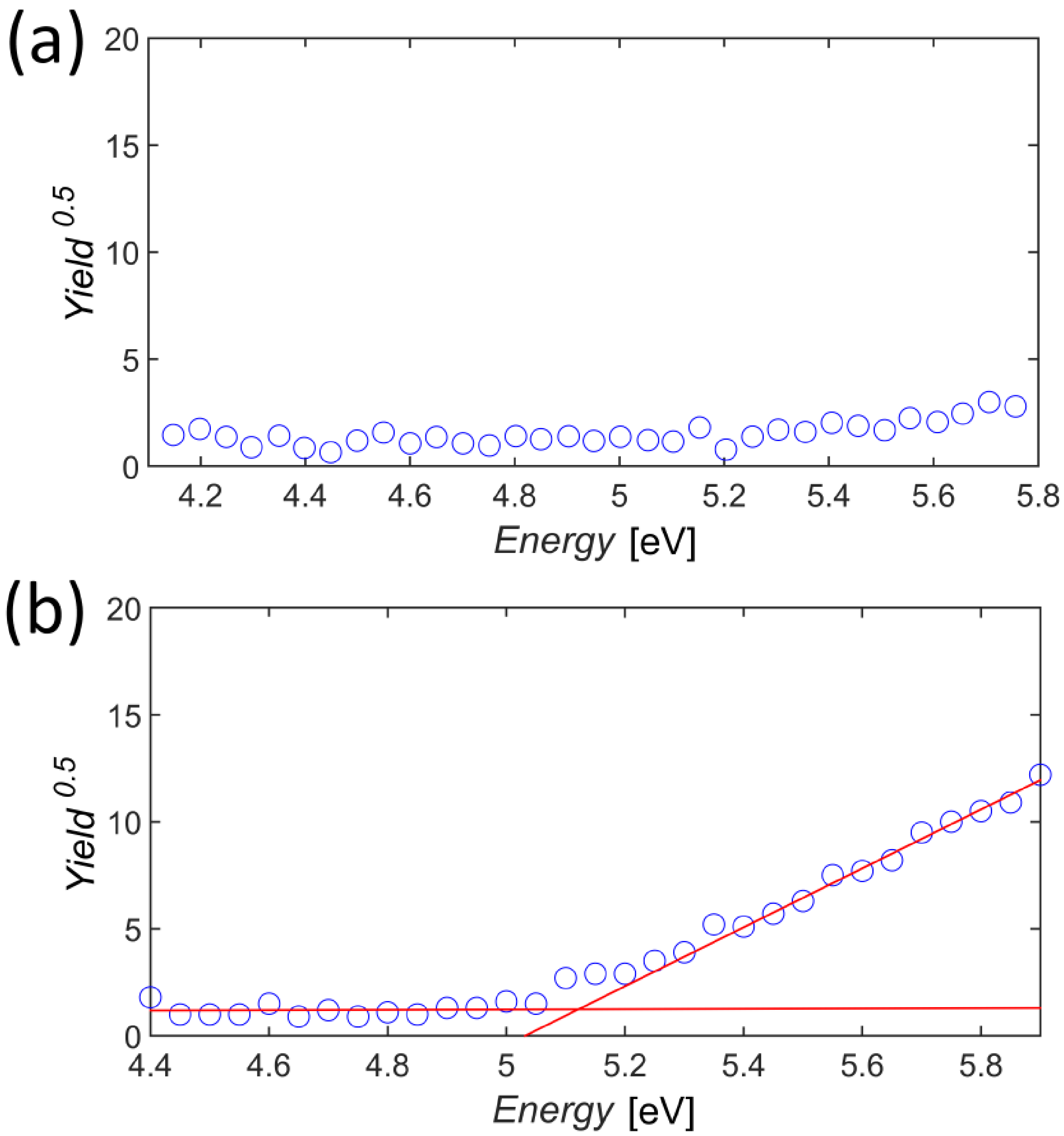

Figure S3. (a) Reference PESA measurement of ITO and (b) of a (6,5) SWCNT film on ITO. Both measurements were performed at 50 nW. The intersection of the background line and the photoemission curve provides a (6,5) SWCNT film HOMO energy of 5.1 eV.

Transfer Matrix Calculations

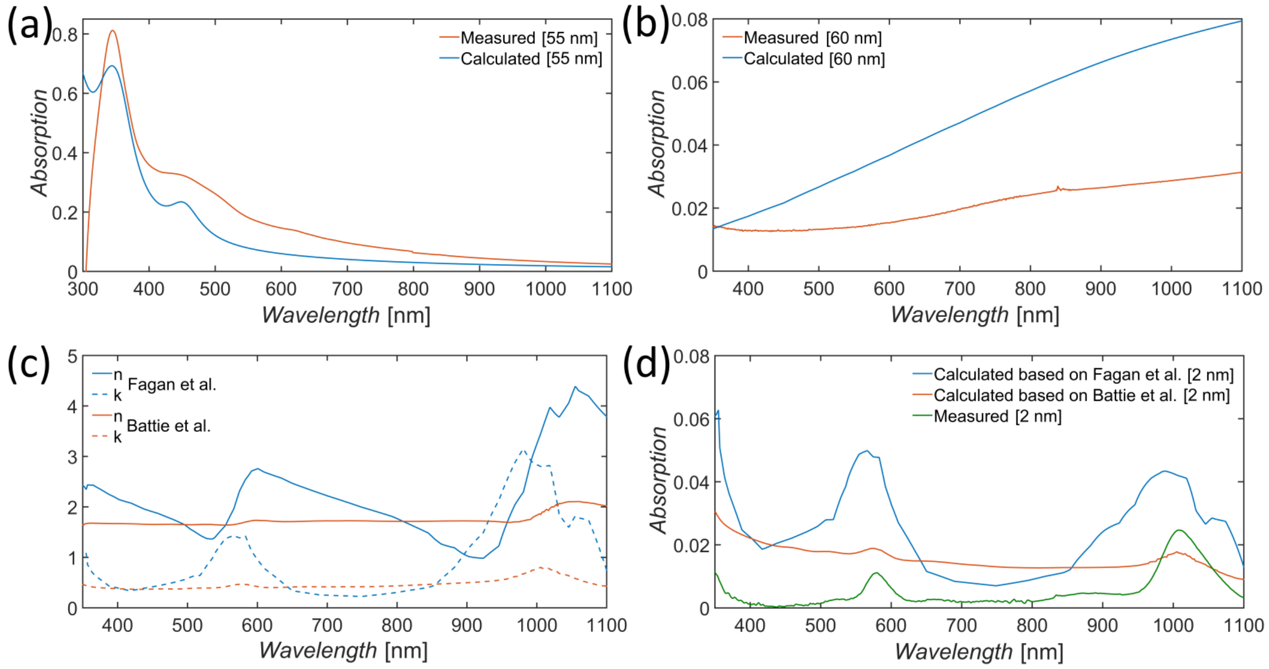

Figure S4. Comparison of calculated and measured absorption spectra for (a) C_{60} and (b) PEDOT:PSS on glass. The absorption of PEDOT:PSS is overestimated in the calculation but the overall curve shape matches the measurement. (c) Comparison of complex refractive indices for (6,5) SWCNTs (d) Comparison of the calculated and measured absorption of (6,5) SWCNTs on glass.

Transfer matrix calculations (TMCs) were performed with a modified version of the program provided by the McGehee Group at Stanford and outlined by Burkhard et al.(30) The complex refractive indices (n and k) for ITO were taken from the library provided along with the MATLAB® code. Optical data for PEDOT:PSS was provided by the producer H.C. Starck. The optical properties of the float glass were taken from the "Optical Glass – Data Sheets" provided by Schott AG and are available online at "refractiveindex.info". The properties of C_{60} were calculated based on the formula by Ren et al. and the values for Ag were taken from Palik et al.(31)

For (6,5) SWCNTs the complex refractive index from Fagan et al. and the intrinsic relative permittivity from Battie et al. was compared to absorption measurements of our films.(32) For Fagan's approach, the overall curve shape matches the one measured from the nanotube film fairly well. The problem is a broadening of S_{11}, an overestimate in intensity at S_{22} and the overall curve roughness. For Battie's approach, the intensity values are a better match, but there is a broad absorption throughout the entire spectrum instead of distinct absorption peaks as our film measurements indicate in Figure S4 (d). As discussed in the main text the discrepancies in calculated and measured SWCNT absorption is caused by different preparation techniques of the nanotubes. Due to these discrepancies and the low absorbance of the nanotube films of ~ 2.5 %, nanotube contribution was neglected in the TMCs in this study.

Thin film absorption I_{abs} in Figure S4 (a), Figure S4 (b) and Figure S4 (d) was calculated based on the complex refractive index ($\tilde{n} = n + i \cdot k$) of the different materials and with Equation S2, Equation S3 and Equation S4.(7) The simulated layer stack consisted of glass, the appropriate layer thicknesses stated in Figure S4, and air. The absorption coefficient α is determined by the complex part of the material's refractive index, k, and by the wavelength, λ:

$$\alpha(x, \lambda) = \frac{4 \cdot \pi \cdot k(x, \lambda)}{\lambda} \tag{S2}$$

The absorption of a specific material was then calculated based on the local absorption rate, β:

$$\beta(x, \lambda) = \alpha(x, \lambda) \cdot n(x, \lambda) \cdot |E|^2 \tag{S3}$$

$$I_{abs}(\lambda) = \int \beta(x, \lambda)\, dx \tag{S4}$$

The exciton generation rate, G, is calculated based on the local energy absorption, Q, at each position and wavelength, with the local energy absorption being:

$$Q(x, \lambda) = \beta(x, \lambda) \cdot AM1.5, \tag{S5}$$

and

$$AM1.5 = \frac{1}{2} c \varepsilon_0 |E_0^+(\lambda)|^2 \tag{S6}$$

with c the speed of light, ε_0 permittivity of free space and $|E_0^+(\lambda)|^2$ the incident electric field, G was determined by:

$$G = \iint \frac{Q(x, \lambda) \cdot \lambda}{h \cdot c} d\lambda dx, \tag{S7}$$

where h is Planck's constant and c is the speed of light.(7)

Parametric Study

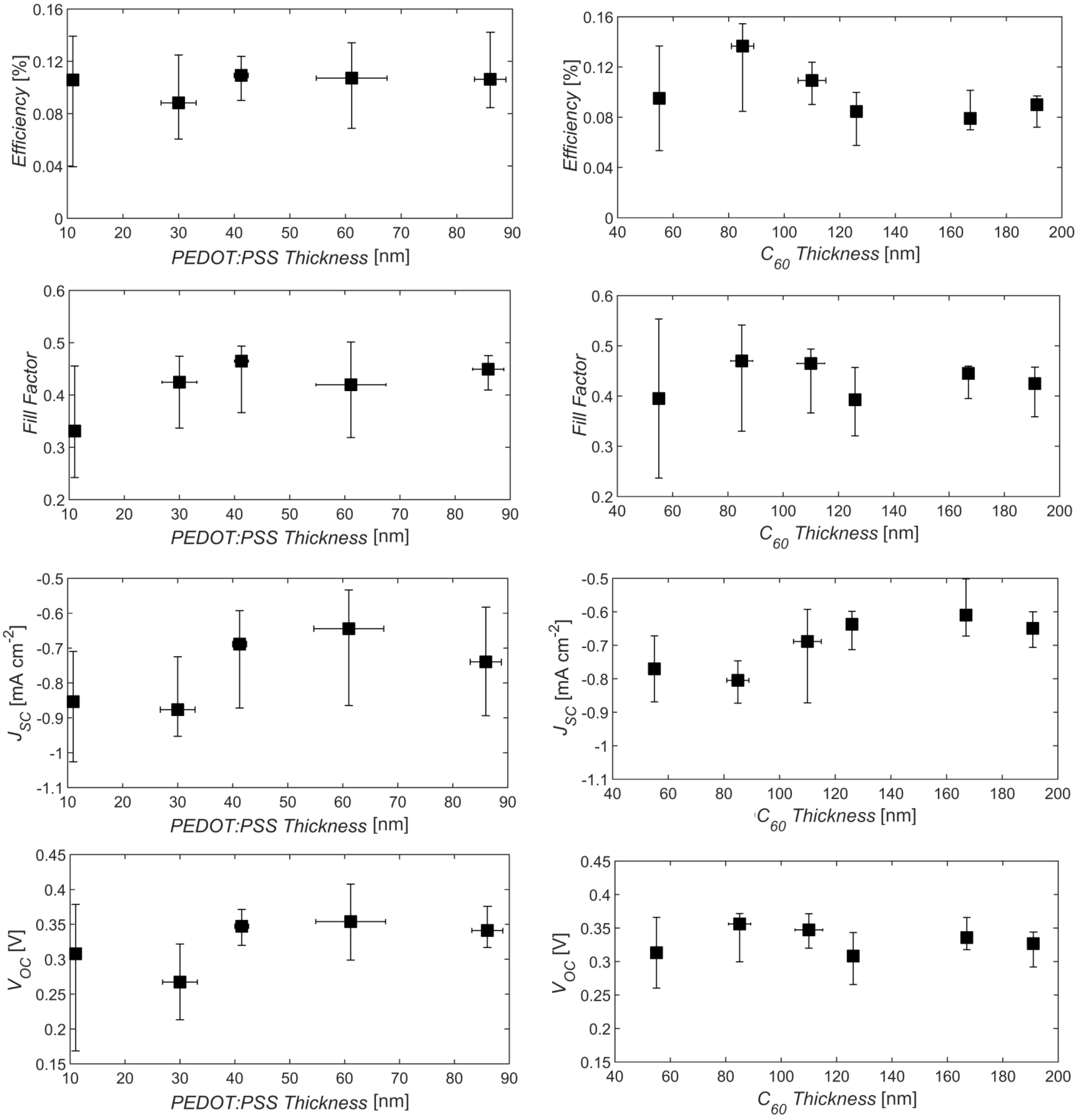

Figure S5. Part 1 of the detailed median results for the parametric study of PEDOT:PSS and C_{60} thicknesses shown in Figure 4 (a) and Figure 4 (b) of the main text.

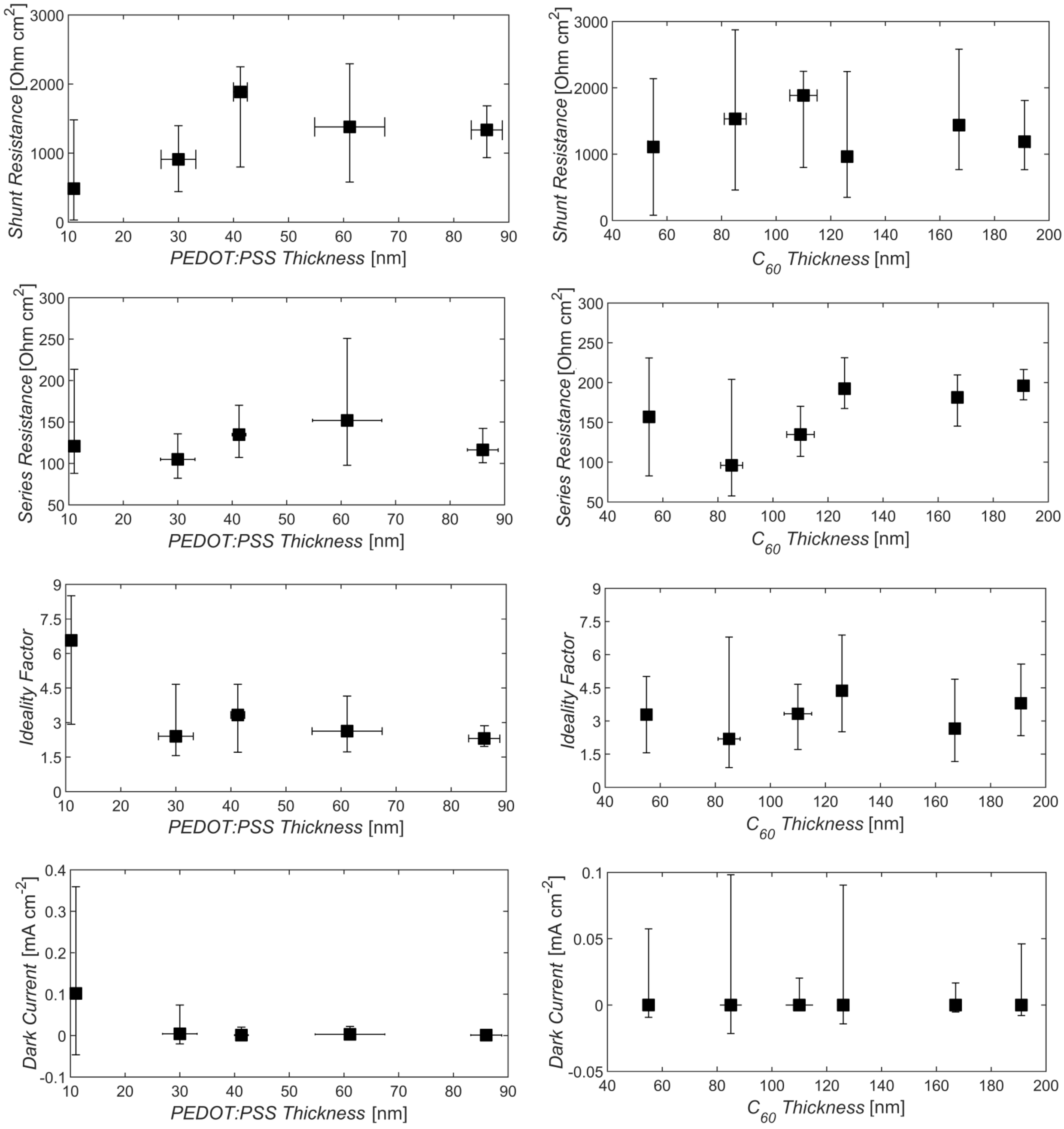

Figure S6. Part 2 of the detailed median results for the parametric study of PEDOT:PSS and C$_{60}$ thicknesses shown in Figure 4 (a) and Figure 4 (b) of the main text.

J-V curve for solar cell without PEDOT:PSS

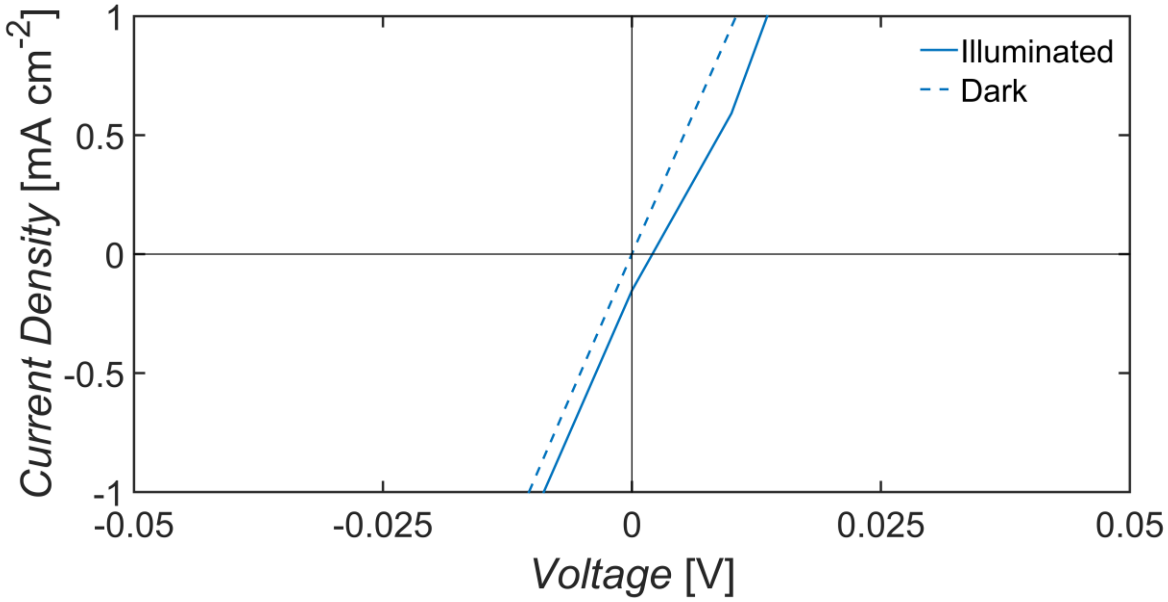

Figure S7. *J-V* curve of a solar cell without PEDOT:PSS (stack design: ITO/SWCNTs/C_{60}/Ag).

External quantum efficiency (EQE) analysis

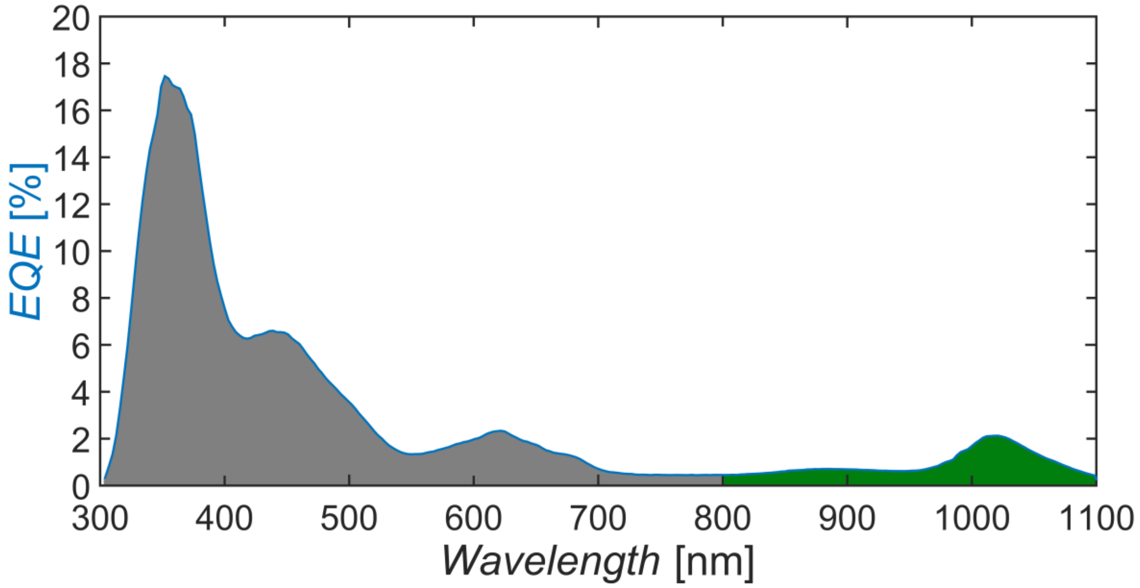

Figure S8. EQE spectrum of a solar cell with ~ 41 nm PEDOT:PSS and ~ 85 nm C_{60}. The photocurrent contribution from C_{60} is highlighted in grey, while the contribution from the S_{11} region of the SWCNTs is highlighted in green.

Optimization of $|E|^2$ at (6,5) absorption

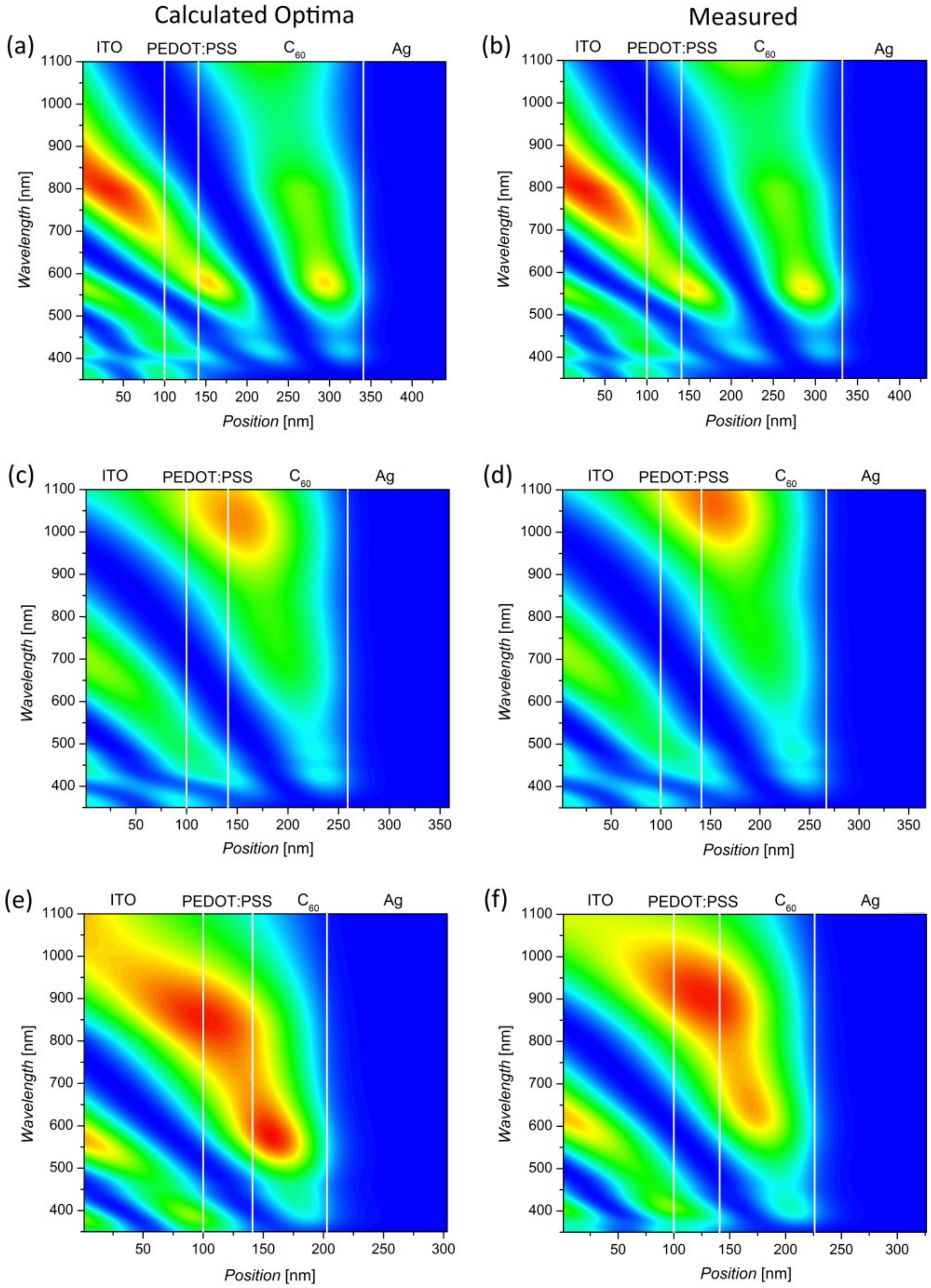

Figure S9. Comparison of $|E|^2$ for calculated optima and actual solar cells with varying thicknesses of C_{60} for a maximum $|E|^2$ at S_{22} (a) and (b), 200 and 191 nm C_{60}, respectively, S_{11} (c) and (d), 118 and 126 nm of C_{60}, respectively, and equal $|E|^2$ at both transitions (e) and (f), 62 and 85 nm of C_{60}, respectively, throughout the solar cell stack.

Exciton generation rate

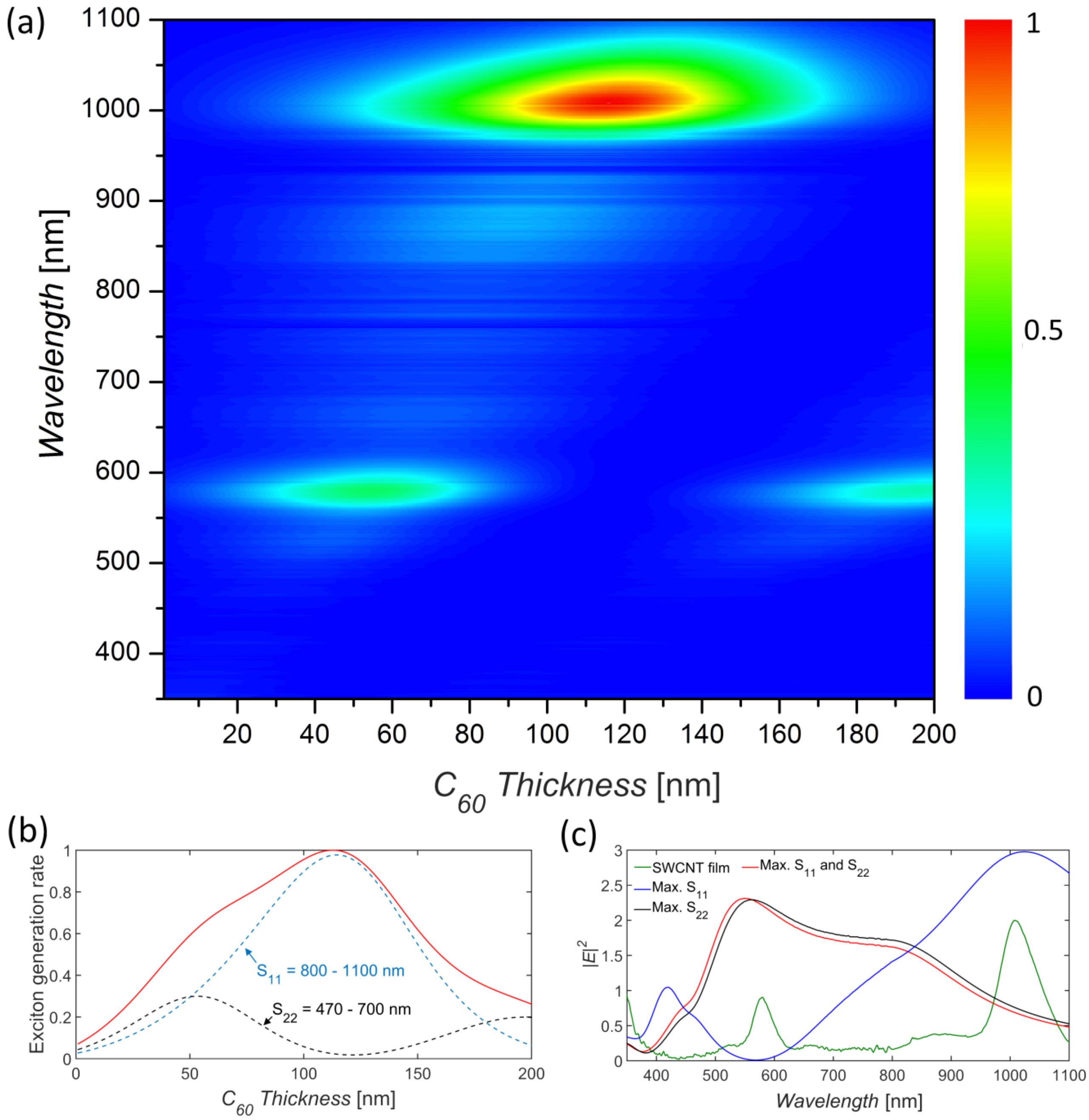

Figure S10. (a) Normalized exciton generation rate for 41 nm PEDOT:PSS and varying thicknesses of C_{60}. (b) In order to optimize light absorption at S_{11} and S_{22} of the (6,5) nanotube film, the exciton generation rate was integrated between 800 to 1100 nm (blue dashed curve) and 470 to 700 nm (black dashed curve), respectively. The intersection points in (b) resemble equal contribution from S_{11} and S_{22} to the exciton generation rate (50 nm and 180 nm). The maximum contribution from S_{22} and S_{11} was found to occur at 53 and 198 nm, and 114 nm of C_{60}, respectively. The corresponding electric fields are shown in (c) for the calculated optima at the intersection of PEDOT:PSS and C_{60}.

Determination of internal quantum efficiency (IQE)

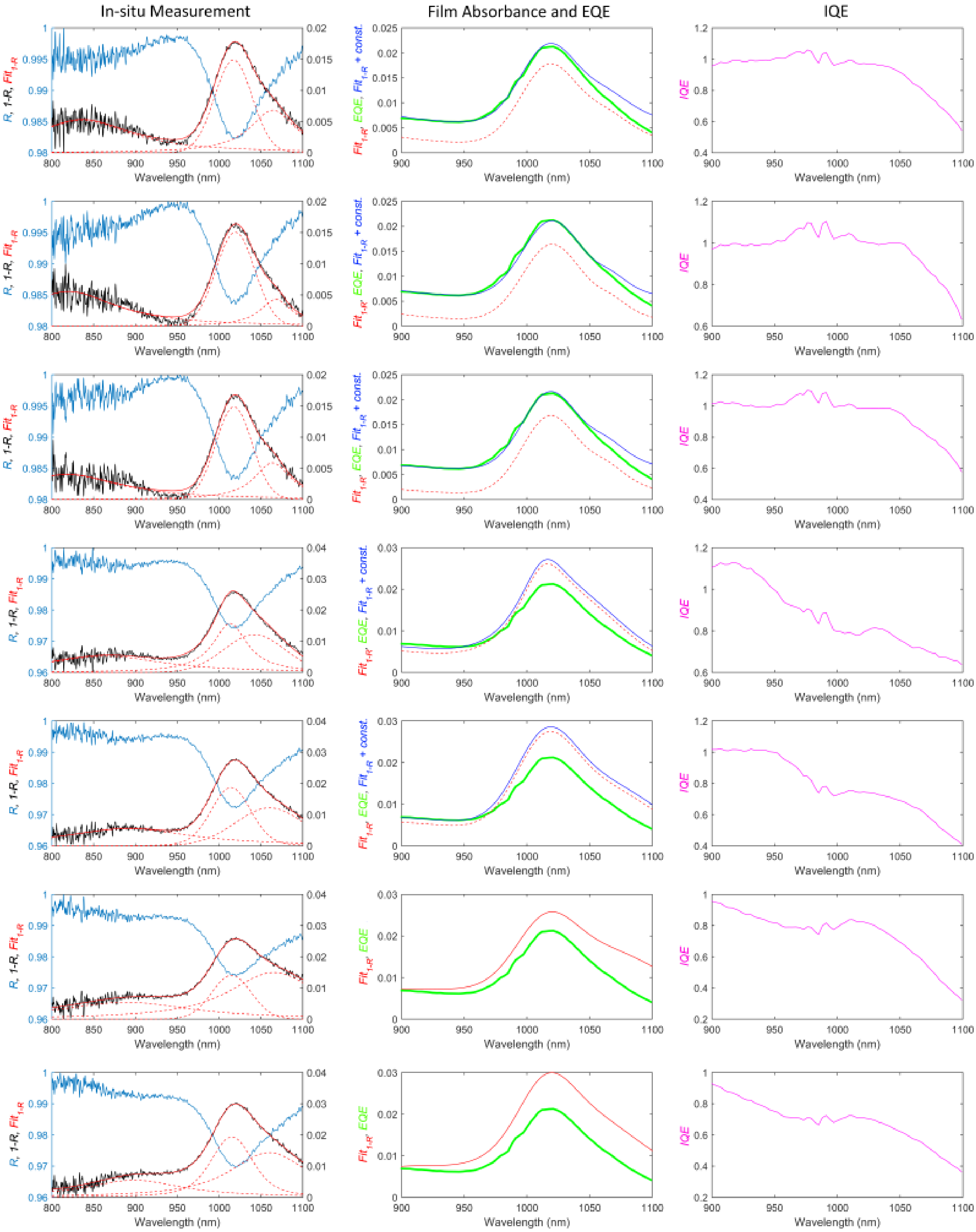

Figure S11. The internal quantum efficiency (IQE) was determined by measuring the absorbance of the nanotube film *in situ* in each final solar cell device. In order to measure absorbance only from the SWCNTs, the background was measured at the solar cell stack (Glass/ITO/PEDOT:PSS/C_{60}/Ag) without SWCNTs. Absorbance was obtained from reflectance (R) measurements in the active area (blue curve), where absorbance is 1-R (black curve). Due to the noisy signal the reflectance curve was manually shifted to have a maximum value of 1. The absorbance curve was then fitted with three Voigt profiles using the software “Fityk” (red curve). Underestimating the background correction necessitated addition of a constant value for some fitted curves (blue corrected curve in middle column) to guarantee a reliable IQE calculation without overestimating the true value. Due to the uncertainty caused by the noisy signal below 900 nm, EQE (green) and IQE (purple) curves are displayed in the range from 900 to 1100 nm.

The technique of measuring the SWCNT absorption *in situ via* reflectance measurements was adopted from Bindl et al.(33) It was outlined by Armin et al.(34) that a reliable IQE calculation should follow the subsequent routine: EQE measurement, reflectance measurement of whole cell and then transfer matrix calculation to determine absorption in each layer and overall parasitic absorption. Without considering the parasitic absorption the “IQE-like” curve is spectrally not flat and underestimates the true IQE. Having well defined refractive indices for all materials used, this is a promising approach to accurately calculate IQE.

Without the refractive index of (6,5) SWCNTs we were not able to perform a transfer matrix calculation to determine the parasitic absorption within the solar cell. Instead, we calculated IQE based on EQE and reflectance measurements with the likelihood of underestimating true IQE. For the first five measurements, a constant value was added to the absorbance curve (most likely due to an insufficient background correction) in order to yield a reliable IQE calculation and not overestimate it. IQE at the S_{11} transition of the (6,5) SWCNTs around 1021 nm was then determined to be 86 ± 12 % by dividing EQE and film absorbance. The measured and calculated J_{SC} (based on Equation 1) were within 6.7 %.

Enrichment of (6,5) SWCNTs

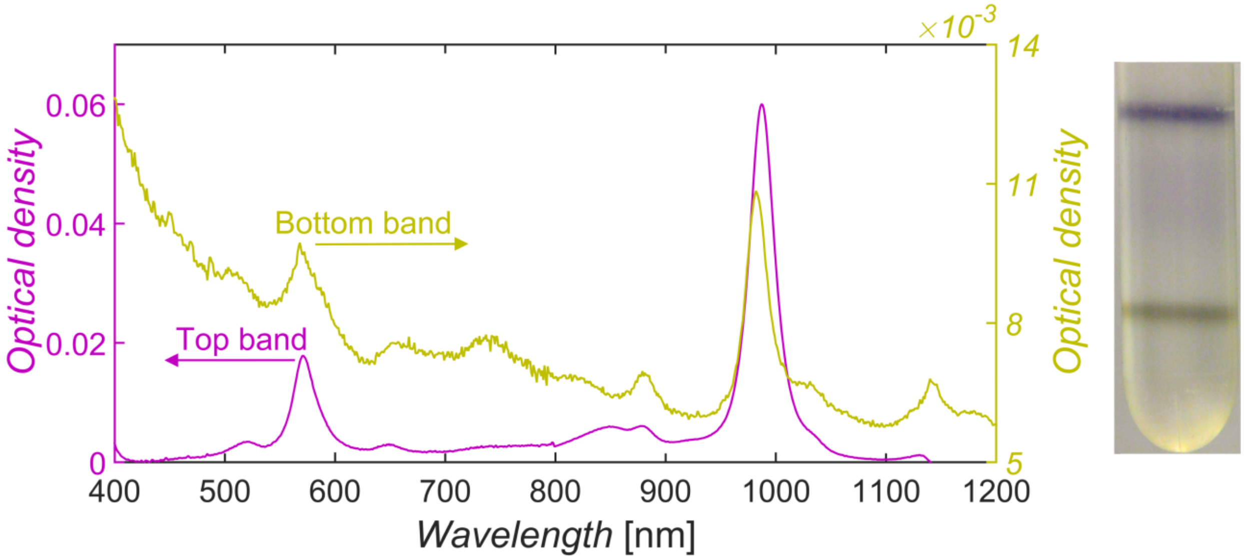

Figure S12. Absorption measurements of the two bands obtained from the as-prepared (6,5) suspension by density ultracentrifugation in 1 wt % SC using a 2 mm path length.

Determination of series resistance (R_S)

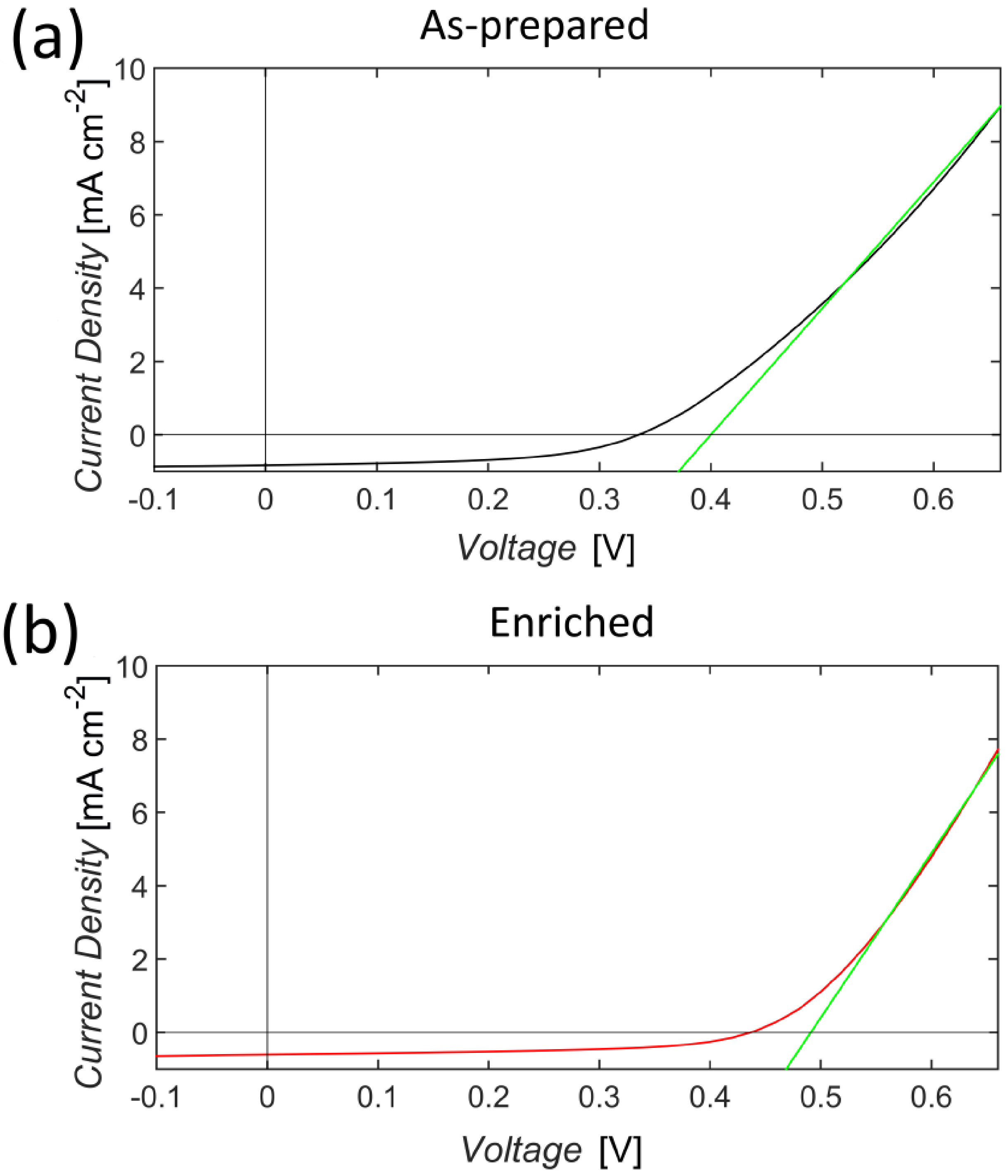

Figure S13. In order to calculate the series resistance a line was fitted to the linear regime of the *J-V* curves (green) of the as-prepared and enriched (6,5) material. The inverse of the slope of the green curve equals the series resistance.

Light Intensity Variation

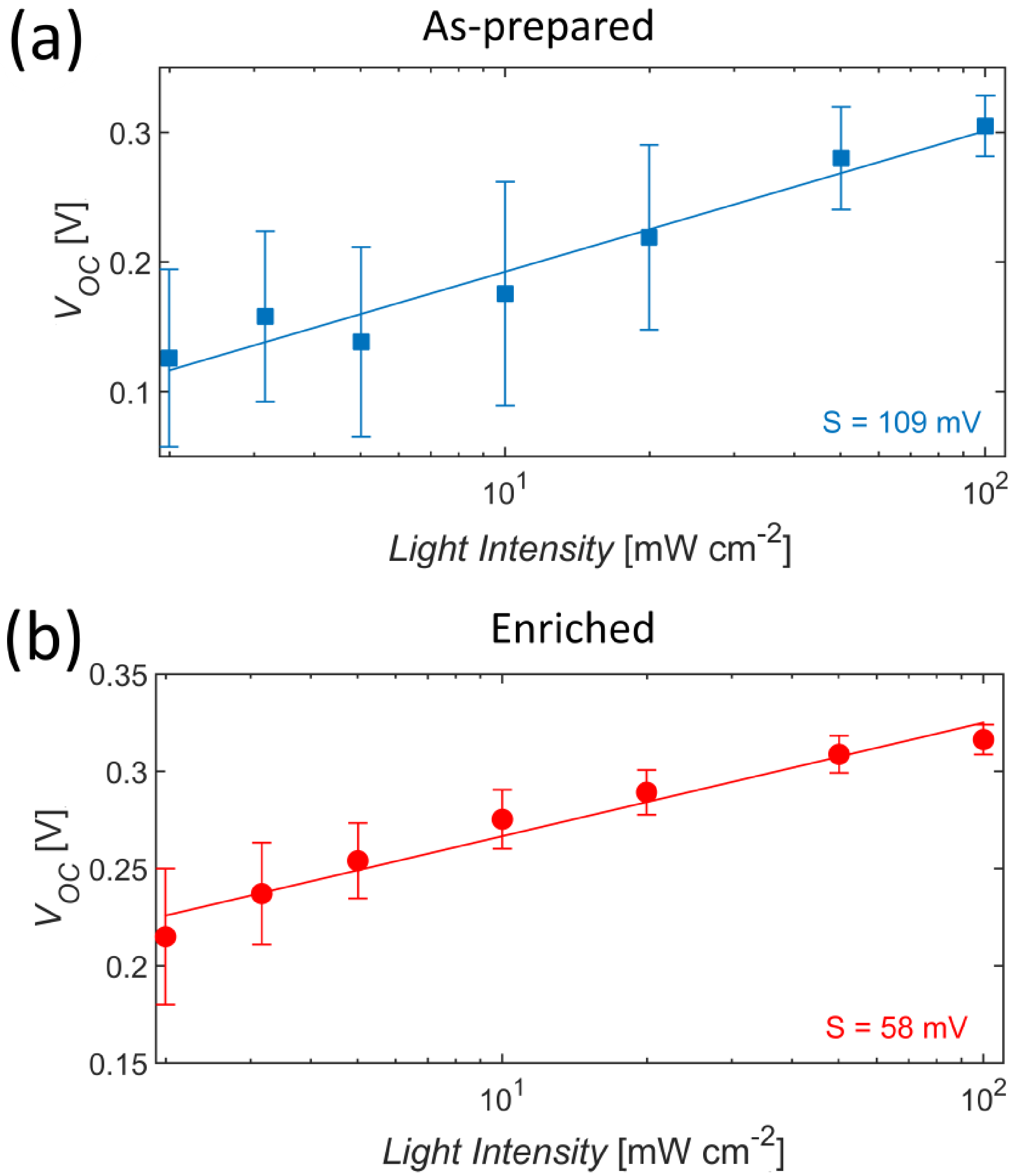

Figure S14. (a) and (b) V_{OC} values measured for varying light intensity from solar cells made from as-prepared and enriched (6,5) material. V_{OC} was set equal to $S \cdot \ln(I) + \text{constant}$, with S being the slope under investigation.

Comparison of a solar cell with and without SWCNTs

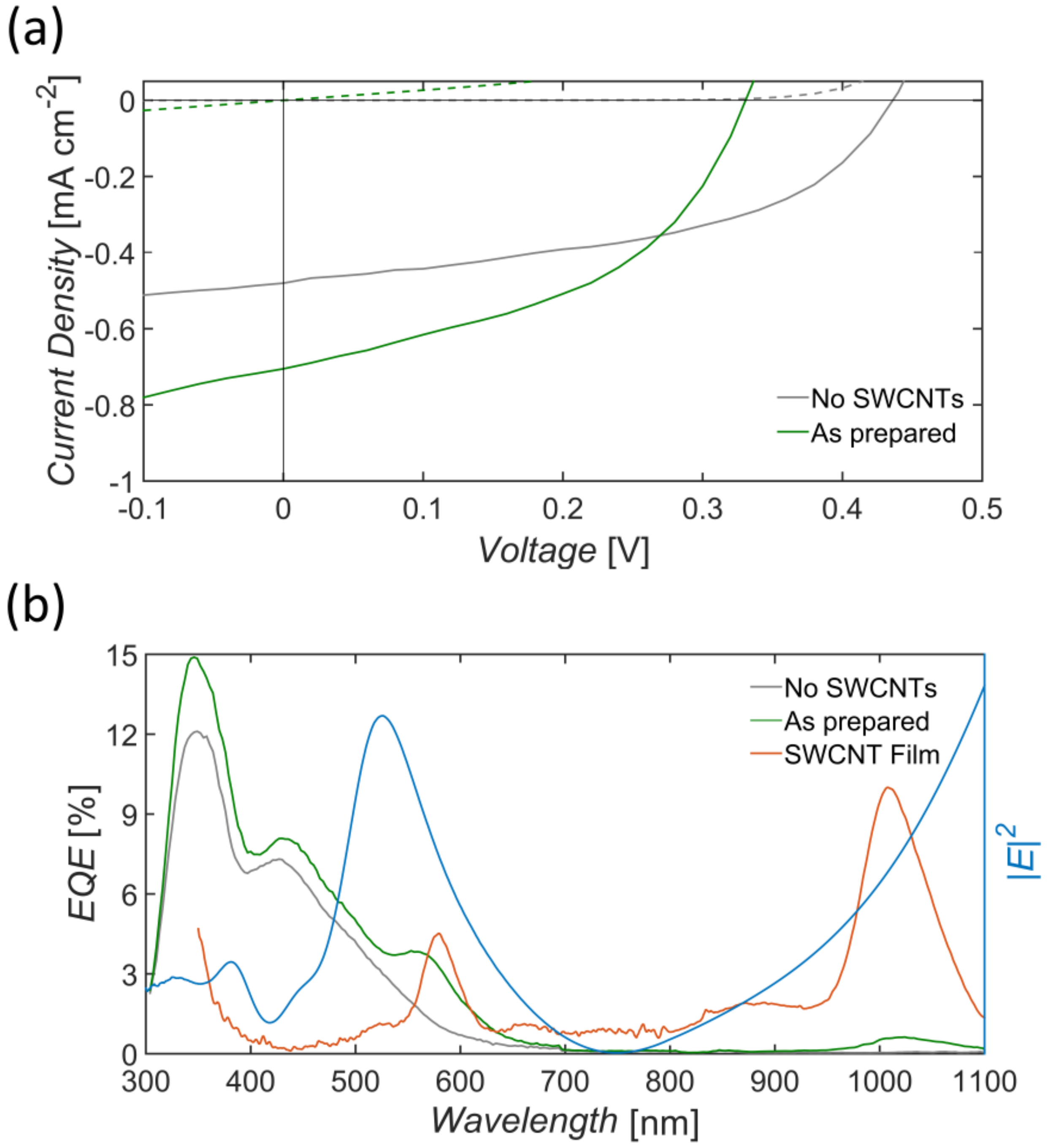

Figure S15. Comparison of *J-V* curves (a) and EQE measurements (b) for solar cells with 41 nm PEDOT:PSS and 167 nm C_{60} with (green) and without (grey) as prepared (6,5) SWCNTs. For the solar cell without SWCNTs the V_{OC} is comparable to (6,5) enriched devices which demonstrates the influence of metallic SWCNTs on the overall device performance as discussed in the main text. The "C_{60}-only" solar cell has a smaller current density than solar cells with as prepared SWCNTs. The increase in J_{SC} in (a) is also displayed in (b) by an increased EQE and resembles the influence of SWCNTs on the current generation. In addition to quantum efficiencies, $|E|^2$ and the SWCNT film absorbance were also plotted to demonstrate the effect of light absorption at S_{22} and S_{11} on the EQE spectrum of solar cells with nanotubes.

– This page intentionally left blank –

7.5 Supporting Information: Probing the Diameter Limit of Single Walled Carbon Nanotubes in SWCNT:Fullerene Solar Cells

Photo-electron yield spectroscopy in air (PESA)

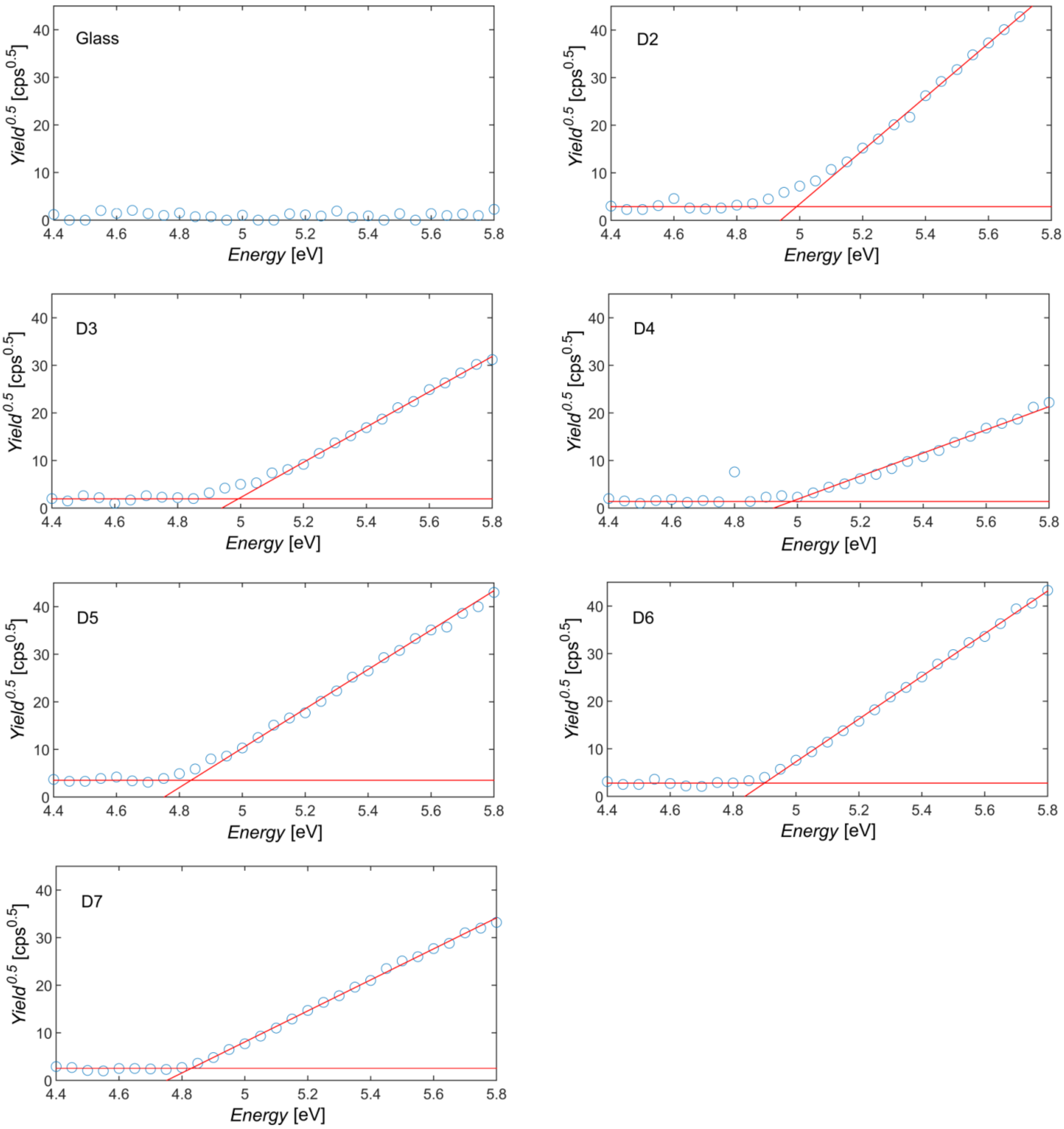

Figure S1. All PESA measurements were performed on BS 7011 microscope glass slides (VWR) at 800 nW. The intersection of the background line and the photoemission curve was used to determine the HOMO level of the different SWCNT films.

Photoluminescence contour map and dispersion / film absorbance fit of D1

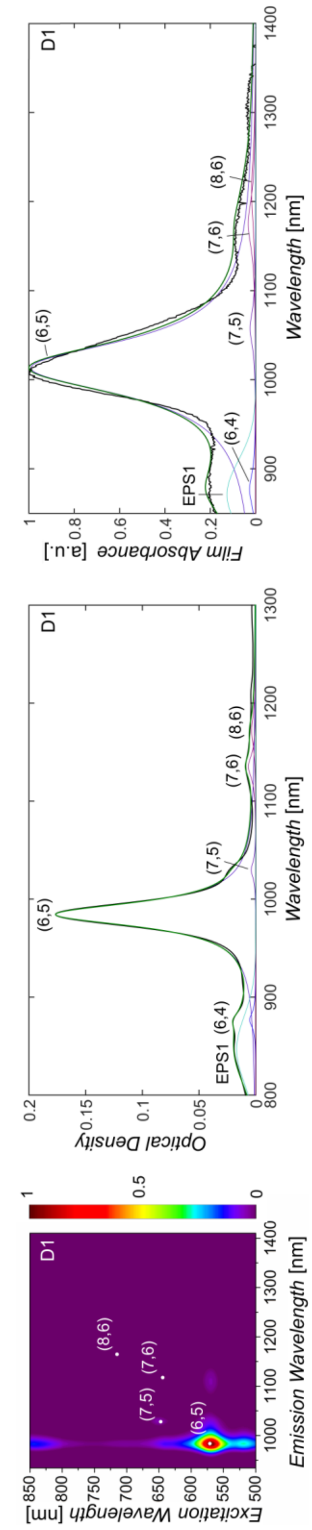

Figure S2. Photoluminescence contour map of (6,5) enriched dispersion D1 and corresponding fits of optical density and film absorbance measurements. The original measurements are shown in black, while the sum of the fits and the exciton phonon sideband (EPS) is shown in green.

J-V results

All devices in this study were characterized using *J-V* measurements. The results for single walled carbon nanotube (SWCNT) films from dispersions with increasing average nanotube diameter (D2 to D7) are shown in Figure S3 and are summarized in Table S1. The results for D1 are discussed in more detail elsewhere.(24) Although dispersion D5 had the highest amount of different chiralities, solar cells prepared from these solutions performed best. We attribute this to competing trends between an increase in mixed chiralities that first causes a decrease in fill factor (*FF*) and device performance on the one hand and on the other hand an ongoing decrease in metallic nanotubes due to repeated gel loading and washing that causes a higher semiconducting purity and therefore a larger fill factor and increased efficiencies.(35)

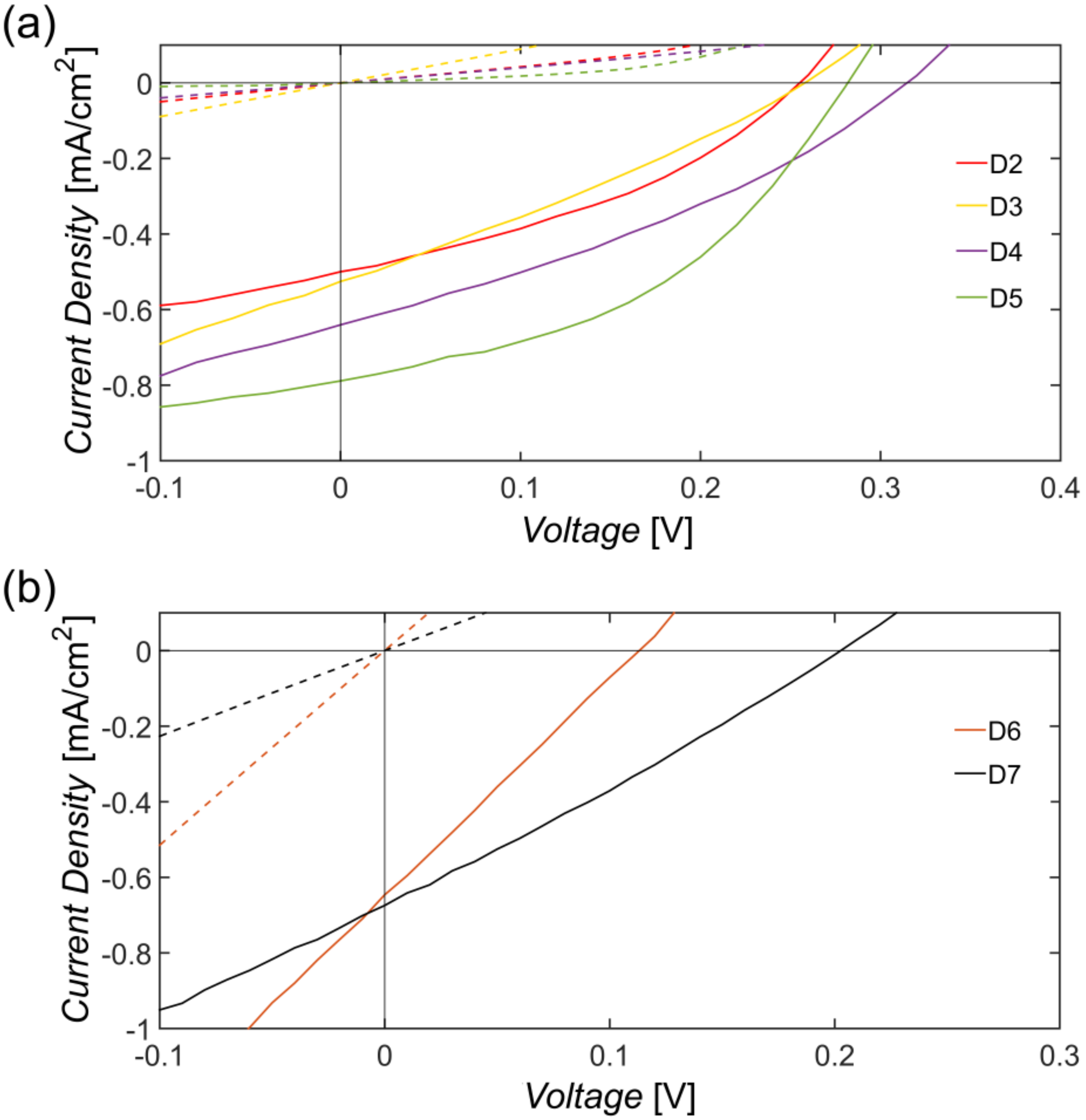

Figure S3. *J-V* measurements prepared from (a) HiPco and (b) (9,8) enriched (D6) and arc discharge dispersions (D7).

Table S1. Key performance data for solar cells prepared from HiPco (D2 to D5), (9,8) enriched (D6) and arc discharge dispersions (D7).

Dispersion	V_{OC} **(V)**	J_{SC} **(mA/cm^2)**	***FF*** **(%)**	η **(%)**
D2	0.26	0.50	37	0.05
D3	0.26	0.53	29	0.04
D4	0.32	0.64	32	0.07
D5	0.28	0.79	43	0.10
D6	0.11	0.65	25	0.02
D7	0.20	0.67	27	0.04

Internal reflectance measurements

Following the approach outlined in our last work,⁽²⁴⁾ the internal reflectance was determined for all devices by first taking a background measurement of the layer stack glass/ITO/PEDOT:PSS/C_{60}/Ag. The actual reflectance was then determined for the active solar cell. In order to not underestimate the film absorbance, reflectance values were corrected in such a way that the maximum value was equal to one. Subtracting the reflectance from 1 yielded the internal film absorbance, as exemplarily demonstrated in Figure S4 (a). Compared to nanotube film measurements on glass the shape of the internally determined film absorbance are comparable up to 1200 nm, as shown in Figure S4 (b). For larger wavelengths, background correction caused a variation in absorbance. To compensate for this, the film absorbance measured on glass was multiplied with the calculated electric field intensity $|E|^2$ at the interface of PEDOT:PSS and C_{60} to yield a realistic in-situ film absorbance in the solar cell. Subsequently the adjusted film absorbance on glass was fitted to the internal absorbance between 900 and 1200 nm. The resulting film absorbance is shown in Figure S4 (b) and was used to determine the mean maximum absorbance and the mean absorbance of each SWCNT chirality.

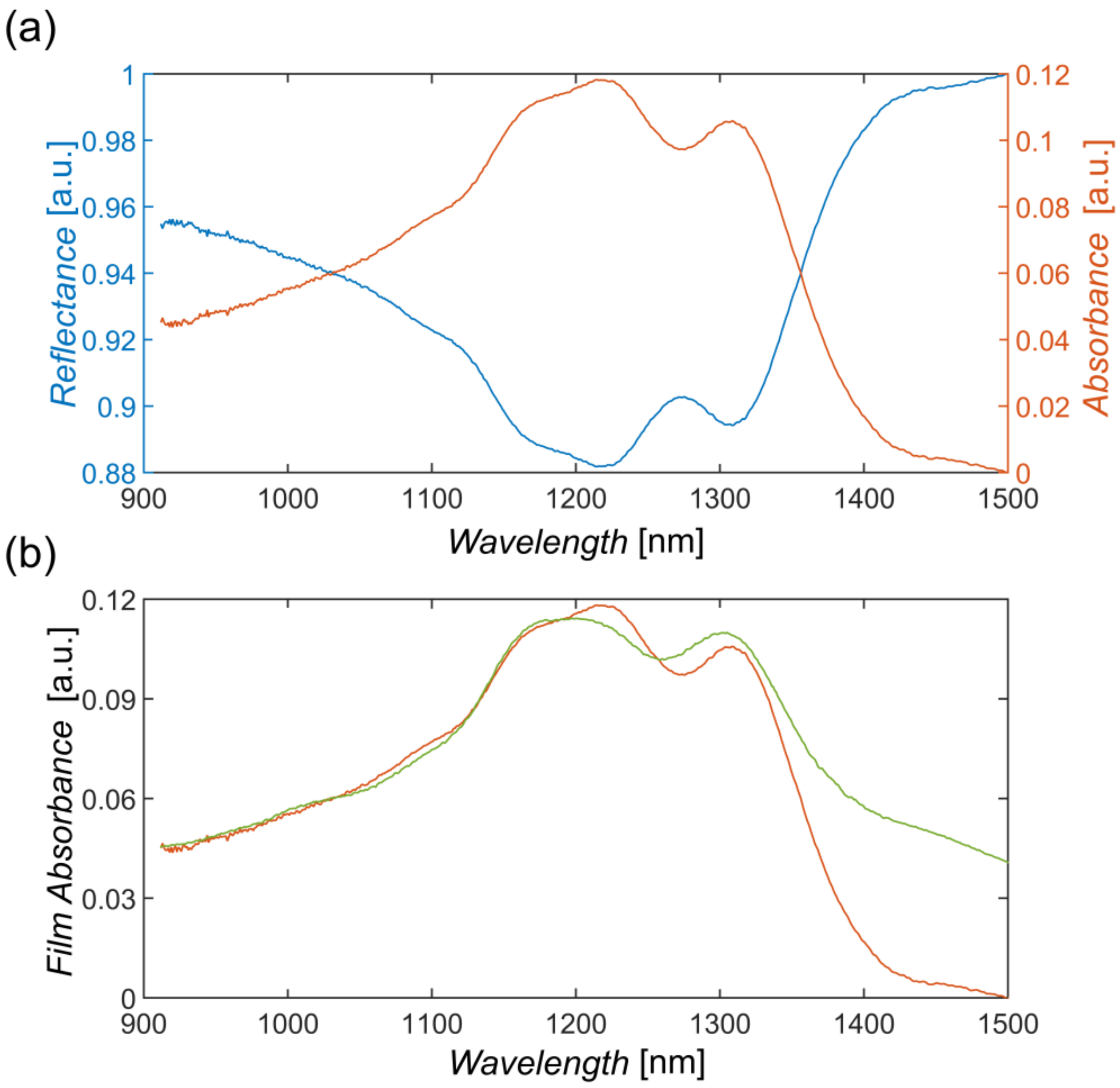

Figure S4. (a) Mean film absorbance was determined for all devices by first measuring the reflectance (blue curve). The film absorbance was obtained by subtracting the measured reflectance from 1 (red curve). (b) The nanotube film absorbance measurement on glass was multiplied with the electric field intensity $|E|^2$ to yield the expected absorbance profile of the nanotube film in-situ. This film profile was fitted to the measured film absorbance in the wavelength range 900 to 1200 nm (green curve) to yield the final in-situ SWCNT film absorbance used for further calculations.

EQE results of (6,5) enriched D1

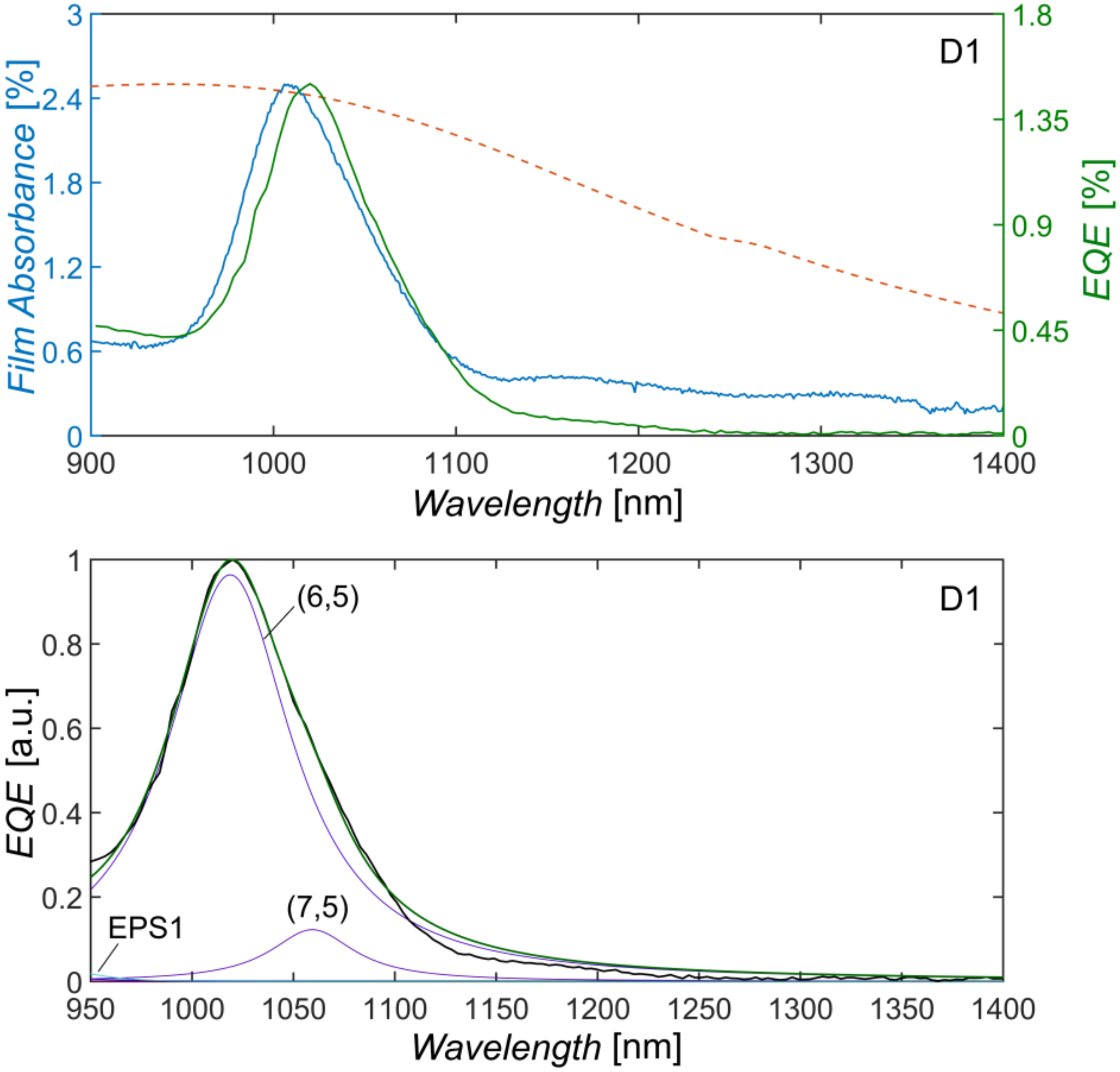

Figure S5. Film absorbance (blue), EQE (green) and electric field intensity $|E|^2$ (red) for (6,5) enriched D1 material. It is apparent, that the EQE follows the film absorbance. On the right hand side, the fit of the EQE measurement is shown in green, while the original measurement is shown in black.

EQE results for (9,8) enriched and arc discharge material

The strongly fluctuating EQE signal from nanotube films prepared from D6 and D7 is in fact noise. No current signal was measured within the wavelength regime corresponding to SWCNT positions (blue curve), as verified in Figure S6 and Figure S7.

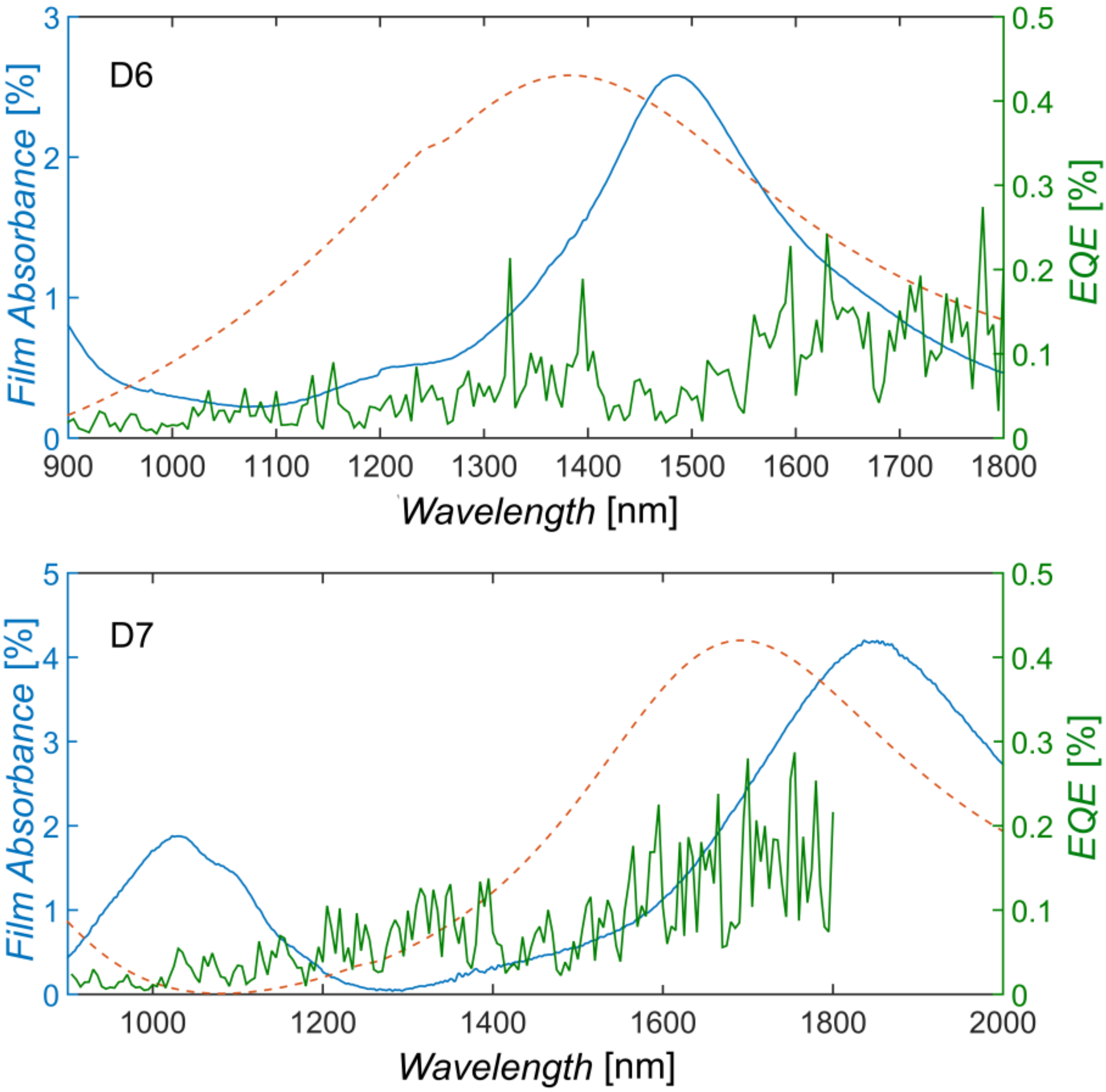

Figure S6. Film absorbance measurements along with EQE results and calculated electric field intensities for C_{60} thicknesses of 170 nm for D6 and 240 nm for D7. Although a sufficient electric field at the S_{11} absorption of the nanotubes was provided, no clear EQE signal was measureable.

Sample current from EQE measurements

In order to verify that no current was measured for (9,8) enriched (D6) and arc discharge dispersions (D7) in the wavelength regime of SWCNTs, the raw measured sample current (not corrected for light intensity) is plotted for all EQEs that are shown in Figure 4 and Figure S7. Solar cells prepared from HiPco starting material (D2 to D5) clearly show a SWCNT contribution in the wavelength regime between 800 and 1400 nm, while solar cells prepared from large diameter nanotubes (D6 and D7) deliver a photocurrent for C_{60} but show no signal for wavelengths larger than 800 nm.

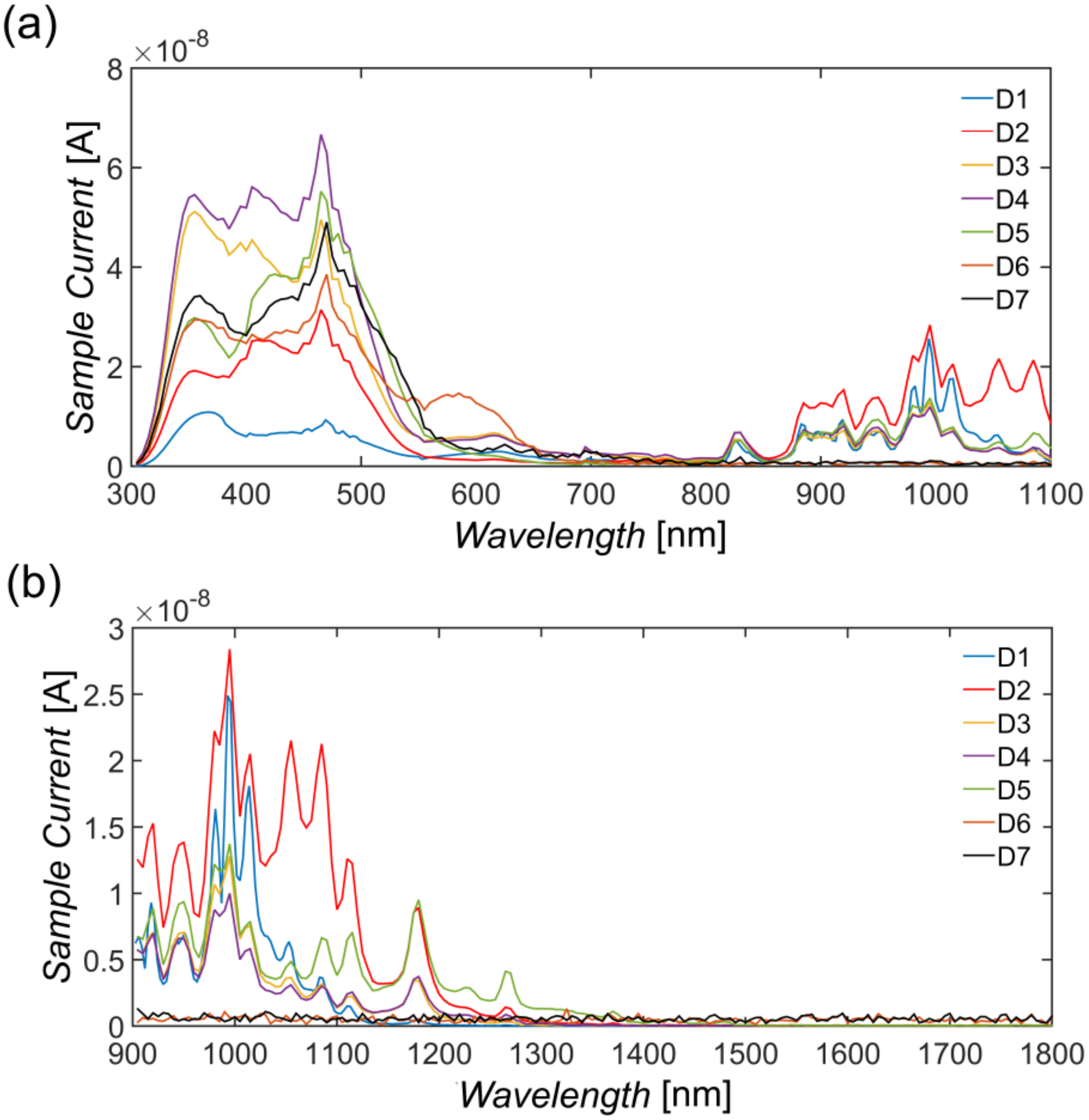

Figure S7. Measured EQE sample current of solar cells prepared from HiPco starting material (D1 to D5) and for (9,8) enriched (D6) and arc discharge (D7) dispersions. In (a) the current measured from C_{60} (300 to 700 nm) is larger than that from SWCNTs (800 to 1100 nm). (b) The current drop-off for D2 to D5 ranges between 1300 and 1400 nm. For larger wavelengths, no current could be detected, indicating a contribution from SWCNTs. Likewise, no current from D6 or D7 was measured.

Determination of different LUMO levels

According to the comprehensive work of Larson et al., large differences in LUMO energy of [6,6]-Phenyl C_{61} butyric acid methyl ester ($PC_{61}BM$) are reported in the literature.$^{(36)}$ Nevertheless, a difference of 80-90 mV in the reduction potential of $PC_{61}BM$ to that of C_{60} was found. Assuming a LUMO level of C_{60} of -4.05 eV, a 90 mV difference results in a LUMO level of $PC_{61}BM$ of -3.96 eV. Considering the differences in reduction potential reported by Kooistra for $PC_{61/71/84}BM$, namely -1.078 V, -1.089 V and -0.73 V, respectively, the LUMO levels of $PC_{71}BM$ and $PC_{84}BM$ are -3.95 eV and -4.31 eV, respectively. Considering the work of Yang et al., the same procedure can be applied to calculate the LUMO of C_{70} and C_{84}.$^{(37)}$

Exciting S_{22} of D6 and D7

By changing the C_{60} thickness, while all other layer thicknesses in the solar cell are kept constant, the electric field intensity $|E|^2$ at the position of the SWCNTs (interface of PEDOT:PSS and C_{60}) can be controlled. By choosing a C_{60} thickness of 124 nm, an $|E|^2$ distribution was generated as shown in Figure S8. Despite the electric field at the S_{22} positon of D6 and D7 being sufficiently strong, neither an EQE nor a current was detected from the SWCNTs.

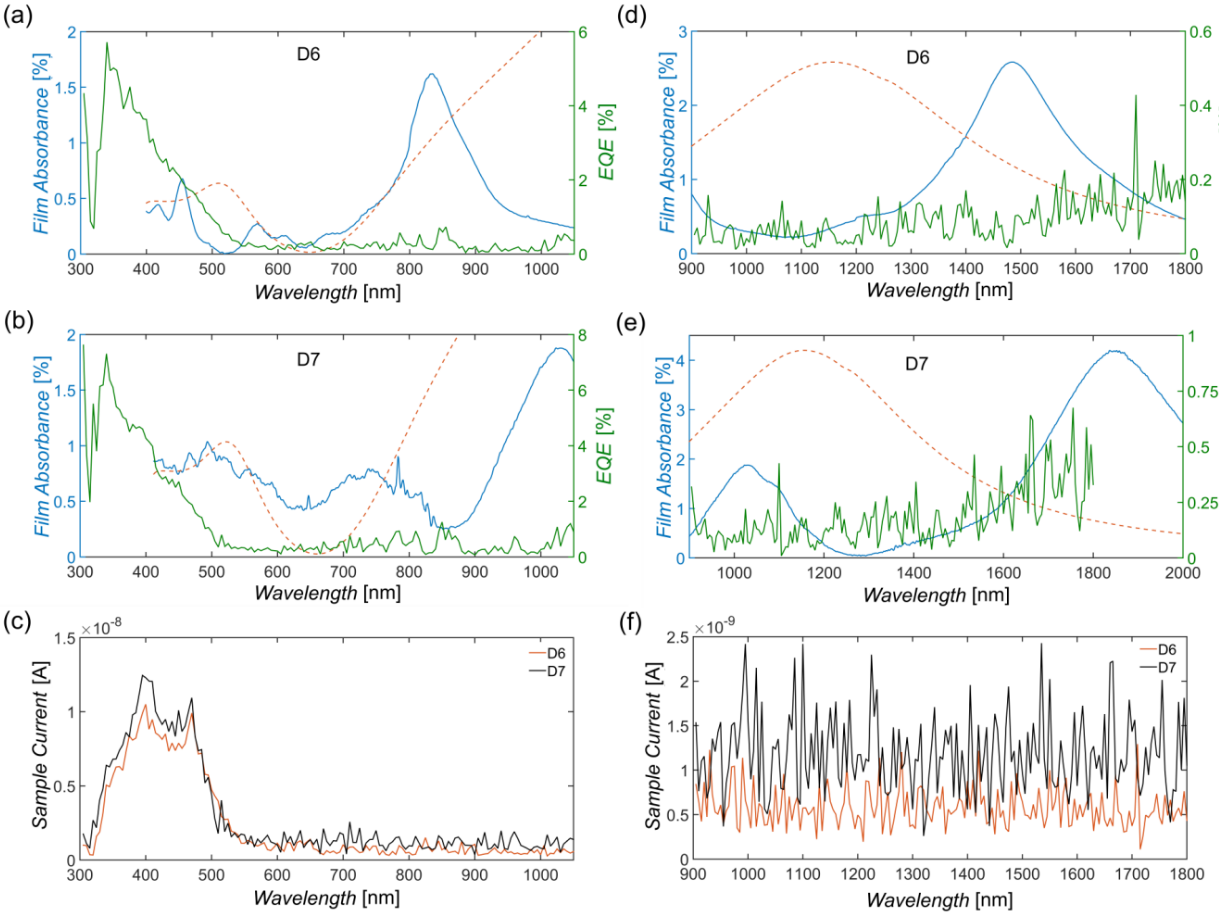

Figure S8. EQE (green), film absorbance (blue) and electric field intensity $|E|^2$ (red) for two different wavelength regimes, and raw current measurement for D6 and D7 with a clear signal from C_{60} (a,b and c) but no contribution from S_{22} or S_{11} from the SWCNTs (d, e and f). Together with EQE and film absorbance, the electric field intensity $|E|^2$ at the positions of the nanotubes is indicated with a dotted red line. For clarity, $|E|^2$ was normalized to the maximum film absorbance shown in (d) and (e).

Correction factor for exciton phonon sideband (EPS)

As outlined in the main document and proposed in Equation 7, a correction factor in the calculation of the transferred spectral weight from S_{11} to the exciton phonon sideband (EPS) is needed. As an example, the (6,5) enriched dispersion D1 was fitted with a correction factor f_1 of 0.019 in Figure S9 (a) and without f_1 in Figure S9 (b). The quality of the fit was determined via a chi square test:

$$\chi^2 = \sum \frac{(y_{fit} - y_i)^2}{y_i} \qquad \text{(S1)}$$

With y_{fit} being the sum of each Lorentzian and Gaussian at a given wavelength and y_i the measured optical density at the same wavelength. For the fits shown in Figure S9, χ^2 was calculated to be 0.056, and 0.062, for fits with and without correction factor f_1, respectively.

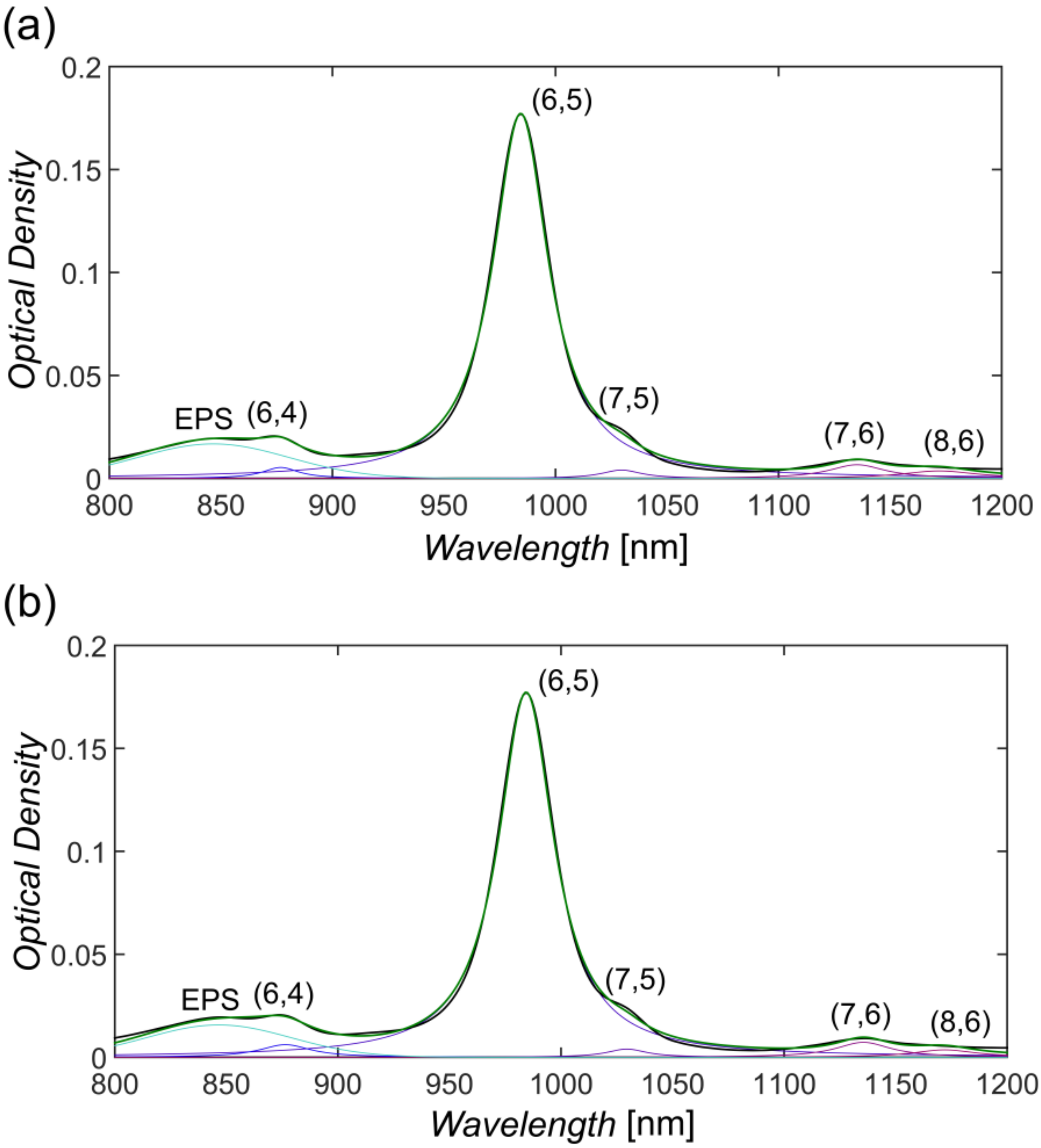

Figure S9. Two fits of the same optical density measurement (1 % sodium cholate, optical path length of 2 mm) of (6,5) enriched HiPco dispersion. (a) was fitted using a correction factor f_1 as proposed in Equation (7) in the main document, while (b) was fitted without correction factor. The better fit is obtained by using a correction factor as verified by calculating the chi-square value according to Equation S1.

Fitting results of SWCNT dispersions and films

Table S2. Center of each SWCNT in the HiPco dispersion / film measurements, respectively.

SWCNT	D1 (nm)	D2 (nm)	D3 (nm)	D4 (nm)	D5 (nm)
(6,4)	877/877	-	-	-	-
(9,1)	-	-	915/927	912/926	909/944
(8,3)	-	-	956/956	955/955	950/985
(6,5)	984/1013	984/1024	982/997	977/993	-
(7,5)	1030/1058	1030/1060	1023/1051	1024/1041	1021/1021
(10,2)	-	-	-	1054/1086	1057/1089
(9,4)	-	-	1112/1137	1114/1131	1105/1140
(8,4)	-	1120/1160	1119/1137	1122/1162	1116/1156
(7,6)	1135/1175	1138/1170	1129/1164	1127/1156	1127/1167
(9,2)	-	-	-	-	1142/1171
(8,6)	1172/1212	1172/1172	1182/1222	1183/1214	1174/1209
(10,3)	-	-	-	-	1251/1291
(9,5)	-	-	1252/1292	1254/1294	1251/1291
(11,1)	-	-	-	-	1267/1307
(8,7)	-	-	1286	1282/1310	1285/1323
(9,7)	-	-	-	1323/1323	1324/1327
(10,6)	-	-	-	1393/1393	1380/1418

Table S3. Full width at half maximum (FWHM) of all SWCNTs in HiPco dispersion / film measurements, respectively.

SWCNT	D1 (nm)	D2 (nm)	D3 (nm)	D4 (nm)	D5 (nm)
(6,4)	18.49/45.14	-	-	-	-
(9,1)	-	-	19.56/46.95	20.88/52.2	19.09/41.99
(8,3)	-	-	20.40/48.96	20.80/52	22.76/50.08
(6,5)	30.41/74.23	29.97/74.21	30.00/72.01	27.64/69.1	-
(7,5)	20.68/50.48	28.20/69.84	30.69/73.65	29.66/74.2	31.01/68.23
(10,2)	-	-	-	22.85/57.1	28.37/62.41
(9,4)	-	-	21.76/52.23	21.70/54.2	26.12/57.46
(8,4)	-	23.73/58.76	21.85/52.44	21.93/54.8	28.41/62.50
(7,6)	29.21/71.30	41.84/103.62	31.87/76.49	40.33/100.8	32.37/71.21
(9,2)	-	-	-	-	23.05/50.71
(8,6)	41.74/101.88	45.12/111.74	41.51/99.61	35.71/89.3	40.64/89.40
(10,3)	-	-	-	-	44.56/98.03
(9,5)	-	-	37.88/90.91	34.53/86.3	44.45/97.78
(11,1)	-	-	-	-	46.76/102.87
(8,7)	-	-	47.22/113.33	45.82/114.6	47.08/103.57
(9,7)	-	-	-	46.86/117.1	48.29/106.23
(10,6)	-	-	-	49.35/123.4	49.42/108.71

Table S4. Concentration of each SWCNT in the different HiPco dispersion / film measurements, respectively.

SWCNT	D1 (%)	D2 (%)	D3 (%)	D4 (%)	D5 (%)
(6,4)	1.7/1.5	-	-	-	-
(9,1)	-	-	1.2/1.4	0.4/0.4	0.7/0.7
(8,3)	-	-	1/1.1	0.4/0.4	1.1/1.2
(6,5)	91.2/91.8	11.2/11.7	8.2/8.9	1.4/1.5	-
(7,5)	1.4/1.5	60.1/58	14.4/12.8	5.4/4.9	2/1.8
(10,2)	-	-	-	1.1/1.3	4.1/3.6
(9,4)	-	-	2.1/1.9	3.0/2.7	8.3/7.3
(8,4)	-	2.6/2.8	5.9/5.3	7.9/8.4	3.8/3.4
(7,6)	3.2/2.9	21.5/22.8	38.2/37.8	18.6/16.8	4.5/4.0
(9,2)	-	-	-	-	2.8/2.8
(8,6)	2.5/2.3	4.6/4.8	19.5/20.4	34.9/34.9	25.4/24.9
(10,3)	-	-	-	-	10.2/11.0
(9,5)	-	-	4.7/5.1	8.2/9.1	12.3/12.5
(11,1)	-	-	-	-	7.1/7.6
(8,7)	-	-	4.9/5.3	12.1/13.4	10.1/10.9
(9,7)	-		-	2.6/2.9	5.3/5.7
(10,6)	-		-	4.0/3.6	2.5/2.7

Table S5. Fitting results for the exciton phonon sideband (EPS) in dispersion / film measurements.

	D1	D2	D3	D4	D5
EPS1	(6,5)	(7,5)	(7,6)	(7,6)	(8,6)
EPS2	-	(7,6)	(8,6)	(8,6)	(9,5)
FWHM1 (nm)	80/90.18	57.58/61.76	35.28/105.82	47.14/141.43	48.97/146.91
FWHM2 (nm)	-	51.82/55.58	31.75/95.24	43.61/130.84	44.07/132.22
Center1 (nm)	846.6/870.9	880.2/905.5	959.0/980.3	956.9/974.3	991.1/1011.4
Center2 (nm)	-	959.4/984.0	997.0/1021.1	996.5/1015.1	1037.7/1068.4
f_1	0.019/-0.046	0.004/-0.05	-0.043/0.071	-0.028/0.073	-0.031/0.0543

Scanning electron microscopy (SEM) images of SWCNT films

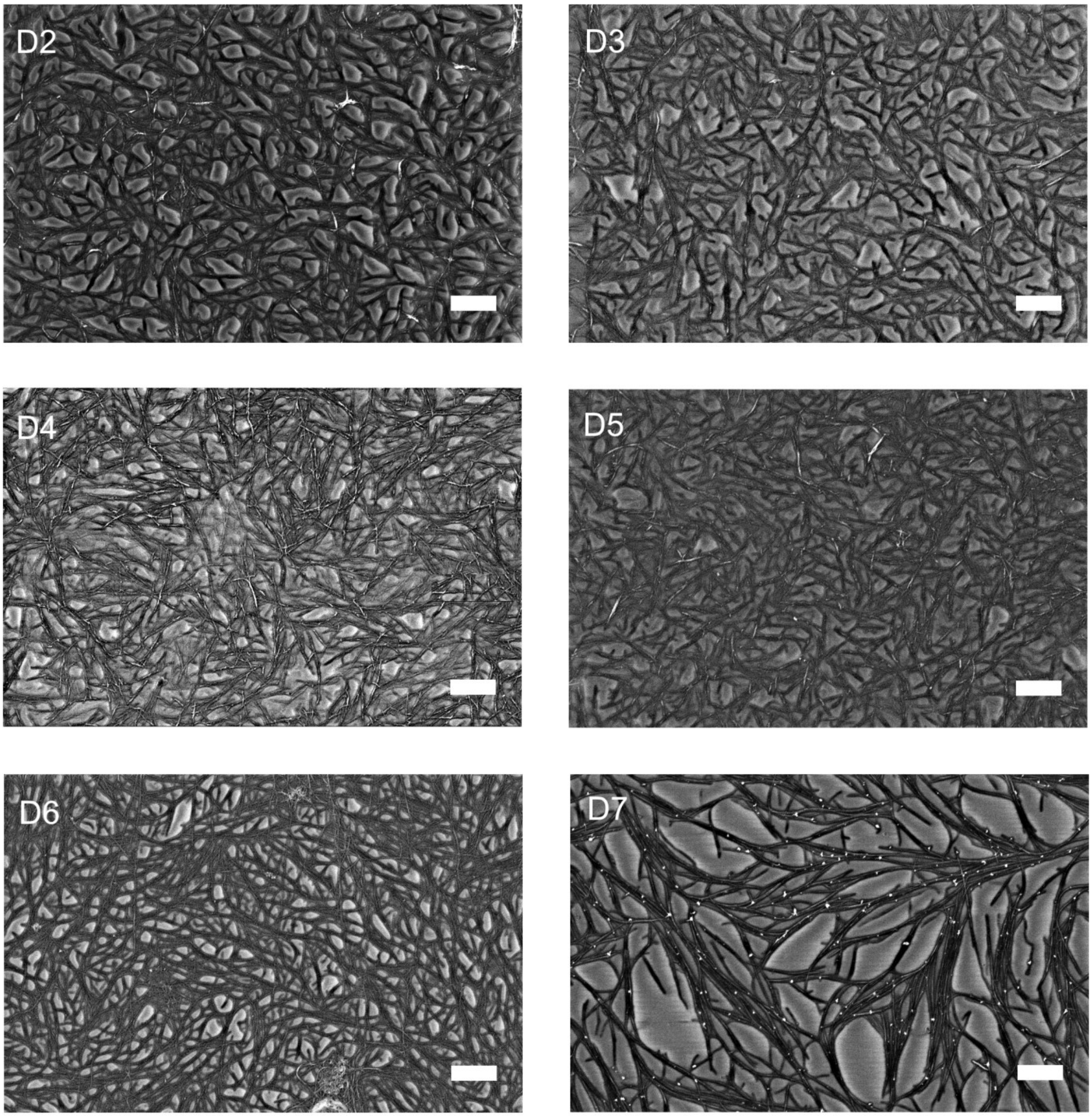

Figure S10. SEM images of all nanotube films tested in this study. While films prepared from dispersions D2 – D6 have the same film morphology, films prepared from D7 clearly have a smaller surface coverage. The scale bar in all images is 1 µm.

Background subtraction for dispersions and films

The background subtraction for dispersions was adapted from Nair et al.,$^{(13)}$ by fitting a curve of the shape $k\ /\ \lambda^b$, with *k* and *b* being fitting parameters and λ the wavelength in nm. The background of the SWCNTs films was taken to be a convolution of a Fano line shape that is proportional to $(a + \varepsilon)^2/(1 + \varepsilon^2)$ with *a* being a fitting parameter and $\varepsilon = (E - E_{res})/(\Gamma/2)$ with *E* being the energy in eV, E_{res} the resonance energy of the exciton and Γ the broadening of the peak width, and a Lorentzian that is defined as $h/(1 + ((E - E_{cent})/(\Gamma_l/2))^2)$, with *h* being the height of the peak, E_{cent} the position of the maximum and Γ_l the full width at half maximum (FWHM) of the peak.$^{(26)}$

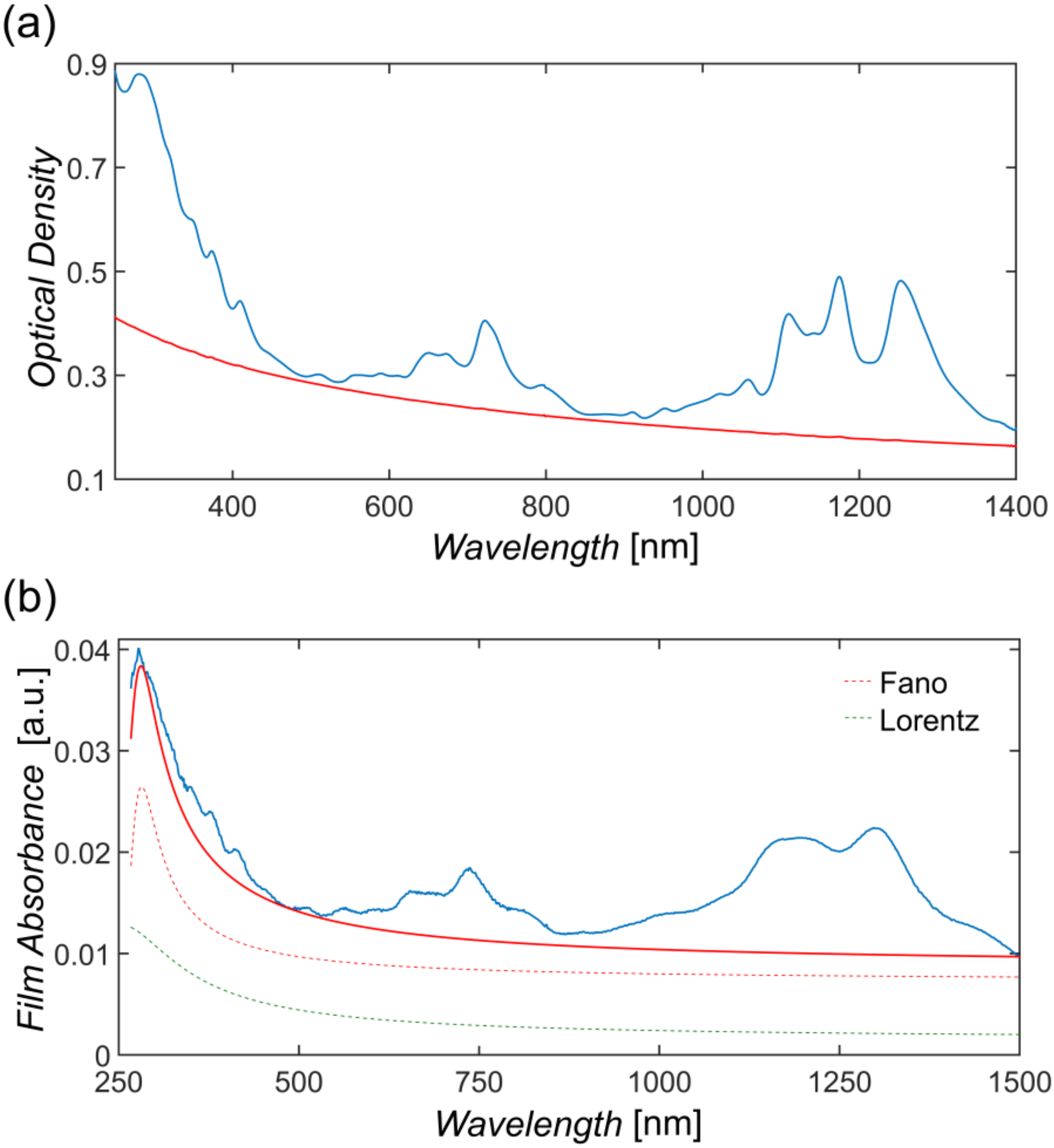

Figure S11. (a) Background subtraction of optical density measurement of dispersion D5. (b) Background subtraction of a nanotube film prepared from D5 by a convolution of a Fano and Lorentzian line shape.

7.6 References

(1) J. H. Poynting, *Philosophical Transactions of the Royal Society of London* **1884**, 175, 343; F. Richter, M. Florian, K. Henneberger, *EPL (Europhysics Letters)* **2008**, 81, 67005.

(2) J. Peatross, M. Ware, *Physics of Light and Optics*, optics.byu.edu 2015.

(3) D. J. Griffiths, R. College, *Introduction to electrodynamics*, Vol. 3, prentice Hall Upper Saddle River, NJ, 1999.

(4) H. Fujiwara, *Spectroscopic ellipsometry: principles and applications*, John Wiley & Sons, 2007.

(5) E. Hecht, *Optics*, Addison-Wesley, 2002.

(6) L. A. A. Pettersson, L. S. Roman, O. Inganäs, *Journal of Applied Physics* **1999**, 86, 487.

(7) Y. Li, *Three Dimensional Solar Cells Based on Optical Confinement Geometries*, Springer Science & Business Media, 2012.

(8) D. D. Tune, A. J. Blanch, C. J. Shearer, K. E. Moore, M. Pfohl, J. G. Shapter, B. S. Flavel, *ACS Applied Materials & Interfaces* **2015**, 7, 25857.

(9) M. Pfohl, K. Glaser, A. Graf, A. Mertens, D. D. Tune, T. Puerckhauer, A. Alam, L. Wei, Y. Chen, J. Zaumseil, A. Colsmann, R. Krupke, B. S. Flavel, *Advanced Energy Materials* **2016**, 1600890.

(10) S. M. Bachilo, M. S. Strano, C. Kittrell, R. H. Hauge, R. E. Smalley, R. B. Weisman, *Science* **2002**, 298, 2361.

(11) S. Cambré, W. Wenseleers, *Angewandte Chemie International Edition* **2011**, 50, 2764.

(12) L. Papula, in *Mathematische Formelsammlung: Für Ingenieure und Naturwissenschaftler*, Springer Fachmedien Wiesbaden, Wiesbaden **2014**, 311.

(13) N. Nair, M. L. Usrey, W.-J. Kim, R. D. Braatz, M. S. Strano, *Analytical Chemistry* **2006**, 78, 7689.

(14) J. J. Olivero, R. L. Longbothum, *Journal of Quantitative Spectroscopy and Radiative Transfer* **1977**, 17, 233.

(15) F. Schreier, *Journal of Quantitative Spectroscopy and Radiative Transfer* **2011**, 112, 1010.

(16) R. B. Weisman, S. M. Bachilo, *Nano Letters* **2003**, 3, 1235.

(17) J. J. Crochet, J. D. Sau, J. G. Duque, S. K. Doorn, M. L. Cohen, *ACS Nano* **2011**, 5, 2611; F. Wang, M. Y. Sfeir, L. Huang, X. M. H. Huang, Y. Wu, J. Kim, J. Hone, S. O'Brien, L. E. Brus, T. F. Heinz, *Physical Review Letters* **2006**, 96, 167401.

(18) V. Perebeinos, J. Tersoff, P. Avouris, *Physical review letters* **2005**, 94, 027402.

(19) Y. Kadria-Vili, S. M. Bachilo, J. L. Blackburn, R. B. Weisman, *The Journal of Physical Chemistry C* **2016**, 120, 23898.

(20) K. Liu, X. Hong, S. Choi, C. Jin, R. B. Capaz, J. Kim, W. Wang, X. Bai, S. G. Louie, E. Wang, F. Wang, *Proceedings of the National Academy of Sciences* **2014**, 111, 7564.

(21) A. V. Naumov, S. Ghosh, D. A. Tsyboulski, S. M. Bachilo, R. B. Weisman, *ACS Nano* **2011**, 5, 1639.

(22) S. R. Sanchez, S. M. Bachilo, Y. Kadria-Vili, C.-W. Lin, R. B. Weisman, *Nano Letters* **2016**, 16, 6903.

(23) R. M. Jain, R. Howden, K. Tvrdy, S. Shimizu, A. J. Hilmer, T. P. McNicholas, K. K. Gleason, M. S. Strano, *Adv Mater* **2012**, 24, 4436.

(24) M. Pfohl, K. Glaser, J. Ludwig, D. D. Tune, S. Dehm, C. Kayser, A. Colsmann, R. Krupke, B. S. Flavel, *Advanced Energy Materials* **2016**, 6, 1501345.

(25) S. Berciaud, L. Cognet, P. Poulin, R. B. Weisman, B. Lounis, *Nano Letters* **2007**, 7, 1203.

(26) Y. Tian, H. Jiang, I. V. Anoshkin, L. J. I. Kauppinen, K. Mustonen, A. G. Nasibulin, E. I. Kauppinen, *RSC Advances* **2015**, 5, 102974.

(27) Y. Tian, H. Jiang, J. v. Pfaler, Z. Zhu, A. G. Nasibulin, T. Nikitin, B. Aitchison, L. Khriachtchev, D. P. Brown, E. I. Kauppinen, *The Journal of Physical Chemistry Letters* **2010**, 1, 1143.

(28) A. J. Ferguson, A.-M. Dowgiallo, D. J. Bindl, K. S. Mistry, O. G. Reid, N. Kopidakis, M. S. Arnold, J. L. Blackburn, *Physical Review B* **2015**, 91, 245311.

(29) R. J. Meier, *Vibrational Spectroscopy* **2005**, 39, 266.

(30) G. F. Burkhard, E. T. Hoke, M. D. McGehee, *Advanced Materials* **2010**, 22, 3293.

(31) E. D. Palik, *Handbook of optical constants of solids*, Vol. 3, Academic press, 1998; S. L. Ren, Y. Wang, A. M. Rao, E. McRae, J. M. Holden, T. Hager, K. Wang, W. T. Lee, H. F. Ni, J. Selegue, P. C. Eklund, *Applied Physics Letters* **1991**, 59, 2678.

(32) J. A. Fagan, J. R. Simpson, B. J. Landi, L. J. Richter, I. Mandelbaum, V. Bajpai, D. L. Ho, R. Raffaelle, A. R. H. Walker, B. J. Bauer, E. K. Hobbie, *Physical Review Letters* **2007**, 98, 147402; Y. Battie, D. Jamon, A. En Naciri, J.-S. Lauret, A. Loiseau, *Applied Physics Letters* **2013**, 102, 091909.

(33) D. J. Bindl, M. S. Arnold, *The Journal of Physical Chemistry C* **2013**, 117, 2390.

(34) A. Armin, M. Velusamy, P. Wolfer, Y. Zhang, P. L. Burn, P. Meredith, A. Pivrikas, *ACS Photonics* **2014**, 1, 173.

(35) G. S. Tulevski, A. D. Franklin, A. Afzali, *ACS Nano* **2013**, 7, 2971.

(36) B. W. Larson, J. B. Whitaker, X.-B. Wang, A. A. Popov, G. Rumbles, N. Kopidakis, S. H. Strauss, O. V. Boltalina, *The Journal of Physical Chemistry C* **2013**, 117, 14958.

(37) Y. Yang, F. Arias, L. Echegoyen, L. P. F. Chibante, S. Flanagan, A. Robertson, L. J. Wilson, *Journal of the American Chemical Society* **1995**, 117, 7801.